The University of Nottingham

School of Physics & Astronomy

DLTS CHARACTERISATION OF DEFECTS IN III-V COMPOUND SEMICONDUCTORS GROWN BY MBE

by

RIAZ HUSSAIN MARI
M.Sc. (Physics)

Thesis submitted to the University of Nottingham for

the degree of Doctor of Philosophy

August 2011

ABSTRACT

The interest in the growth of III-V compound semiconductors such as GaAs and AlGaAs on high index planes has increased tremendously over the last few years. The structural, optical and electrical properties of III-V based structures are found to improve by growing on (n11) planes. For example the amphoteric nature of silicon (Si) facilitates the Molecular Beam Epitaxy (MBE) growth of p-type GaAs/AlGaAs heterostructures on (311)A that have higher hole mobilities than those based on the conventional Be-doped p-type on (100) GaAs plane. The incorporation of intentional impurities, such as Si or Be in III-V semiconductors, have desirable effects in terms of controlling the electrical conductivity of the materials. However, other unintentionally incorporated impurities and defects have deleterious effects on the electrical and optical properties of III-V based devices.

In this thesis, current-voltage-temperature (I-V-T), capacitance-voltage (C-V) Deep Level Transient Spectroscopy (DLTS) and Laplace DLTS techniques have been used to investigate defects in several MBE III-V epilayers and modulated structures grown both on the conventional (100) and non-(100) GaAs substrates. These include: (i) n-type silicon-doped (n11)B (n = 2-5) GaAs epitaxial layers; (ii) n-type silicon-doped (100) and (311)B GaAs/AlGaAs multi-quantum well (MQW); (iii) n-type silicon-doped (100) MQWs grown at different substrate temperatures, arsenic overpressures and arsenic species (As_2 and As_4); (iv) p-type Be-doped (100) and (311)A AlGaAs epitaxial layers; (v) GaAs/AlGaAs two dimensional electron gas (2DEG); (vi) commercially grown high electron mobility transistors (HEMT).

The main findings of the experimental results are given in the following:

(i) n-type silicon-doped (n11)B (n = 2-5) GaAs: the overall density of defects is highest in (211)B and lowest in (511)B. The number of detected defects is minimum in (511)B. The common carbon background impurity in MBE is observed only in (100) substrates.

(ii) n-type silicon-doped (100) and (311)B GaAs/AlGaAs MQWs: the concentration of the only trap is higher in (100) than in (311)B orientation. Furthermore, in (100) the observed trap electrically charged, while it has neutral nature in (311)B.

(iii) n-type silicon-doped (100) MQWs grown at different substrate temperatures, arsenic overpressures and arsenic species (As_2 and As_4): the average trap concentration for As_2 samples is lower than As_4 samples. In addition, the concentration of the common V_{As}-related point defect decreases with increasing growth temperature and arsenic overpressure.

(iv) p-type Be-doped (100) and (311)A AlGaAs: the number of hole traps in (311)A decreases from five to one when the Be-doping level varies from 1×10^{16} cm^{-3} to 1×10^{17} cm^{-3}. For (100) the detected hole levels are three, four and two for Be-concentrations of 1×10^{16} cm^{-3} , 3×10^{16} cm^{-3} and 1×10^{17} cm^{-3}, respectively. In addition, an electron emitting level is observed only in (100) samples doped to 1×10^{17} cm^{-3}.

(v) GaAs/AlGaAs 2DEG and HEMT devices: one major defect, assigned to the DX center, is common in both in-house grown 2DEG and commercially HEMT devices. It behaves as a generation-recombination center, and its concentration is directly related to the silicon doping level in the AlGaAs layer. The HEMT

devices which showed poor frequency response are found to have the highest concentration of the DX center.

PUBLICATIONS

1. **Riaz H Mari**, Muhammad Shafi, Mohsin Aziz, Almontaser Khatab, David Taylor, Mohamed Henini, *"Electrical characterisation of deep level defects in Be-doped AlGaAs grown on (100) and (311)A GaAs substrates by MBE"* Nanoscale Research Letters **6**, 180 (2011).
2. D. L. Sales, E. Guerrero, J. F. Rodrigo, P. L. Galindo, A. Yáñez, M. Shafi, A. Khatab, **R. H. Mari**, M. Henini, S. Novikov, M. F. Chisholm, and S. I. Molina, *"Distribution of Bismuth Atoms in Epitaxial GaAsBi"* Applied Physics Letters **98**, 101902 (2011).
3. **Riaz H Mari**, M Aziz, M Shafi, A Khatab, D Taylor, and M Henini, *"Effect of epitaxial layer thickness on the deep level defects in MBE grown n-type* $Al_{0.33}Ga_{0.67}As$" (**Submitted** to Physica Status Solidi C 2011)
4. A. Khatab, M Shafi, **Riaz H Mari**, M Aziz, M Henini, M. Sadeghi and S. Wang, *"Comparative Optical Studies of GaInAs/GaAs Quantum Wells Grown by MBE on Conventional and High Index GaAs Planes"* (**Submitted** to Physica Status Solidi C 2011)
5. M. Shafi, **R. H. Mari**, A. Khatab, M. Henini, A. Polimeni, M. Capizzi and M. Hopkinson, *"Deep Levels in* $GaAs_{1-x}N_x$ *Grown by Molecular Beam Epitaxy"* (**Submitted** to Journal of Applied Physics 2011)
6. J. Ibáñez, R. Oliva, M. De la Mare, M. Schmidbauer, S. Hernández, P. Pellegrino, D. J. Scurr, R. Cuscó, L. Artús, M. Shafi, **R. H. Mari**, M. Henini, Q. Zhuang, A. Godenir, and A. Krier, *"Structural and Optical Properties of Dilute*

InAsN Grown by Molecular Beam Epitaxy" Journal of Applied Physics **108,** 103504 (2010)

7. M. Shafi, **R. H. Mari,** A. Khatab, D. Taylor and M. Henini, *"Deep-level Transient Spectroscopy of GaAs/AlGaAs Multi-Quantum Wells Grown on (100) and (311)B GaAs Substrates"* Nanoscale Research Letters **5,** 1948–1951 (2010).
8. R. Kudrawiec, P. Poloczek, J. Misiewiciz, M. Shafi, J. Ibáñez, **R. H. Mari,** M. Henini, M. Schmidbauer, S. V. Novikov, L. Turyanska, S. I. Molina, D. L. Sales and M. F. Chisholm, *"Photomodulated transmittance of GaAsBi layers grown on (100) and (311)B GaAs substrates"* Microelectronics Journal **40,** 537 (2009).
9. M. Shafi, **R. H. Mari,** M. Henini, D. Taylor and M. Hopkinson, *"Electrical Properties of Nitrogen-related Defects in n-type GaAsN Grown by Molecular Beam Epitaxy"*, Physica Status Solidi C **6,** No. 12, 2652 (2009).
10. **R. H. Mari,** M. Shafi, M. Henini and D. Taylor, *"Laplace DLTS of Molecular Beam Epitaxy GaAs Grown on (100) and (211)B Substrates"*, Physica Status Solidi C **6,** No. 12, 2873 (2009).
11. R. Kudrawiec, M. Syperek, P. Poloczek, J. Misiewiciz, **R. H. Mari,** M. Shafi, M. Henini, Y. Gobato, S. V. Novikov, J. Ibáñez, M. Schmidbauer and S. I. Molina, *"Carrier localization in GaAsBi Probed by Photomodulated Transmittance and Photoluminescence"* Journal of Applied Physics **106,** 023518 (2009).

CONFERENCE PRESENTATIONS

1. Oral presentation in Semiconducting and Insulating Materials Conference (SIMC- XV), held at the University of Vilinius, Lithuania, June 15-19, (2009), *"Laplace DLTS of Molecular Beam Epitaxy GaAs Grown on High Index GaAs Substrates"*
2. Poster presented in Essex meeting of COST Action MP0805 on 'Novel Gain Materials and Devices Based on III-V-N Compounds', 24th May (2009), *"High Resolution Laplace DLTS investigation if Nitrogen related defects in dilute n-type GaAsN"*
3. Poster presentation at Semiconducting and Insulating Materials Conference (SIMC- XVI), held at the KTH, Kista-Stokholm, Sweden, June 20-23, (2011), *"Laplace Deep-level Transient Spectroscopy of Cubic-GaN Grown by MBE on SiC"*

ACKNOWLEDGEMENTS

First and foremost, I would like to express my deepest gratitude to my supervisor Professor M. Henini for his valuable guidance and support during my PhD. Without his encouragement and guidance, the completion of this work would not have been possible. I would also like to thank Dr. James Sharp for his valuable suggestions.

Thanks go to Robert Chettle for providing electronic support, Jas Chauhan and David Taylor for their assistance in processing the Schottky diodes, Prof. Abdelmadjid Mesli (IM2NP; Marseille, France) for helpful discussions regarding DLTS and Laplace DLTS data analysis, and all other collaborators named in the publications list.

The financial support of University of Sindh, Jamshoro and Higher Education Commission of Pakistan (HEC) is very much appreciated.

Finally, I would like to thank my parents and my family for their love and unconditional support during all these years, and I wish to dedicate this thesis to them.

TABLE OF CONTENTS

List of Figures

List of Tables

CHAPTER 1

INTRODUCTION

Practical semiconductors contain a number of intrinsic and extrinsic defects with energies located in their band gaps. These defects severely affect the device performance. For example the non-radiative defects degrade the efficiency of light emitting diodes (LEDs) and lasers.

Overall, there is a general lack of knowledge of the key parameters of the defects involved, and therefore it is very important to characterise these defects and provide feedback information to the growers to improve the quality of the semiconductor materials.

The characterisation techniques are divided in two main categories, namely optical and electrical. It is well known that optical techniques such as photoluminescence can only detect shallow and radiative defects. However, conventional deep level transient spectroscopy (DLTS) and high resolution Laplace DLTS are powerful electrical techniques that can be used to probe the existence of deep centers, localized states, disorder effects due to crystalline imperfections, impurities and nonradioactive defects.

1.1 BACKGROUND

The revolutionary importance of semiconductor materials was realised in 1947 after the invention of the transistor, which was first fabricated from the elemental semiconductor germanium (Ge). Ge was considered as the most useful technological material for about one decade. In 1960 silicon (Si) replaced Ge due to its thermal stability, availability of stable oxide (SiO_2), abundance, and the development of Si-based integrated circuits. The small bandgap energy (1.1 eV at room temperature), indirect bandgap nature, and low carrier mobility of Si limit its applications for (i) electronic devices operating at high temperatures, and (ii) optoelectronic devices emitting in the visible spectrum range [1]. After the elemental semiconductors Ge and Si, gallium arsenide (GaAs), a III-V compound semiconductor, was considered as a potential candidate in semiconductor technology due to its versatile properties such as wide energy gap (1.42 eV at room temperature) and direct bandgap nature. In addition, the energy bandgap can be tuned up to the bandgap (2.16 eV at room temperature) of aluminium arsenide (AlAs) by substituting Ga atoms with Al atoms and forming the aluminium gallium arsenide (AlGaAs), a ternary III-V compound semiconductor.

Traditionally, Si and Be are used as donor (n-type) and acceptor (p-type) dopants, respectively, in Molecular Beam Epitaxy (MBE) GaAs and AlGaAs grown on (100) substrate [2-5]. Previously reported studies suggest that the electrical and optical properties of Si-doped GaAs and AlGaAs are better than those of Be doped layers [6, 7]. Furthermore, it was also observed that the electron mobility in Si-doped bulk GaAs and GaAs/AlGaAs single heterostructures is higher than the hole mobility of similar Be-doped MBE structures grown on (100) GaAs substrate. In order to obtain p-type GaAs, AlGaAs and GaAs/AlGaAs heterostructures with improved crystal

quality, electrical and optical properties, Si can be used as an acceptor dopant. Si is a group IVA element, and in III-V semiconductors it can occupy either a Ga site (donor; n-type) or an As site (acceptor; p-type). In MBE, the occupation of this amphoteric dopant depends on the substrate orientation. For example, Si incorporates preferentially as a donor in (N11)B and as an acceptor in (N11)A GaAs surfaces, where N = 1,2,3 [8], A and B refer to a Ga and an As terminated surface, respectively. The Si occupancy can also be influenced by the growth temperature [9] and As/Ga flux ratio [7]. Transmission Electron Microscopy (TEM) [10] studies also confirm that better surface morphologies are obtained for Si-doped GaAs MBE grown on (110) as compared to Be-doped samples. TEM results elucidated that the defects observed between the buffer layer and the doped epitaxial layer extend more in Be-doped samples than in Si-doped samples. It was argued that the extension of these defects into the Be-doped epitaxial layers may be due to Be-diffusion and segregation. To explore the effect of substrate orientation on the incorporation of nonradiative defects in epitaxial layers and heterostructures, two sets of n-type silicon-doped GaAs and GaAs/AlGaAs MQWs were investigated. The orientations of the GaAs substrates employed were (n11)B where n = 2-5.

The incorporation of Be in AlGaAs grown on (100) and (311)A has been investigated by Galbiati et al. [11]. Photoluminescence and Hall measurement results [11] confirmed that carrier mobility and optical properties of AlGaAs grown on (311)A are better than those grown on (100) substrate. The improvement in mobility and optical properties is likely to be due in part to the reduction of defects in (311)A during MBE growth. In order to confirm the assumption of reduced defects in AlGaAs epitaxial layers grown on (311)A, DLTS and Laplace DLTS measurements are carried out.

In addition to high index planes, the growth of GaAs and AlGaAs also depends on the use of arsenic species such as dimer (As_2) and tetramer (As_4). It is believed that the population of Ga and As atoms at the surface depends on substrate temperature and relative As-to-Ga ratio reaching the surface [12]. As_4 has a higher evaporation probability as compared to Ga, and therefore it is possible that the deficiency of As atoms in GaAs can cause arsenic-vacancy (V_{As}) defects by using As_4. The sticking efficiency of As_2 is reported to be greater than that of As_4. Thus in order to overcome the As deficiency in GaAs, As_2 can be used instead of As_4. Part of this thesis contains a comparative electrical study of GaAs/AlGaAs multi-quantum well structures using As_2 and As_4.

It is well known that the carrier mobility in modulated semiconductor structures, such as two dimensional electron gases (2DEGs) and high electron mobility transistors (HEMTs), is much higher than in GaAs epilayers. This is due to the presence of impurities in the host materials and scattering processes [13]. In this work the relationship between defects and Si-doping concentration in the AlGaAs layer of 2DEG devices has been studied. In addition, this study includes the investigation of defects in commercial HEMT devices.

1.2 OBJECTIVES

The purpose of this thesis is to investigate the electrically active deep level defects in III-V based semiconductor structures, namely:

(i) Si-doped MBE GaAs grown on (211)B, (311)B, (411)B, (511)B GaAs orientations. The properties of these structures will be compared with conventional Si-doped structures grown on the (100) plane.

(ii) Be-doped MBE AlGaAs epitaxial layers grown on (100) and (311)A GaAs substrates.

(iii) Si-doped GaAs/AlGaAs multi-quantum well structures grown on (100) and (311)B substrates.

(iv) Si-doped GaAs/AlGaAs grown on (100) plane using different arsenic species (As_2 and As_4), growth temperatures, and arsenic overpressures.

(v) AlGaAs/GaAs two dimensional electron gas (2DEG) systems having different Si-doping concentrations in the AlGaAs layer, and commercial High Electron Mobility Transistor (HEMT) devices.

1.3 SCHEME OF THE THESIS

This thesis is organised as follows:

Chapter 1 contains the background and research objectives.

Chapter 2 is devoted to the description of the fundamental concepts of semiconductors, crystal structure, principles of heterostructure devices, and the properties of GaAs and AlGaAs.

Chapter 3 provides information on defects in semiconductors, generation-recombination centers, kinetics of defects, and literature survey of defects in GaAs and AlGaAs. The importance and growth of III-V compound materials on high index planes will be also covered.

Chapter 4 explains the experimental techniques used in this thesis including Deep Level Transient Spectroscopy (DLTS) and Laplace DLTS. The description of their hardware and software implementation will be presented.

Chapter 5 gives the details of the samples investigated in thesis and the experimental procedures.

Chapter 6 is based on the DLTS and Laplace DLTS experimental results for a set of n-type Si-doped GaAs samples grown on (100), (211)B, (311)B, (411)B and (511)B GaAs substrates.

Chapter 7 contains DLTS and Laplace DLTS experimental results for a set of Be-doped $Al_{0.29}Ga_{0.61}As$ samples grown on (100) and (311)A GaAs substrates with Be doping ranging from 1×10^{16} -1×10^{17} cm^{-3}.

Chapter 8 is divided into two sections: (i) DLTS and Laplace DLTS experimental results of $GaAs/Al_{0.33}Ga_{0.66}As$ multi-quantum well structures grown on (100) and (311)B GaAs substrates; (ii) experimental results of $GaAs/Al_{0.33}Ga_{0.66}As$ multi-quantum well structures grown on (100) at different growth temperatures, arsenic overpressures, and arsenic species (As_2 and As_4).

Chapter 9 deals with DLTS and Laplace DLTS investigation of defects in in-house MBE grown 2DEG and commercially grown High Electron Mobility Transistors (HEMT) devices.

Chapter 10 is based on the overall conclusion of the research work carried out in this thesis and suggestions about future work.

CHAPTER 2

FUNDAMENTAL CONCEPTS OF SEMICONDUCTORS

This chapter describes the fundamental concepts of semiconductors, including crystal structure, density of states, semiconductor band gap, heterostructures and carrier mobility. In addition, some important properties of III-V compound materials such as GaAs and AlGaAs are discussed generally.

2.1 INTRODUCTION

Semiconductor materials are the backbone of modern electronic industry and according to the economical surveys, it was expected that in 2010 the volume of the electronic industry, which is based on the fabrication of semiconductor devices [14], will be about 10% of the gross world product (GWP). This industry is based on the production of computers, cell phones, light emitting diodes (LED), detectors, solar cells, etc from different semiconductor materials.

The classification of solid materials is generally based on the energy gap between their conduction and valence bands. Most of the common materials have energy gaps in the range from zero to few electron volts (eV). According to this classification principle materials having an energy gap of ~0 eV are referred to as metals or semi-metals. On the other hand, materials with energy gaps greater than 3 eV are frequently known as insulators, whereas semiconductor materials have energy gaps spanning from ~0.1 eV to ~ 3 eV between its conduction and valence bands [15].

According to the resistivity theory, semiconductor materials are also defined as the materials having resistivities from 10^{-2} Ω cm to 10^{9} Ω cm.

Semiconductor materials are divided into two categories known as elemental and compound materials. Examples of elemental semiconductors are Silicon (Si), Germanium (Ge), and carbon (C), which belong to group IV elements in the periodic table. Compound semiconductor materials are formed by adding two or more than two elements from the different groups of the periodic table. For example GaAs is the most familiar compound semiconductor material, which is formed by combining Gallium (Ga), group III element, with Arsenic (As), group V element. Other III-V compound semiconductors include InP and GaP. Another important class of semiconductors is known as II-VI compound materials such as Zinc Sulphide (ZnS) and Mercury Cadmium Telluride (HgCdTe).

The electrical properties of the semiconductors can be controlled in different ways, such as temperature, variation of the amount of shallow impurity incorporation, and by electrical or optical injections. In the following section two different types of semiconductors based on their purity are discussed.

2.2 INTRINSIC AND EXTRINSIC SEMICONDUCTORS

Undoped semiconductors are known as intrinsic semiconductors. This type of semiconductors is considered to be pure from any impurity that can play an important role by changing the electrical properties of the material. Intrinsic semiconductors posses equal number of electrons and holes in their respective bands at 0K and behave as insulators at this low temperature. However, the current can flow through these types of materials at a certain temperature which is sufficient to provide the thermal energy to excite the electrons from valence band to conduction

band. The photo-excitation is another source of excitation of electrons from valence band to conduction band and increases semiconductor material's conductivity.

If a certain amount of impurity atoms is added to a pure semiconductor, it is said to be an extrinsic semiconductor, and this process is known as doping. The electrical properties of the resulting material are moderated by doping level. The dopant atoms can produce an excess number of electrons or holes, and create an n-or p-type semiconductor, respectively. For example, incorporation of Si and Be (beryllium) in GaAs produces n- and p-type GaAs, respectively. Further details of the doping mechanisms will be covered in chapter 3.

2.3 CRYSTAL STRUCTURE

Semiconductor materials are also known as crystalline materials. Crystalline property of any material depends on the process of arrangement of their atoms. In an ideal case the crystal structure is defined as the structure which is formed by the periodic repetition of an infinite number of atoms. In terms of a lattice, the crystal structure can be defined as a group of atoms located at each lattice point. The group of atoms form basis and the repetition of the basis in space results in the form of a crystal structure.

The basis is the building block of a crystal structure. It is composed of a number of atoms. In some cases, it consists of only a single atom [16, 17]. An example of the basis is shown in Figure 2.1 for two atoms.

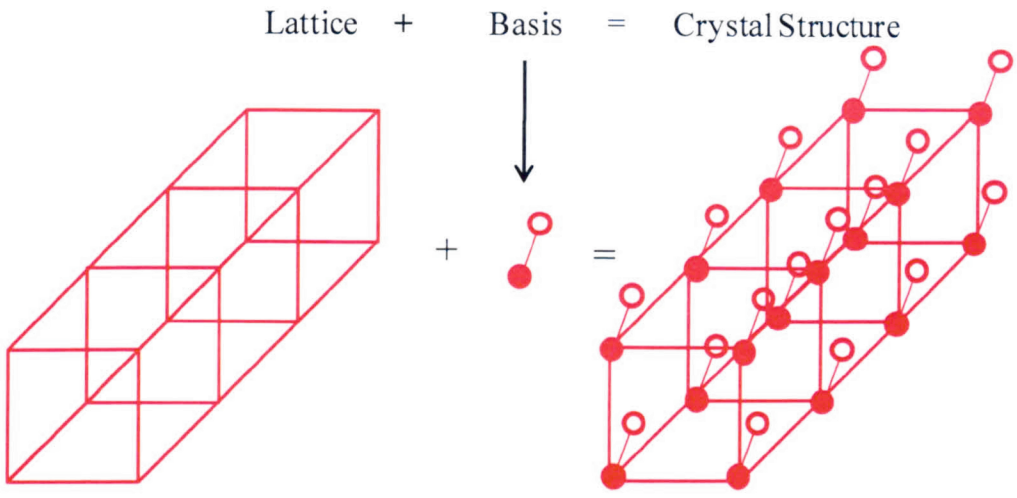

Figure 2.1: The formation of the crystal structure from the combination of lattice and basis is shown. The basis consists of two atoms shown as solid and open circles.

The lattice is defined as the proper position where the basis lies to form a crystal structure (Figure 2.1 and Figure 2.2). The site of the regular arrangement of the basis in the crystal structure is known as the lattice point. It can be obtained by the primitive translation vectors indicated by $\mathbf{a_1}$, $\mathbf{a_2}$, and $\mathbf{a_3}$ (Figure 2.2). These translation vectors are used to specify the position of a point that exists within the lattice. The mathematical expression used to locate the position of the points is given by equation 2.1.

$$\mathbf{C} = c_1\mathbf{a_1} + c_2\mathbf{a_2} + c_3\mathbf{a_3} \qquad 2.1$$

where $\mathbf{C}$ is the point that is located in the crystal structure, c_1, c_2, and c_3 are the integers corresponding to three different axes, and $\mathbf{a_1}$, $\mathbf{a_2}$, and $\mathbf{a_3}$ are the fundamental translation vectors.

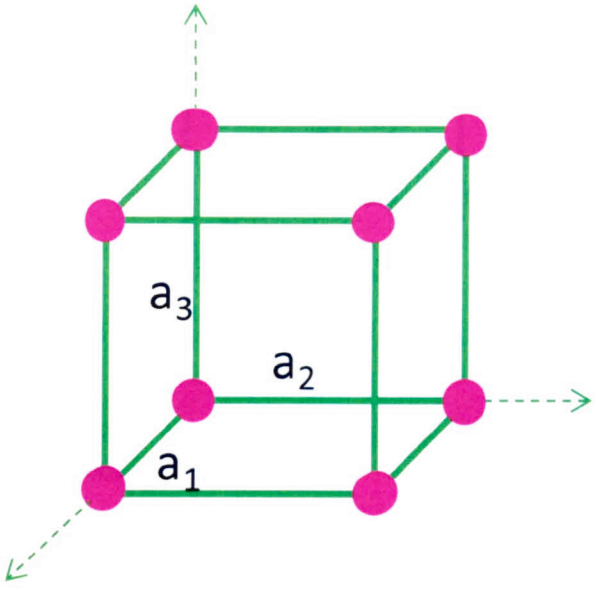

Figure 2.2: Simple cubic system represented by $\mathbf{a_1}$, $\mathbf{a_2}$, and $\mathbf{a_3}$ translation vectors.

There are some important types of primitive cells known as simple cubic (sc), body-centred cubic (bcc), and face-centred cubic (fcc). The structure of these crystal lattices depends on the occupation of the lattice sites. For a simple cubic system (Figure 2.3 (a)) all the three axis are perpendicular to each other, and the sides are equal in magnitude. Each lattice site is occupied by a lattice point (host atom). Body-centred cubic system is shown in Figure 2.3 (b) and can be obtained by introducing an additional atom at the middle of the simple cubic system. The addition of this atom makes the lattice arrangement in such a way that each host atom has bonds with eight neighbouring atoms. The occupation of the host atoms at each face of a simple cubic system, as shown in Figure 2.3 (c), allows the formation of bonds diagonally. This type of structure is known as the face-centred cubic system.

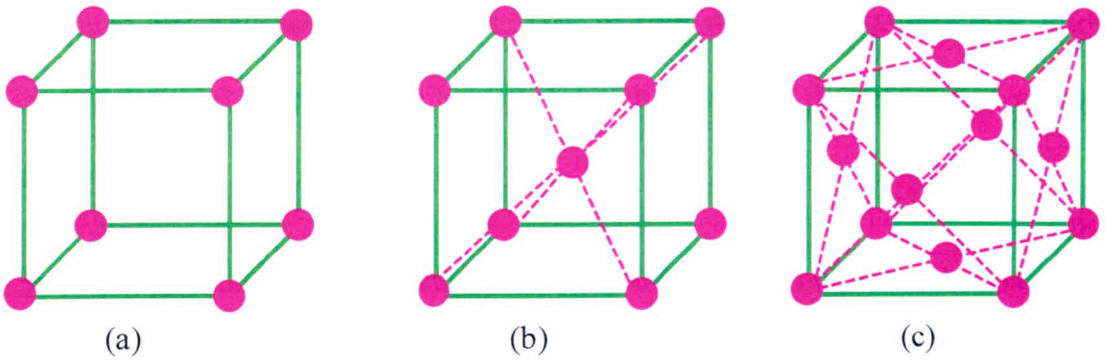

Figure 2.3: The arrangement of atoms in (a) simple cubic, (b) body centred cubic and (c) face centred cubic system is represented.

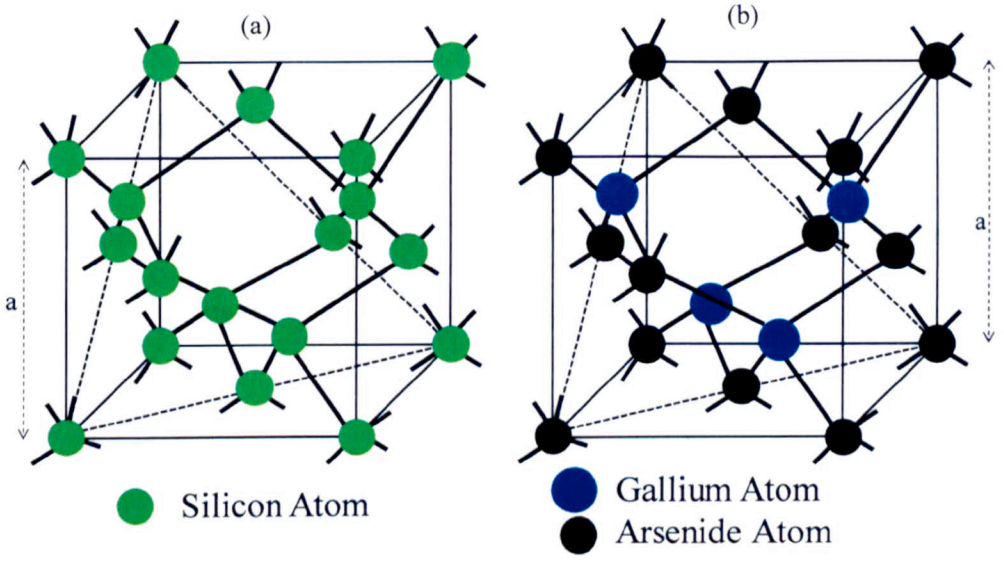

Figure 2.4: Examples of (a) diamond and (b) zincblende structures for silicon and GaAs, respectively [18].

In addition to sc, bcc, and fcc there are also two other most important crystal structure types. These are known as the diamond (Figure 2.4 (a)) and zincblende (Figure 2.4 (b)). Most popular elemental semiconductor materials such as silicon, germanium, and carbon have the diamond like structure, which is formed between the same types of atoms. In diamond structure each atom makes bonds with four adjacent atoms of the same group. The zincblende structure, which is the moderated form of fcc, is formed by two different types of atoms. The most popular III-V

compound materials such as GaAs and GaP possess the zincblende structure. Both the diamond and zincblende structures have the form of the tetrahedral crystal structures.

The crystalline solid can be described by **a**, **b**, and **c**, the primitive basis vectors in such a way that the crystal structure remains the same under translation through a vector ***R***. The translation vector ***R*** is an integral multiple of the basis vectors (***a***, ***b***, and ***c***) and is defined as

$$\mathbf{R} = p\mathbf{a} + q\mathbf{b} + r\mathbf{c} \qquad 2.2$$

where p, q, and r are integers and ***a***, ***b***, and ***c*** the primitive vectors.

The reciprocal lattice basis vectors ***a****, ***b****, and ***c**** in terms of direct basis vectors (***a***, ***b***, and ***c***) are written as

$$\mathbf{a}^* = 2\pi \left[(\mathbf{b} \times \mathbf{c}) / (\mathbf{a}.\mathbf{b} \times \mathbf{c}) \right],$$

$$\mathbf{b}^* = 2\pi \left[(\mathbf{c} \times \mathbf{a}) / (\mathbf{a}.\mathbf{b} \times \mathbf{c}) \right],$$

$$\mathbf{c}^* = 2\pi \left[(\mathbf{a} \times \mathbf{b}) / (\mathbf{a}.\mathbf{b} \times \mathbf{c}) \right]$$

here $\mathbf{a}^*.\mathbf{a} = 2\pi$ and $\mathbf{a}.\mathbf{b}^* = 0$ and so on, whereas the denominators are the same because $\mathbf{a}.\mathbf{b} \times \mathbf{c} = \mathbf{b}.\mathbf{c} \times \mathbf{a} = \mathbf{c}.\mathbf{a} \times \mathbf{b}$, is known as the volume enclosed by the vectors (**a**, **b**, **c**).

The position of the reciprocal lattice vector (***G***), in a reciprocal space is given as

$$\mathbf{G} = \mathrm{h}\,\mathbf{a}^* + \mathrm{k}\mathbf{b}^* + \mathrm{l}\,\mathbf{c}^* \qquad 2.3$$

where h, k, l are integers.

The relationship between direct lattice and reciprocal lattice is given by

$$\mathbf{G} \cdot \mathbf{R} = 2\pi \times \text{integer} \qquad 2.4$$

Thus, each vector of the reciprocal lattice is perpendicular to a set of planes in the direct lattice. The relationship between the volume of direct lattice (V_c) and the volume of reciprocal lattice (V_c^*) is given by

$$V_c^* = {(2\pi)^3}/{V_c} \qquad 2.5$$

where V_c represents the volume of direct lattice and is equal to $\mathbf{a}.\mathbf{b} \times \mathbf{c}$.

The knowledge of the orientation of the semiconductor crystal and the properties of its surface are very important for the fabrication of devices. For example (1) metallisation that provides contacts to the devices is very sensitive to the surface quality; (2) edge-emitting lasers rely on the orthogonal natural cleavage planes of the crystal for high performance operation. The orientation information for a crystal can easily be obtained from the study of Miller indices of a plane. The method of finding of the Miller indices is discussed below.

Consider a three dimensional crystal plane whose three basis vectors are **x**, **y**, and **z**. The Miller indices of this plane can be obtained in the following way:

(i) find the intercepts of the planes along three basis vectors (these intercepts can be in terms of lattice constant or primitive cells)

(ii) take the reciprocals of intercepts along each axis

(iii) reduce the reciprocals of these intercepts into smallest values in such a way that the smallest three integers have the same ratio

The result obtained from above three steps be enclosed in a parenthesis (hkl) called the Miller indices of a single plane with intercepts at 1/h, 1/k, and 1/l on the **x**, **y**, and **z**-axis, respectively. However, {hkl} represents the Miller indices of a full set of planes of equivalent symmetry, such as {100} for (100), (010), (001), $(\bar{1}00)$, $(0\bar{1}0)$, $(00\bar{1})$.

Examples of some crystal structures and Miller indices of the planes are given in Figure 2.5. For example consider a plane with an intercept at x = a, on the x-axis, where it does not intercept with the other two axes (y and z). Therefore, it is convenient to say that the plane is parallel to y- and z-axis. In case of the plane parallel to y- and z-axis its intercepts are considered to be at ∞. Thus the intercepts for such a plane are a, ∞, ∞. The fractional reciprocals are a/a, a/∞, a/∞. Thus the reciprocals result are (1, 0, 0) and the Miller indices of this plane are (100). In a similar way, the Miller indices of other planes are determined as shown in Figure 2.5.

The planes of a cubic crystal system containing the 0's and 1's only such as (100), (110), and (111) are known as the low index planes. However, the planes containing higher values such as (n11), where n = 2,3,4,5,..., are known as high index planes.

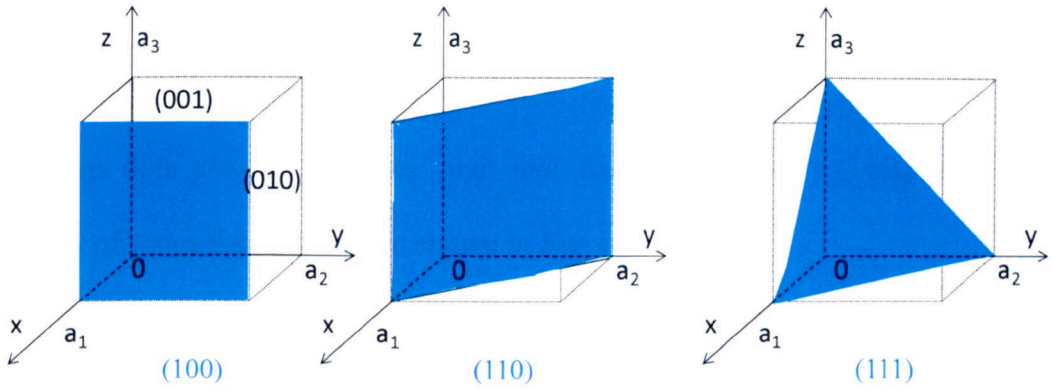

Figure 2.5: Representation of some Miller indices.

2.4 DENSITY OF STATES IN SEMICONDUCTORS

The atoms of solid materials are so close to each other that they can easily interact by means of their electric fields. The interaction leads to the splitting of energy levels into a finite number of electronic states [19]. The electrons then tend to occupy the sublevels with lower energy states. This results in the creation of conduction and valence bands of the material. During the conduction process the electrons are excited from valence band to the conduction band of a semiconductor material. The vacancy that is created in the valence band due to the migration of electron carries a positive charge and is known as a hole. The density of states {N(E)} of semiconductors is defined as the number of states at a certain energy level that are available to be occupied. N(E) is directly related to the availability of the energy states for the occupation in a certain energy level and depends on the confinement of charge carriers and their degree of freedom.

Material dimensions are the most important for the charge carrier confinement which facilitates the number of degree of freedom. The density of states for different degrees of freedom is illustrated in Figure 2.6. In case of bulk materials the carriers have three degrees (3D) of freedom. In quantum wells, quantum wires, and quantum

dots the carriers are confined in two (2D), one (1D) and zero (0D) dimensions, respectively. Therefore the charge carriers in quantum wells, quantum wires and quantum dots possess two, one and zero degrees of freedom, respectively. The density of states for each case is shown in Figure 2.6.

The density of states for three dimensional systems is proportional to square root of energy. In case of two dimensional systems it follows the step like function. However, for one and zero dimensional system the density of states is proportional to $(E)^{-1/2}$ and independent of (delta function) energy, respectively. The relationship between density of states and energy for the different systems is illustrated in Figure 2.6 [18].

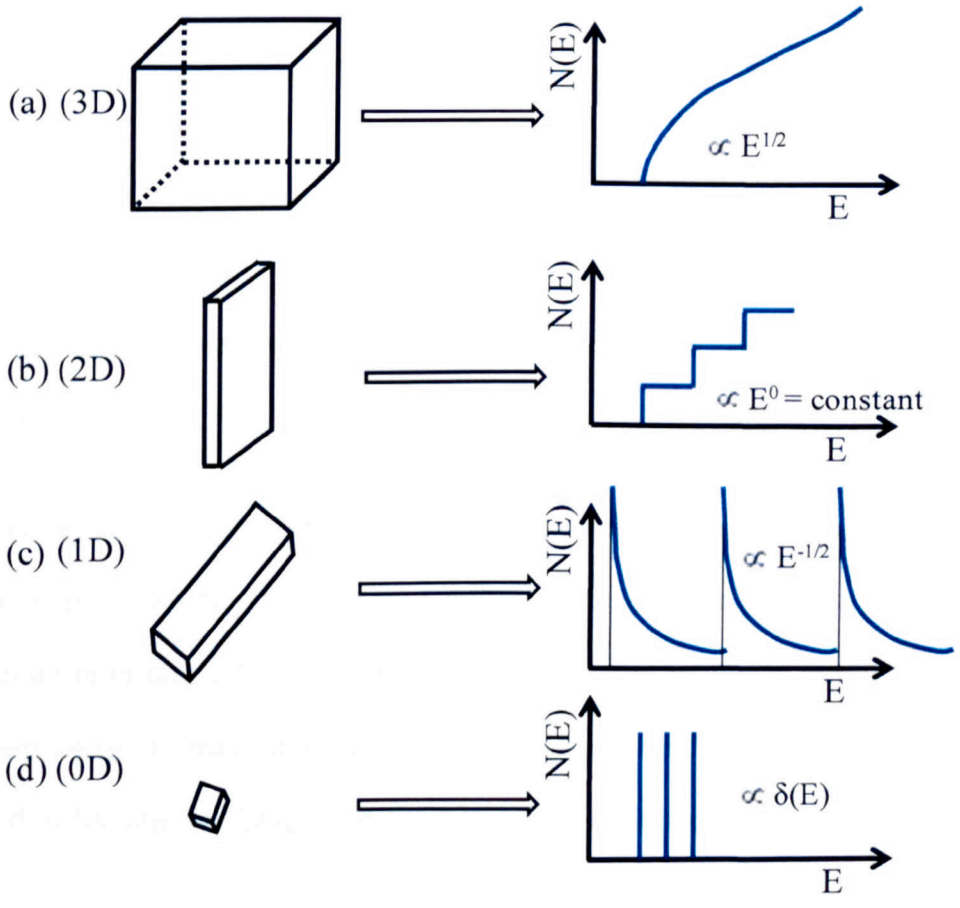

Figure 2.6: Density of states N(E) for (a) bulk semiconductor (3D), (b) quantum well (2D), (c) quantum wire (1D), and quantum dot (0D) [18].

2.5 ENERGY BANDGAP

The energy and wave vector (E-k) (Figure 2.7) relationship gives information regarding energy band gap of semiconductor materials, which have two types of bands, conduction band which remains empty at lower temperature (~0 K) and the valence band called the filled band. These energy bands are separated from each other by a forbidden region. No carrier occupies the energy levels within this forbidden energy band. This energy difference between conduction and valence band is called the band gap or energy gap (E_g). As mentioned in section 2.1, metals, semiconductors, and insulators can be distinguished from each other on the basis of the gap between their conduction and valence bands.

At around k = 0, the conduction and valence bands have parabolic shape. The energy of conduction (E_c) and valence (E_v) bands is given as

$$E_c = E_g + \frac{h^2 k^2}{8\pi^2 m_e}, \quad E_v = -\frac{h^2 k^2}{8\pi^2 m_h} \qquad 2.6$$

where h is Plank's constant, k is Boltzmann constant, m_e is mass of electron and m_h is mass of hole.

The energies are calculated with respect to the maxima of valence band. For very low temperatures (~0 K) the electrons are confined in the valence band and the material behaves as an insulator. By increasing the material temperature the electrons acquire sufficient energy to make transition from the valence band to conduction band and hence, they become available for electrical current conduction.

2.6 DIRECT AND INDIRECT BANDGAP

A semiconductor can have a direct or indirect energy band gap. This result depends on the position of valence band maxima and conduction band minima with respect to wave vector (k). If the valence band maxima and conduction band minima lie at the same value i.e. k = 0, the material is said to be direct band gap. On the other hand, if the valence band maxima and conduction band minima lie at different values of wave vector (k), then the material is said to be indirect band gap. The most familiar examples of indirect and direct band gap material are Si and GaAs, respectively, as shown in Figure 2.7.

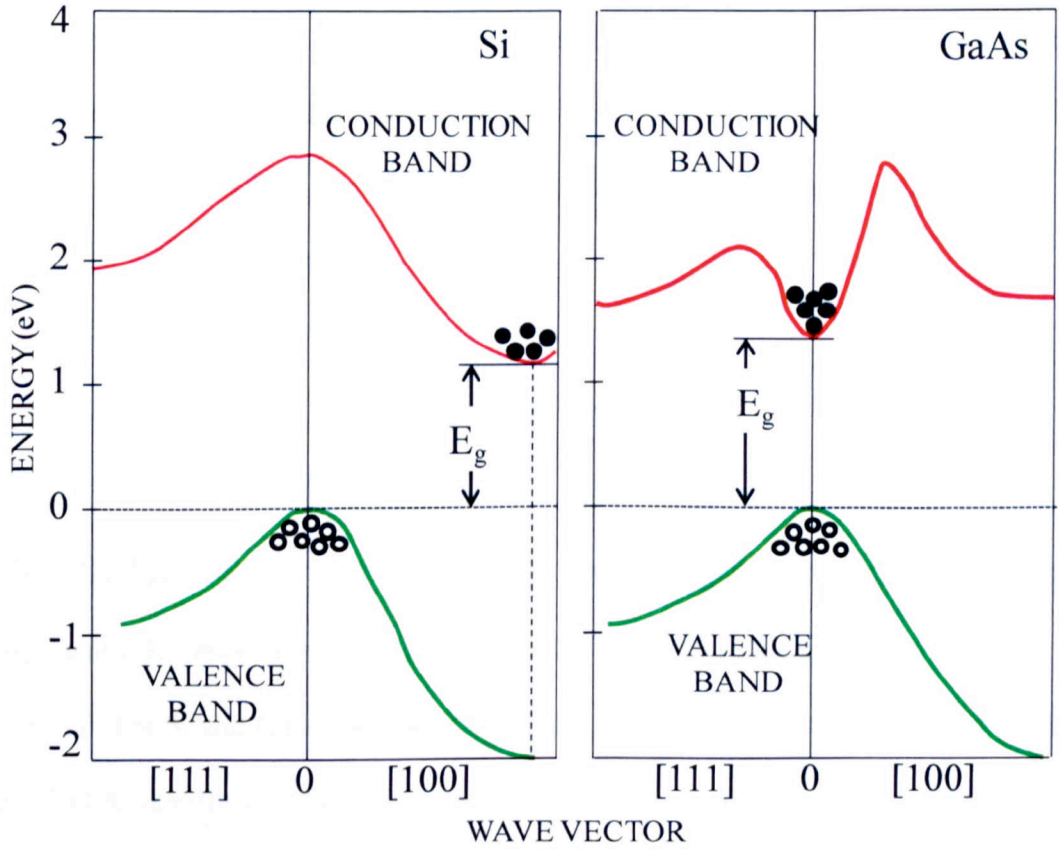

Figure 2.7: Energy-band structures of silicon and gallium arsenide; electrons and holes are shown in full and open circles, respectively [18].

2.7 EFFECT OF TEMPERATURE ON ENERGY BANDGAP

Semiconductors such as Si and GaAs have a negative temperature coefficient i.e. their energy band decreases with increasing the thermal energy. The energy bandgap of pure Si and GaAs at room temperature is 1.12 eV and 1.42 eV, respectively. However, it increases to ~ 1.17 eV and 1.52 eV for Si and GaAs, respectively, when the temperature reaches ~0 K. The mechanism involved in the decrease of the energy gap of the material is the effect of inter atomic spacing between the atoms of the semiconductors. This can be explained by the fact that as the temperature of the semiconductors increase, the thermal vibrational energy of the atoms also increase, which results in the increase of the vibrational amplitude of atoms and thus the increase of inter atomic spacing. This means that the potential that electrons face in the material also decreases, the energy bandgap of the semiconductor decreases. The effect of temperature on energy bandgap of semiconductor materials is mathematically expressed as

$$E_g(T) \approx E_g(0) - \frac{\propto T^2}{T + \beta} \qquad 2.7$$

where $E_g(T)$ and $E_g(0)$ are the temperature dependent bandgap energy, and bandgap energy at 0 K, respectively. Whereas, $\propto$ and β are empirical parameters related to the material. For Si and GaAs, $\propto = 4.9\times10^{-4}$ and 5.4×10^{-4} eV/K, respectively and $\beta = 655$ and 204 K, respectively [18].

2.8 HETEROJUNCTION STRUCTURES

Heterojunctions are formed by growing two different semiconductor materials on top of each other, provided that their energy bandgap differ. The most common examples

of heterojunction structures are multi-quantum wells (MQWs) and superlattices (SLs).

The performance of MQWs and SLs depends on the growth quality, which can be degraded due to various reasons. For example the lattice mismatching between two semiconductor materials produces defects at the interface of the heterojunction. To avoid the creation of these interface defects both semiconductors forming the heterojunction should be lattice matched. For example, GaAs/AlGaAs(or AlAs) are good examples of lattice matched systems.

If there is a large difference between the lattice constants of the two materials, then the defects at the junction interface tend to increase. For example, in case of the growth of epitaxial materials, if the lattice constant of the substrate material is higher than that of the material used in the epitaxial growth, tensile strain occurs in the heterostructure (Figure 2.8 (a)). On the other hand, if the lattice constant of the substrate is lower than that of the epitaxial material then compression strain is produced (Figure 2.8(b)).

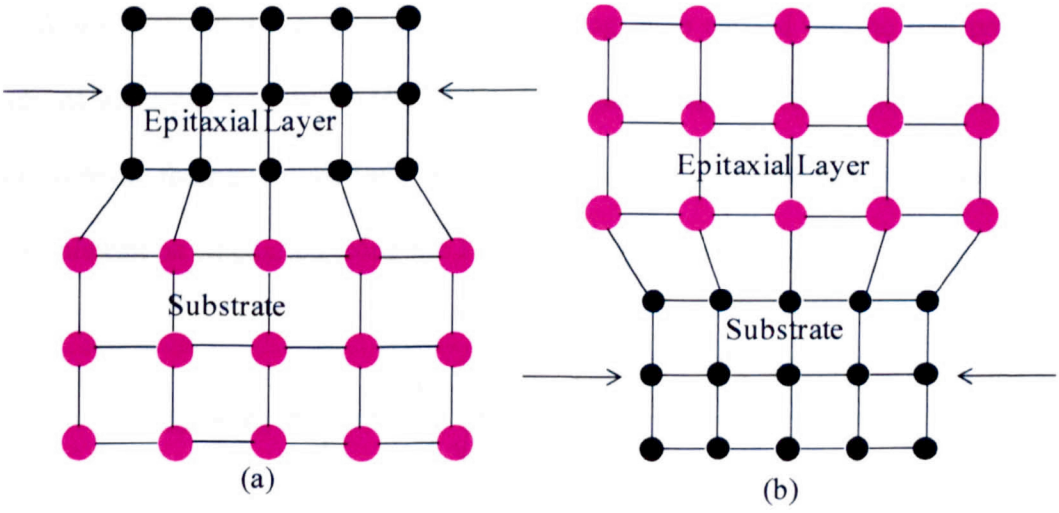

Figure 2.8: Lattice mismatching is illustrated between two materials with different lattice constants.

Up to some critical thickness, good quality heterojunctions can be grown even if the lattice constant of the two materials differ from each other. The surface terminating dangling bonds of very thin epitaxial layer produce strain to the material and adjust its lattice constant with the lattice constant of the substrate. This results in the decrease of the interface defects [18]. The lattice-match can empirically be expressed by the change in lattice constant at the interface of two materials and is given by

$$\frac{\Delta a}{a} = \frac{a_{layer} - a_{sub}}{a_{sub}}$$

where a_{layer} is lattice constant of layer and a_{sub} is lattice constant of substrate.

In addition to the lattice matching, the size of the atoms of two different materials, electronegativity (χ), and energy band alignment play an important role during the heterojunction structure growth. If the size of the atoms is different for two different materials, then strain is produced during heterojunction growth process.

The ability of an atom to attract the electron towards itself and make a chemical bond is called electronegativity (χ). Electronegativity is a unitless quantity and referred to as Pauling scale after the name of Linus Pauling, who carried out the first principal study of electronegativity in 1932 [20]. Consider A and B two different materials used to make the heterojunction. The difference in the electronegativity of these two materials can be calculated using the Pauling's empirical formula.

$$\chi_A - \chi_B = \left[(eV)^{-\frac{1}{2}}\right] \sqrt{E_D(AB) - \frac{[E_D(AA) + E_D(BB)]}{2}} \qquad 2.8$$

where χ_A and $\chi_B$is the electronegativity of A and B, respectively, and $E_D\,(AB)$, $E_D(AA)$ and $E_D(BB)$ are the dissociation energies in eV between the atoms AB, AA and BB, respectively. The factor $\left[(\mathrm{eV})^{-\frac{1}{2}}\right]$ is used to render the value of electronegativity unitless.

Another important parameter that is of critical interest during the heterojunction growth is the band alignment between two semiconductor materials. As mentioned above in this section that heterojunction structures are formed by growing materials of different band gaps on top of each other. It is therefore of great importance to have knowledge of the band gaps of the different materials involved and how the energy bands align with respect to each other. There are three different types of band alignments as shown in Figure 2.9, and these are known as type-I or straddled alignment, type-II or staggered alignment and type-III or broken gap alignment.

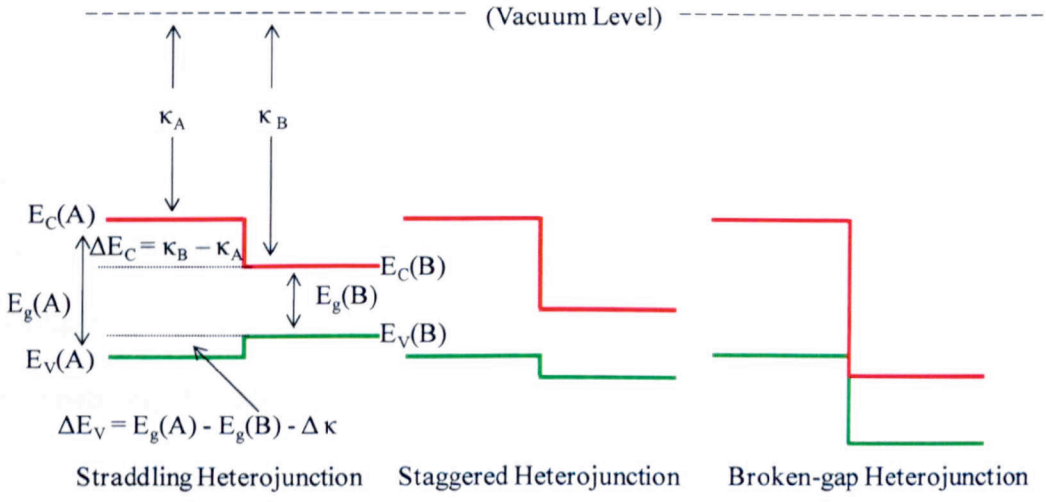

Figure 2.9: Classification of heterojunctions according to their band alignment, where E_C, E_V, E_g, ΔE_C, ΔE_V and κ are the conduction band, valence band, energy gap, conduction band offset, valence band offset and electron affinity of the materials A and B.

If the conduction band of the material with higher energy gap lies within the conduction band of the material with lower energy, and the valence band of the

higher energy gap material lies within the valence band of the lower bandgap material, the alignment is said to be type-I or straddled alignment. AlGaAs/GaAs and InGaAs/InP heterostructures are examples of type-I heterojunctions. However, if the conduction band of the higher bandgap material lies within the conduction band of the lower bandgap material and the valence band of lower band gap material lies in the valence band of higher energy gap material then the resulting alignment is said to be type-II or staggered alignment. The example of type-II heterojunction is GaAsSb/GaInAs heterojunctions. The type three band alignment is formed when both the conduction and valence band of the higher energy gap material lies within the conduction band of lower band gap material. Type-III alignment is obtained during the growth of GaSb/InAs heterostructures, for example.

The first theoretical model known as electron affinity model was proposed by Anderson in 1962 [21] to calculate the band offset of an ideal heterostructure. For the purpose of understanding the electron affinity model let us consider, A and B be the two semiconductor materials. The electron affinity and energy gap of the materials A and B are κ_A, and κ_B, and E_{gA} and E_{gB}, respectively. The sum of the energy released by an electron to move from vacuum level to semiconductor A (κ_A) from there to B and finally from semiconductor B back to the vacuum level must be equal to zero. Mathematically it is expressed as

$$\kappa_A - \Delta E_C - \kappa_B = 0 \qquad 2.9$$

$$\Delta E_C = \kappa_A - \kappa_B \text{ and } \Delta E_V = \Delta E_g - \kappa_B \qquad 2.10$$

where ΔE_C and ΔE_V is the conduction band and valence band offset energies, respectively.

Anderson model gives the best accurate value for some but not all of the heterostructures. The main reason of the failure of this model, given by Kroemer [22] is the formation of the semiconductor surface dipoles. These dipoles are formed due to the rearrangements of the atoms at semiconductor surface, and their presence affects the electron affinity measurement, and thus the band offset of the heterostructures.

The properties of binary semiconductors such as energy gap, and lattice constant will change with the addition of some other element from the same group in the periodic table. For, example the addition of aluminium in GaAs changes the properties of $Al_xGa_{1-x}As$ (x is Al content). The change in the energy gap of the resulting ternary material with respect to x can be calculated by

$$E_{g,ABC}(x) = x.E_{g,AB} + (1-x).E_{g,AC} - b.x(1-x) \qquad 2.11$$

where $E_{g,ABC}(x)$ is the content (x) dependent energy gap of the material obtained from A, B, and C, three different semiconductor materials. The factor $b.x(1-x)$ is usually negligible for most semiconductors because the value of the bowing coefficient (b) is often less than 1eV.

The relationship between lattice constant and the constituent x is given by Vegard's law [23]. According to Vegard's law the x dependent lattice constant of the ternary material can be written as

$$a_{ABC}(x) = x.a_{AB} + (1-x).a_{AC} \qquad 2.12$$

here $a_{ABC}(x)$ is lattice constant of the resulting ternary material.

2.9 ELECTRICAL PROPERTIES OF SEMICONDUCTORS

The electrical properties of semiconductor such as the carrier mobility play an important role in the performance of semiconductor devices. Following sections are devoted to explain the carrier mobility and its effect on device performance.

2.9.1 CARRIER MOBILITY

The carrier mobility is defined as the average drift velocity per unit electric field in a semiconductor. It is mathematically expressed as

$$\mu = \frac{v_d}{E} = \frac{q\tau_c}{m^*} \qquad 2.13$$

where μ is the carrier mobility, v_d is carrier average drift velocity, E is the applied electric field, q is charge, τ_c is the mean free time between two successive collisions of the carrier, m^* is the carrier effective mass.

The average drift velocity of the carriers in a semiconductor is affected by scattering of the carriers between each other and with other imperfections (defects) in the material and by the relaxation time between two scattering events. These scattering mechanisms result in a decrease of the carrier mobility. In order to enhance the mobility of carriers it is important to increase the relaxation time (mean free time). This can be achieved by reducing the number of scatterers and defects.

Besides these, the carrier mobility also decreases with increasing the impurity doping concentration and temperature. When the doping concentration increases, the probability of collisions between carriers and impurity atoms increases. As a consequence, the carrier average velocity and hence the mobility reduces as well.

Moreover, by increasing the temperature the amplitude of the thermal vibration of the atoms in a semiconductor crystal increases and so the number of phonons increases. These phonons also interact with the carriers and reduce the carrier mobility. The effect of these parameters on the carrier mobility is mathematically represented as

$$\mu(T) \propto T^{-3/2} \text{ and } \mu(N) \propto \frac{T^{3/2}}{N} \qquad 2.14$$

where T is temperature and N is the doping concentration [18, 24].

2.9.2 EFFECT OF CARRIER MOBILITY ON DEVICE PERFORMANCE

The carrier mobility affects the device performance through its frequency response in two different ways. First, for low electric field, the carrier mobility is proportional to its velocity, and therefore the frequency response of higher mobility material is high because the carriers take less time to travel through the device. The second effect is related to the current flow through the device which is directly related to the carrier mobility.

The device geometry affects the mobility of the carriers in some devices. For example in Metal oxide field effect transistors (MOSFET) surface scattering of the carriers plays major role in reducing the carrier mobility. The carriers at oxide-semiconductor interface create more scattering mechanisms such as the Coulomb scattering from oxide charges and interface states, and surface roughness scattering. These scatterings reduce the mobility of MOSFET devices [25, 26].

2.10 GENERAL PROPERTIES OF Gallium Arsenide (GaAs)

GaAs is one of the most familiar and most investigated III-V compound semiconductor material and is formed by combining Ga (group-III) and As (group-V) elements from the periodic table. It was first produced by Goldschmidt in 1920's [27]. However, its properties remained unexplored up to 1952.

GaAs crystal posses zincblende structure type, in which a face-centered cubic lattice (fcc) of As with Ga atoms positioned on the body diagonals as shown in Figure 2.10. These Ga atoms also lie on a fcc displaced relative to the As lattice by one quarter the body diagonal of the cube.

The band structure of GaAs is shown in Figure 2.11. It can be seen that both the conduction band minima and the valence band maxima lie at the same value of wave vector at $k = 0$. Therefore, the transition of an electron from valence band to conduction band needs a change in energy, but no change in momentum is required. According to energy band diagram definition the nature of the GaAs band gap is direct. This is an important property, as compared to Si which has an indirect band gap, for devices used in optoelectronics applications. Moreover, GaAs possesses a higher carrier mobility than Si, and is preferably used in high frequency devices.

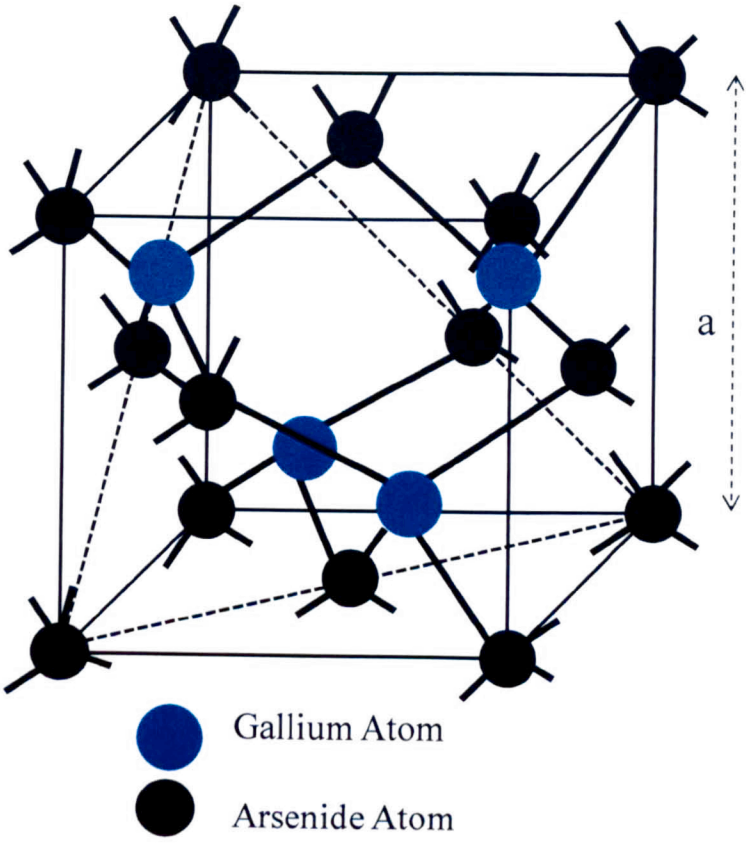

Figure 2.10: Zincblende structure of GaAs.

The resistivity of GaAs is very high ~ 10^8 Ω-cm compared to Si (6.4×10^2 Ω-cm at 20 °C), which makes it more suitable to be used as a semi-insulating substrate for integrated circuits. In addition, due to the fact that the energy gap of GaAs is higher than that of Si, the GaAs devices are more reliable to operate at higher temperatures than Si devices.

Besides the above mentioned selected properties, some other important properties of intrinsic GaAs at room temperature (300K) are given in Table 2.1.

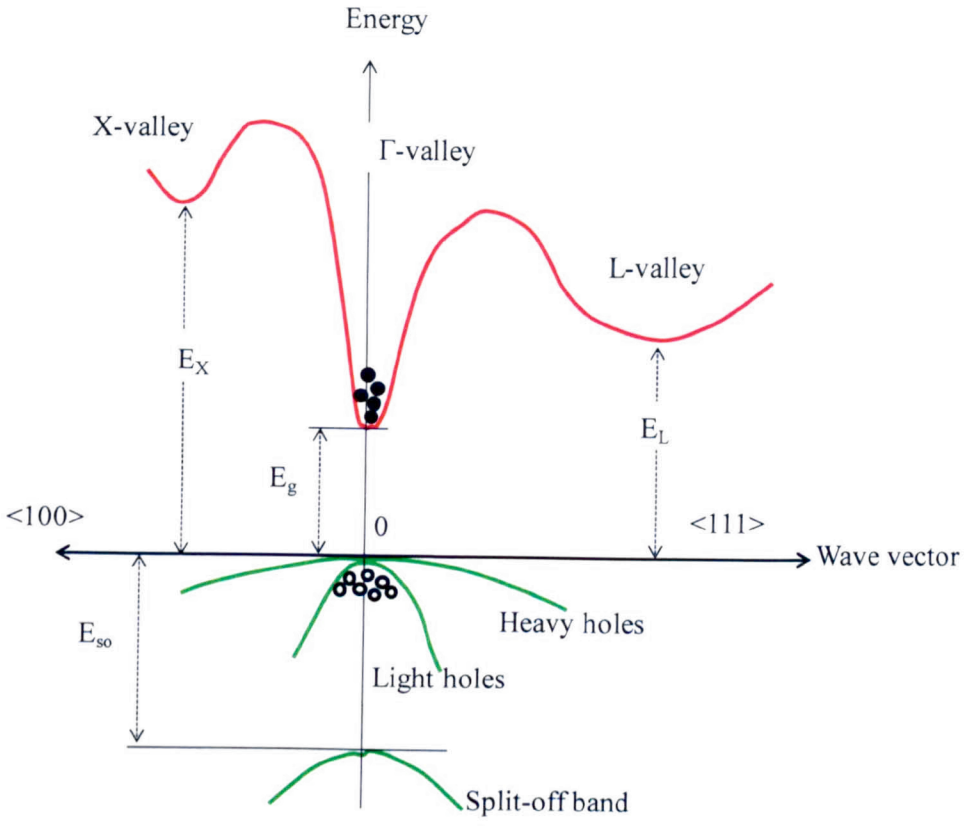

Figure 2.11: The energy band diagram of GaAs is illustrated for the three different conduction valleys (X, Γ and L)

Table 2.1: Some important properties of intrinsic GaAs, AlAs and AlGaAs at 300K; h_h and l_h stand for heavy hole and light hole, respectively[28, 29]

Parameter	GaAs	AlAs	$Al_xGa_{1-x}As$
Crystal Structure	Zincblende	Zincblende	Zincblende
Lattice constant (Å)	5.6533	5.6611	5.6533 + 0.0078x
Crystal density (g/cm^3)	5.360	3.760	5.360-1.6x
Energy band gap (eV)	1.42	2.168	x<0.45 1.424+1.247x x>0.45 1.9+0.125x+ 0.143x^2
Band type	Direct	Direct	Changes from Direct to indirect with Al content
Electron effective mass	0.063 m_0	0.150 m_0	0.063+0.083x mo (x<0.45)
Hole effective mass	0.62m_0 (h_h) 0.087m_0 (l_h)	0.76m_0 (h_h) 0.15 m_0 (l_h)	0.62 + 0.14x (h_h) 0.087 + 0.063x (l_h)
Dielectric constant (static)	12.85	10.06	12.85-2.84x
Specific heat(cal/gK)	0.08	0.11	0.08+0.03x
Electron affinity (eV)	4.07	3.4	4.07-1.1x (0<x<0.45) 3.46-0.14x (0.45<x<1)

2.11 GENERAL PROPERTIES OF $Al_xGa_{1-x}As$

The energy band gap of a semiconductor is one of the most significant parameters which enhance its scope for various optical devices operating in different energy range. For example the ability to control the band gap of GaAs by incorporating aluminium (Al) in the host material will extend its application range from near infrared to visible region; the band gap energy at 300 K can span from 1.42 eV

(GaAs) for x = 0 to 2.168 eV (AlAs) for x = 1. The energy change of the different conduction valleys (X, Γ, and L) at 0K with respect to Al content (x) is shown in Figure 2.12. In addition it is observable that at a certain value of Al content (x = 0.44) the transition from direct to indirect bandgap takes place for AlGaAs material.

It is assumed [30, 31] that the relationship between energy gap and alloy composition follows equation (2.11). The bowing coefficient for $Al_xGa_{1-x}As$ is less than 1 eV so it is neglected and therefore the energy gap can be calculated from equation as

$$E_{g,Al_xGa_{1-x}As} = x.E_g(GaAl) + (1-x).E_g(AlAs) \qquad 2.15$$

The above energy gap equation is valid only if the lattice constant of the material changes linearly and the energy gap has nonlinear bowing with the constituent x.

The lattice constant of $Al_xGa_{1-x}As$ obeys Vegard's law [23] and varies linearly with Al content (x) in GaAs. This linear relationship between x and lattice constant is shown in Figure 2.13.

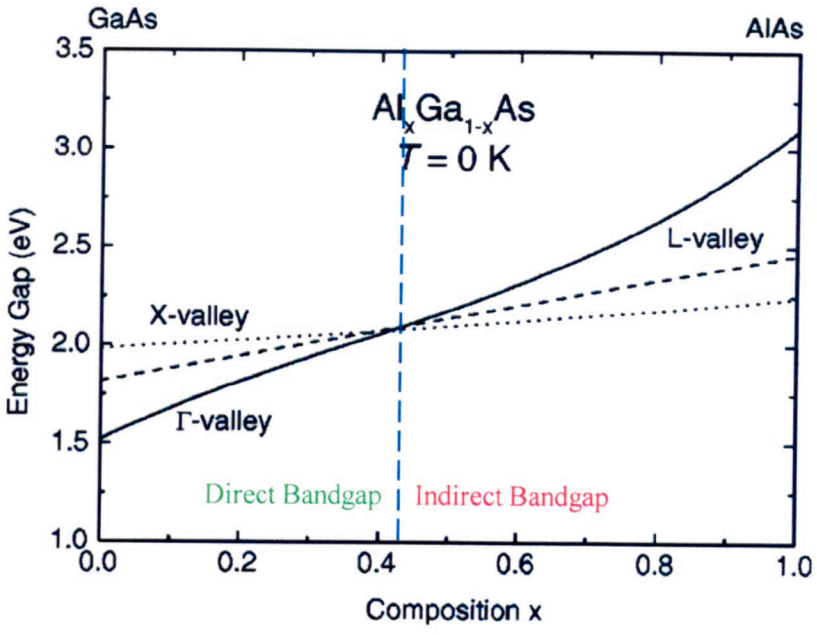

Figure 2.12: Schematic illustration of change in the energy gap of AlGaAs at 0K for x = 0 (GaAs) to x = 1 (AlAs); X, Γ, and L are the conduction valleys [30].

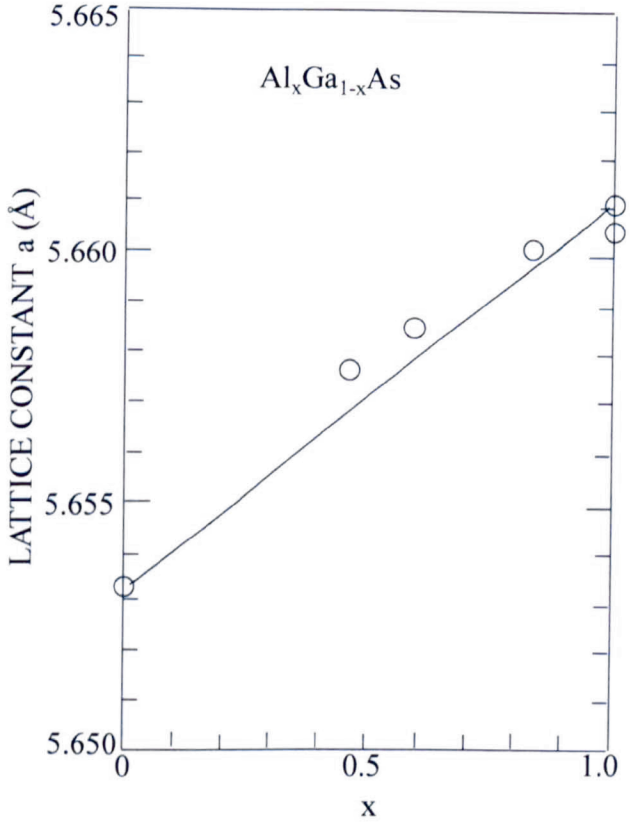

Figure 2.13: Change in lattice constant of $Al_xGa_{1-x}As$ as a function of x [29].

In addition to change in the material band gap and lattice constant, other parameters such as density, thermal expansion coefficient and electron transport properties of the material also change.

Since the semiconductor materials are grown at various temperatures, therefore, the change of the lattice parameter with respect to temperature is a very important factor to take into consideration. During the epitaxial growth, defects can be created at the interface due to the change of the lattice constant as a function of growth temperature and it will affect the device performance. The first mathematical relationship between the lattice constant and temperature was developed by Kudman and Puff [32] in 1972. The authors suggested a linear relationship between lattice constant and temperature for ternary semiconductor materials. This is given by

$$a_T = a_0(1 + \alpha T) \qquad 2.16$$

where a_T, a_0, α an T are the temperature dependent lattice constant, lattice constant at a temperature of 0 °C, linear coefficient of thermal expansion and temperature in °C, respectively.

Transport phenomenon plays an important role in the mobility of charge carriers in semiconductors like $Al_xGa_{1-x}As$ alloy, where for example electrons face potential fluctuations that are created due to the compositional disorder. This effect produces an irregular scattering process, called alloy scattering. Alloy scattering potential, which is caused by the change in the electronegativity of atoms, results from the covalent bonds [29]. Some important parameters of $Al_xGa_{1-x}As$ alloy are also mentioned in Table 2.1.

CHAPTER 3

DEFECTS IN SEMICONDUCTORS AND THEIR PROPERTIES

This chapter is based on the description of various types of defects such as intrinsic and extrinsic defects and their behaviour in semiconductor materials. The defect carrier kinetics is also described on the basis of Shockley-Read-Hall theory. In addition, the effect of electric field on the carrier emission rates from the defects is also discussed, and finally the literature regarding the defect characterisation in III-V compound such as GaAs and AlGaAs has been reviewed. The importance of high index planes for the high quality materials have been discussed as well.

3.1 CLASSIFICATION OF SEMICONDUCTOR DEFECTS

Ideally the crystal structure is defined as the structure which is formed by the periodic repetition of an infinite number of unit cells along three crystallographic orientations. In a practical case a number of different types of defects exist within the crystal structure. These defects may be the intrinsic or due to the impurity incorporation known as extrinsic defects.

Extrinsic defects in the semiconductor crystal may be created intentionally to obtain the desired electrical properties of the material or unintentionally during growth. Incorporation of carbon impurity in GaAs during MBE growth is the best example of unintentionally introduced impurities. Different types of crystal defects are described here.

3.1.1 POINT DEFECTS

The point defects, also known as zero-dimensional or atomic size defects, are formed due to the missing of an atom from its regular site, or the occupation of an atom by prohibited (interstitial) site in the crystal structure. These defects alter the electrical and optical properties of the materials by creating some energy states within the energy band gap of the materials. Different types of point or zero–dimensional defects are briefly defined below [33].

a) VACANCIES

The vacancy known as the Schottky defect is shown in Figure 3.1(a). It is defined as the missing of an atom from its lattice site in a crystal plane. In the case of Schottky defect formation the displaced atom moves from its original position within the crystal to the surface by leaving a vacancy at its actual site within the crystal.

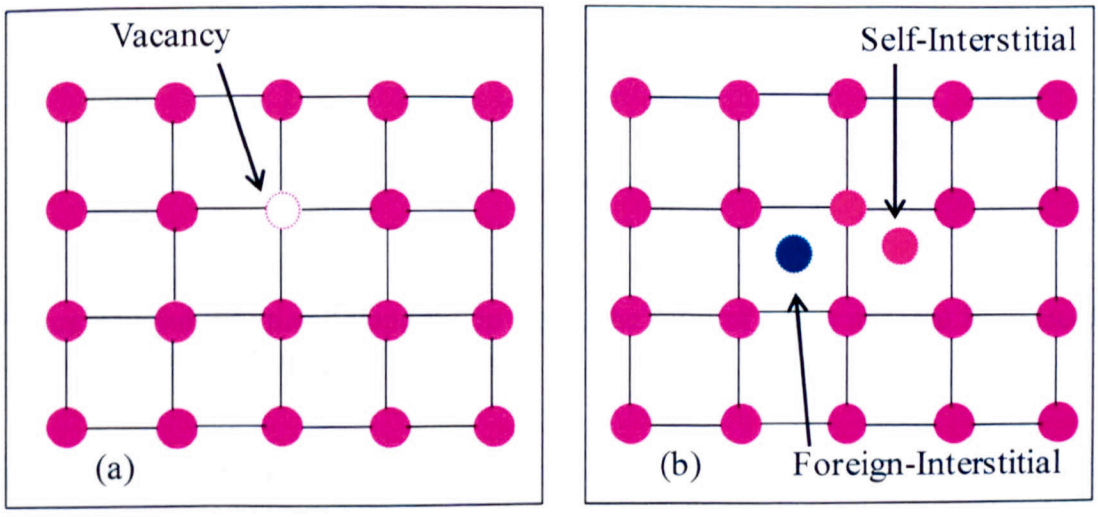

Figure 3.1: (a) Vacancy (the missing of an atom from a crystal) type defect, (b) Self-interstitial and foreign-interstitial defects.

b) INTERSTITIAL

An interstitial defect is defined as the defect that can be created due to the insertion of a host atom at the site other than its regular sites, known as self-interstitial or due to impurity-incorporated atoms known as the foreign-interstitial as shown in Figure 3.1 (b).

c) SUBSTITUITIONAL IMPURITY

These types of defects are formed during the incorporation of an impurity in a pure semiconductor material. In this process a foreign atom replaces a host atom from its regular position. Figure 3.2 represents the formation of a substituitional impurity.

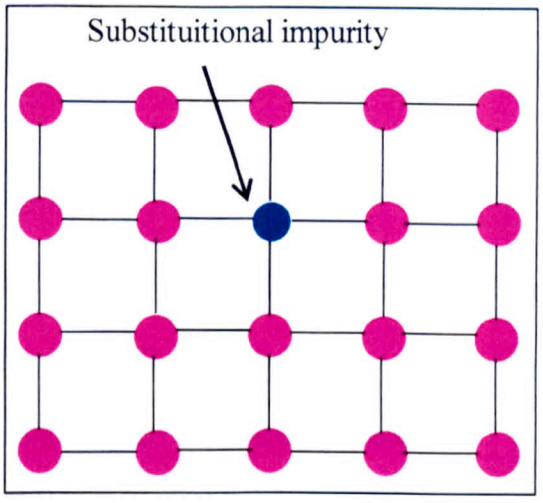

Figure 3.2: Substituitional impurity, in which the atom of a host material is replaced by the atom of another type of material.

d) ANTISITE DEFECTS

The antisite defect is created in the host material when the site of one type of atom is occupied by other type of atom and vice-versa. Figure 3.3 shows an example of gallium-antisite (As_{Ga}) created in GaAs.

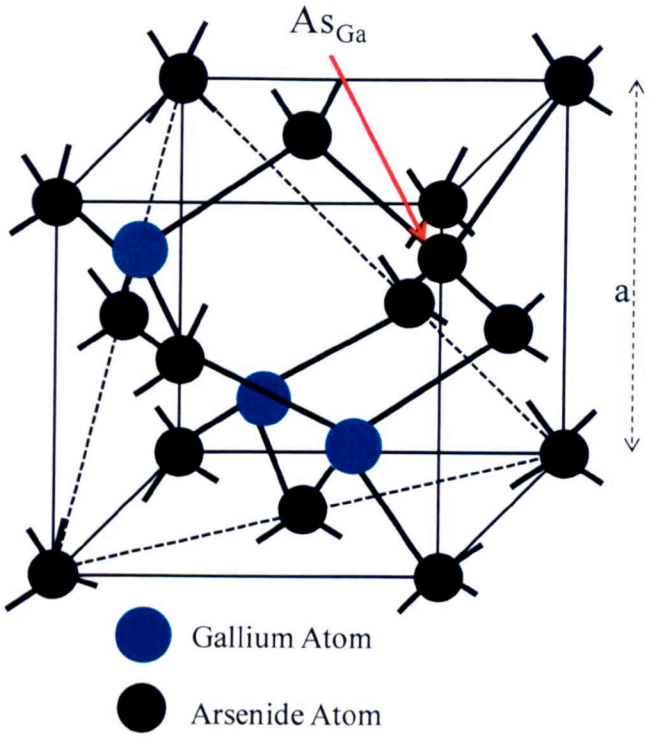

Figure 3.3: The position of Gallium atom is occupied by an Arsenic atom to form the antisite defect.

3.1.2 COMPLEX DEFECTS

These types of defects are created by the formation of a pair of either the same type of defect or different type of defects in the semiconductor crystal structure. Few of the major types of complex defects are discussed below.

a) FRENKEL DEFECT

As illustrated Figure 3.4 (a) the Frenkel defect is formed by the combination of a vacancy and an interstitial defect.

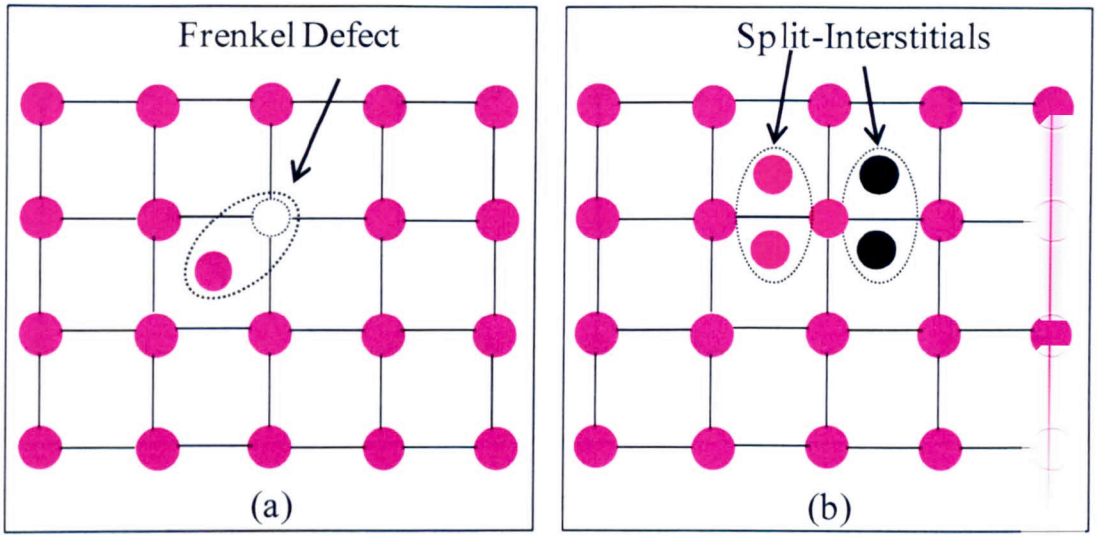

Figure 3.4: (a) Frenkel defect involving the combination of a vacancy and interstitial, (b) Formation of split-interstitial defect.

b) SPLIT-INTERSTITIAL

If two closely spaced interstitial defects interact with each other by Coulomb interaction, then the resultant defect level is known as split-interstitial. These interstitial pairs may be formed between same type of atoms such as the host atoms or the impurity atoms as shown in Figure 3.4 (b).

c) VACANCY-COMPLEXES

Different vacancy related complexes exist in semiconductor materials. These types of complexes are formed by different means such as the formation of a vacancy-impurity complex involving a pair of defects such as a vacancy and a foreign interstitial. The defect complex formed between two adjacent vacancies is known as di-vacancy complex. Another type of vacancy related complex can be formed when two vacancies are separated by the interstitial defect known as the split-vacancy. These types of defect complexes are shown in Figure 3.5 (a).

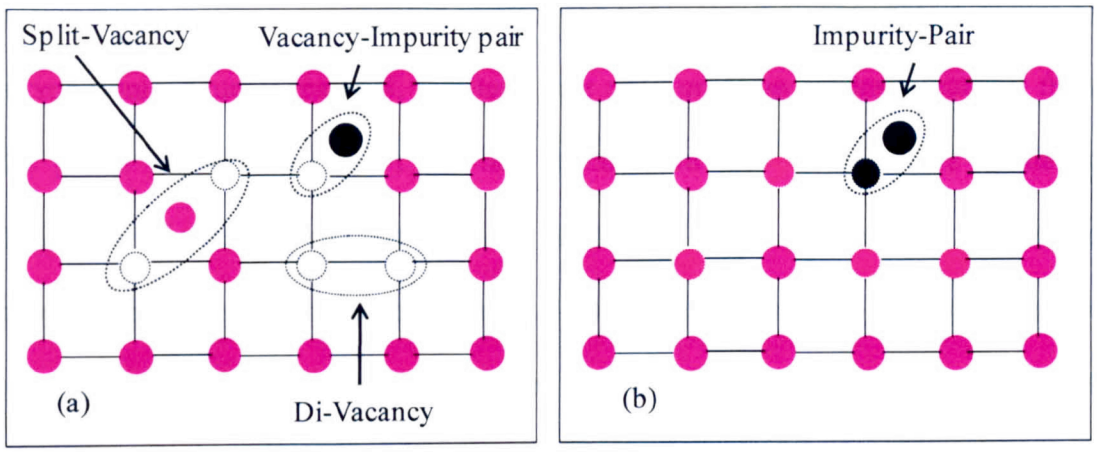

Figure 3.5: (a) Different types of vacancy related defect complexes such as vacancy-vacancy (Di-Vacancy), Vacancy-Impurity, and Split-Vacancy, (b) Illustration of an impurity pair defect complex.

d) IMPURITY RELATED COMPLEXES

Other defect complexes, referred to as impurity related complexes, can exist in semiconductors. These defects are formed when a substitutional impurity atom interacts by coulomb interaction with another impurity atom located at an interstitial site. This type of impurity complex is sketched in Figure 3.5 (b).

3.1.3 DONOR-ACCEPTOR PAIRS

The donor and acceptor defects are defined as the defects that contribute in the addition of electrons and holes to the conduction and valence band of the host material, respectively. This is because the ionization energy of these impurities is small and can easily be ionized at room temperature. As an example, the ionization energy of a donor impurity is ~7 meV for GaAs. Donor levels behave as neutral levels when filled by electrons and positively charged when they emit an electron. However, the acceptor impurities behave as negatively charged atoms when they capture electrons and behave as neutral when they emit an electron. For example, the addition of extrinsic atoms from the group in the periodic table higher than that of the

host material increases the number of electrons in the resulting material i.e. makes an n-type semiconductor material. Similarly, the addition of an extrinsic material from the group lower than that of the host material in the periodic table creates a deficiency of electrons and results in the addition of holes. The resulting material is known as p-type semiconductor material. In addition to acceptors and donors some other type of defects can be created when the impurity atoms of the same group of periodic table are added to the host material. These type of centres are known as isoelectronic or isovalent centres [14].

3.1.4 LINEAR OR 1-D DEFECTS

These types of defects are different than those of zero-dimensional defects. These defects are mostly created during the material growth, and involve a row of atoms rather than isolated atoms such as in the case of zero-dimensional defects. The main cause of these defects is the lattice mismatch between the substrate and the epitaxial layer grown on it.

The edge dislocation and screw dislocation are the two main types of 1-D defects. The edge dislocation shown in Figure 3.6 occurs as the boundary between the slipped and un-slipped crystal planes, when one of the planes of the crystal is displaced as compared to the other plane. The direction of the propagation of edge dislocation is into the plane and normal to the displacement direction.

Another type of dislocation known as screw dislocation (Figure 3.7) is created at the boundary between displaced and non displaced planes; the direction of this type of defect is parallel to the displacement direction [33].

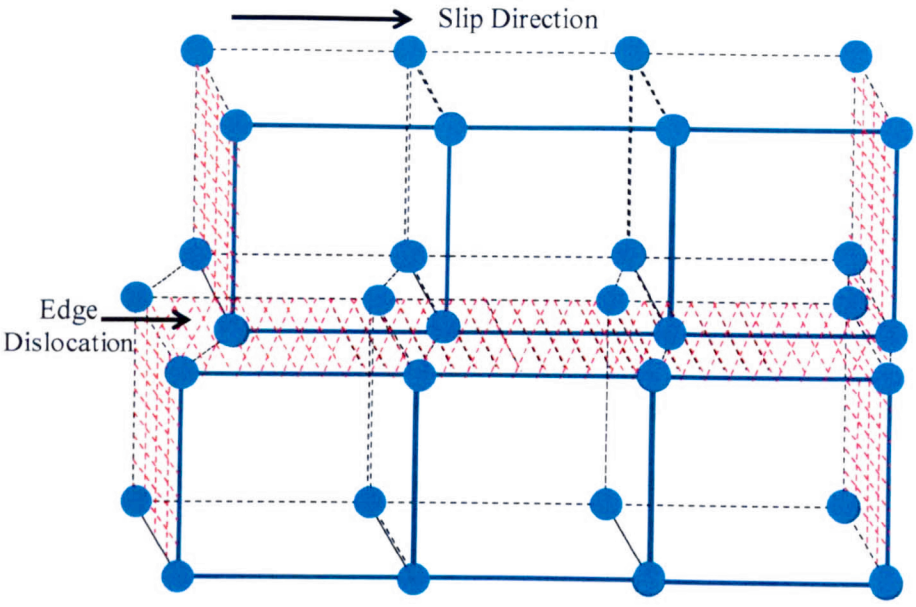

Figure 3.6: Illustration of the edge dislocation together with the direction of the Slip.

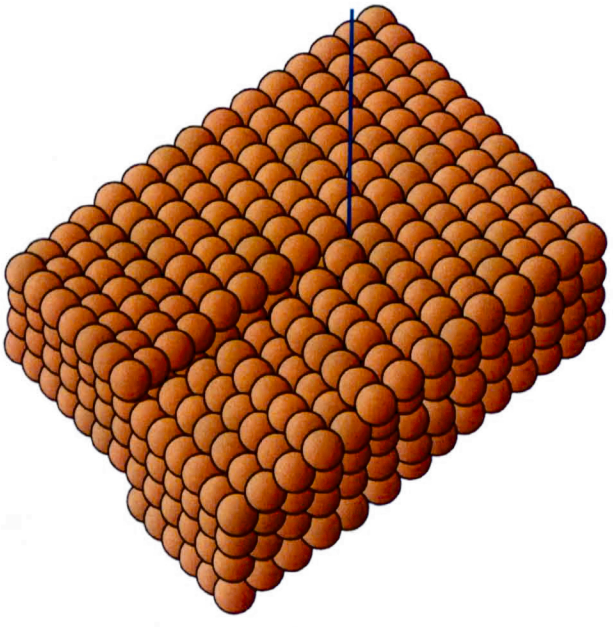

Figure 3.7: Illustration of screw dislocation.

3.1.5 SURFACE OR 2-D DEFECTS

The occurrence of plastic deformation is due to the change in the inter-atomic arrangement of the crystal. This change in the inter-atomic space occurs by moving

one part of the plane above and the other part below. This type of crystal movement is known as slip. The surface that contains the slip is known as the slip plane. The slip direction is the same as the direction of the motion of the planes. The crystal structure can be maintained after the slip, if and only if the slip vector and translation vectors are equal to each other.

There is another type of 2-D defects that occurs during the crystal deformation. This is known as twining. The difference between slip and twining is mainly related to the magnitude of the deformation; the magnitude of the deformation of slips is higher than that for the twining. In twining, the partial displacement occurs only in the neighbouring crystal planes. Therefore, the deformed part of the plane is the mirror image of the un-deformed part as shown in Figure 3.8.

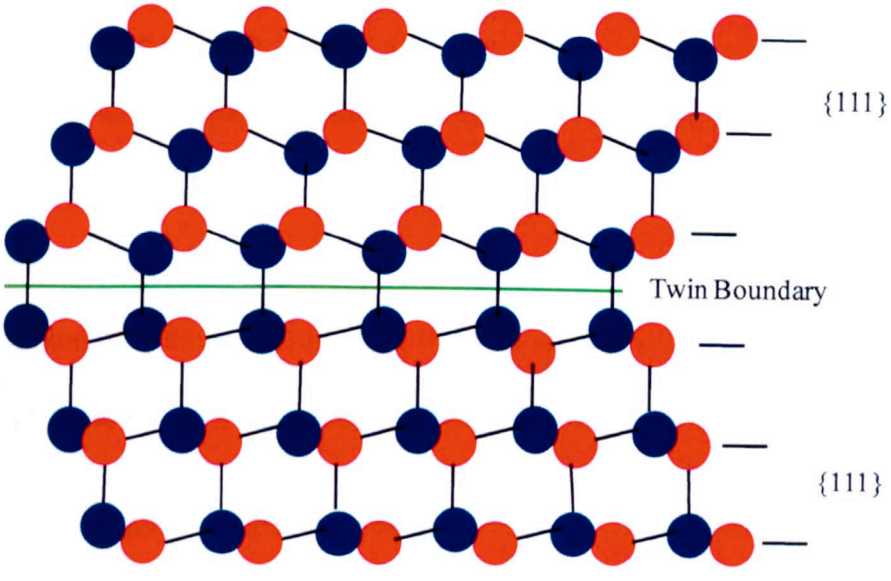

Figure 3.8: The arrangement of two different types of atoms is shown in such a way that the twin boundary is formed.

3.1.6 SHALLOW AND DEEP LEVEL DEFECTS

There are two general terms mostly used in the literature to categorise the defects in the semiconductor material according to their position with respect to conduction or

valence band energies (Figure 3.9) of the material. The defects having their energy levels close to the conduction or valence band are known as the shallow levels. Whereas, on the other hand the defects having their energy states near the middle of the band gap are said to be deep levels. The shallow levels have low ionization energies (<0.1 eV), and are easily ionized at room temperature and therefore, contribute to the current flow mechanisms in the semiconductors.

The shallow level defects are sometimes known as the shallow donors or shallow acceptors depending on the contribution of excess electrons to the conduction band or the excess of holes to the valence band of the host materials, respectively. For example, the addition of phosphorus (P) atoms to Si bulk material results in the addition of extra electrons to the conduction band of the resulting material and makes Si as an n-type material. On the other hand, if Si is doped with Ga, the element from group three in the periodic table, it adds excess number of holes to the valence band and makes Si as a p-type semiconductor material. The Ga in this case is known as the acceptor material and the P is known as the donor material. Some more familiar examples quoted in the reviewed article [34], are given here, such as the incorporation of Lithium (Li) in GaN. If the Li atom sits on the Ga site, it behaves as an acceptor. However, if it sits on the interstitial site it behaves as a donor.

As deep levels have activation energies > 0.1 eV below the conduction band or above the valence band, they cannot be ionised at room temperature and their contribution to the current flow is very small as compared to that of the shallow levels.

The deep centres affect the electronic and optical properties of semiconductors. When they act as nonradiative centres the luminescence properties of the material are

degraded. In addition, these centres create energy states within the forbidden energy band of the semiconductor materials, and thus, play an important role in avoiding the band to band transition of the carriers. Sometimes, they behave as generation, recombination, or trapping centres.

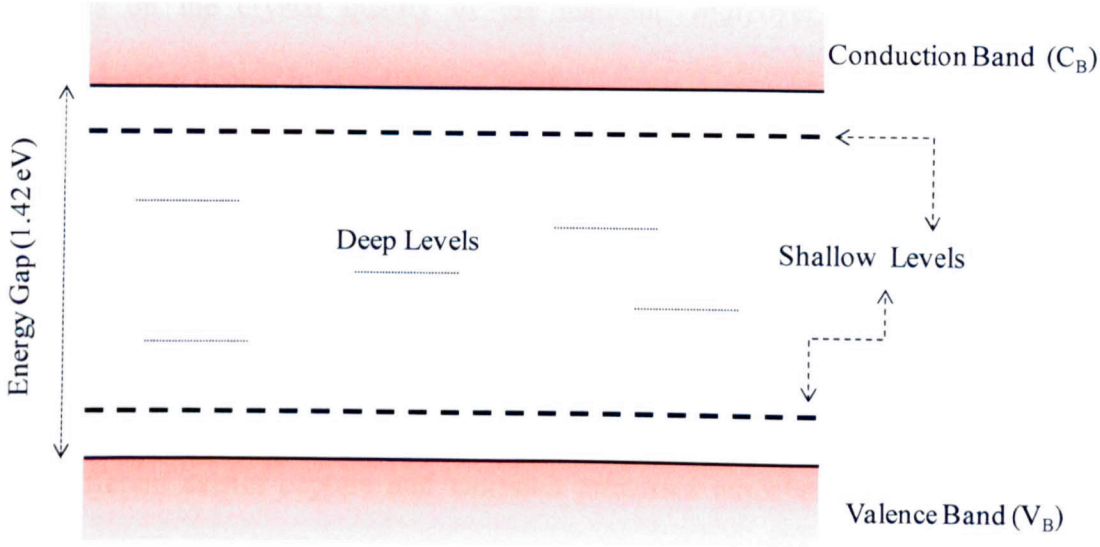

Figure 3.9: Shallow and deep level defects are sketched within the band gap of GaAs material (the scale is not real).

Beside the fact that these deep centres affect the efficiency of the optical devices such as LED's by affecting the carrier life time, these defects behave as trapping centres and reduce the free carrier concentration of the materials. Therefore, they play an important role in the formation of semi-insulating semiconductor materials. For example, EL2, the well known deep level in GaAs behaves as a killing centre. Its existence reduces the free carrier concentration in GaAs, and thus makes the GaAs a semi-insulating (highly resistive) material, mostly used as a substrate during the growth of III-V semiconductor materials and in integrated circuits [35-37].

3.2 GENERATION-RECOMBINATION STATISTICS

The carrier generation-recombination centers are the sources that affect the performance of semiconductor devices. This is because it affects the carrier life time of semiconductors. According to Schockley and Read [38] the carrier life time depends on the crystal quality of the material. Moreover, the generation and recombination occurs in two different ways;

(i) the band to band, which occurs mostly for the pure semiconductors and is known as the direct recombination.

(ii) Recombination via the defect energy states that exist within the material band gap and this is called the indirect recombination.

The different carrier capture and emission processes associated with the traps are shown in Figure 3.10. There are different carrier capture mechanisms, and are discussed in the following section.

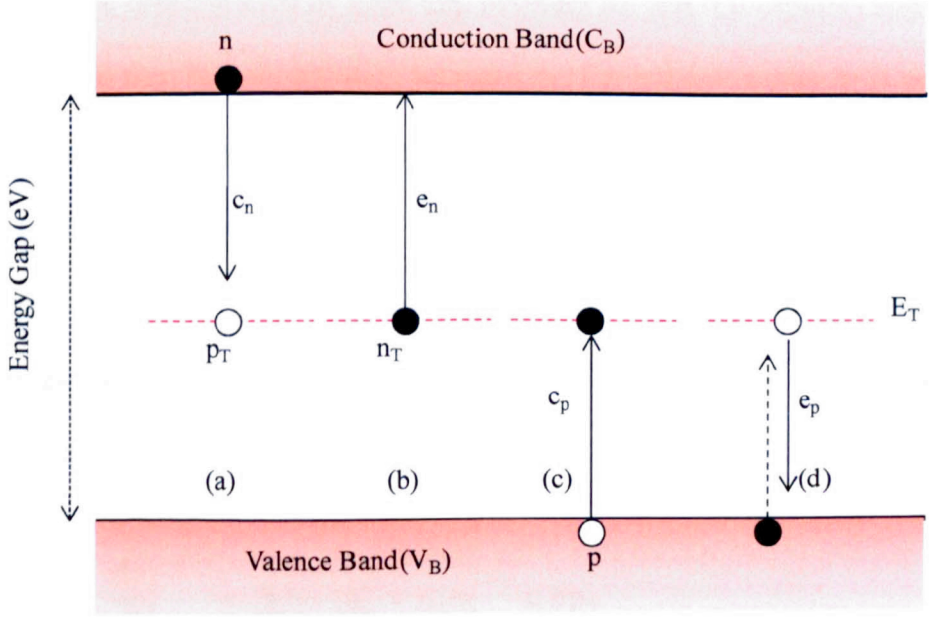

Figure 3.10: The different carrier trapping processes are shown; (a) electron capture, (b) electron emission, (c) hole capture and (d) hole emission [25].

3.2.1 ELECTRON CAPTURE MECHANISM

Consider a defect level of energy (E_T) and concentration (N_T) lying within the forbidden energy gap of the semiconductor, n and p are the density of electrons and holes resulting from the shallow level dopants, respectively. To understand the capture and emission mechanism of defects; consider that the defect captures an electron from conduction band as shown in Figure 3.10 (a), characterised by capture coefficient (c_n). When the electron is captured there are two possibilities; (i) it emit the electron back to the conduction band known as electron emission (e_n) [Figure 3.10 (b)], (ii) capture a hole from valence band called hole capture coefficient (c_p) as shown in Figure 3.10 (c). After any of the two processes shown in Figure 3.10 (b & c) there are two possibilities; (i) emit hole to the valence band (e_p) or (ii) capture electron from conduction band.

If the generation-recombination (G-R) center captures electrons from conduction band then the concentration of filled trap becomes n_T, and if it captures hole from the valence band then its concentration becomes p_T. For a donor center n_T is neutral and p_T is positively charged whereas in the case of an acceptor center n_T is negatively charged and p_T is neutral. The total concentration (N_T) of G-R is equal to the sum of n_T and p_T i.e. $N_T = n_T + p_T$. The electron density in conduction band (n), hole density in valence band (p), n_T and p_T change with time. The change of n with respect to time is mathematically expressed by

$$\left.\frac{dn}{dt}\right|_{G-R} = (b) - (a) = e_n n_T - c_n n p_T \qquad 3.1$$

Equation (3.1) describes the change in electron density in conduction band with respect to time. It is based on emission and capture process. One can notice that

electron emission depends only on the concentration of the traps filled by electrons and the emission rate, i.e. process (b) = $e_n n_T$. Whereas, the capture process involves the presence of electrons in the conduction band, c_n and p_T, i.e. process (a) = $c_n n p_T$.

Similarly, for holes the mathematical expression can be written as

$$\left.\frac{dp}{dt}\right|_{G-R} = (d) - (c) = e_p p_T - c_p p n_T \qquad 3.2$$

The emission rate e_n (equation 3.1) is defined as the number of electrons per second emitted by G-R to the conduction band and $c_n n$ is the concentration of electrons captured from conduction band [e_n = 1/sec]. The capture coefficient c_n depends on electron capture cross-section (σ_n) and thermal velocity (v_{th}) and is given by

$$c_n = \sigma_n v_{th} \qquad 3.3$$

where $v_{th} = \sqrt{\frac{3kT}{m^*}}$, k is Boltzmann constant, T is temperature in Kelvin and m* is the effective mass which can be obtained from Energy-Momentum (E-K) diagram $\left[\frac{1}{m^*} = \frac{4\pi^2}{h^2}\left(\frac{d^2E}{dk^2}\right)\right]$.

The capture cross-section of the center also depends on its nature i.e. the capture cross-section of negatively (repulsively) charged centers is smaller than that for neutral or positively (attractively) charged centres. The capture cross-section of neutrally charged centers is roughly equal to the atomic size (10^{-15} cm^2).

The concentration of the filled trap changes with respect to time during the emission or capture process and is given by

$$\left.\frac{dn_T}{dt}\right|_{G-R} = \frac{dp}{dt} - \frac{dn}{dt} = (c_n n + e_p)(N_T - n_T) - (c_p p + e_n)n_T \qquad 3.4$$

Since n and p are two time dependent variables in equation 3.4, therefore it is difficult to solve. For simplicity, consider the case that n and p are constant in the quasi-neutral region and the solution for n_T is given by

$$n_T(t) = n_T(0)\exp\left(\frac{-t}{\tau}\right) + \frac{(e_p + C_n n)N_T}{e_n + C_n n + e_p + C_p p}\left(1 - \exp\left(\frac{-t}{\tau}\right)\right) \qquad 3.5$$

Here $n_T(0)$ is concentration of filled G-R center at time t = 0 and $\tau = 1/(e_n+c_n n+e_p+c_p p)$.

For the steady state when $t \rightarrow \infty$, n_T is given by

$$n_T = \frac{e_p + C_n n}{e_n + C_n n + e_p + C_p p} N_T \qquad 3.6$$

The equations (3.5) and (3.6) are the basis of deep level impurity measurements.

For a particular case when there is n-type semiconductor in which p can be neglected, then equation (3.5) becomes

$$n_T(t) = n_T(0)\exp\left(\frac{-t}{\tau_1}\right) + \frac{(e_p + C_n n)N_T}{e_n + C_n n + e_p}\left(1 - \exp\left(\frac{-t}{\tau_1}\right)\right) \qquad 3.7$$

here $\tau_1 = 1/(e_n+c_n n+e_p)$.

Now consider a Schottky diode on an n-type semiconductor. In the absence of any bias (i.e. under zero bias) $c_n >> e_n$, and $n_T \approx N_T$. When a reverse bias is applied $e_n >> c_n$.

Equation (3.7) can be further simplified if we consider that the traps are in the upper half of the energy gap of the material so that the probability of emission of electrons to the conduction band is much higher than the probability of emission of holes to valence band, i.e. $e_n >> e_p$ so that e_p can be neglected. For this case the solution of equation (3.7) is written by

$$n_T(t) = n_T(0)\exp\left(\frac{-t}{\tau_e}\right) \approx N_T \exp\left(\frac{-t}{\tau_e}\right) \qquad 3.8$$

where $\tau_e = 1/e_n$, and $n_T(0)$ is the density of filled center at time t = 0.

The steady state trap density n_T for reversely biased space charge region is

$$n_T = \frac{e_p}{e_n + e_p} N_T \qquad 3.9$$

When the applied voltage changes from the reverse steady state bias to zero bias the carriers (electrons) from the neutral semiconductor region will rush to be captured by the traps in p_T (traps that have already captured the holes) state. In this way the density of the traps filled with electrons will change with respect to time, and the rate of change is given by

$$n_T(t) = N_T - [N_T - n_T(0)] \exp\left(\frac{-t}{\tau_c}\right) \qquad 3.10$$

where $\tau_c = 1/c_n$, n and n_T are the initial steady state concentration given by equation (3.9) and n_T (0) is the concentration of filled center at time t = 0.

3.3 EFFECT OF ELECTRIC FIELD ON CARRIER EMISSION RATES

The DLTS [39] working principle is based on measurement of junction capacitance transient that is produced during the filling and empting process of the traps by applying electrical pulses of different amplitudes. The use of the electrical pulses (bias) produce an electric field within the junction which will be discussed in chapter 4. In addition to the applied bias the doping concentration also enhance the electric field strength up to many thousands of V/cm within the junction [40]. The high amplitude electric field interacts with the defect associated potential barrier, and normally reduces its barrier height. This results in an enhancement of the carrier emission rate. The study of the effect of electric field on emission rate is very important because it provides useful information regarding defect charge states.

There are three different mechanisms responsible for enhancement of emission rates within the junction [41-44]

a) Poole-Frenkel Effect

b) Direct Tunnelling

c) Phonon-Assisted Tunnelling

Particularly, Poole-Frenkel effect is responsible for the emission of carriers from charged centres only. Whereas, both the direct and phonon-assisted tunnelling are observed for all type of charge states including neutral defect states [41]. All of these three mechanisms are illustrated in Figure 3.11.

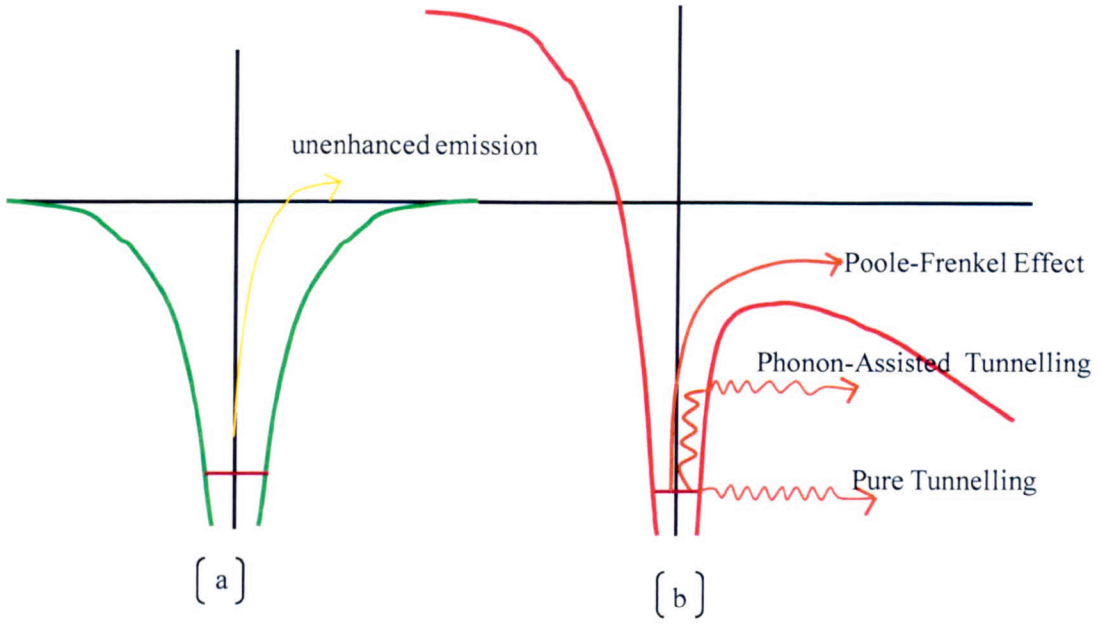

Figure 3.11: The carrier emission process is shown in the absence of applied electric field (a), and three different carrier emission processes namely, Poole-Frenkel Effect, Phonon-Assisted Tunnelling and pure-Tunnelling are shown in the presence of applied electric field (b).

3.4 DISTINCTION BETWEEN POOLE-FRENKEL AND TUNNELLING EFFECT

Ganichev et al. [42] proposed a simple model to easily differentiate Poole-Frenkel and Phonon-Assisted Tunnelling effects on the emission rates. The authors proposed that if the plot ln (e_n) versus $(E)^{1/2}$ (E is electric field) results in a straight line then the emission from a defect level follows the Poole-Frenkel effect. However, at high electric fields phonon-assisted tunnelling becomes dominant and the carrier emission rates increase logarithmically with the square of applied electric field. If the carrier emission rate at low electric field satisfies the conditions of phonon-assisted tunnelling then it is obvious that the emission rate is obtained from a neutral defect level.

Mathematically the phonon-assisted tunnelling follows the relation

$$\frac{e(F)}{e(0)} = \exp\left(\frac{F^2}{F_c^2}\right) \qquad 3.11$$

where e(F), e(0), F and Fc are the emission rate in the presence of applied electric field, emission rate in the absence of electric field, applied electric field, and characteristic electric field [$F_c = (\frac{3m^*\hbar}{q^2\tau_2^3})^{1/2}$], respectively, m^* is the effective mass, τ_2 is the tunnelling time, h is Plank's constant and q is electronic charge.

The tunnelling time (τ_2) for the carriers can be calculated by equating the slope of equation (3.11) to the value of F_c and solving equation (3.12) [45].

$$\tau_2 = \frac{\hbar}{2kT} \pm \tau_1 \qquad 3.12$$

where plus and minus signs stand for adiabatic potential structures for substituitional impurities and autolocalized centers, respectively and τ_1 is the time constant and is equal to the order of inverse local impurity vibration frequency.

3.5 DEFECTS IN III-V COMPOUND SEMICONDUCTORS

It is a well-known fact that the devices fabricated from semiconductor materials do not perform as predicted. The degradation of the devices is due to the existence of the different types of defects in the semiconductor materials. For this reason the identification and characterization of defects is essential to provide the feedback for the growth of good quality materials. This section is based on the literature review regarding the defects in GaAs and AlGaAs compound materials.

3.5.1 Defects in Gallium Arsenide (GaAs)

The native defects in the material are mostly created during the growth process. These defects include vacancies, interstitials, antisites and their complexes as well. The mechanism of creation of these types of defects is reported in the literature.

In GaAs two types of vacancies exist; Ga vacancy (V_{Ga}) and As vacancy (V_{As}). Kobayashi et al. [46] experimentally verified that by varying the As/Ga ratio, i.e. (As/Ga > 2) during MBE growth a number of Ga vacancies (V_{Ga}) are created in the epitaxial layers due to the shortage of Ga atoms in the material. The authors also expected to have As vacancies in the material for As/Ga< 1 but there were no evidences found for the existence of V_{As} vacancies. It was suggested that the absence of V_{As} is due to some residual background doping during growth. The evidence of V_{As} in MBE grown GaAs was found by Ky et al. [47] when performing Photoluminescence (PL) studies. The samples that showed this type of vacancy defect were grown under As-poor conditions. In addition the authors proposed that the presence of V_{As} may result in the formation of Ga antisite defects (Ga_{As}) and may also create Ga-vacanies (V_{Ga}).

The most common and famous intrinsic defect in bulk and epitaxial as-grown GaAs is known as EL2 level. The position of this trap in the energy gap observed from DLTS measurements is ~0.8 eV below the conduction band edge [48]. The concentration of EL2 in bulk and epitaxially grown materials is ~ 10^{16} cm^{-3} and ~ 10^{14} cm^{-3}, respectively [49]. In addition it is found that its concentration depends on growth conditions. For example it increases with As/Ga ratio [50-52]. These studies support that it is an As related trap [53]. Bardeleben et al. [49] suggested a more complex nature of EL2 rather than just an isolated As_{Ga} defect. It was assigned to an As_{Ga} and an intrinsic interstitial (As_i).

EL3, a defect level with an activation energy ranging from 0.408 eV [54] to 0.56 eV [55], is detected in GaAs material. Although there are still controversial theories in the literature regarding its origin, Mortane et al. [56] suggested that this defect is composed of Arsenic-interstitial (As_i) –Arsenic-vacancy (V_{As}) complex. However, the authors [55] reported that its origin could be related to an impurity, i.e. sulphur (S) in their case.

Another group of deep level defects called EL5 and EL6 exist in GaAs. Their energy with respect to conduction band edge is reported to be ~0.35 eV to ~0.43 eV [57]. The origin of these defect levels is even more controversial. It was suggested that these defects are impurity related [51, 58, 59] and due to native point defects [60, 61]. In order to clarify the origin of these defects an attempt was made by Yakimova et al. [57] on the Metalorganic vapor-phase epitaxially (MOVPE) grown GaAs samples using DLTS measurements. The authors explained that As interstitials (As_i) and Ga vacancies (V_{Ga}) complexes are the origins of EL5 defect. Their results were in correlation to the previous work carried out by Zahu et al.[62] and Tabata et al. [59]. They found that the concentration of the defect level with an energy ~ 0.47 eV and ~0.45 eV vary with As/Ga ratio. The deep level EL6 is tentatively assigned to V_{Ga}-V_{As} complex [63]. It is therefore, concluded that EL2, EL3, EL5, and EL6 traps are related to native defects in GaAs material.

3.5.2 Defects in Aluminium Gallium Arsenide (AlGaAs)

Aluminium Gallium Arsenide ($Al_xGa_{1-x}As$), the most famous III-V material after GaAs, has got interesting properties including the ability of tuning up its energy gap between GaAs and AlAs, and a direct band gap up to x~0.4 [64]. A multitude of

studies have been carried out to characterise deep level defects in AlGaAs and the findings are summarised below.

Yamanaka et al. [64] observed seven (ME1-ME7) electron traps in MBE grown $Al_xGa_{1-x}As$ (x = 0.07 to 1.0) layers using DLTS technique. It was found that the activation energy of all traps increased up to the aluminium content x = 0.4 (the cross-over point from direct to indirect band gap) and then decreased for x > 0.4. However, the energy of two of the traps (ME2 and ME3) remained the same. The possible origin of the defects was also discussed. ME2 and ME3 were found to be similar to the famous DX center in $Al_xGa_{1-x}As$, which is usually observed for x >0.35 and with an activation energy of ~0.42 eV. It was observed that the concentration of ME4, ME5 and ME6 is related to the doping impurities, but the other parametric studies such as V/III ratio and growth temperature reveal that the nature of ME4 and ME5 is not the same. The trap ME4 is attributed to aluminium and oxygen, and ME5 and ME6 are possibly associated to arsenic oxide originating from the arsenic source. Whereas, ME7 is possibly related to group III-vacancy and is probably related to EL2 in Vapour-phase Epitaxy (VPE) grown GaAs layers.

It seems from the available literature [65] that DX-centre is the most important trap in $Al_xGa_{1-x}As$ that controls the electrical properties of the material. The name of this deep center (DX) was proposed by Lang et al. [60, 66] in a view that the defect responsible for persistent photoconductivity (PPC) in III-V semiconductors is a complex of substituitional donor atom (D) and an unknown lattice defect (X). It was further suggested that X may possibly be related to As vacancy (V_{As}). In addition there are different suggestions available in the literature regarding the origin of DX center. Hayakawa et al. [6] proposed that the DX-center could be related to group III vacancy, the As interstitial or the antisite defect (As_{III}) in $Al_xGa_{1-x}As$. The authors

investigated the effect of V/III flux ratio on the defects in MBE grown $Al_xGa_{1-x}As$ (x = 0.7) epitaxial layers, and observed that the concentration of the DX defect increases continuously by increasing V/III flux ratio from 1 to ~4.5. However, Mizuta et al. [67] suggested the substituitional donors as an origin of DX center.

In addition, the energy of the DX center also changes with respect to the Al fraction (x) in AlGaAs. The energy of DX center as a function of x, obtained from Hall measurements, is plotted in Figure 3.12 with respect to the three conduction minima. It is clear that the activation energy of the DX center increases with x up to the direct-indirect crossover of the energy band gap. Whereas, in the indirect bandgap region the energy difference between the DX center and X-valley decreases, i.e. the activation energy of the center decreases for $x > 0.4$. Another important thing to note that the DX center energy is nearly parallel to the energy of L-minima [65].

The DLTS studies carried out by Calleja et al. [68] on MBE grown Si:AlGaAs epitaxial layers confirm the position of DX center to be ~160 meV below the L-minima for higher x (i.e. x = 0.74). On the contrary some other studies [69] regarding the relationship between L-minima and DX center energy does not support the linear relationship, and therefore, it is proposed that DX center is related to all the conduction band minima i.e. Γ-, L- and X-minima rather than only L-minima.

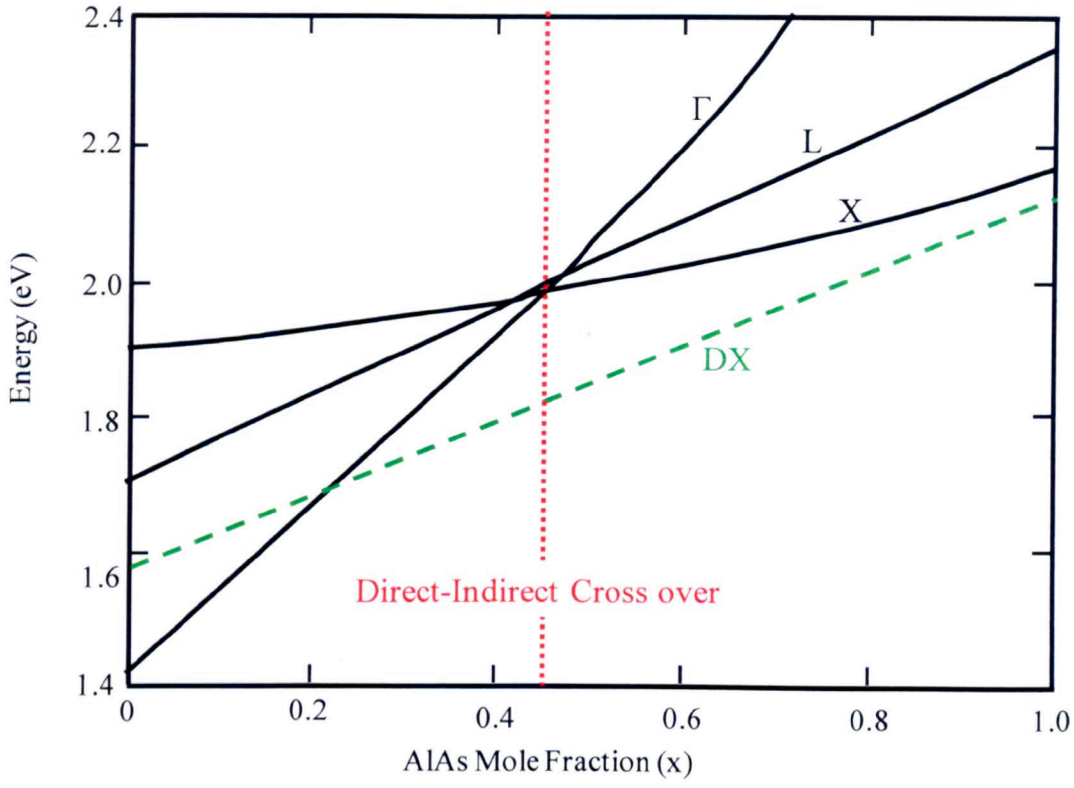

Figure 3.12: Schematic illustration of energy change of DX center with respect to three conduction band minima of AlGaAs [65].

3.6 GaAs AND $Al_xGa_{1-x}As$ SEMICONDUCTORS GROWN ON HIGH INDEX PLANES

Group IV element silicon is most widely used as n-type dopant in (100) plane MBE grown GaAs [5, 70]. However, it behaves as an amphoteric dopant in III-V compound materials such as in GaAs and AlGaAs. It can be incorporated in GaAs as a donor/n-type (Si occupies Ga atom position) or acceptor/p-type (Si occupies As atom position) impurity depending on the substrate orientation, growth temperature and As/Ga ratio. It has been reported in the literature that for the (N11)A GaAs orientations, silicon behaves as a p-type dopant for $N < 4$. As shown in Figure 3.13, A-face refers to a Ga terminating face where Si makes bonding with Ga atoms and occupies an As site and behaves as p-type dopant. However, in B-face, which refers

to an As terminating face, the Si atoms make bonding with As atoms, and therefore they occupy a Ga site and the resulting material is n-type [70]. Although Be is mostly used as a p-type dopant in MBE grown GaAs and AlGaAs, it has some disadvantages with regard to Si. For example Be has a higher diffusion coefficient and is less purer than Si, and therefore, the quality of Si-doped p-type GaAs is better than Be-doped GaAs. The electronic and optoelectronic properties of p-type Si-doped devices [6] are expected to be superior to p-type Be-doped devices. It is also mentioned by Xu et al. [7] that at higher As/Ga flux ratio, the Si is compelled to occupy Ga site and lead to n-type behaviour on (110) orientation. Transmission Electron Microscopy (TEM) measurements were performed to investigate the surface morphology on MBE samples grown on (110) using Si and Be dopants. TEM results elucidated that the defects observed between the buffer layer and the Si-doped epitaxial layer, extend more in Be-doped samples. They concluded that the extension of these defects into Be-doped epitaxial layers may be due to Be-diffusion and segregation.

Gonzalez-Borrero et al. [9] also experimentally confirmed the n- to p-type transition of Si- doped MBE layers grown on non-(100) planes for different As/Ga ratios. It was found that conversion from V_{Ga} to V_{As} takes place when changing the V/III ratio and growth temperature. Li et al. [8] also demonstrated that p-type Si doping is reproducible in AlGaAs and GaAs grown on (311)A GaAs planes. Their results also showed that higher hole concentration (4×10^{19} cm^{-3}) is obtained for the samples grown on (311)B substrate using low As_4 flux and higher growth temperatures (>660 °C), whereas, an electron concentration of $1 \times 10^{19} cm^{-3}$ is obtained for samples grown with higher As_4 flux and low growth temperatures (< 500°C). This confirms that the amphoteric nature of Si depends not only on the As/Ga ratio but also on the substrate temperature as well.

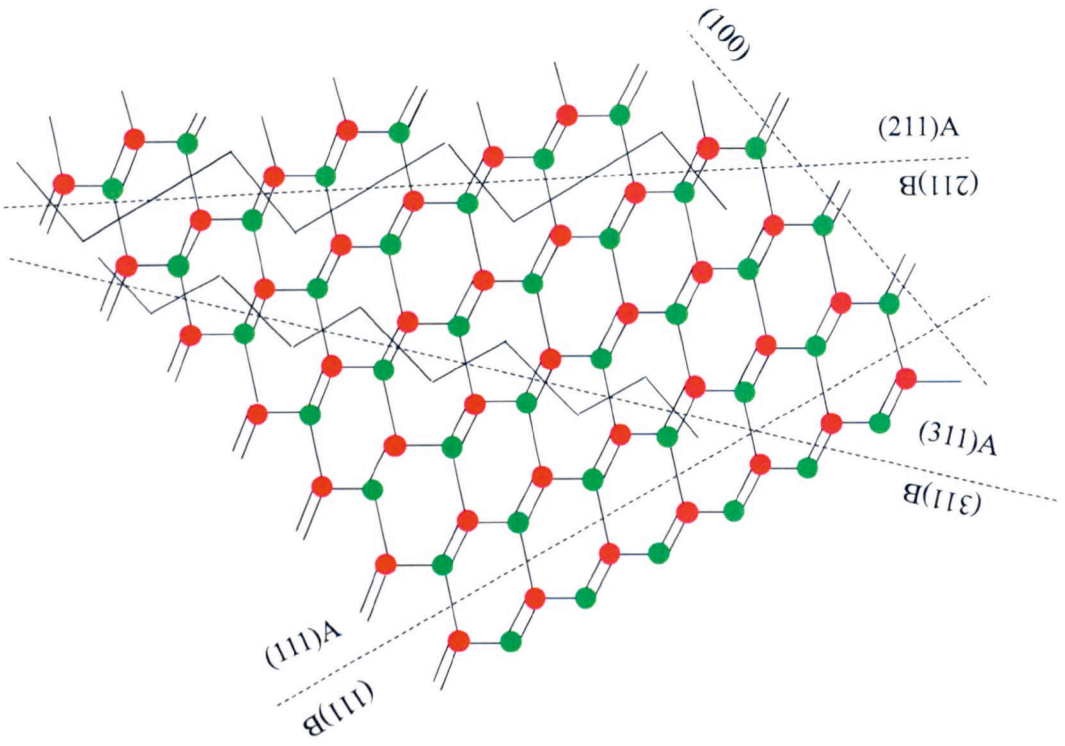

Figure 3.13: Atomic arrangement for each terminating plane in comparison to (100) plane. The green and red circles represent group V and group III atoms, respectively [71].

Studies of Si-doped AlGaAs/GaAs heterostructures grown on A-faces of GaAs substrates using techniques such as Atomic Force Microscopy (AFM), TEM, Hall Effect and Photoluminescence (PL) confirm that they are of better quality in terms of surface morphology and luminescence as compared to those grown on conventional (100) substrates [72]. Pavesi et al. [73] carried out detailed PL studies on MBE Si-doped GaAs epitaxial layers grown on (100), (111)A, (111)B, (211)A, (311)A, (311)B and (110) substrates using different doping levels and confirmed the amphoteric nature of Si.

From the literature survey carried out it has been noted that the use of DLTS and Laplace DLTS for the defect characterization in materials grown on high index planes is very scare. Sarmiento et al. [74] used DLTS on MBE samples grown on on-

axis (100) and off-axis (4° towards the (111)) GaAs substrates. The authors observed two traps in each orientation, they attributed them to EL3 (As-Vacancy) and EL2 (As- antisites), respectively.

CHAPTER 4

EXPERIMENTAL TECHNIQUES

Deep level Transient Spectroscopy (DLTS) is considered to be one of the most powerful techniques for the characterisation of electrically active defects lying within the semiconductor material band gap. This method relies mainly on the change in the junction capacitance of the device under investigation due to the charging and decharging of the traps present in the material. The process of filling and emptying the defects with charge carriers is achieved by employing a train of electrical pulses. This chapter discusses the Schottky devices required for the DLTS measurements, the conventional DLTS and high resolution Laplace DLTS techniques.

4.1 SCHOTTKY DIODE: PROPERTIES AND CHARACTERISATION

4.1.1 ENERGY BAND DIAGRAM

A Schottky diode is formed when a metal of work function (Φ_m) is brought into contact with either a p-type or n-type semiconductor with a work function $\Phi_s < \Phi_m$. The metal and semiconductor are so close to each other that the interfacial layer between them can be ignored. When isolated, the Fermi-energy levels in the metal and semiconductor are different. When the two materials are brought into contact the Fermi-energy levels in the metal and semiconductor become equal due to the flow of electrons from n-type semiconductor to metal. This process creates an equal

number of holes on semiconductor side. The schematic diagram showing the Schottky junction in equilibrium condition is shown in Figure 4.1. The parameters Φ_m, Φ_s, κ_n and Φ_{Bn}, are the metal work function (energy difference between Fermi level and Vacuum level), semiconductor work function, electron affinity (energy from bottom of the conduction band to vacuum level), and barrier height (difference between metal work function and electron affinity), respectively. In addition, E_C, E_F, E_T, and E_V represent conduction band, Fermi level, trap energy, and valence band energies, respectively.

In an ideal case, the separation between metal and semiconductor is very small and is about equal to the inter-atomic distance. Due to the very small separation the electrons flow easily and do not face any barrier. The barrier height and built-in potential are given by

$$\Phi_{Bn} = \Phi_m - \kappa_n$$

and

$$V_{bi} = \Phi_m - \Phi_s$$

By applying an external voltage to the Schottky diode, its depletion width changes, i.e. it increases with reverse bias and decreases with forward bias. The junction is said to be forward biased when the negative voltage is applied to n-type semiconductor side and positive to the metal. In this case, the built-in potential is reduced by the applied voltage (V_F) and is given by ($V_{bi} - V_F$). This is due to the fact that the semiconductor Fermi level increases with respect to the metal Fermi level. The reduction of the built-in potential allows the flow of electrons through the junction. Whereas, if the junction is reverse biased using a voltage (V_R), where the

positive voltage is applied to n-type semiconductor and negative to the metal side, the built-in voltage becomes (V_{bi} + V_R). In this case the semiconductor Fermi level decreases with respect to that of the metal, which results in an increase of the band bending and consequently an enhancement of the built-in potential. This has the effect of a reduction in the flow of electrons.

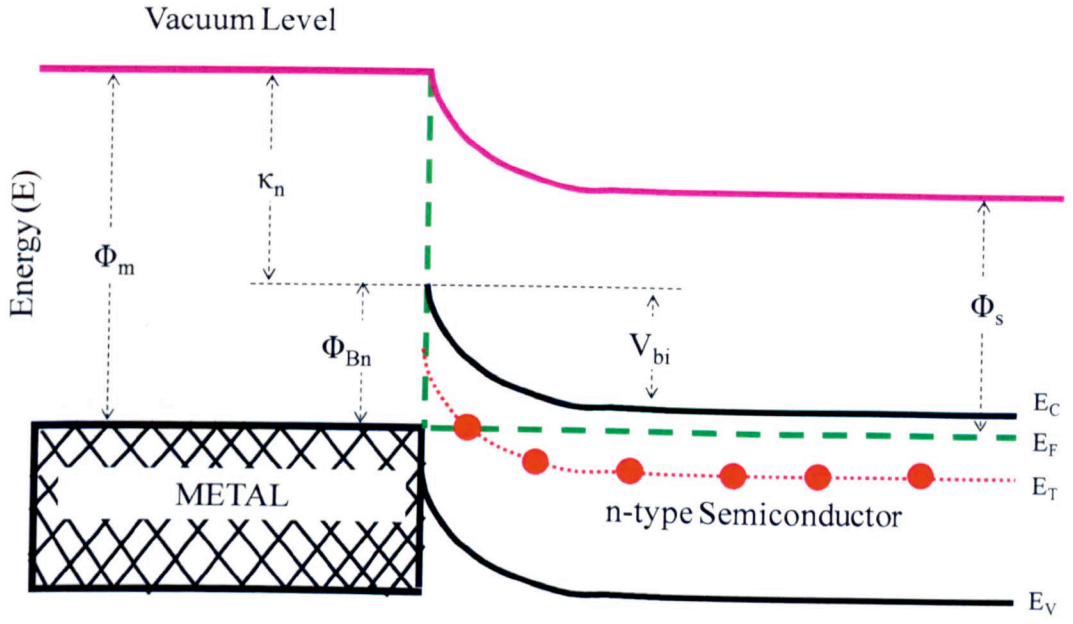

Figure 4.1: Schematic representation of Schottky contact between metal and semiconductor.

4.1.2 DEPLETION WIDTH

The depletion region of a Schottky diode behaves in the same manner as an abrupt (p^+ - n) junction. It is produced due to the depletion of free carriers. The depletion width of the junction (W) is calculated from Poisson's equation using the boundary conditions from junction interface (x = 0) to the start of the neutral region of the semiconductor (x = W). The net potential is given by Poisson's equation.

$$V = \frac{1}{\varepsilon_s} \int_0^W x\,\rho(x)\,dx \qquad 4.1$$

where ε_s is the semiconductor dielectric constant and x is the distance from junction to semiconductor. Considering that the charge density (ρ) is uniform, then it is given by

$$\rho = qN_{scr}$$

where N_{scr} is known as the density of charges in the depletion region or space charge region.

Thus from equation (4.1) the junction depletion width can be given by

$$W = \left[2\varepsilon_s \frac{V}{qN_{scr}}\right]^{1/2} \qquad 4.2$$

The effect of applied bias on the junction depletion width can be deduced from equation (4.2).

Therefore, the depletion width for the forward and reverse bias conditions is given by equations (4.3) and (4.4), respectively

$$W = \left[2\varepsilon_s \frac{(V_{bi} - V_F)}{qN_{scr}}\right]^{1/2} \qquad 4.3$$

$$W = \left[2\varepsilon_s \frac{(V_{bi} + V_R)}{qN_{scr}}\right]^{1/2} \qquad 4.4$$

According to the depletion region approximation, the depletion region is completely depleted from the free carriers. Therefore, the sharp boundary exists between the depleted and neutral regions. This is only possible for an ideal case. Practically, it is very difficult to get a sharp boundary between depleted and neutral regions because some charges are not depleted from the depletion region near neutral region. This small region called Debye Length (L_D) is given by

$$L_D = \left[\frac{\varepsilon_s kT}{q^2 N_{scr}}\right]^{1/2} \qquad 4.5$$

where k is Boltzmann constant, T is the temperature in Kelvin, and q is the electronic charge. The application of the depletion approximation is much more favourable when $L_D << W$. This condition is mostly satisfied for the low-doped semiconductors, or for the junction with large reverse bias [18].

4.1.3 DEPLETION JUNCTION CAPACITANCE

The capacitance (C) of a Schottky junction is similar to the capacitance of a parallel plate capacitor and mathematically given by

$$C = \frac{dQ}{dV} \qquad 4.6$$

where dQ is the charge in the depletion region and dV is the applied voltage.

The junction capacitance (C) also depends on the junction depletion width as given by the following the equation (4.7)

$$C = \frac{A\,\varepsilon_s}{W} \qquad 4.7$$

In equation (4.7), A is the diode area and W is the junction depletion width. Using equation (4.2) and (4.7) the junction capacitance can be written as [25, 75]

$$C = \frac{dQ}{dV_R} = \frac{A}{2}\left[\frac{2\varepsilon_s\, qN_{scr}}{V_{bi} + V_R}\right]^{1/2} \qquad 4.8$$

where V_R is the reverse bias and N_{scr} is the ionized impurity density in the space charge region. Equation (4.8) shows a relationship between junction capacitance and applied reverse bias (V_R). According to this equation, by increasing V_R the junction capacitance decreases.

The average doping concentration and the built-in potential of a device can be derived from the slope and intercept of a linear relationship between $1/C^2$ versus V_R, respectively. The linearity between $1/C^2$ and V shows that N_d is uniform throughout the depletion region. A non-uniformity of N_d would result in a non-linear relationship between $1/C^2$ and V_R [18].

4.1.4 TRANSIENT CAPACITANCE

The capacitance transient of a Schottky diode can be deduced from equation (4.8) considering $N_{scr} = N_D - n_T$ in case of shallow level donors. Thus the equation (4.8) can be written as

$$C = \frac{A}{2}\sqrt{\frac{2\varepsilon_s\, qN_D}{(V_{bi} + V_R)}}\sqrt{1 - \frac{n_T(t)}{N_D}} \qquad 4.9$$

or

$$C = C_0 \sqrt{1 - \frac{n_T(t)}{N_D}} \qquad 4.10$$

where C_0 is the capacitance of a device in the absence of deep level impurities at a reverse bias V_R and is given by

$$C_0 = \frac{A}{2} \sqrt{\frac{2\varepsilon_s q N_D}{(V_{bi} + V_R)}}$$

If we consider $N_T << N_D$ then the solution of equation (4.10) using first order expansion is given by

$$C \approx C_0 \left(1 - \frac{n_T(t)}{2N_D}\right) \qquad 4.11$$

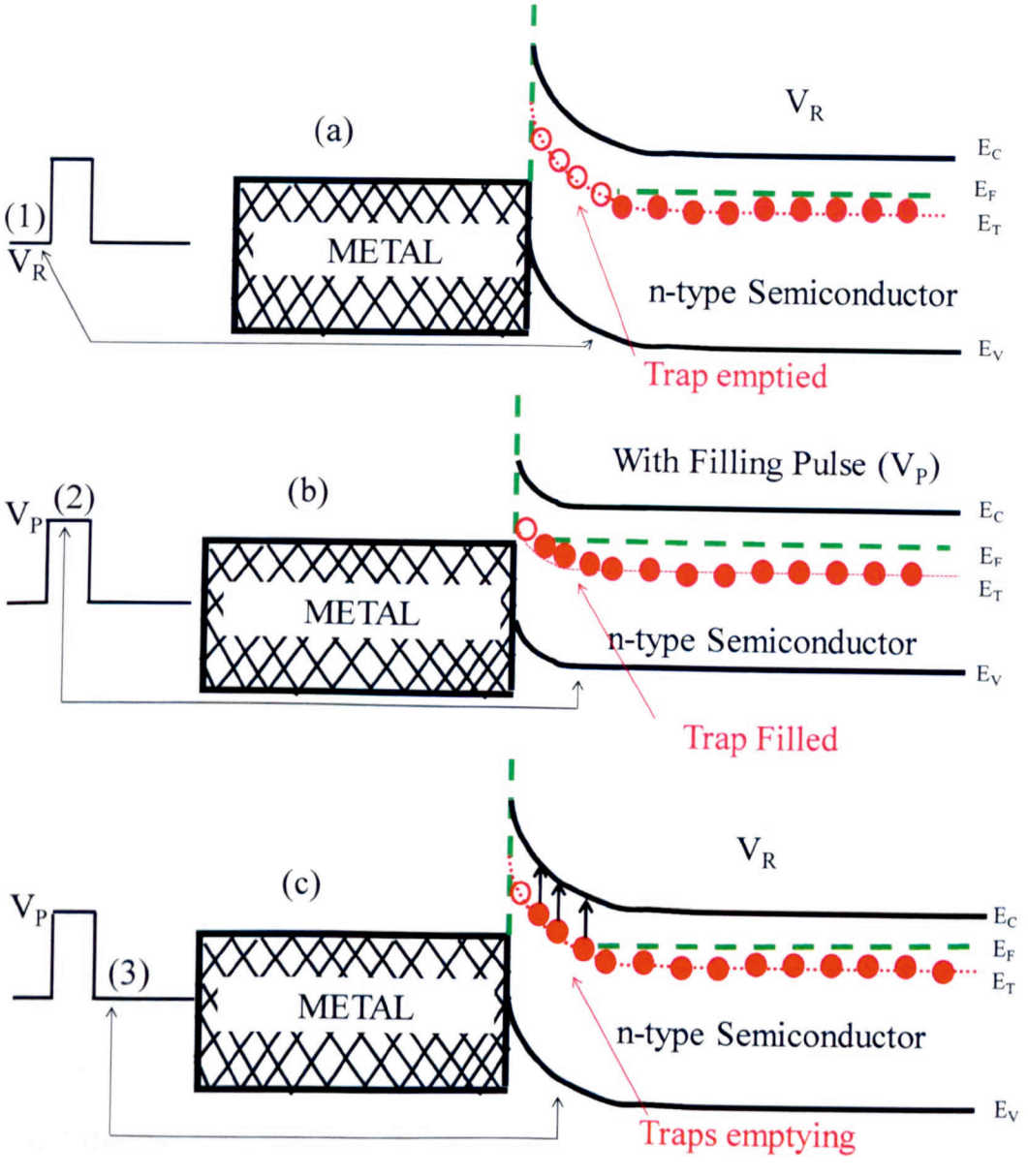

Figure 4.2: Illustration of the band diagram of an n-type Schottky diode under different bias conditions: (a) under reverse bias ($V = V_R$), (b) under filling pulse condition ($V = V_P$) , and (c) under reverse bias ($V = V_R$).

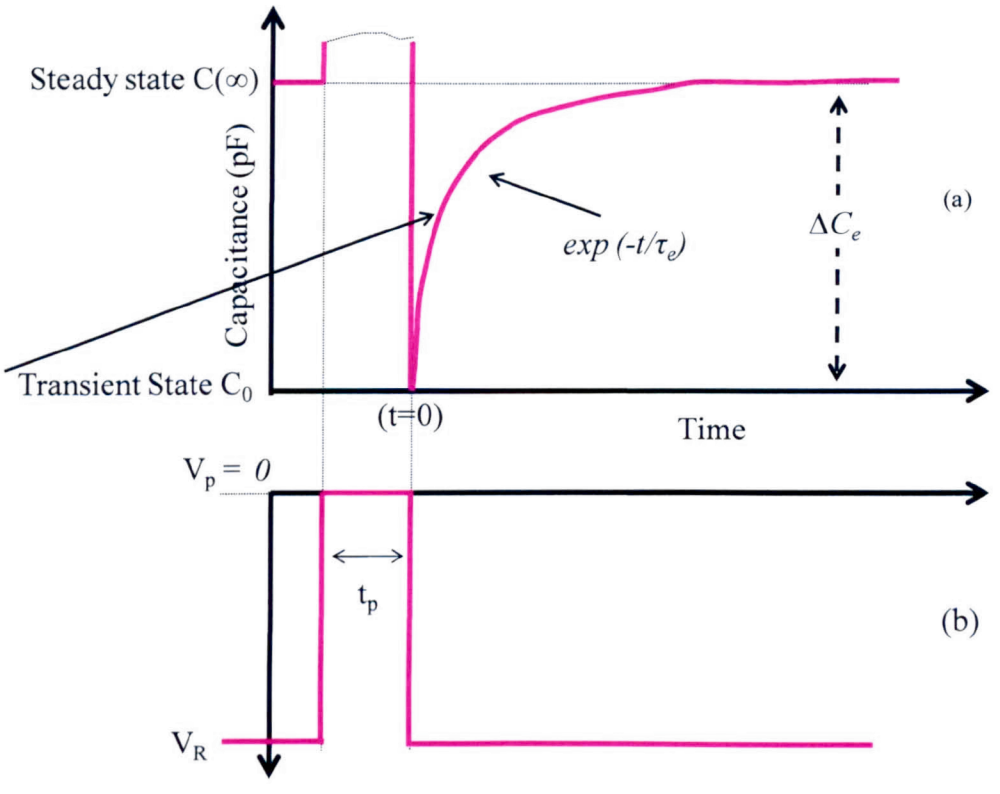

Figure 4.3: (a) Exponential capacitance transient response of the Schottky diode for different bias conditions shown in (b).

4.1.5 EMISSION OF MAJORITY CARRIERS

When the junction device is zero biased (Vp = 0) as shown in Figure 4.2 (b), the traps are allowed to capture majority carriers, i.e. electrons in this case. When a reverse bias is applied to the diode the traps start emptying as shown in Figure 4.2 (c), and the diode capacitance changes exponentially with time. The exponential change in the diode capacitance is shown in Figure 4.3 (a) for t > 0. Therefore, the resulting capacitance of the diode can mathematically be deduced using equation (3.8) in chapter 3 and equation (4.11).

$$C = C_0 \left[1 - \left(\frac{n_T(0)}{2N_D}\right) \exp\left(\frac{-t}{\tau_e}\right)\right] \qquad 4.12$$

This equation is schematically shown in Figure 4.3 (a) for $t > 0$.

From the capacitance – time relationship the value of τ_e can be derived, and from the reverse biased capacitance change the value of $n_T(0)$ can be obtained. If one define $\Delta C_e = C(t = \infty) - C(t = 0)$ then

$$\Delta C_e = C_0 \frac{n_T(0)}{2N_D} \qquad 4.13$$

The capacitance difference is given by

$$C(\infty) - C(t) = C_0 \frac{n_T(0)}{2N_D} \exp\left(\frac{-t}{\tau_e}\right) \qquad 4.14$$

The slope of the plot ln $[C(\infty) - C(t = 0)]$ versus t is equal to $-1/\tau_e$, whereas, the intercept is equal to ln $[n_T(0)\, C_0 / 2N_D]$.

The emission time constant of the carriers for a given trap can be deduced by considering the capture and emission coefficients as discussed in chapter 3. Recalling equations (3.1) and (3.2), it is evident that emission and capture coefficients are related to each other. Considering the detailed balance principle which states that $dn/dt = 0$ under equilibrium condition and considering that the trap concentration (N_{T0}) is equal to sum of n_{T0} and p_{T0}. Therefore, equation (3.1) becomes

$$e_{n0} n_{T0} = c_{n0} n_0\, p_{T0} = c_{n0} n_0 (N_T - n_{T0}) \qquad 4.15$$

In equation (4.15) subscript '0' represents the respective values in equilibrium state.

The values of carrier concentration at equilibrium state (n_0) and the filled trap concentration at equilibrium state (n_{T0}) are

$$n_0 = n_i \exp\left[\frac{(E_F - E_i)}{kT}\right]; \text{ and } n_{T0} = \frac{N_T}{1 + \exp((E_T - E_F)/kT)} \qquad 4.16$$

where n_i is the intrinsic carrier density, E_F is Femi energy level, E_i is the reference energy level i.e. $E_i = E_C$ for n-type semiconductor and $E_i = E_V$ for p-type semiconductors [18, 26].

By combining equation (4.15) and (4.16) carrier emission rate in equilibrium state is given by

$$e_{n0} = c_{n0} n_i \exp\left[\frac{(E_T - E_i)}{kT}\right] \qquad 4.17$$

For holes a similar equation (4.17) exists, and the relationship between emission and capture coefficients remain the same for equilibrium condition i.e. $e_{n0} = c_{n0}\, n_0$ and $e_{p0} = c_{p0}\, p_0$,

For electrons

$$n_0 = n_i \exp\left[\frac{(E_T - E_i)}{kT}\right] \qquad 4.18$$

and similarly for holes

$$p_0 = n_i \exp\left[\frac{-(E_T - E_i)}{kT}\right]$$

The emission time constant of the carriers can be obtained from equation (4.17) using $e_n = 1/\tau_e$ and $c_n = \sigma_n v_{th}$ for electrons

$$\tau_e = \frac{\exp\left[\frac{(E_i - E_T)}{kT}\right]}{\sigma_n v_{th} n_i} = \frac{\exp\left[\frac{(E_c - E_T)}{kT}\right]}{\sigma_n v_{th} N_c} \qquad 4.19$$

where v_{th} is carrier thermal velocity, σ_n is capture cross-section and N_c is the effective density of states in conduction band. The quantities v_{th} and N_c are mathematically given below

$$v_{th} = \sqrt{\frac{3kT}{m^*}} \qquad 4.20$$

$$N_c = 2\left(\frac{2\pi m^* kT}{h^2}\right)^{3/2} \qquad 4.21$$

where h is Planks constant and m^* is the electron effective mass which can be derived from E-k diagram (chapter 3).

For simplicity, using $\gamma_n = (v_{th}/T^{1/2}) \times (N_c/T^{3/2})$, the emission time constant can be written as

$$\tau_e T^2 = \frac{\exp\left[\frac{(E_c - E_T)}{kT}\right]}{\sigma_n \gamma_n} \qquad 4.22$$

The slope of $\ln(\tau_e T^2)$ or $\ln(e_n/T^2)$ versus 1/T is equal to $[(E_c\text{-}E_T) / k]$ and the intercept is equal to $(1/\sigma_n N_c V_{th})$ which are used to deduce the trap activation energy and capture cross-section, respectively [25, 26].

4.1.6 CAPTURE OF MINORITY CARRIERS

Let suppose that a Schottky diode is reverse biased for a long time, and therefore all the traps are emptying [Figure 4.2 (a)]. After a filling pulse is applied the state of the traps goes from a filling to an emptying as shown in Figure 4.2 (c) to Figure 4.2 (b).

The concentration of the filled trap is given by equation (3.10), which is rewritten

$$n_T(t) = N_T - [N_T - n_T(0)] \exp\left(\frac{-t_f}{\tau_c}\right) \qquad 4.23$$

where τ_c is capture time constant and t_f is filling time. For long filling time, $t_f >> \tau_c$, it is assumed that all the traps are filled by capturing electrons and $n_T\ (t \rightarrow \infty) \approx N_T$. However, for very small filling time i.e. $t_f << \tau_c$ the concentration of filled traps $n_T\ (t \rightarrow 0) \approx 0$.

Substituting equation (4.23) in equation (4.12), the filling pulse dependent reverse bias capacitance of a Schottky diode is given by

$$C(t) = C_0\left[1 - \frac{[N_T - (N_T - n_T(0))] \exp\left(\frac{-t_f}{\tau_c}\right)}{2N_D} \exp\left(\frac{-(t - t_f)}{\tau_e}\right)\right] \qquad 4.24$$

Here τ_c is the capture time which can be obtained by changing the filling pulse time.

Using $t = t_f$ in equation (4.24), the transient capacitance [Figure 4.3 (a)] is given by

$$C(t_f) = C_0\left[1 - \frac{[N_T - (N_T - n_T(0))] \exp\left(\frac{-t_f}{\tau_c}\right)}{2N_D}\right] \qquad 4.25$$

Considering the difference between two capacitance i.e. $\Delta C_c = [C(t_f) - C(t_f = \infty)]$, equation (4.25) can be written as

$$\Delta C_c = C(t_f) - C(t_f = \infty) = C_0 \frac{N_T - n_T(0)}{2N_D}\left[\exp\left(\frac{-t_f}{\tau_c}\right)\right] \qquad 4.26$$

The solution for filling pulse time (t_f) can be extracted from equation (4.26) and is written as

$$\ln(\Delta C_c) = \ln\left[C_0 \frac{N_T - n_T(0)}{2N_D}\right] - \frac{t_f}{\tau_c} \qquad 4.27$$

The slope of a plot of $\ln(\Delta C_c)$ versus (t_f) is equal to $[-1/\tau_c = -\sigma_n v_{th} n]$ and the intercept is equal to $\ln[C_0 \{N_T - n_T(0)\}/2N_D]$. To draw this type of plot one needs to perform the DLTS measurements by varying the filling pulse time [25, 26].

4.2 DEEP LEVEL TRANSIENT SPECTROSCOPY (DLTS)

Deep Level Transient Spectroscopy (DLTS) is a very popular defect characterization technique that depends on the change of the junction capacitance of diodes such as p-n or Schottky diodes. Since its invention by Lang in 1974 [39], DLTS is considered to be the most powerful technique for the assessment of electrically active defect states present in semiconductors.

The DLTS signal is obtained from the capacitance transient which originates due to the filling and empting of the defect levels by applying electrical pulses to the sample under observation. This section will cover the basic understanding of the principle of operation of DLTS.

4.2.1 WORKING PRINCIPLE OF CONVENTIONAL DLTS

D.V Lang [39] introduced the conventional DLTS technique in 1974 This technique is based on the rate window concept where the capacitance is measured at two different times t_1 and t_2 ($t_2 > t_1$). The DLTS signal (S) is basically the change in capacitance between t_1 and t_2 [$S = \Delta C = \{C(t_2) - C(t_1)\}$]. Therefore, the DLTS signal (S) is mathematically written as

$$S(T) = C(t_1) - C(t_2) = \frac{C_0\, n_T(0)}{2N_d}\left[\exp\left(\frac{-t_2}{\tau_e}\right) - \exp\left(\frac{-t_1}{\tau_e}\right)\right] \qquad 4.28$$

equation (4.28) can be rewritten as

$$S(T) = \Delta C_0\left[\exp\left(\frac{-t_2}{\tau_e}\right) - \exp\left(\frac{-t_1}{\tau_e}\right)\right] \qquad 4.29$$

$\Delta C_0 = \frac{C_0 n_T(0)}{2N_d}$ is the change in capacitance.

The maximum amplitude of the DLTS signal is obtained when the inverse emission rates (τ_{max}) is equal to the DLTS rate window as described below. The value of $\tau_{e,max}$ can be deduced by taking the first derivative of equation (4.28) and equating it to zero i.e. $\frac{dS(T)}{dt} = 0$.

then

$$\tau_{e,max} = \left(\frac{t_2 - t_1}{\ln\left(t_2/t_1\right)}\right), \text{ for } \tau = \tau_{e,max} \qquad 4.30$$

Equation (4.30) is known as the rate window. By changing the values of two measurement times one can change the value of the rate window and thus the peak maximum can be obtained at different temperatures.

The DLTS signal generation process is schematically represented in Figure 4.4 (a). It can be seen that the emission rates become faster and faster with increasing the temperature of the sample. The DLTS signal peaks when the inverse of emission rate $\tau = \tau_{e,max} = 1/e_n$ matches $\Delta t = t_2 - t_1$ [25, 26].

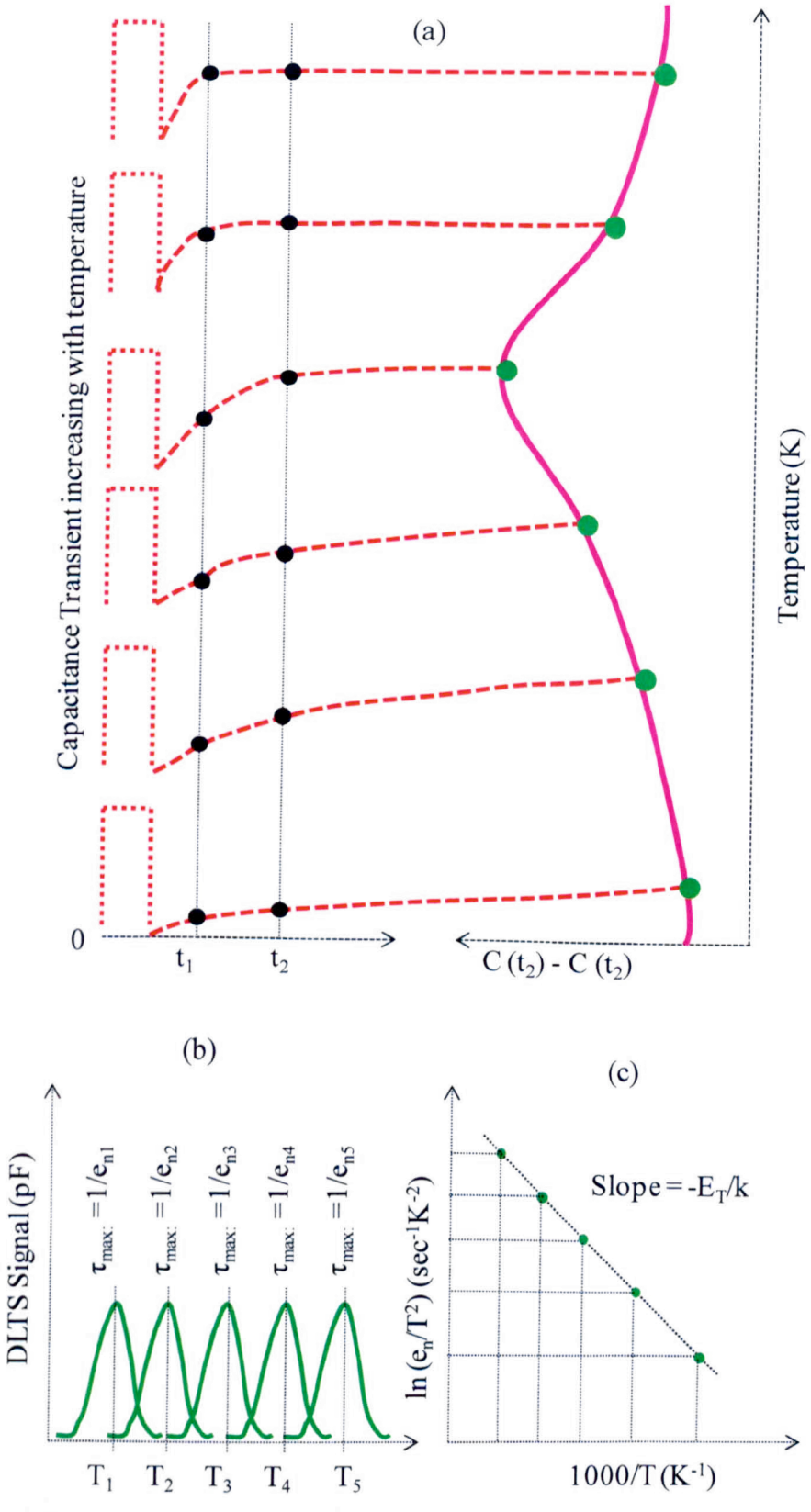

Figure 4.4: The generation of DLTS signal from capacitance transient is illustrated in (a); (b) represents the change in peak position for different rate windows, and (c) the Arrhenius plot for the calculation of trap activation energy (E_T).

4.2.2 APPLICATIONS OF DLTS

This section is devoted to the applications of the DLTS technique for the characterization of electrically active defects. The measurement procedures and the analysis of the data will be discussed to show how to obtain the different trap parameters such as activation energy, capture cross-section and trap concentration. The effect of the electric field on the carrier emission rates will be also presented.

4.2.3 TRAP ACTIVATION ENERGY

One of the most important parameters of defects is the activation energy E_T (eV). This value is referred with respect to the conduction or valence band energy for electron or hole traps, respectively, within the band gap.

As explained in the previous section the conventional DLTS relies on the use of different rate windows to determine the emission rates at different temperatures. For example, by using equation (4.19) the electrons emission rates can be written as

$$e_n = \sigma_n \langle v \rangle_{th} N_c \exp\left(-\frac{\Delta E}{kT}\right) \qquad 4.31$$

where $\Delta E = E_c - E_T$ is the trap activation energy with respect to conduction band energy, σ_n is apparent capture cross-section of trap, $\langle v_{th} \rangle$ average carrier thermal velocity equation (4.20) and N_C is the density of states in conduction band equation (4.21).

The plot of $\ln\left(e_n/T^2\right)$ versus (1000/T) should be a straight line. The factor $(1/T^2)$ appears because of the temperature effect on V_{th} and N_c. The slope of the plot is used to calculate the trap activation energy (eV), whereas (equation 4.22) the intercept at

(1000/T) = 0 is used to deduce the value of the apparent capture cross-section of the trap.

4.2.4 TRAP CONCENTRATION

The trap concentration (cm^{-3}) is directly related to the amplitude of the conventional DLTS peak. The mathematical relation to calculate the trap concentration can be derived from equation (4.11) [39].

Considering that the filling pulse is applied for sufficient time so that the trap is completely filled and using equation (4.11) and $n_T(t) = N_T$,

$$\Delta C_0 = C_\infty \left(1 - \frac{N_T}{2N_D}\right) - C_\infty$$

For $N_T << N_D$

$$\Delta C_0 = C_\infty \left(\frac{N_T}{2N_D}\right)$$

Therefore,

$$N_T = 2\, N_D \frac{\Delta C_0}{C_\infty} \qquad 4.32$$

where N_T is the trap concentration, ΔC_0 is the conventional DLTS peak amplitude and C_∞ is the capacitance at maximum reverse bias [25, 26].

4.2.5 TRAP CAPTURE CROSS-SECTION

In addition to trap activation energy, the capture cross-section of the defect is also very important parameter of a defect level. There are two different ways by which

the trap capture cross-section can be determined. The first and simplest way is to infer its value from the intercept of the Arrhenius plot of ln $[e_n/T^2]$ versus (1000/T) using equation (4.22). This is known as the apparent capture cross-section. This value may deviate from the real value because of the following two main reasons: (i) a very small error in the extrapolation process can cause a large error in the calculated value, (ii) the capture cross-section is assumed to be temperature-independent which is not always the case.

There is another procedure which allows the direct measurement of the capture cross-section of the defect level. This technique is known as the direct filling pulse method. In this case, the DLTS measurements are carried out at a constant rate window using different durations of the trap filling pulse (t_f). The number of trapped carriers will depend on the duration of the filling pulse. The longer the pulse the more carriers will be trapped and therefore the amplitude of the resulting DLTS peak will increase with t_f. For a certain maximum value of t_f the trap will be completely filled with carriers and the DLTS peak saturates.

The relationship between the DLTS peak height (S), and duration of the filling pulse, t_f is expressed as

$$1 - \frac{S_{t_f}}{S_o} = \exp\left(-\frac{t_f}{\tau}\right) \qquad 4.33$$

where S_o is the saturated DLTS peak height for the maximum filling pulse time, t_f is the filling pulse duration and τ is the capture time constant [$\tau = 1/(n\, C_n)$], where n is the effective doping concentration or electron density in the conduction band and C_n is the capture rate and is given by $C_n = \sigma_n \langle vth \rangle$.

Therefore, the capture cross-section can be calculated from the slope of the graph $\ln[1 - (S_{tf}/ S_o)]$ versus t_f which is given by $\sigma_n = \left(\frac{1}{\tau\, n\langle v_{th}\rangle}\right)$ [76-78].

Sometimes, the capture cross-section can have a temperature-dependence relationship which follows equation (4.34).

$$\sigma_n = \sigma_\infty \exp\left(-\frac{\Delta E_\sigma}{kT}\right) \qquad 4.34$$

where ΔE_σ is the energy barrier faced by an electron (or hole) to be captured by the defect.

The values of σ_∞ and ΔE_σ can be deduced from the intercept and the slope of the plot of $\ln(\sigma_n)$ versus 1000/T, respectively.

It is worth pointing out that ΔE_σ can be used to determine the real value of the activation energy of the trap using $\Delta E_{meas} = \Delta E + \Delta E_\sigma$, here ΔE_{meas} is the apparent activation energy, ΔE is the actual activation energy of the defect and ΔE_σ is the barrier energy obtained from the temperature dependent capture cross-section measurements (equation 4.34) [76].

The physical mechanism involved behind this phenomenon is explained by Henry et al. [77] with the help of the model shown in Figure 4.5. In this model the authors propose that the position of the defect energy level changes within the band gap. The responsible factor for this change is the lattice vibration in the crystal. This process is known as the capture of the carriers by multiphonon emission.

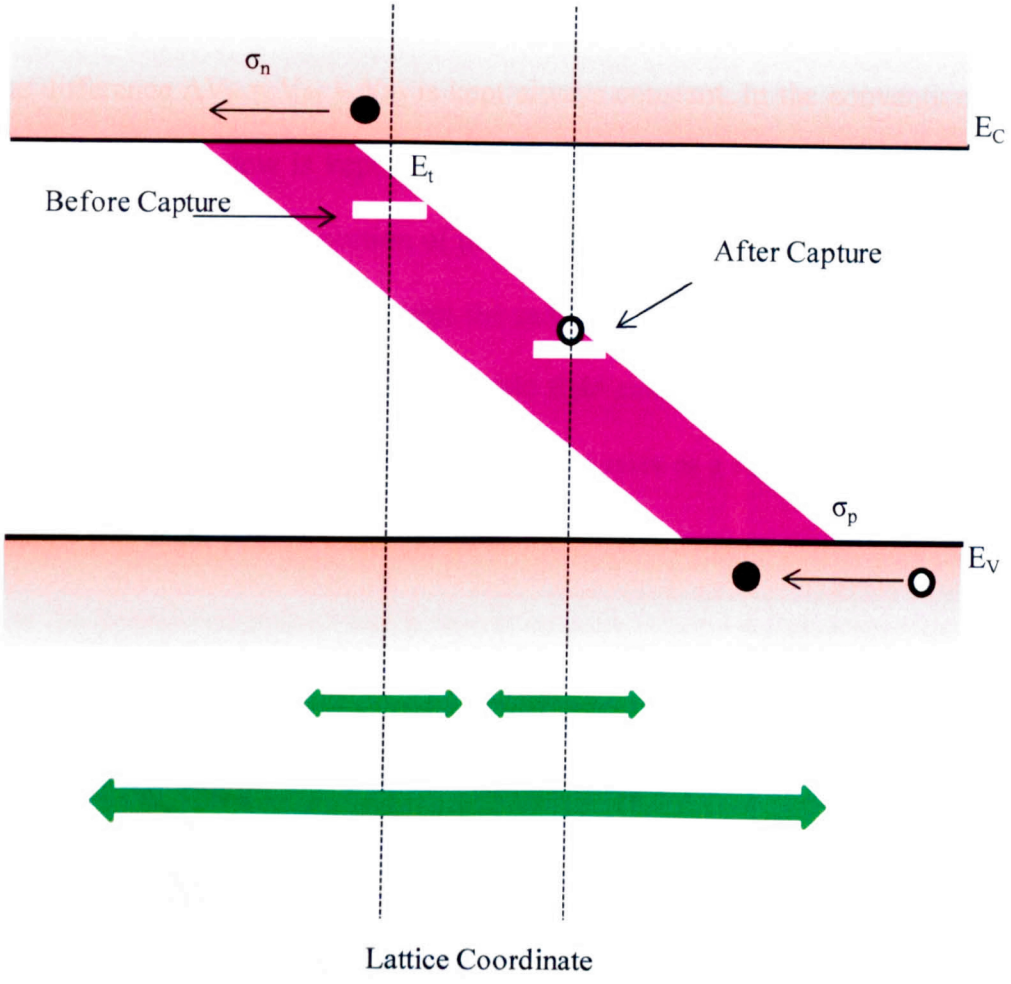

Figure 4.5: Schematic diagram illustrating the mechanism of nonradiative capture of electron taking place. The vertical dashed lines represent the lattice coordinate equilibrium positions. The diagonally shaded region within the band gap shows the way that the trap energy changes with the lattice vibration. The smaller two arrows (green) represent the amplitude of the thermal vibrations before and after electron capture. The large arrow (green) shows the amplitude of the lattice vibrations relative to the new equilibrium position after the capture [77].

4.2.6 EFFECT OF THE ELECTRIC FIELD ON THE EMISSION RATES

The effect of the junction electric field on the carrier emission rates is discussed in chapter 3. In this section the measurement procedure is described. The measurements are carried out by using the double pulse method in which the sample is biased by applying two pulses with same reverse bias (V_R) and different filling pulse heights

V_{P1} and V_{P2}, in such a way that $V_{P2} < V_{P1}$ as schematically illustrated in Figure 4.6. The difference $\Delta V_P = V_{P1} - V_{P2}$ is kept always constant. In the conventional DLTS mode the rate window is kept constant. The purpose of this is to keep the electric field uniform within each portion of the junction under investigation. In addition, the amplitude level of V_R is always kept the same. By applying electrical pulses V_{P1} and V_{P2} of different height the junction electric field can be changed. This will allow the investigation of the dependence of the emission rates as a function of electric field in separate and small portion of the junction.

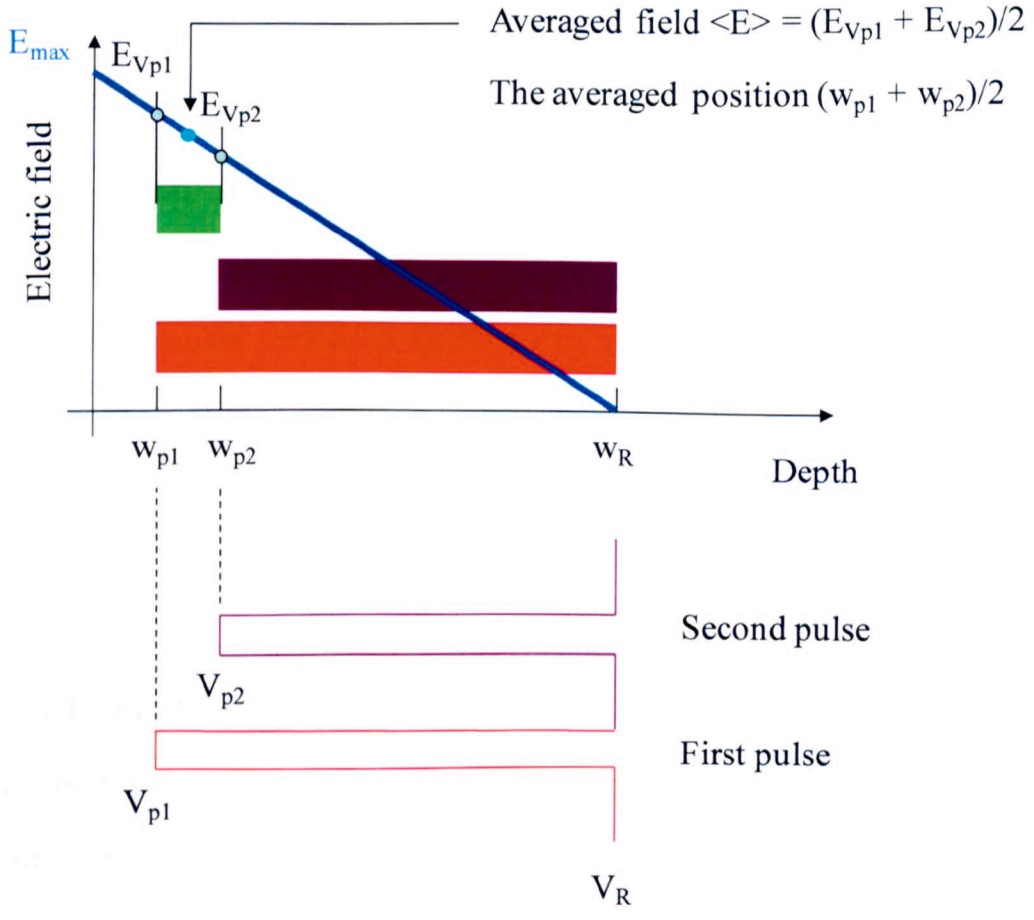

Figure 4.6: Illustration of the process of measurement of electric field dependent emission rates.

4.3 PRINCIPLES OF LAPLACE DLTS

Although DLTS [39] is considered to be the most powerful technique for the characterization of defects in semiconductors, its poor resolution has always been a questionable problem. The resolution of DLTS signal depends on the exponential behaviour of the emission rates. However, if the emission rates do not follow an exponential behaviour the resolution of the signal becomes poor. The deviation from the exponential behaviour is due to: (i) the emission of carriers detected from closely spaced defects and (ii) the effect of the junction electric field on the carrier emission rates. In addition, Ikossi-Anastasiou and Roenker [79] suggested that the emission from a trap having very high concentration i.e. comparable to the material doping concentration can cause the non-exponential behaviour of the capacitance transient.

To overcome the problems associated with the resolution of DLTS signals resulting from non-exponential behaviour of capacitance transient, is to consider that the capacitance transient contains a spectrum of emission rates. The recorded transient [f(t)] can be shown by a mathematical relation

$$f(t) = \int_0^\infty F(s)\, e^{-st}\, ds \qquad 4.35$$

where F(s) is the spectral density function [80]. The representation of capacitance transient f(t) in equation (4.35) is the Laplace transform of the actual spectral density function [F(s)].

To deduce the different emission rates embedded in f(t) one needs to apply any suitable algorithms that perform the inverse Laplace transform for the function f(t)

[80]. Laplace DLTS shows the output intensity as a function of emission rates and the area under the peaks is related to the trap concentration.

Due to its high resolution, Laplace DLTS has been used to separate the conventional DLTS peaks obtained from very closely spaced defects, for example when their emission rates are different from each other, or in some cases even if the emission rates are nearly similar but their energies are different. For example, Laplace DLTS has been used previously [81] to separate the two closely spaced hydrogen and gold related defects in silicon. Conventional DLTS scan in Figure 4.7 shows only one broad peak for both defects. However Laplace DLTS shows two well resolved peaks related to hydrogen and gold [82]. In addition Figure 4.8, represents an example where Laplace DLTS technique is applied to resolve the closely spaced defects in an n-type GaAs sample used in this study. Laplace DLTS output represents the amplitude of the capacitance (pF) versus emission rate (1/sec). Three different routines called FLOG, CONTIN and FTIKREG are applied simultaneously to obtained the solution for equation (4.35).

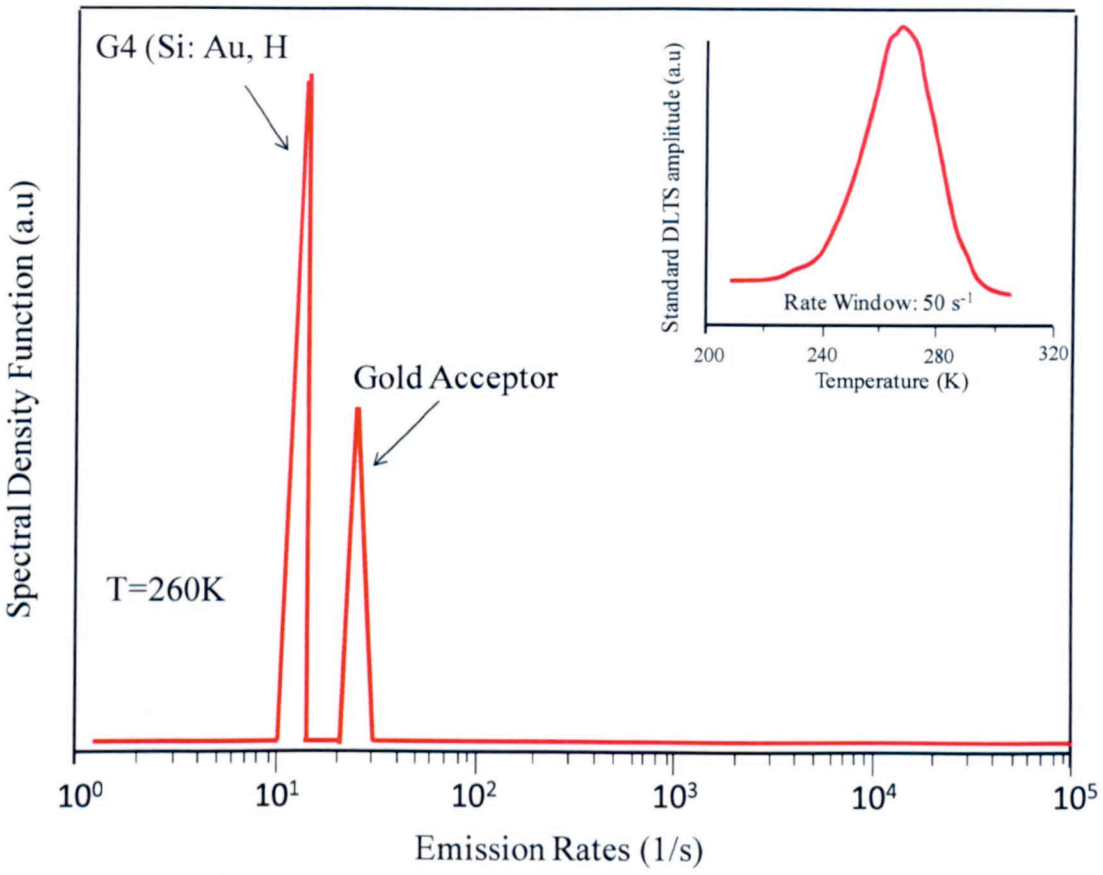

Figure 4.7: DLTS and LDLTS spectra of hydrogenated silicon containing gold [82].

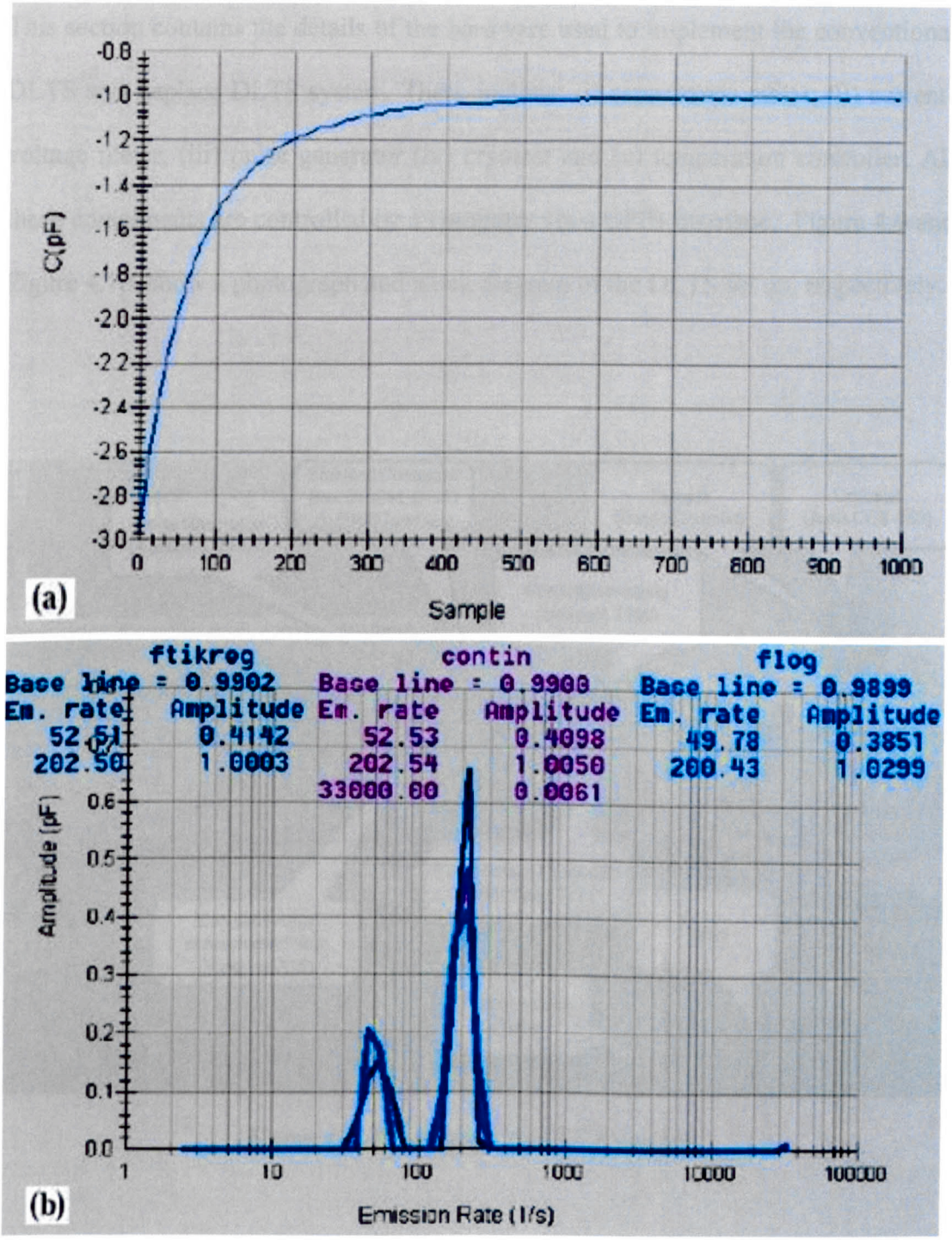

Figure 4.8: In part (a) the capacitance transient obtained during Laplace DLTS measurements and (b) two well resolved peaks are shown.

4.4 DESCRIPTION OF THE DLTS HARDWARE SETUP

This section contains the details of the hardware used to implement the conventional DLTS and Laplace DLTS system. These include: (i) capacitance meter, (ii) current-voltage meter, (iii) pulse generator (iv) cryostat and (v) temperature controller. All these components are controlled by a computer via a GPIB interface. Figure 4.9 and Figure 4.10, show a photograph and block diagram of the DLTS set up, respectively.

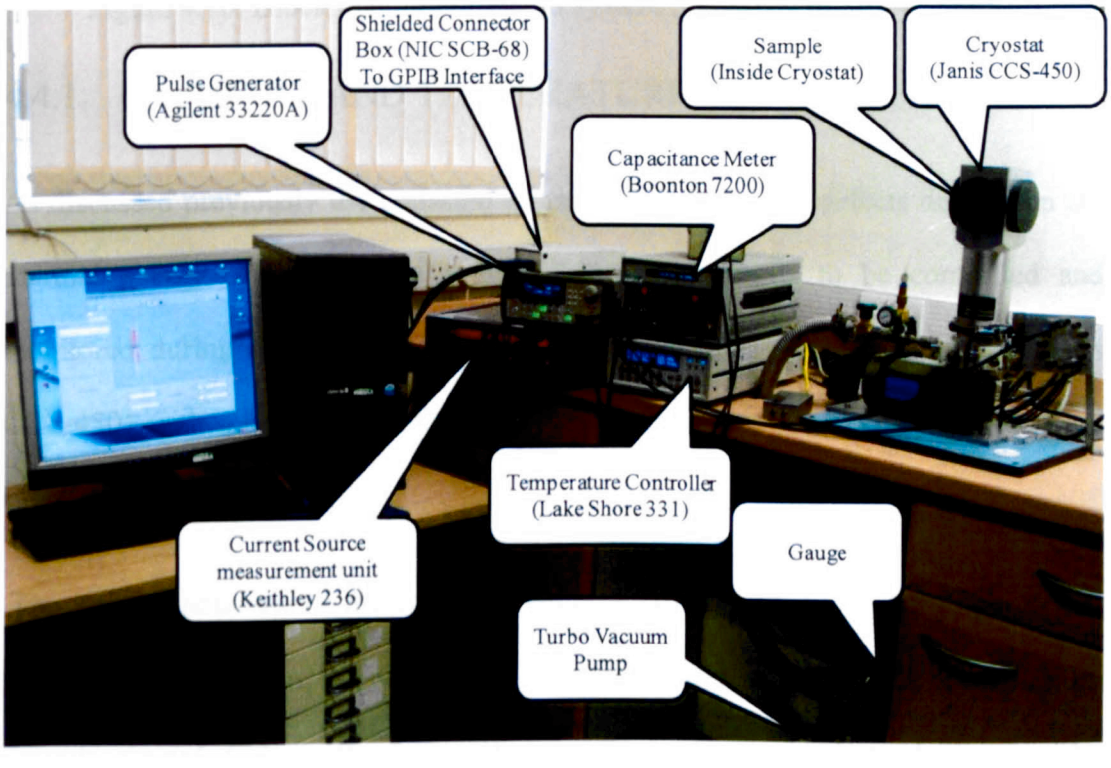

Figure 4.9: Photograph of DLTS system.

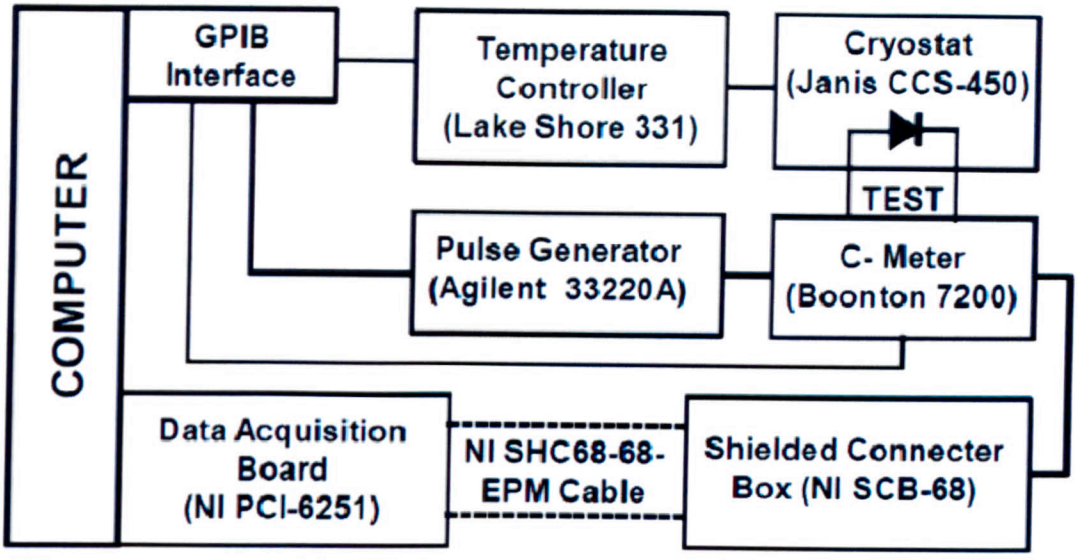

Figure 4.10: Block diagram of DLTS system (Courtesy of Dr. M. Shafi).

4.4.1 CRYOSTAT AND TEMPERATURE CONTROLLER

As discussed previously the emission of charge carriers from defects depend on the thermal energy. Therefore, the sample temperature needs to be controlled and monitored during DLTS measurements. For this purpose a cryostat (model Janis CCS-450) with an associated temperature controller (model Lake Shore 331) are used.

The internal structure of the cryostat system is consists of: (i) a cold finger which accommodates the sample holder, (ii) a radiation shield, (iii) lightweight aluminium vacuum shroud, (iv) electrical ports for sample contacts and thermal sensors. The cryostat operates with a compressor which ensures the continuous flow of helium gas (He) through a high efficiency flexible six feet cryogen transfer line. It is based on close-cycle refrigeration principle. Model CCS-450 operates in the temperature range 10K to 450K with ±1K [83].

The Lake Shore 331 [84] temperature controller is used to control two temperature sensors, one of them is located very close to the sample.

4.4.2 CAPACITANCE METER

A Boonton capacitance meter, model 7200,[85] is employed to measure the capacitance transients. The signal to noise ratio (S/N) of Boonton 7200 model is better than the conventional model Boonton 72BD model. The Boonton 7200 has a good time response of ~120μs, which makes this apparatus very suitable for DLTS system operation. The sampling frequency for measuring the capacitance transients is 1MHz. The capacitance meter is also used to perform standard capacitance-voltage (C-V) measurements.

4.4.3 PULSE GENERATOR

DLTS measurements require a train of electrical pulses to continuously fill and empty the traps as discussed previously. The Agilent 33220A [86] which has the ability to generate electrical pulses of different width (t_p) ranging from 20nsec to 990msec with an output voltage ranging from -10V to +5V, has been used.

4.4.4 CURRENT-VOLTAGE (I-V) SOURCE-METER

For reliable DLTS measurements, the samples should exhibit very low reverse currents. Therefore, current-voltage (I-V) measurements are performed to select the best samples. For this purpose a current-voltage source-meter, model Keithley 236 [75], has been utilised. This offers a source voltage and source current in the range 100μV-110V and 100fA-100mA, with a good sensitivity of ±10μV and 10fA, respectively.

4.4.5 DATA ACQUISITION INTERFACE

This is very essential component that allows the collection and processing of capacitance transients. Here a National Instruments (NI) data acquisition (DAQ) card (model PCI-6251) has been used for this purpose. The NI PCI-6251 is a high-speed multifunction DAQ signal card optimised for superior accuracy at fast sampling rates. It is 16-bit with maximum sampling frequency of 200 kHz. The DAQ offers ± 10.0V input/output voltages. These PCI-based boards offer a simple, seamless bridge between the computer and the GPIB instruments.

Capacitance transient data is collected through the DAQ with a suitable shielded input/output 68-pin terminal board (NI SCB-68), which is connected with a matching shielded cable (NI SHC68-68EPM).

4.4.6 COMPUTER INTERFACE

All the equipments are controlled remotely using a general-purpose interface bus (GPIB), which provides a standard high-speed interface for communication between instruments and computer.

4.5 SYSTEM SOFTWARE

The software used to control each piece of equipment, collect and analyse the capacitance transients was developed by Prof. L. Dobaczewski and co-workers (Institute of Physics Polish Academy of Sciences, Warsaw, Poland) and Prof. A. R. Peaker et. al. (University of Manchester, UK) under the project "Copernicus Project CIPA CT-94-0172 and The Foundation for Polish Science Serial No: C3.2.041" [87]. The provided software operates in two modes, namely conventional DLTS and

Laplace Transient processing mode. The conventional DLTS mode utilizes the rate window concept as discussed in section 4.2.1, and the Laplace DLTS mode of operation uses the application of algorithms that contain three mathematical routines that will be discussed in the Laplace DLTS section below.

4.5.1 CONVENTIONAL DLTS MEASUREMENT MODE

In this mode the software offers three types of different routines, namely TrapView version 4.0, Multiple rate windows and Exponential Fitting. All these routine are based on rate window concept and discussed below.

In "TRAPVIEW VERSION 4.0" measurement mode there is a choice to select only one pair of rate windows out of five provided rate window pairs; namely (4,10 Hz), (20,55 Hz), (80,200 Hz), (400, 1 kHz), (2,5 kHz) [87].

In "MULTIPLE RATE WINDOWS" operation mode, the software utilizes nine different rate windows simultaneously to collect capacitance transient's data by scanning the sample temperature continuously. The minimum rate window value starts from 2.5 Hz to a maximum of 5 kHz with three different settings [87]. The multi-rate windows mode has the advantage of obtaining nine different DLTS spectra in one temperature scan, and of course this mode saves a lot of time.

The "EXPONENTIAL FITTING" measurement mode is different from TRAP VIEW and MULTI RATEE WINDOWS. This allows to take only a single scan at a time by selecting only one rate window [87].

4.5.2 LAPLACE DLTS MEASUREMENT MODE

Laplace DLTS is an isothermal DLTS technique, where the capacitance transients are measured at a fixed temperature. The transients are then averaged to improve the

signal to noise (S/N) ratio, and different algorithms are applied to generate the LDLTS peaks as shown in Figure 4.7 and Figure 4.8 [87].

CHAPTER 5

EXPERIMENTAL DETAILS

In this chapter the experiment details are presented which consist of the growth and processing of all the samples used in this study. In addition, the details of the measurements carried out such as, Current-Voltage (I-V), Capacitance-Voltage (C-V), conventional DLTS and Laplace DLTS measurements are explained.

5.1 SAMPLES USED IN THIS STUDY

n-type GaAs, and n- and p-type AlGaAs samples are grown on non (100) planes to investigate the electrical properties of the defects present in epitaxial layers grown on different Miller indices. The details of each set of samples is given below.

5.1.1 Gallium Arsenide (GaAs) Samples

GaAs epitaxial layers were grown on (100), (211)B, (311)B, (411)B, and (511)B GaAs substrates by Molecular beam Epitaxy (MBE) in a Varian Gen II system. The growth parameters are: 580 °C growth temperature, 1μm per hour growth rate and $1.2x10^{-5}$ Torr arsenic overpressure. The As:Ga beam equivalent pressure ratio as measured by an ionization gauge was approximately 12:1. The samples were rotated during growth in order to improve the uniformity of the layers. The epitaxial layers consisted of 0.2μm undoped GaAs buffer layer followed by 1.5μm silicon-doped GaAs region schematically shown in Figure 5.1 (a). For the samples grown on

(411)B and (511)B all the growth parameters are the same except the thickness of the buffer layer (0.1μm), doped layer thickness (2.0μm) and Si doping (n= 2×10^{16} cm^{-3}).

The electron concentration as determined by Hall measurements was 1×10^{17} cm^{-3}. The epitaxial layers were processed into circular mesas of various diameters ranging from 0.25 to 1mm using photolithography and wet chemical etching techniques. Ge/Au/Ni/Au were first evaporated and alloyed to form ohmic contacts to the doped layer immediately above the undoped GaAs buffer layer. Schottky contacts (Figure 5.1) were processed and samples mounted on TO5 header for electrical measurements.

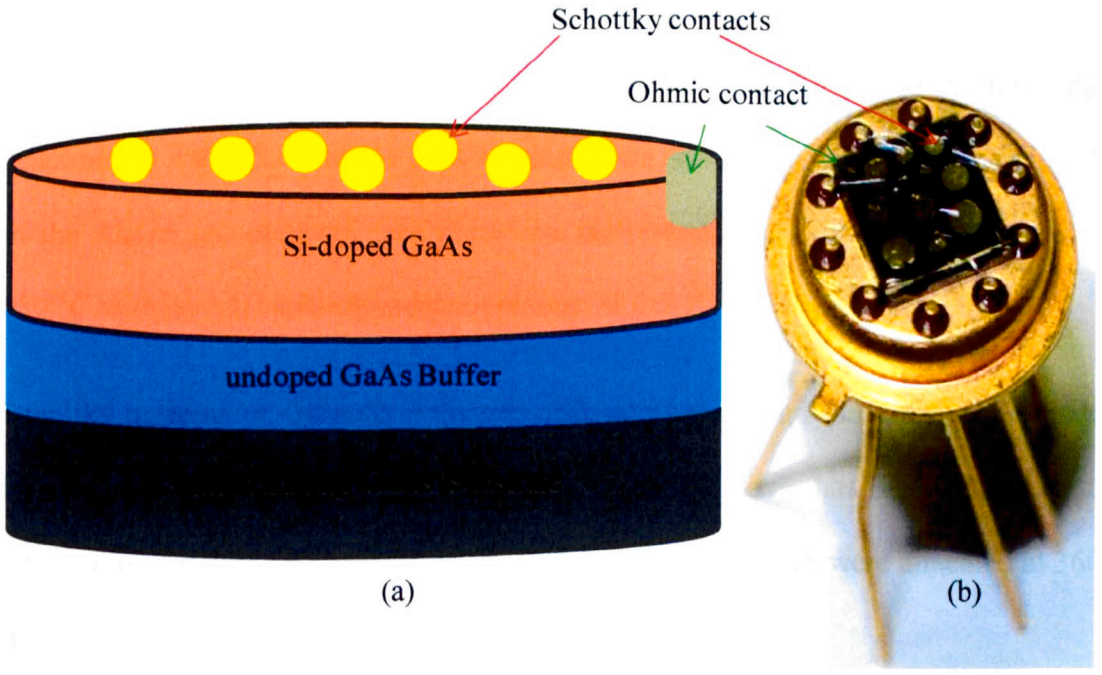

Figure 5.1: (a) The Schematic diagram of n-type GaAs sample and (b) Photograph of samples mounted on TO5 header

5.1.2 Aluminium Gallium Arsenide (AlGaAs) Samples

Three different sets of $Al_xGa_{1-x}As$ samples are investigated in this work. These are (i) bulk p-type Beryllium doped $Al_xGa_{1-x}As$ samples grown on high index planes, (ii) $GaAs/Al_xGa_{1-x}As$ multi-quantum well (MQW) structure grown on (100) and (311)B GaAs substrate, and (iii) MQW structures grown on (100) plane at different growth temperatures and arsenic overpressures using As_2 and As_4. The growth details for each set of the samples is given below.

5.1.3 p-type $Al_xGa_{1-x}As$ Samples

A set of six AlGaAs samples with different Be-doping concentrations (1×10^{16} cm^{-3} to 1×10^{17} cm^{-3}) were grown on semi-insulating (100) and (311)A GaAs substrates using a Varian Gen-II MBE system. The samples, labelled as NU1362-NU1367, are described in Table 5.1 and the layer structures are shown in Figure 5.2. The growth of the $Al_xGa_{1-x}As$ epitaxial thin films was performed at a substrate temperature of 680 °C with an As_4 beam-equivalent pressure of 2×10^{-5} Torr.

Schottky contacts of different diameters ranging from 0.25mm to 1mm, were made by evaporating Ti/Au on the top of AlGaAs layer. Top layer has been etched up to 600 nm for the deposition of ohmic contacts [Au/Ni/Au] which were annealed at 360 °C.

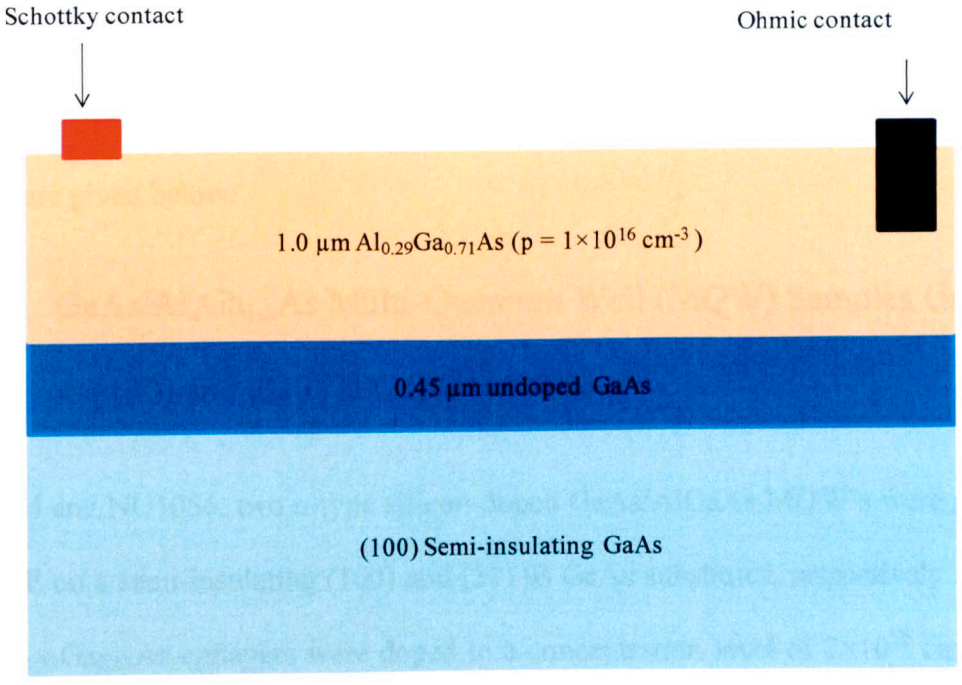

Figure 5.2: The layer structure of p-type $Al_{0.29}Ga_{0.71}As$ samples.

Table 5.1: The growth parameters of Be-$Al_{0.29}Ga_{0.71}As$ samples are shown.

Sample ID	Substrate type	Intentional doping (cm^{-3})	Growth Temperature (°C)	Be-doped layer thickness (µm)
NU1362	(100)	1×10^{16}	680	1.00
NU1363	(311)A	1×10^{16}	680	1.00
NU1364	(100)	3×10^{16}	680	1.00
NU1365	(311)A	3×10^{16}	680	1.00
NU1366	(100)	1×10^{17}	680	1.00
NU1367	(311)A	1×10^{17}	680	1.00

5.1.4 Multi-Quantum Well (MQW) GaAs/$Al_xGa_{1-x}As$ Samples

Two types of GaAs/AlGaAs multi-quantum well structures are investigated and their details are given below.

5.1.5 GaAs/$Al_xGa_{1-x}As$ Multi-Quantum Well (MQW) Samples Grown on (100) and (311) B GaAs Substrates

NU1054 and NU1056, two n-type silicon-doped GaAs/AlGaAs MQW's were grown by MBE on a semi-insulating (100) and (311)B GaAs substrates, respectively. GaAs and $Al_{0.33}Ga_{0.67}As$ epilayers were doped to a concentration level of 2×10^{16} cm^{-3} and 1.33×10^{16} cm^{-3}, respectively, and the growth temperature of the buffer and the epitaxial layers was 580 °C and 630 °C, respectively. Layer structure of the samples starting from the substrate is: 1μm GaAs ($n = 2 \times 10^{16}$ cm^{-3}) buffer layer, 0.14μm $Al_{0.33}Ga_{0.67}As$ ($n = 1.33 \times 10^{16}$ cm^{-3}) barrier, a 60 periods GaAs (50 Å) ($n = 2 \times 10^{16}$ cm^{-3}) /$Al_{0.33}Ga_{0.67}As$ (90 Å) ($n = 1.33 \times 10^{16}$ cm^{-3}) MQWs, 0.14 μm $Al_{0.33}Ga_{0.67}As$ ($n = 1.33 \times 10^{16}$ cm^{-3}) barrier. The layer structures are illustrated in Figure 5.3.

Ohmic contacts were made on n-type-doped AlGaAs layer using wet chemical etching, metal evaporation of Ge/Au/Ni/Au (54-nm/60-nm/20-nm/136-nm thick layers) and annealing at 360 °C for 30 sec. The Schottky contacts were fabricated by evaporating Ti/Au (40 nm/175 nm) on the top of the n-type-doped $Al_{0.33}Ga_{0.67}As$ layer.

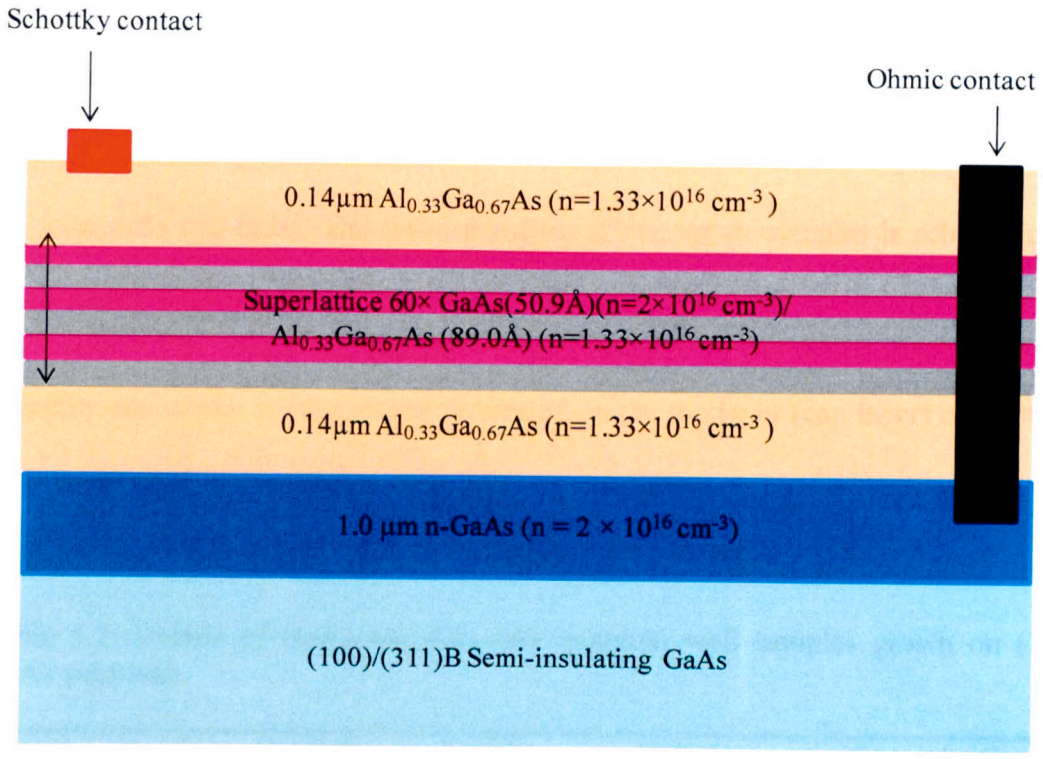

Figure 5.3: Layer structure of MQW samples grown on (100) and (311)B GaAs substrates.

5.1.6 GaAs/$Al_xGa_{1-x}As$ MQW Samples Grown at Different Temperatures and Arsenic Overpressures using As_2 and As_4 Species

Another set of six GaAs/AlGaAs MQW samples [Table 5.2], namely: NU777, NU778, NU780, NU781, NU784 and NU785 was investigated. These samples were grown on (100) GaAs substrates only. The growth parameters of the samples were: growth rate 1monolayer/sec and 45 monolayer/sec for GaAs and $Al_{0.33}Ga_{0.67}As$, respectively, As_2 and As_4 fluxes were obtained using a commercial cracker furnace (with the sublimation and cracker operating zone at 400 and 700°C, respectively). The growth temperatures 600 °C, 650 °C and 675 °C were used. Because of the different growth temperatures, the samples were grown at different As_2 and A_4 over pressures of 1.2×10^{-5} Tor, 2×10^{-5} and 3×10^{-5} Tor, respectively. The sample layer

structure starting from substrate consists: n^+ GaAs ($n\sim3 \times10^{18}$ cm^{-3}) substrate, 1μm GaAs buffer layer, 0.14 μm thick $Al_{0.33}Ga_{0.67}As$ layer ($n = 2\times10^{16}$ cm^{-3}), 60 loops of each 50.9Å GaAs quantum well and 84.8Å $Al_{0.33}Ga_{0.67}As$, respectively, and 0.14 μm $Al_{0.33}Ga_{0.67}As$ cap layer. The layer structure of this set of samples is schematically illustrated in Figure 5.4.

Schottky and ohmic contacts were processed on the top layer (cap layer) and bottom layer (substrate), respectively.

Table 5.2: Details of GaAs/$Al_{0.33}Ga_{0.67}As$ quantum well samples grown on (100) GaAs substrate.

Sample ID	Arsenic Species	Growth temperature (°C)	Arsenic over pressure (Torr)	Si-doping GaAs/$Al_{0.33}Ga_{0.67}As$ (cm^{-3})	GaAs/$Al_{0.33}Ga_{0.67}As$ (thickness) (Å) 60 Loops each GaAs/ $Al_{0.33}Ga_{0.67}As$
NU780	As_2	600	1.2×10^{-5}	2×10^{16}	50.9/84.8
NU781	As_4	600	1.2×10^{-5}	2×10^{16}	50.9/84.8
NU778	As_2	650	2.0×10^{-5}	2×10^{16}	50.9/84.8
NU784	As_4	650	2.0×10^{-5}	2×10^{16}	50.9/84.8
NU777	As_2	675	3.0×10^{-5}	2×10^{16}	50.9/84.8
NU785	As_4	675	3.0×10^{-5}	2×10^{16}	50.9/84.8

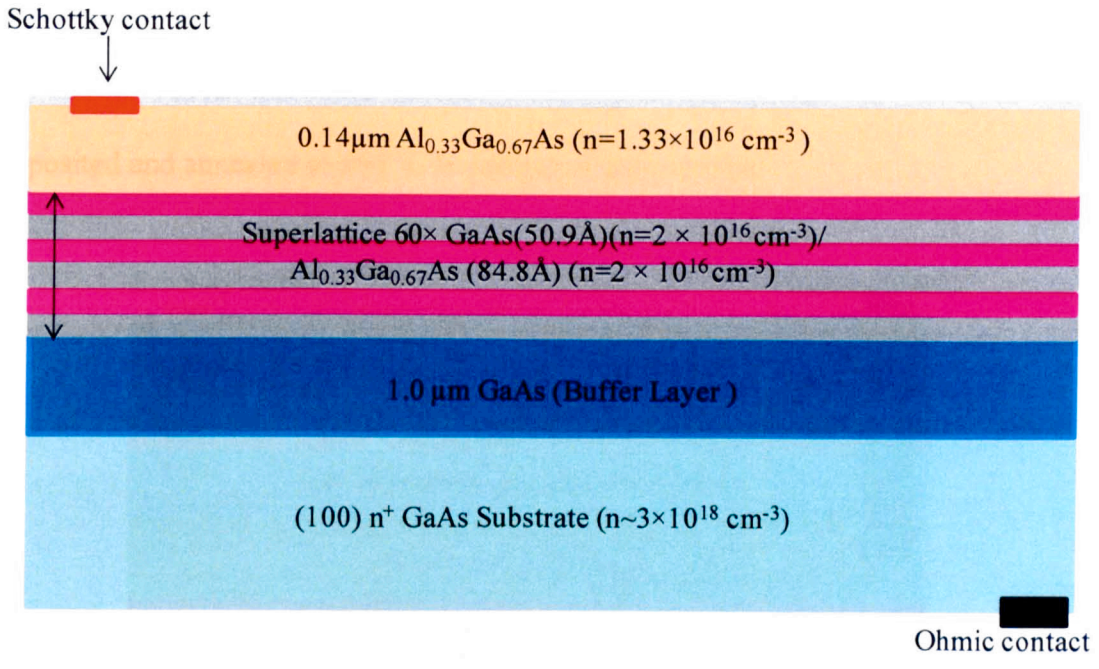

Figure 5.4: Layer structure of MQW samples grown on (100) GaAs substrate using As_2 and As_4.

5.1.7 Two Dimensional Electron Gas (2-DEG) Samples

The purpose of the study of 2-DEG devices is to compare these samples to those of High Electron Mobility Transistor (HEMT) grown by a commercial company. The layer structures and Schematic band diagram of the 2-DEG devices namely NU1297 and NU1280 are shown in Figure 5.5 and Figure 5.6, respectively.

The growth rate, Arsenic beam equivalent pressure, and growth temperature are 1μm/hr for GaAs and 0.5μm/hr for AlGaAs, 1.2×10^{-5} Torr, and 630 °C, respectively. The layer structure starting from substrate is: Semi-insulating GaAs substrate, 1.1μm GaAs buffer layer, 100×GaAs (25.4Å)/$Al_{0.33}Ga_{0.67}As$ (25.4Å) super-lattice, 0.5μm undoped GaAs, an undoped 407Å $Al_{0.33}Ga_{0.67}As$ spacer, 0.2 μm $Al_{0.33}Ga_{0.67}As$ (n $=1\times 10^{17}$ and $1.33 \times 10^{18}cm^{-3}$ for NU1297 and NU1280, respectively), 169.6 Å GaAs cap layer.

The Schottky and Ohmic contacts were made side by side without any etching of the top layer. Ti/Au was used for the Schottky contacts, and Ge/Au/Ni/Au were deposited and annealed at 360 °C to form an ohmic contact.

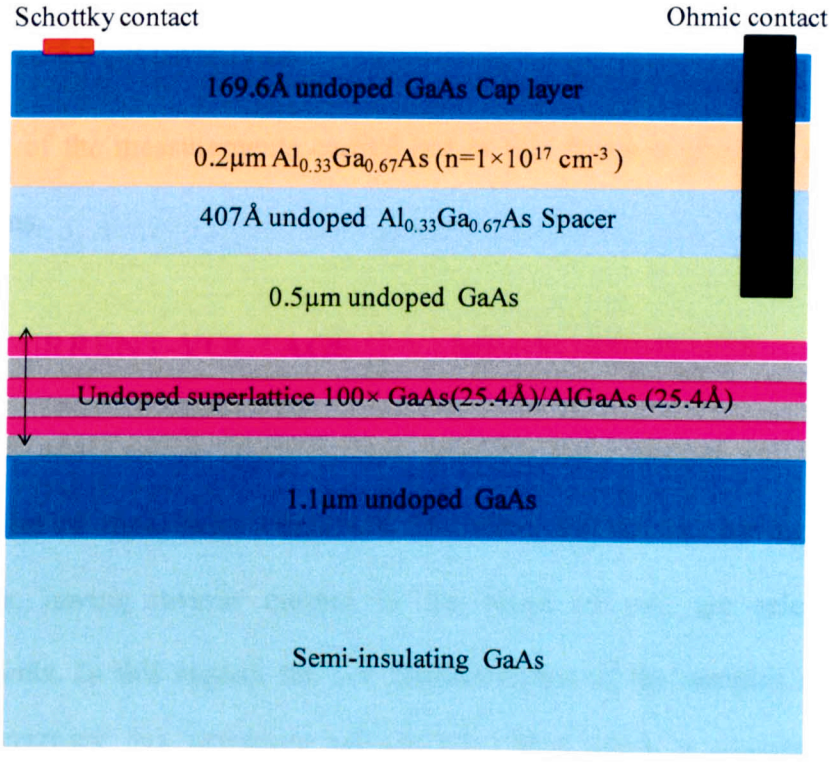

Figure 5.5: Schematic diagram of the layer structure of 2-DEG sample.

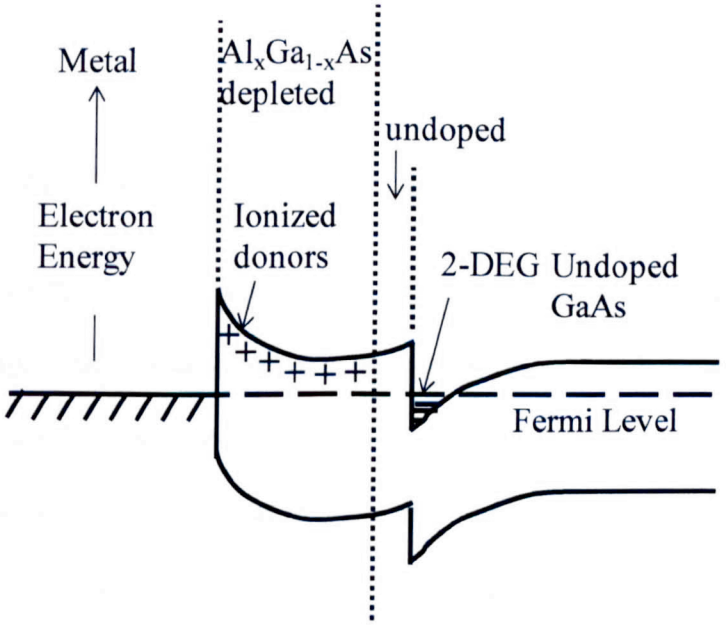

Figure 5.6: Illustration of the energy band diagram of the 2-DEG.

5.1.8 Commercially Grown HEMT Devices

Due to the confidential agreement with commercial company the details of the samples are not provided.

5.2 MEASUREMENTS

The detail of the measurements carried out in this thesis is given in the following sub-sections.

5.2.1 CURRENT-VOLTAGE (I-V) MEASUREMENTS

The DLTS and Laplace DLTS system used for these studies are based on the measurement of capacitance transients. Therefore, the devices having low reverse current i.e. having reverse current in the range of μA, are selected for the measurements. In this regard, the I-V characteristics of the samples are measured using KEITHLEY 236 SOURCE MEASURE UNIT which is computer controlled using the provided software. The current values are measured with 50 mV increment. Depending on the diode quality steady state, reverse biases ranging from -1 to -5V were applied.

5.2.2 CAPACITANCE-VOLTAGE (C-V) MEASUREMENTS

The analysis of the C-V characteristics provides important parameters such as the built-in voltage, the background doping concentration and concentration depth profile. The DLTS data analysis relies on these parameters. Therefore, C-V characteristics of each device are measured using BOONTON 7200 Capacitance Meter, which is controlled by a computer. It operates at a frequency of 1MHz.

5.2.3 DLTS MEASUREMENTS

DLTS and Laplace DLTS are used as the main tool for the characterisation of deep levels present in the material systems investigated in this thesis. Though the details of the measurements are covered in chapter 4, whereas here the experimental procedure is described. The samples packaged in a TO5 header were mounted on a sample holder. The samples were first cooled down to a temperature of 10K in a Closed Cycle CRYODYNE Refrigerator, Model number CCS-450. DLTS measurements were then started by ramping the temperature at a rate of 2K/min. A train of electrical pulses, generated by a pulse generator (model Agilent 33220 A) was applied to the sample. The filling pulse repetition rate is fixed to 50 Hz for most of the samples. The reverse bias (V_R) and filling pulse (V_P) is applied in such a way that $V_P < V_R$.

5.2.4 Laplace DLTS MEASUREMENTS

For the resolution of the broad featureless DLTS peaks, High Resolution Laplace DLTS measurements were carried out. Laplace DLTS is an isothermal DLTS process, therefore, the measurements are performed at constant temperature within a temperature range where the conventional DLTS peak appears. Further details of the measurements are also covered in chapter 4.

CHAPTER 6

DEEP LEVEL DEFECTS IN GaAs GROWN ON HIGH INDEX GaAs PLANES [(100), (211)B, (311)B, (411)B and (511)B]

6.1 INTRODUCTION

Compound semiconductor structures grown on index planes other than the conventional (100) orientation have attracted a great deal of attention because of their interesting and unusual aspects related to growth, impurity incorporation, electronic properties, piezoelectric effects and laser performance. In addition, it is now well established that the structural, electrical and optical properties of self-assembled nanostructures can be highly sensitive to the substrate orientation [88]. It is important to add that the silicon (a group IVA element) impurity in GaAs grown by Molecular Beam Epitaxy (MBE) can act as either a donor (occupies Ga site) or acceptor (occupies As site). This amphoteric dopant is dependent on the substrate orientation [4, 89]. Silicon is mainly a donor when the growth is on the (100) surface. However, silicon incorporates preferentially as a donor in (N11)B and as an acceptor on (N11)A surfaces (N = 1,2,3), where A and B denote a Ga- and As-terminated plane, respectively. In addition, in (111)A, (211)A, and (311)A planes, silicon may act as a donor or as an acceptor depending on the substrate temperature and the arsenic overpressure used during the MBE growth. This amphoteric nature of silicon could lead to the development of novel devices.

Growth on high index planes opens, therefore, an interesting new research field on the physics of doping, heterostructures and self-assembled nanostructures. Numbers of research groups have been involved in the characterisation of defects in GaAs using different characterisation techniques. The overview of their work is presented in section 3.5.1.

This chapter presents results of electrical characterisation of deep level defects in MBE silicon doped n-type GaAs epilayers grown on (100), (211)B, (311)B, (411)B and (511)B GaAs substrates. Experimental results include current-voltage (I-V) characteristics, capacitance-voltage (C-V) characteristics, conventional DLTS and Laplace DLTS measurements.

In summary, it is observed that the number of electrically active traps is dependent on the substrate orientation. The average density of traps observed in (211)B is maximum, whereas, it is minimum for (511)B substrate. The mid-gap energy level C3 (0.714±0.002 eV), not previously reported in the literature in as-grown MBE GaAs, is only detected in (311)B. It is tentatively assumed to be related to EL2 defect family in GaAs, but its nature is not exactly the same as that of the famous EL2 since the emission rates of C3 are insensitive to the junction electric field. Further investigations in the future are needed to explore its nature. The activation energy of D3 in (411)B, detected for the first time in as-grown MBE GaAs, is similar to that of level EL16 in VPE GaAs. In addition, other defect levels, namely A1 (0.054 ± 0.002 eV) and A2 (0.143 ± 0.003 eV) in (100), D1 (0.139 ± 0.011 eV) in (411)B, and E1 (0.141 ± 0.024 eV) in (511)B, are observed for the first time in MBE grown GaAs. Their origin is not known. However, the nature and properties of D1 in (411)B and E1 in (511)B are similar. All the defects observed here in Si-doped GaAs are neutral, except for D1 and E1 which are charged centers. Comparison between the tunnelling

times data determined experimentally and theoretically ($\tau_2 = \hbar/2k_BT$) suggest that the levels A1 and A2 in (100), B1 and B4 in (211)B, D1 in (411)B and E1 in (511)B are substitutional impurities related defects. In addition, our findings suggest that the common carbon background impurity in MBE is more susceptible to be incorporated in (100) than in high index GaAs substrates.

6.2 EXPERIMENTAL RESULTS AND ANALYSIS

6.2.1 I-V AND C-V CHARACTERISTICS OF DEVICES

In order to select the suitable devices for DLTS and Laplace DLTS measurements, I-V characteristics at 300K were carried out following the experimental procedure described in section 5.2.1. Typical I-V characteristics are shown in Figure 6.1. The reverse current at -3V is less than 1μA for all devices except for the (211)B sample (NU929). It is observed that the reverse current decreases with increasing n for the substrate orientation, i.e. (n11)B where n = 2,3,4,5. The plausible reason for the higher reverse current in NU929 (211)B can be explained by the higher trap concentrations as compared to all other GaAs orientations investigated in this study.

In order to determine the free carrier concentration and the doping profile, C-V measurements were carried out at 300K. The C-V data, plotted in the form of $1/C^2$ versus reverse voltage following equation 4.8, is shown in Figure 6.2. The free carrier concentration, needed to calculate the trap concentration, is determined from the slope of the above relationship.

The linear relationship between $1/C^2$ and reverse bias, as depicted in Figure 6.2, is evidence of the uniform profile of silicon doping in the epitaxial layers.

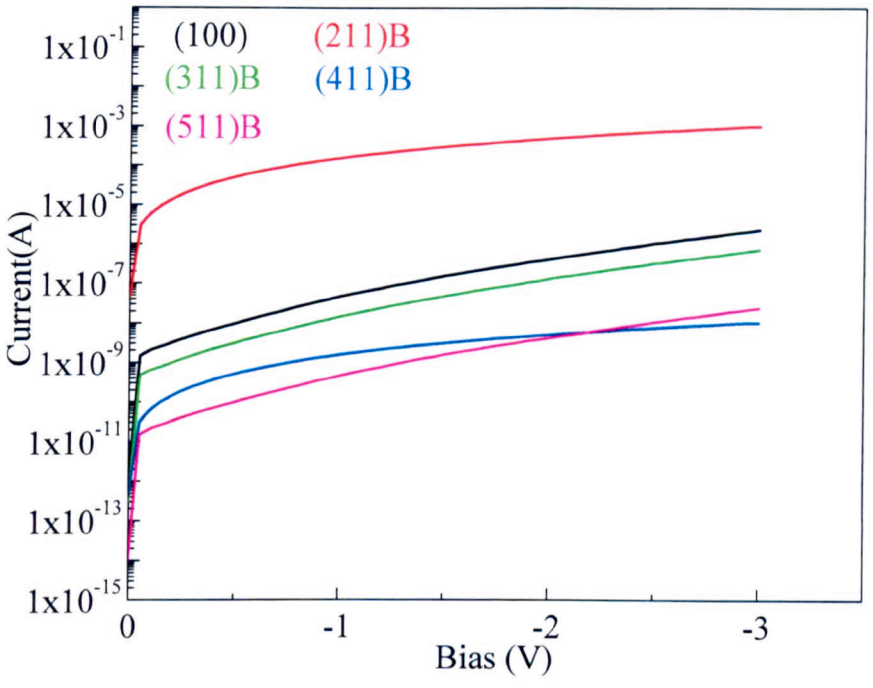

Figure 6.1: Current-Voltage (I-V) characteristics of Schottky diodes fabricated from n-type GaAs grown on various GaAs substrate orientations.

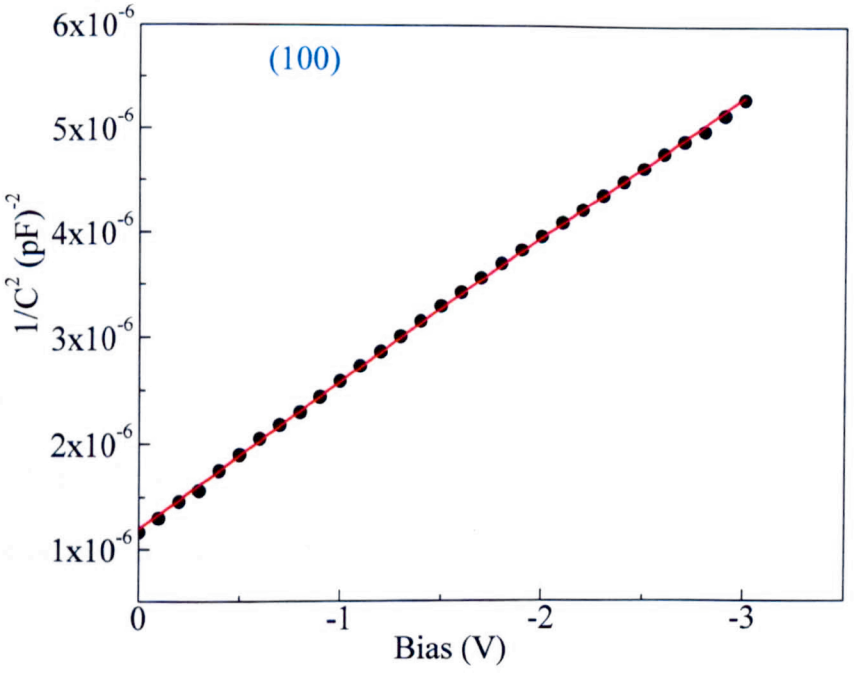

Figure 6.2: $1/C^2$ versus reverse bias of n-type GaAs Schottky diode processed from (100) GaAs plane.

6.2.2 DLTS DATA

In order to detect the defect levels lying within the band gap of these n-type GaAs grown on various GaAs substrate orientations, DLTS measurements were carried out by following the experimental procedure described in section 5.2.3. Typical DLTS spectra are shown in Figure 6.3 (a) – (e) for the samples grown on (100), (211)B, (311)B, (411)B and (511)B, respectively. The measurement parameters used are: reverse bias (V_R) = -3 V, filling pulse height (V_P) = -0.5 V, filling pulse width (t_p) = 1msec and rate window = 50 Hz.

It is worth noting from Figure 6.3 that: (i) for the (100), (211)B and (311)B samples the peaks, related to electron emitting defect levels, are not well unresolved; (ii) for the (411)B and (511)B samples the peaks are well resolved; (iii) the (211)B sample displays a stronger DLTS signal in terms of amplitude; (iv) compared to (100), (211)B and (311)B, the DLTS signals from (411)B and (511)B are weaker. The concentration of defects is directly related to strength of the DLTS signal [39], and therefore the density of traps in (411)B and (511)B is much less than the other planes.

The levels observed in (100), (211)B, (311)B, (411)B and (511) samples are labelled as A, B, C, D and E, respectively. The digits 1, 2, 3, etc, refer to the number of defect levels in respective samples.

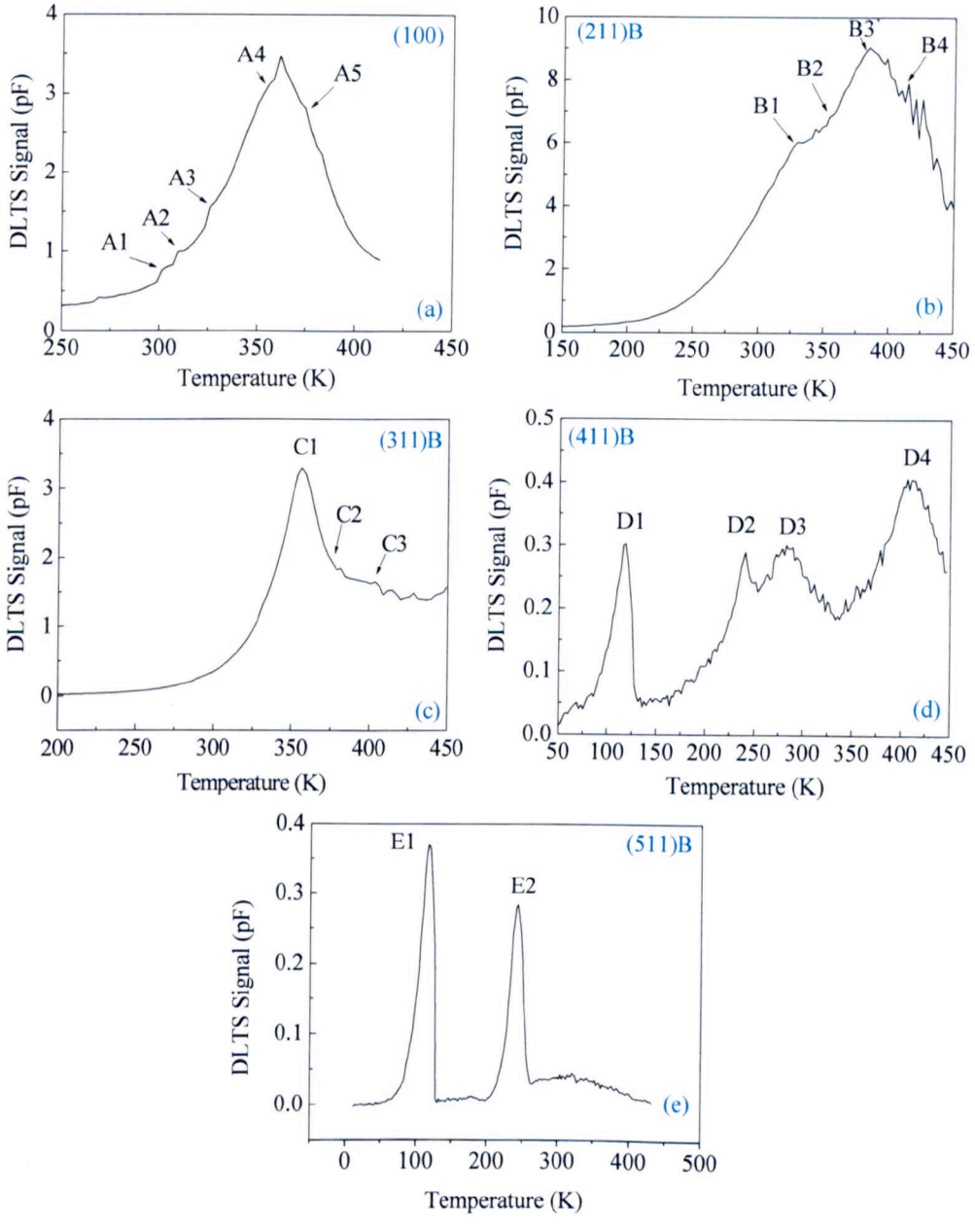

Figure 6.3: The conventional DLTS scans for n-type GaAs samples, grown on (100), (211)B, (311)B, (411)B and (511)B, are shown in (a) – (e), respectively. The measurement parameters are: V_R = -3 V, V_p = -0.5 V, t_p = 1msec, and rate window = 50Hz.

6.2.3 DETERMINATION OF ACTIVATION ENERGIES OF TRAPS

It is difficult to deduce the trap parameters such as activation energy and apparent capture cross-section from DLTS signals because of the overlapping signal peaks.

Laplace DLTS is employed to resolve the peaks, and determine the emission rates of the defects. Emission rates of each defect level are plotted in an Arrhenius plot of $\ln(e_n/T^2)$ versus 1000/T as shown in Figure 6.4. The slope and intercept of each plot is utilised to deduce the activation energy and apparent capture cross-section of respective defect levels. Deduced activation energy, apparent capture cross-section and concentration values of each trap are illustrated in Table 6.1.

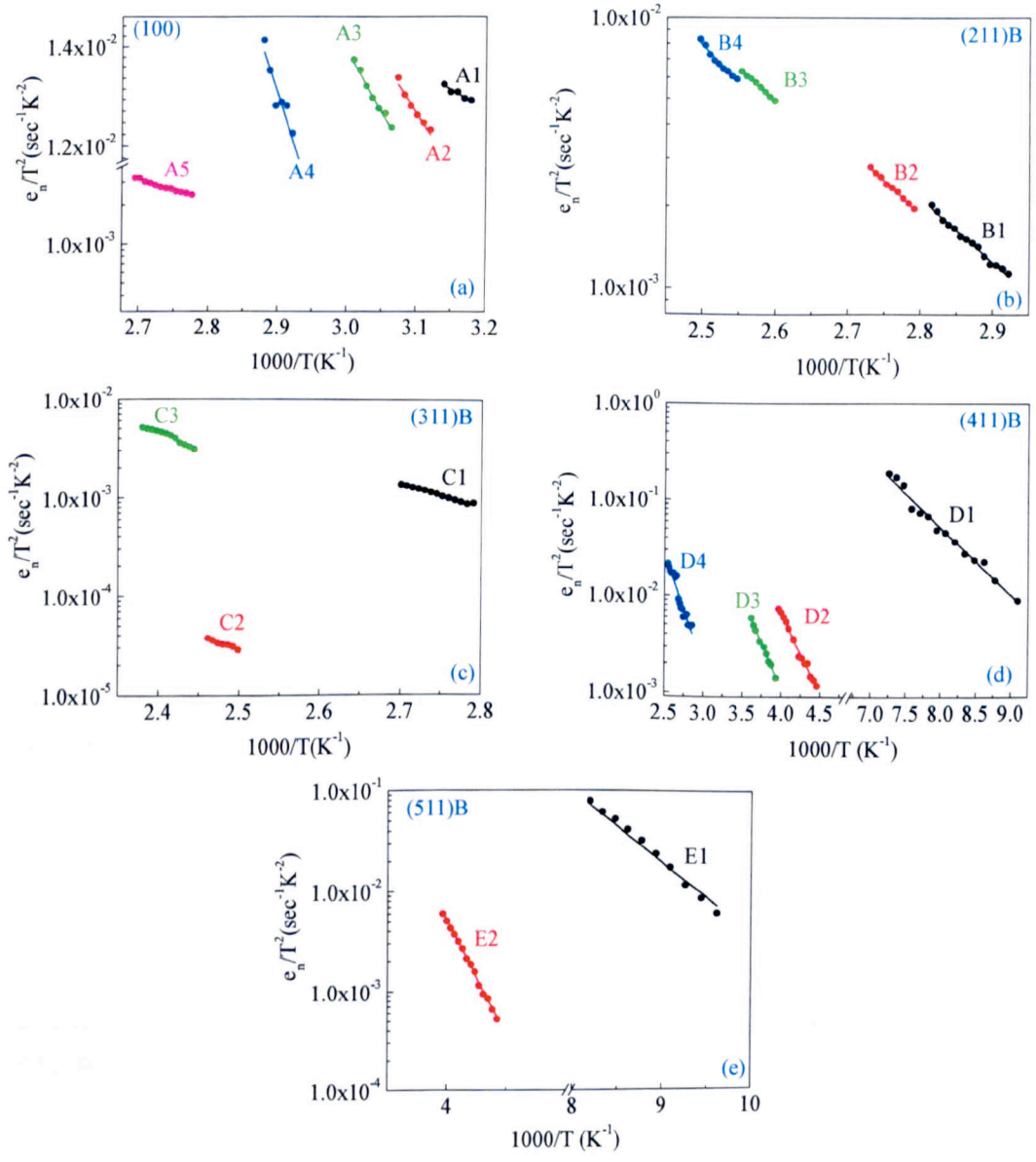

Figure 6.4: Arrhenius plots of traps detected in (a) (100), (b) (211)B, (c) (311)B, (d) (411)B and (e) (511)B.

Table 6.1: The activation energy and capture cross-section, and concentration of the traps are calculated from Laplace DLTS and DLTS measurements, respectively.

Sample ID	Trap	Activation Energy (eV)	Capture cross-section $\sigma_{n(\infty)}$ (cm^2)	Concentration (cm^{-3})
(100)	A1	0.054 ± 0.002	4.92×10^{-23}	5.57×10^{14}
	A2	0.143 ± 0.003	1.14×10^{-21}	6.90×10^{14}
	A3	0.163 ± 0.002	2.14×10^{-21}	1.08×10^{15}
	A4	0.283 ± 0.005	9.19×10^{-20}	2.02×10^{15}
	A5	0.323 ± 0.001	3.48×10^{-20}	1.94×10^{15}
(211)B	B1	0.467 ± 0.002	4.28×10^{-18}	6.38×10^{15}
	B2	0.496 ± 0.001	9.69×10^{-18}	7.23×10^{15}
	B3	0.482 ± 0.001	1.78×10^{-17}	9.54×10^{15}
	B4	0.570 ± 0.002	6.17×10^{-17}	7.95×10^{15}
(311)B	C1	0.465 ± 0.001	4.16×10^{-14}	6.23×10^{15}
	C2	0.572 ± 0.002	1.21×10^{-14}	3.13×10^{15}
	C3	0.714 ± 0.003	1.11×10^{-11}	2.89×10^{15}
(411)B	D1	0.139 ± 0.011	1.01×10^{-17}	3.57×10^{14}
	D2	0.326 ± 0.012	1.26×10^{-17}	3.43×10^{14}
	D3	0.374 ± 0.008	1.92×10^{-17}	3.56×10^{14}
	D4	0.468 ± 0.011	1.13×10^{-17}	4.81×10^{14}
(511)B	E1	0.141 ± 0.024	2.53×10^{-17}	3.06×10^{14}
	E2	0.462 ± 0.007	5.23×10^{-15}	2.35×10^{14}

6.2.4 EFFECT OF THE ELECTRIC FIELD ON THE EMISSION RATES

As discussed in section 3.3, there are cases where the carrier emission rates depend on the junction electric field. In order to investigate the effect of the electric field, Laplace DLTS measurements were carried out by employing the double pulse method as described in section 4.2.6.

To analyse the field dependent emission rate data, a model proposed by Ganichev et al. [42] is used as described in section 3.4. In this work it is found that the emission rates follow the phonon-assisted tunnelling model for the traps A1 [Figure 6.5 (a)], A2 [Figure 6.6(a)], B1 [Figure 6.7 (a)] and B4 [Figure 6.8 (a)], whereas, the emission rates of traps D1 [Figure 6.9 (a, b)], and E1[Figure 6.10 (a, b)] involve two processes depending on the strength of the electric field (E), namely the Poole-Frenkel effect at low E (6.48×10^4 – 8.64×10^6 V/cm) and phonon-assisted tunnelling at high E (1.06×10^6 – 2.66×10^6 V/cm). In addition, the carrier tunnelling time (τ_2) at different temperatures is calculated from equations 3.11 and 3.12. The relationship between τ_2 and temperature is shown in Figure 6.5 (b) for A1, Figure 6.6 (b) for A2, Figure 6.7 (b) for B1, Figure 6.8 (b) for B4, Figure 6.9 (c) for D1 and Figure 6.10 (c) for E1.

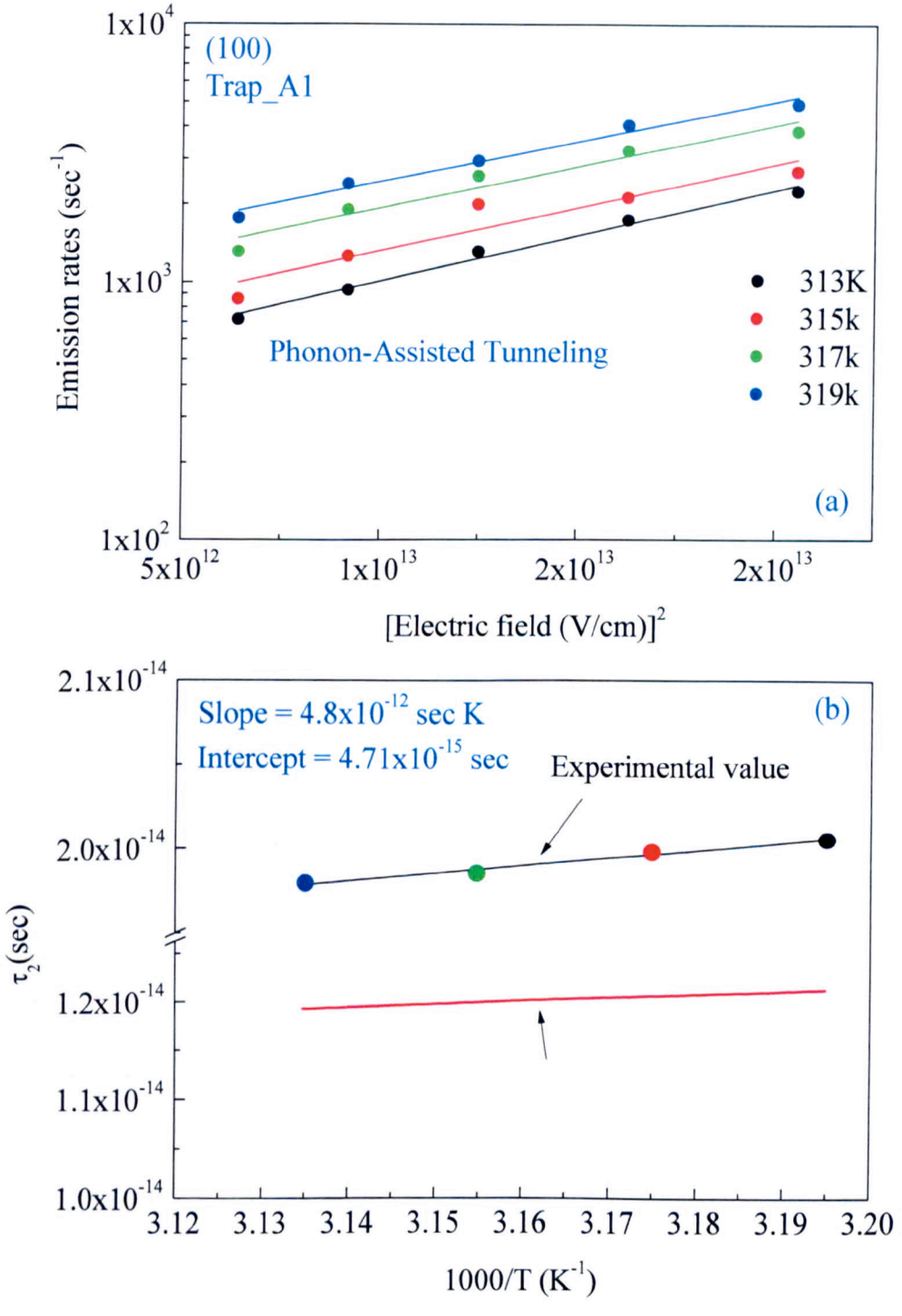

Figure 6.5: Trap A1: (a) Emission rates versus square of junction electric field; (b) tunnelling time τ_2 versus (1000/T): τ_2 is determined from the slope of $\ln(e_n)$ versus E^2 at different temperatures (see Fig.6.5 (a)). The red solid line represents $\hbar/2k_BT$.

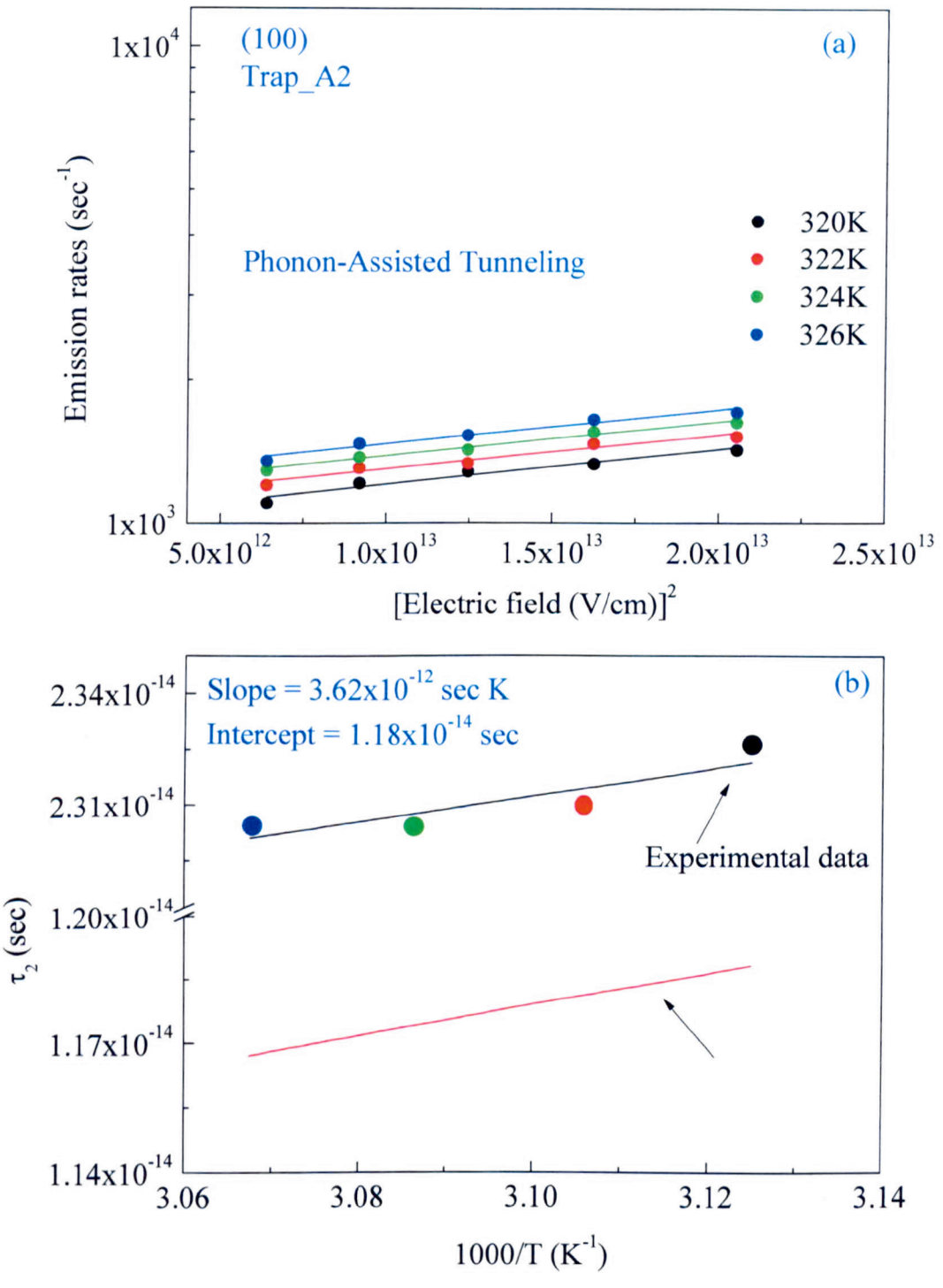

Figure 6.6: Trap A2: (a) Emission rates versus square of junction electric field; (b) tunnelling time τ_2 versus (1000/T): τ_2 is determined from the slope of $\ln(e_n)$ versus E^2 at different temperatures (see Fig.6.6 (a)). The red solid line represents $\hbar/2k_BT$.

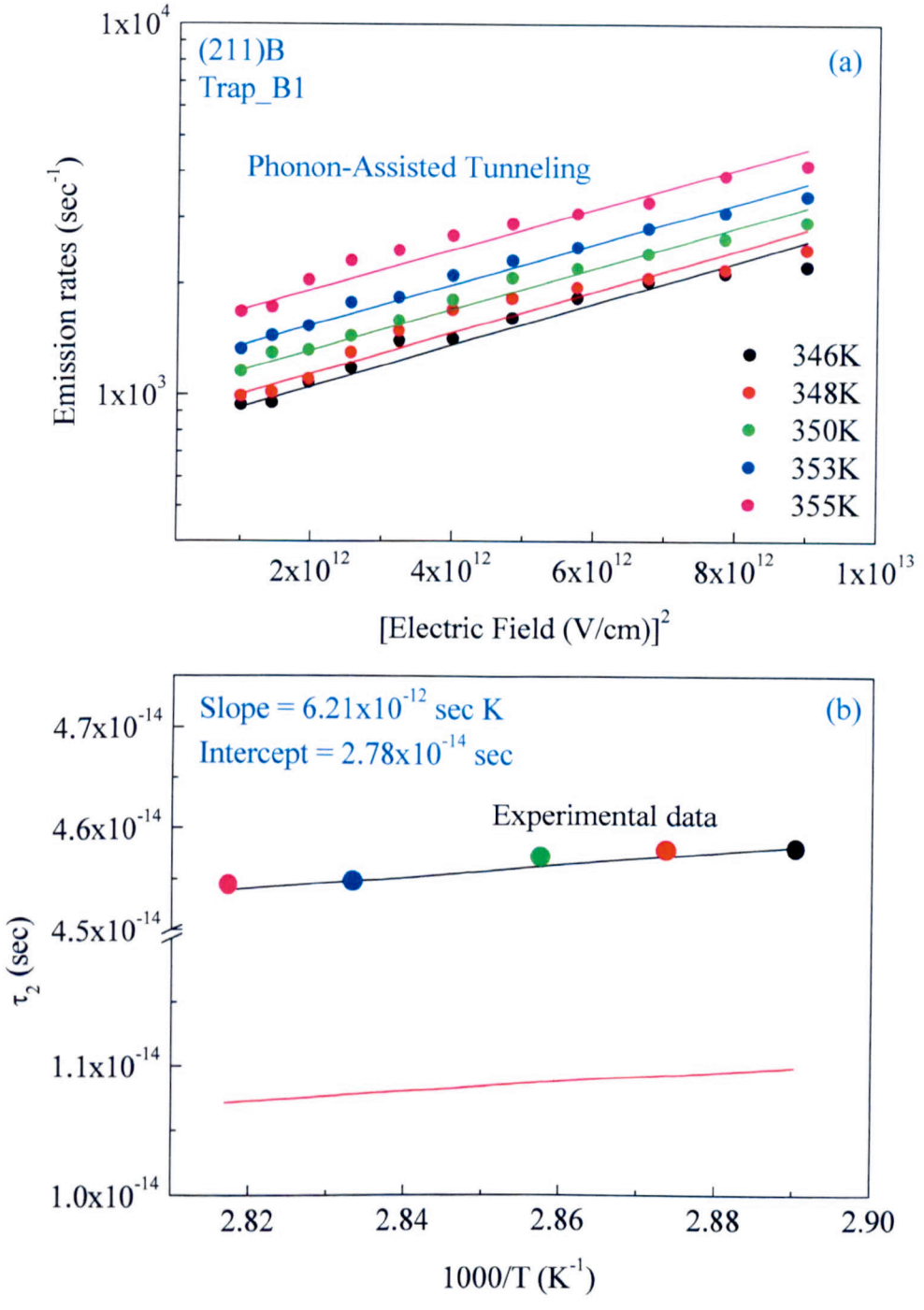

Figure 6.7: Trap B1: (a) Emission rates versus square of junction electric field; (b) tunnelling time τ_2 versus (1000/T): τ_2 is determined from the slope of $\ln(e_n)$ versus E^2 at different temperatures (see Fig.6.7 (a)). The red solid line represents $\hbar/2k_BT$.

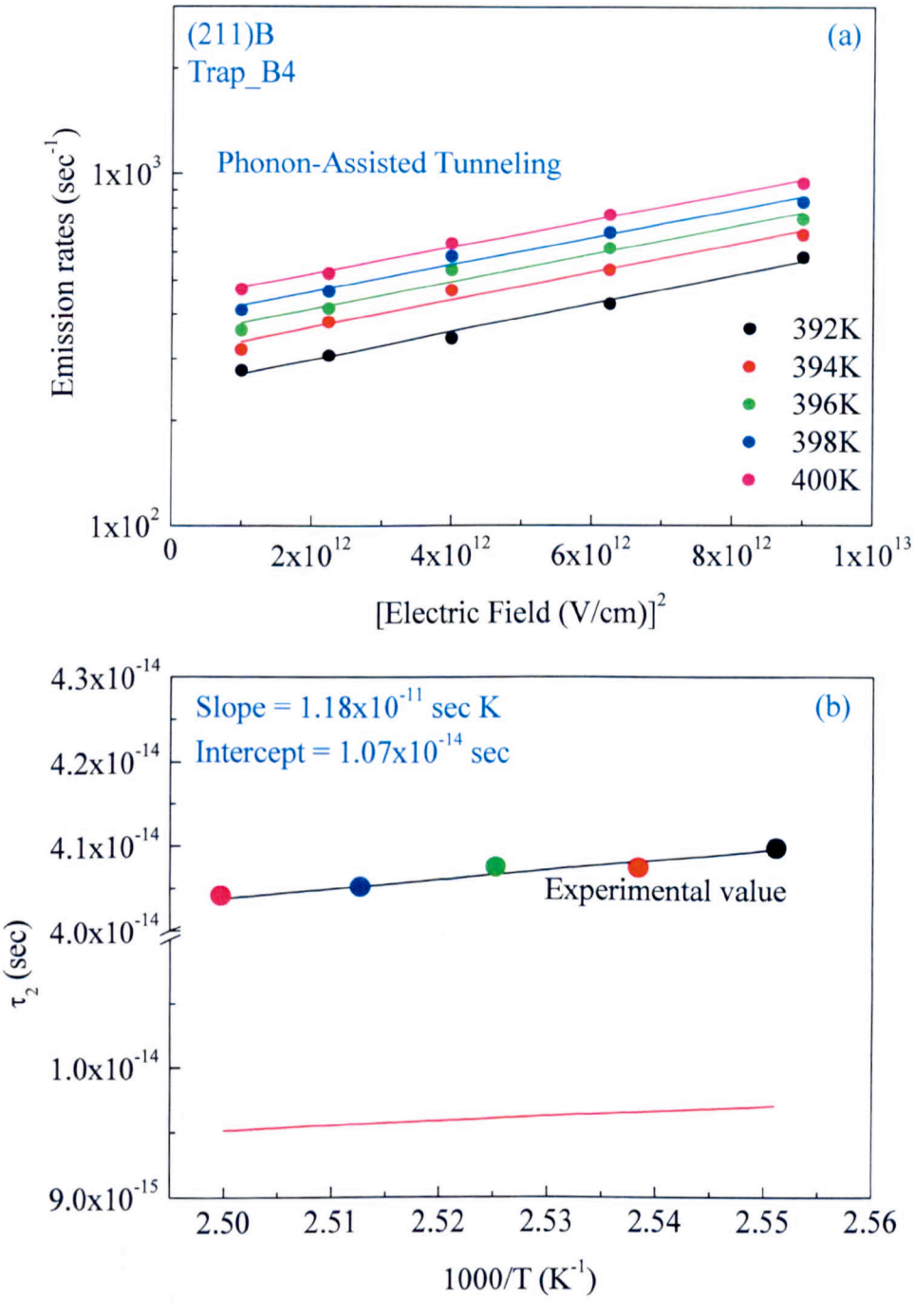

Figure 6.8: Trap B4: (a) Emission rates versus square of junction electric field; (b) tunnelling time τ_2 versus (1000/T): τ_2 is determined from the slope of $\ln(e_n)$ versus E^2 at different temperatures (see Fig.6.8 (a)). The red solid line represents $\hbar/2k_BT$.

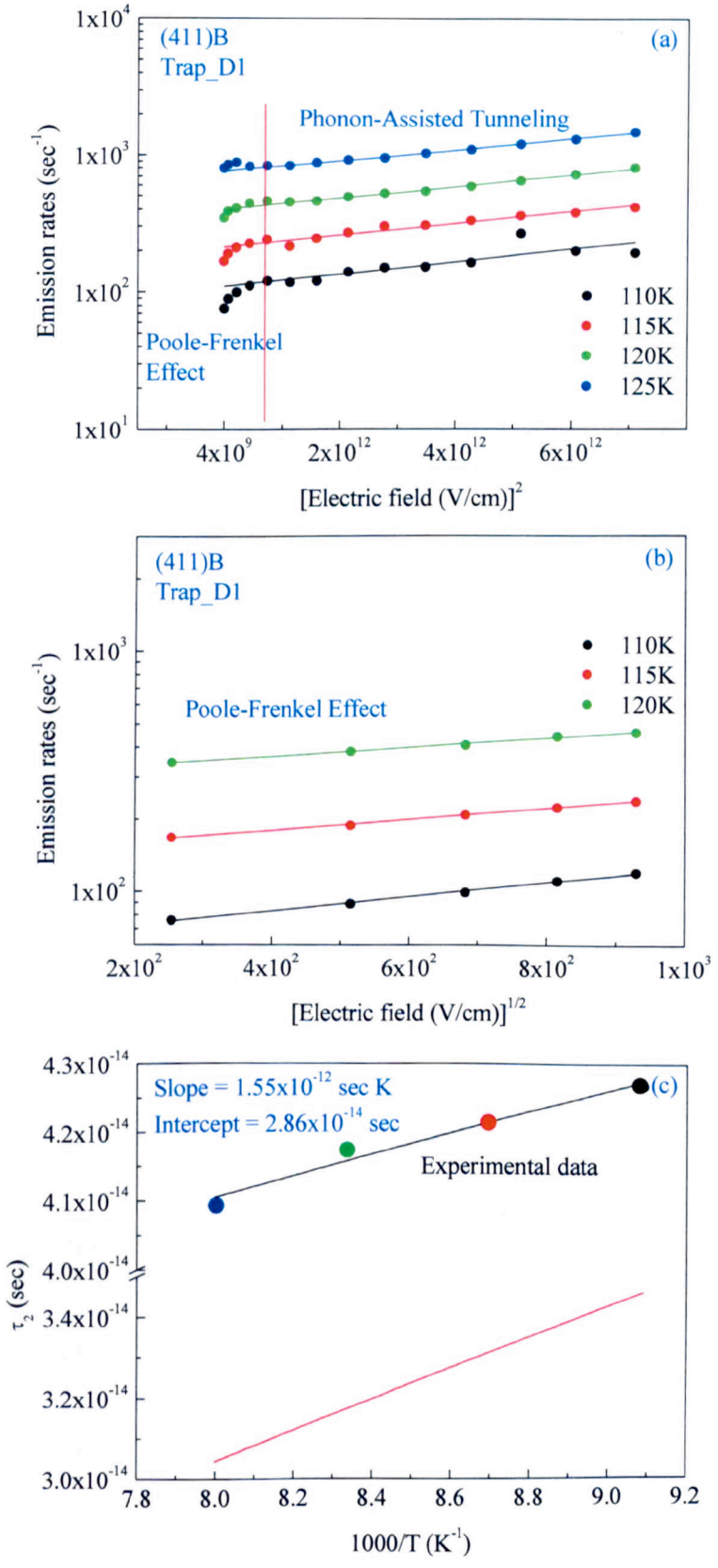

Figure 6.9: Trap D1: (a) Emission rates versus square of junction electric field; (b) Emission rates versus square root of junction electric field; (c) tunnelling time τ_2 versus (1000/T): τ_2 is determined from the slope of $\ln(e_n)$ versus E^2 at different temperatures (see Fig.6.9 (a)). The red solid line represents $\hbar/2k_BT$.

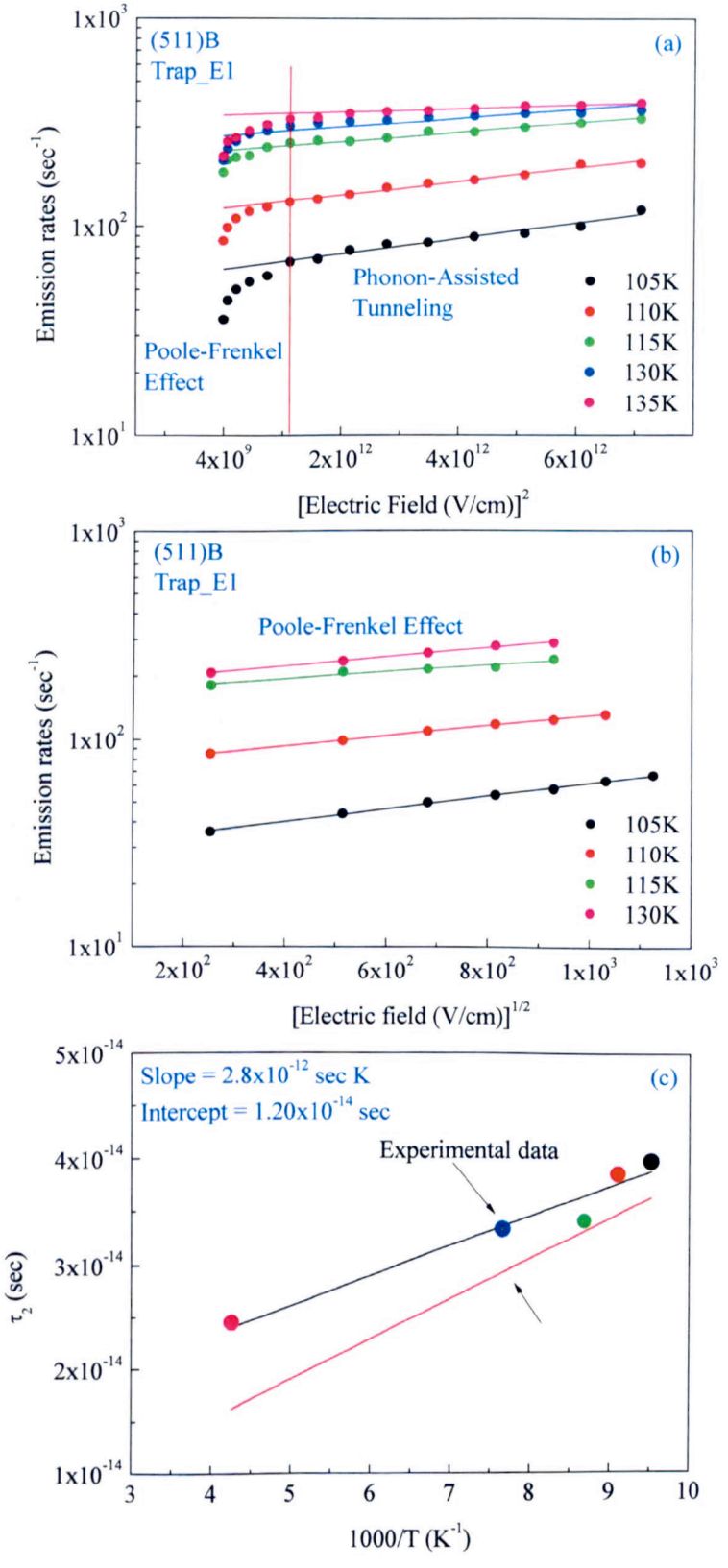

Figure 6.10: Trap E1: (a) Emission rates versus square of junction electric field; (b) Emission rates versus square root of junction electric field; (c) tunnelling time τ_2 versus (1000/T): τ_2 is determined from the slope of $\ln(e_n)$ versus E^2 at different temperatures (see Fig.6.10 (a)). The red solid line represents $\hbar/2k_BT$.

6.2.5 DETERMINATION OF TRAP CONCENTRATION

The concentrations of the defect levels observed in Si-doped n-GaAs samples is calculated by following the experimental procedure described in section 4.2.4 [39]. These are shown in Table 6.1.

6.2.6 BEHAVIOUR OF TRAP CONCENTRATION VERSUS DEPTH

To investigate the concentration depth profile of the traps, Laplace DLTS measurements were carried out by applying the double pulse technique. For this purpose the area under the Laplace DLTS curve is taken into account instead of the DLTS peak height [87]. The calculations of the trap concentrations were performed by using equation 4.32 [39]. Figure 6.11 (a) – (e) illustrates the concentrations versus depth of the traps observed in samples grown on (100), (211)B, (311)B, (411)B and (511)B, respectively.

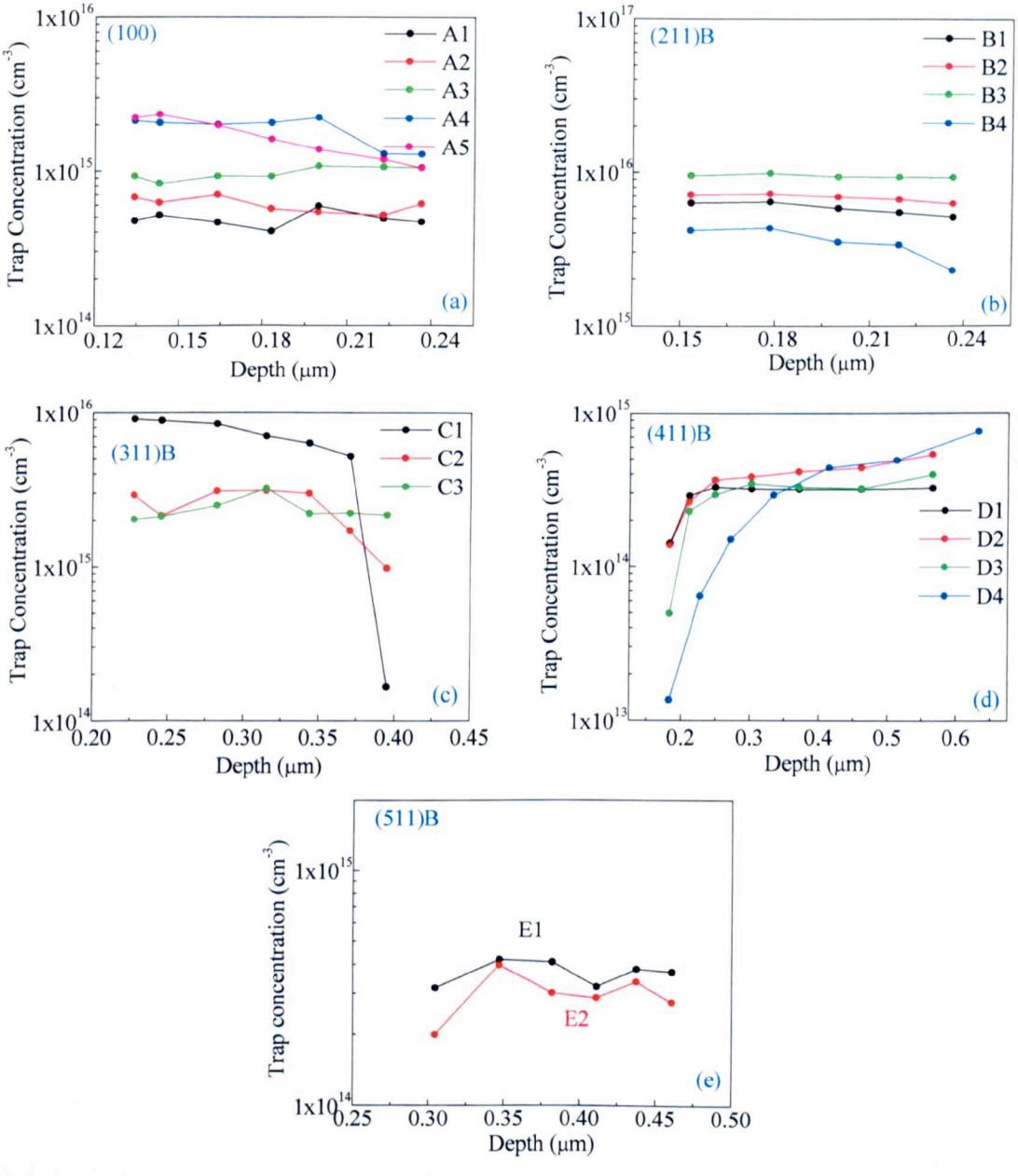

Figure 6.11: Concentration depth profile of the traps detected in the different GaAs orientations.

6.3 DISCUSSION

As shown in Figure 6.3 and Figure 6.4 the number of detected traps in (100), (211)B, (311)B, (411)B and (511)B GaAs substrates is five, four, three, four and two, respectively. For simplicity of the analysis, the traps are grouped according to their activation energies.

The activation energies of traps A5 (0.323±0.001eV) and D2 (0.326±0.012eV) are comparable to the activation energy of the well known M3 (0.31 eV – 0.33 eV) defect in MBE grown GaAs layers [90-93]. Defect level A4 (0.283±0.005 eV) has also a similar energy as M3 (0.29±0.01 eV) that was reported by Okada et al. [94] in MBE samples grown at different temperatures (330 °C and 580 °C). The samples used in this study are grown at temperature of 580 °C. Chand et al. [92] studied MBE GaAs grown on silicon and GaAs substrates. The authors assigned the origin of M3 level to a complex of unknown chemical impurity and an As related native defect in GaAs. Lang et al. [95] supported this finding regarding the nature of M3 trap by investigating As-rich MBE grown n-GaAs. It is worth pointing out that the density of M3 related trap in the sample grown on (100) GaAs substrate is higher than in the sample grown on (411)B (see Table 6.1). The concentration-depth profiles of A5 and D2 [Figure 6.11 (a) and (d)] show different behaviours; the density of A5 in (100) decreases continuously with depth, whereas the density of D2 in (411)B increases up to 0.25 μm then saturates.

The defect level A3 (0.163±0.002 eV) detected in (100) samples could be related to level M1 (0.17 eV) in MBE grown n-GaAs studied by Dautremont-Smith et al. [96]. The authors investigated the effect of hydrogen passivation followed by thermal annealing, and observed that M1 vanishes. It was proposed that M1 could be related

to impurities such as carbon (C) and oxygen (O) in as-grown GaAs. The disappearance of M1 in the hydrogen passivated and annealed samples were accounted for by the fact that C and O are highly reactive with H_2. Lang et al. [95] suggested that M1 is more likely to be related to a chemical impurity or a complex formed between impurities and native defects. In this study the M1 related defect detected only in the (100) plane, can be related to carbon background impurities in our MBE system [97]. This suggests that the common C background impurity in MBE is more susceptible to be incorporated in (100) than in high index GaAs substrates. The A3 concentration depth profile in (100), illustrated in Figure 6.11 (a), reveal that its density (possibly M1 level) is nearly uniform with depth. The emission rates of A3 are found to be electric field insensitive, and therefore it is a neutral defect level.

The activation energies of traps, B1 (0.467±0.002 eV), B2 (0.496±0.001 eV), B3 (0.482±0.001 eV), C1 (0.465±0.001 eV), D4 (0.468±0.011 eV) and E2 (0.462±0.007 eV) observed in the samples grown on (211)B, (311)B, (411)B and (511)B, oriented GaAs substrates, respectively, are comparable to the well-known M4 electron trap (0.45 – 0.51 eV) [95]. There are controversial suggestions reported in the literature regarding the origin of M4 defect. Two suggestions have been put forward regarding the origin of M4: (i) a complex involving a chemical impurity and a native defect [95], and (ii) carbon or oxygen impurities [96]. Comparing the densities of these traps (see Table 6.1), the traps detected in (211)B and (311)B have higher densities than those detected in (411)B and (511)B. Trap E2 observed in (511)B has the lowest density (2.35×10^{14} cm^{-3}). The emission rates of B1 are sensitive to electric field and follow the phonon-assisted tunnelling model [Figure 6.7 (a)]. Since the experimental tunnelling time (τ_2) of B1 at any temperature is higher than the theoretical τ_2 =

$\hbar/2k_BT$, suggests that B1 is related to a substituitional impurity [43, 44]. The concentration depth profile [Figure 6.11 (b) - (e)] shows that the density of B1, B2, B3 in (211)B and E2 in (511)B are uniform with depth, whereas the density of C1 in (311)B and D4 in (411)B decreases and increases with depth, respectively.

Trap levels B4 (0.570±0.002 eV) and C2 (0.572±0.002 eV) observed in (211)B and (311)B, respectively, can be assigned to defect level EL3 (0.572 eV) [98] in Vapour Phase Epitaxial (VPE) GaAs, and a defect with activation energy [Ec-0.58 eV] observed by Liu et al. [99] in epitaxial (MBE) and bulk (Liquid encapsulated Czochralski) grown n-type GaAs. EL3 was assigned to the excess arsenic at the surface. A sulphide treatment was found to significantly decrease the density of EL3. This reduction in density is believed to be due to the sulphide-arsenide reaction, which makes the excess arsenic at the surface soluble in the sulphide solution, and therefore is removed from GaAs. It was concluded that EL3 is most probably an arsenic related defect. However, Martin et al. [98] suggested that the concentration of EL3 depends on growth conditions and thermal annealing, and may be related to point defect or point-defect/impurity complexes. The concentration depth profiles of traps B4 and C2, illustrated in Figure 6.11 (b) and (c), respectively, show that the concentration of both levels decrease with depth. The emission rates of B4, which are sensitive to the applied electric field, follow the phonon-assisted tunnelling model. In addition, since the values of τ_2 for any temperature are greater than the predicted theoretical values $\hbar/2k_BT$ suggests that B4 is an impurity related level [43, 44].

Defect level C3 (0.714±0.003 eV) detected in (311)B is possibly related to EL2 like defect, whose activation energy varies from 0.723 - 0.82 eV [74, 94]. There are different suggestions in the literature regarding the origin of EL2 as discussed in section 3.5.1. According to the findings of Martin et al. [98] there are no evidences

regarding the existence of EL2 defect in MBE as-grown GaAs layers, but EL2 appear after thermal annealing treatment [90, 91, 100]. In addition, Okada et at [94] observed a paramount reduction (3-10 times) in the density of EL2 in H-assisted MBE growth technique as compared to conventional MBE. The concentration depth profile of C3 [Figure 6.11(c)] shows that the concentration is nearly uniform with depth. As EL2 is a major defect in bulk and MOCVD [101] GaAs, it is important that further studies should be carried out to investigate its existence in as-grown MBE GaAs synthesised in different MBE systems worldwide.

Level D3 (0.374±0.008eV) in (411)B GaAs substrate a similar activation energy as EL16 (0.37 – 0.38 eV) reported in VPE grown GaAs layers [98, 102-104]. The origin of EL16 is not yet known. As far as we know it is believed that D3, tentatively assigned to EL16, is observed for the first time in MBE grown GaAs. The concentration depth profile of D3 [Figure 6.11 (d)] shows that its density increases up to 0.32 μm and then saturates. In addition the experimental results confirm that the emission rates of D3 are insensitive to electric field, which confirms that D3 is neutral defect level. To explore the origin of D3 level, further experimental studies, i.e. positron annihilation spectroscopy (PAS) [105], high resolution TEM, Energy Dispersive X-ray analysis or Electron Energy Loss Spectroscopy etc are required.

In addition to the above deep levels, some other traps, namely A1 (0.054±0.002 eV) and A2 (0.143±0.003 eV) in (100), D1 (0.139±0.011 eV) in (411)B and E1 (0.141±0.024 eV) in (511)A, are observed for the first time in MBE grown silicon-doped n-type GaAs. The emission rates of A1, A2, D1 and E1 vary with electric field. The emission rates of A1 and A2 follow the phonon-assisted tunnelling model. However, the emission rates of D1 and E1 obey both the Poole-Frenkel model and

phonon-assisted tunnelling, depending on the strength of the electric field. These findings reveal that A1 and A2 are neutral levels, whereas D1 and E1 carry electrical charge when they emit the carriers. The experimental values of tunnelling time (τ_2) at different temperatures of A1, A2, D1 and E1 which are higher than the values of $\hbar/2k_BT$ suggest that these levels are related to substitutional impurity [43, 44]. The concentration depth profiles of A1 and A2 [Figure 6.11 (a)], D1 [Figure 6.11 (d)] and E1 [Figure 6.11 (e)] shows that the density of A1, A2 and E1 does not change with depth whereas the density of D1 increases up to 0.25 μm and then saturates.

6.4 CONCLUSION

In summary a set of five MBE n-GaAs samples grown on conventional (100) and high index (211)B, (311)B, (411)B and (511)B oriented GaAs substrates were investigated by DLTS and Laplace DLTS. It is revealed that the maximum reverse current flows though the sample grown on (211)B and the lowest reverse current for the (511) sample. The plausible reason for the higher reverse current in NU929 (211)B can be explained by the higher trap concentrations as compared to all other GaAs orientations investigated in this study. It is further observed from DLTS measurements that the concentration of the defects observed in (211)B is higher compared to other samples. Whereas, the sample grown on (511)B has the minimum number of defects with lower concentrations.

In addition, the common defect levels detected on conventional (100) and high index oriented GaAs substrates are summarised below:

(a) A4, A5 and D2 levels detected in (100) and (411)B, respectively, have an activation energy equal to level M3 whose origin is reported to be related to a

complex formed between a chemical impurity and an arsenic related native defect.

(b) A3 in (100) has an activation energy similar to level M1 that has been associated with unwanted impurities such as carbon and oxygen in GaAs.

(c) The activation energies of levels B1, B2, and B3in (211)B, C1 in (311)B, D4 in (411)B and E2 in (511)B are similar to level M4. Two propositions have been put forward as to the origin of M4: (i) a complex defect between a chemical impurity and a native defect; (ii) defect related to carbon or oxygen in GaAs.

(d) The levels B4 in (211)B and C2 in (311)B are similar to EL3 defect, which is related to access arsenic at the surface.

(e) C3, observed only in (311)B and reported here for the first time, is tentatively assigned to the well-known EL2 defect.

(f) D3 in (411)B is similar to EL16 whose origin is not clear yet.

Following defect levels are detected for the first time in MBE GaAs.

(g) A1 and A2 in (100), D1 in (411)B and E1 in (511)B are reported here for the first time. A1 and A2 are neutral defect levels, whereas D1 and E1 are charged levels. Their origin is not known yet.

CHAPTER 7

Be-DOPED $Al_{0.29}Ga_{0.71}As$ LAYERS GROWN ON (100) AND (311)A GaAs SUBSTRATES

The growth of high mobility two-dimensional hole gases (2DHGs) using GaAs-GaAlAs heterostructures has been the subject of many investigations. However, despite of many efforts hole mobilities in Be-doped structures grown on (100) GaAs substrate remained considerably lower than those obtained by growing on (311)A oriented surface using silicon as p-type dopant. In this study we will report on the properties of hole traps in a set of p-type Be-doped $Al_{0.29}Ga_{0.71}As$ samples grown by molecular beam epitaxy on (100) and (311)A GaAs substrates using deep level transient spectroscopy (DLTS) technique. In addition, the effect of the level of Be-doping concentration on the hole deep traps is investigated. It was observed that with increasing the Be-doping concentration from 1×10^{16} to 1×10^{17} cm^{-3} the number of detected electrically active defects decreases for samples grown on (311)A substrate, whereas, it increases for (100) orientated samples. The DLTS measurements also reveal that the activation energies of traps detected in (311)A are lower than those in (100). From these findings it is expected that mobilities of 2DHGs in Be-doped GaAs-GaAlAs devices grown on (311)A should be higher than those on (100).

7.1 INTRODUCTION

High index planes have attracted a great deal of attention for the production of high quality epitaxially grown semiconductor materials. In particular, the incorporation of silicon as an amphoteric dopant in AlGaAs [106, 107] and GaAs [108] grown on high index GaAs substrates have been studied extensively using Hall, photoluminescence and photothermal ionisation measurements. Compared to silicon, beryllium (Be) can be incorporated only as p-type dopant in GaAs [109, 110] and AlGaAs [111]. Photoluminescence studies have been carried out by Galbiati et al. [11] to investigate the effect of Be incorporation and hole mobility in MBE grown p-type AlGaAs on (100) and (311)A GaAs orientations. Their results favour (311)A orientation to have better dopant incorporation efficiency and higher carrier mobility than that of (100) plane. This is due to higher substitutional Be incorporation efficiency in (311)A. It was concluded that good quality p-AlGaAs material can be grown on (311)A substrate using Be dopant. Furthermore, it was also reported that the PL spectra of the samples grown on (100) are affected due to the presence of non-radiative centres compared to those grown on (311)A plane. In the light of the above experimental studies, it is important to study and characterise the electrically active deep level defects present in Be-doped AlGaAs grown on (100) and (311)A.

7.2 EXPERMENTAL RESULTS AND ANALYSIS

7.2.1 I-V AND C-V CHARACTERISTICS OF DEVICES

The current-voltage (I-V) characteristics of each device were obtained by performing the experimental procedure described in chapter 5. Only the diodes having low reverse current were selected for investigation of defects using DLTS and Laplace

DLTS techniques. Typical I-V characteristics are shown Figure 7.1. Reverse currents of a few μA at -3V are obtained, demonstrating the suitability of the devices for defect characterisation.

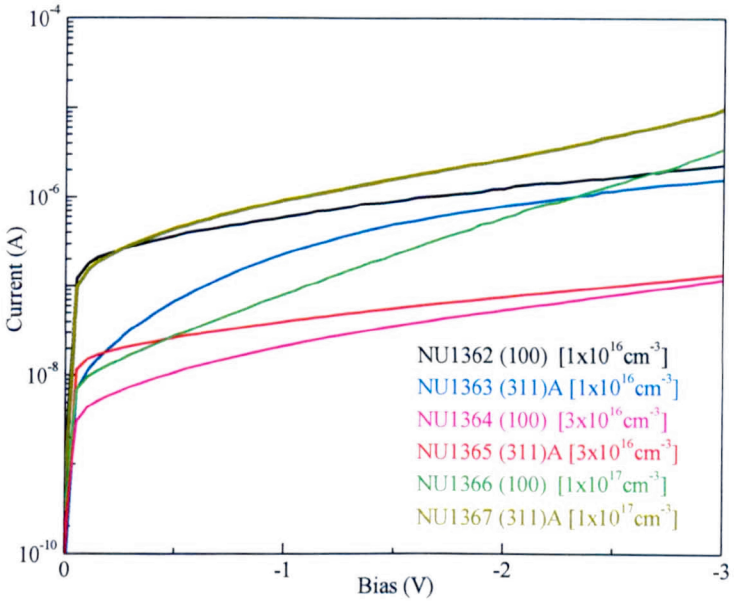

Figure 7.1: Current-Voltage (I-V) Characteristics of Schottky diodes measured at 300K. The diameter of the devices vary from 1mm to 0.25mm.

The Capacitance-Voltage (C-V) measurements at room temperature were performed for each diode following the measurement procedure described in chapter 5. In order to determine the background doping concentration (N_d) of each sample, C-V data was analysed using equation 4.8. The deduced value of N_d will be used to calculate the trap concentration. Figure 7.2 represents the C-V data of one of the samples (NU1362) in the form of $1/C^2$ versus V_R. The slope of this plot is used to calculate N_d using equation 4.8.

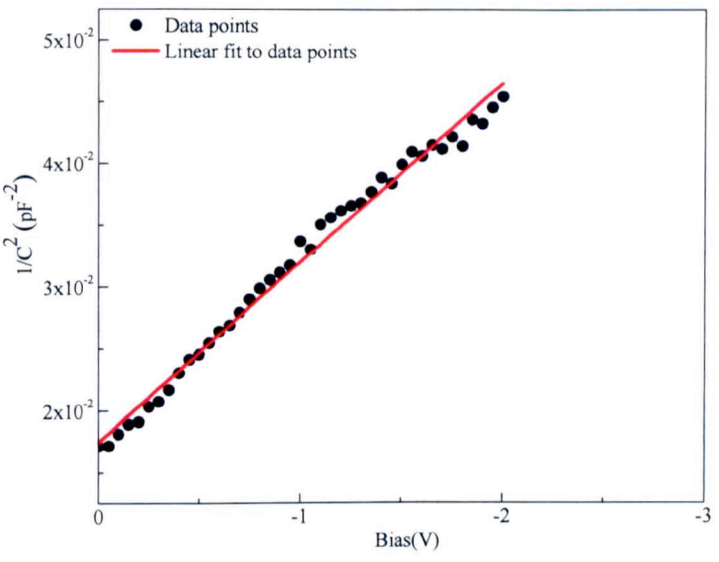

Figure 7.2: Typical $1/C^2$ versus reverse bias (VR) characteristic at 300K.

7.2.2 DLTS DATA

For the DLTS measurements the samples were mounted in a closed-cycle helium-cryostat and cooled down to a temperature of 10 K. The temperature was then ramped to ~400K at the rate of 2K/min and the DLTS signal was recorded as shown in [Figure 7.3 (a)–(f)] for samples NU1362-NU1367, respectively. The measurement parameters used are: a rate window of 50 Hz, quiescent reverse bias $V_R = -3$ V, filling pulse $V_p = -0.5$ V and filling pulse duration $t_p = 1$ ms that was sufficient to fill the traps with carriers.

The DLTS measurements reveal three and four hole traps in NU1362 and NU1364 samples, respectively [Figure 7.3 (a) and (c)] grown on (100) plane with doping concentrations of 1×10^{16} cm^{-3} and 3×10^{16} cm^{-3}, respectively. For NU1366 (100) plane (1×10^{17} cm^{-3}) sample [Figure 7.3 (e)] two hole traps and two electron traps are observed. Whereas the DLTS scans shown in Figures 7.3 (b), (d) and (f) for the (311)A orientation, five, two and one hole traps have been detected in samples NU1363, NU1365 and NU1367 doped with 1×10^{16} cm^{-3}, 3×10^{16} cm^{-3} and

1×10^{17} cm^{-3}, respectively. For convenience holes traps are labelled as HA, HB, HC, HD, HE and HF, in NU1362, NU1363, NU1364, NU1365, NU1366 and NU1367, respectively. The digits, 1, 2, .. correspond to a particular trap in each sample. In this work, the interest is to investigate the majority carrier defect levels, and therefore the electron emitting levels are not investigated.

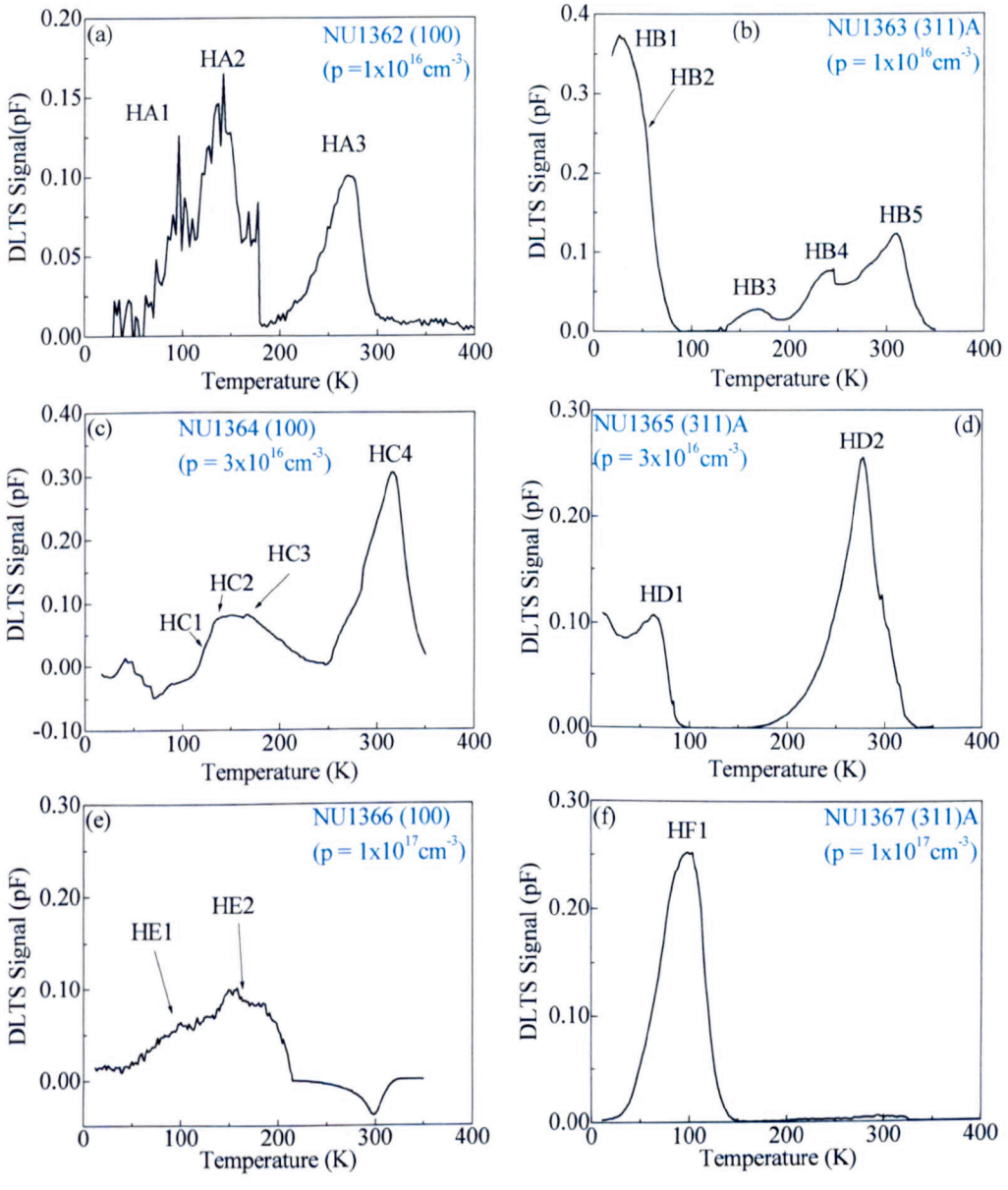

Figure 7.3: Conventional DLTS scans for each MBE grown Be-doped AlGaAs sample; (a) – (f) represent scans for NU1362 –NU1367 samples, respectively. The signal of the traps HA1, HA2, HE1 and HE2 are multiplied by a factor of 10 for clarity.

7.2.3 DETERMINATION OF ACTIVATION ENERGIES OF TRAPS

In order to find out the position of these defect levels within the material band gap, i.e. the activation energy of the defects with respect to the top of valence band, the emission rates of each trap were measured using High Resolution Laplace DLTS technique.

The temperature corrected emission rates of the traps are plotted versus 1000/T in Arrhenius plots [Figure 7.4]. As explained in section 4.2.3 the slope and intercept of these plots are used to determine the activation energies and the apparent capture cross-section of the traps as displayed in Table 7.1.

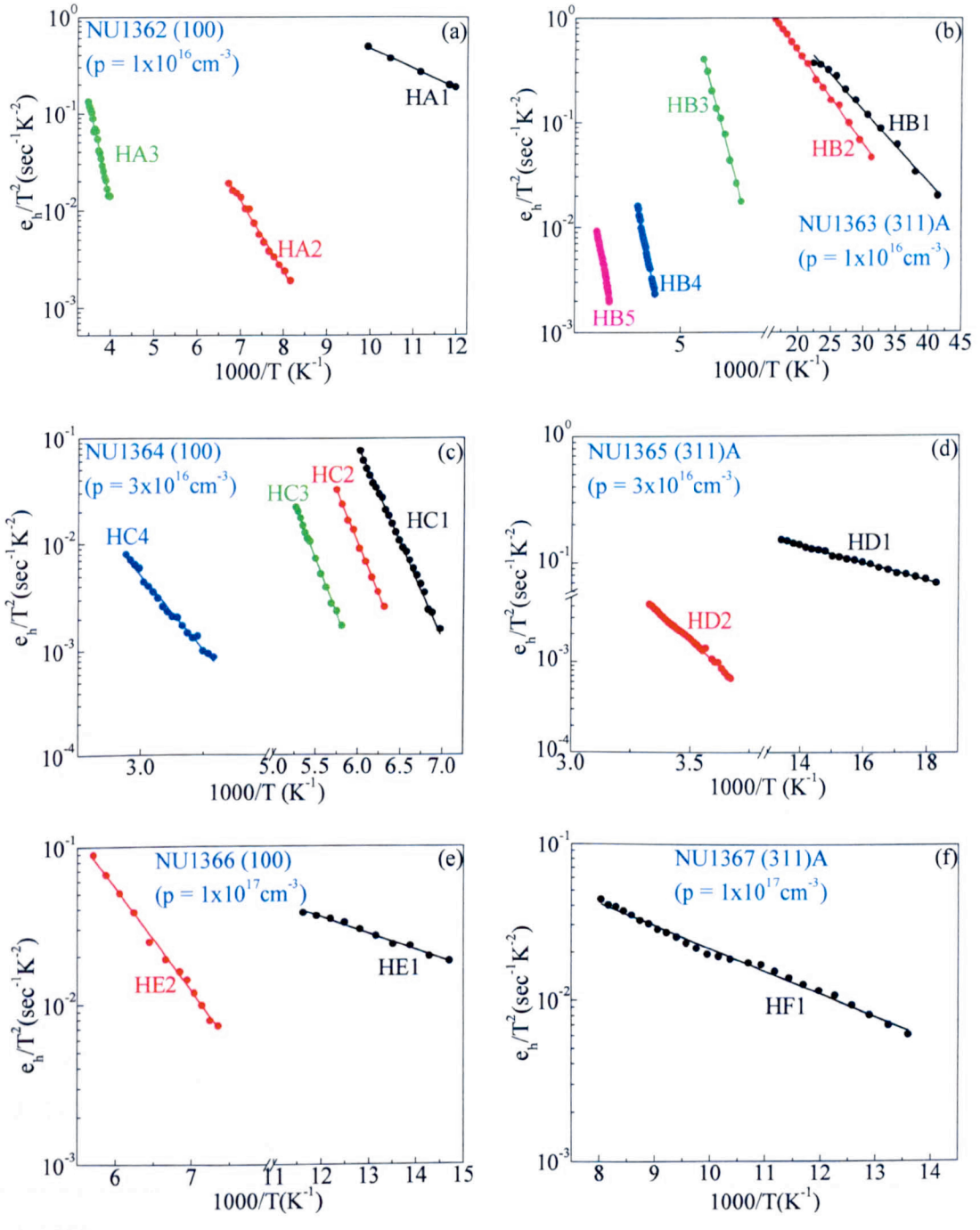

Figure 7.4: Arrhenius plot for each hole trap is obtained from Laplace DLTS measurements. The letters A, B, C, D, E and F refer to samples NU1362, NU1363, NU1364, NU1365, NU1366 and NU1367, respectively.

Table 7.1: Trap parameters calculated from DLTS and Laplace DLTS measurements

Sample ID	Be-doping (cm^{-3})	Trap	Activation energy (eV)	Capture Cross-Section (cm^2)	Concentration (cm^{-3})
NU1362 (100)	1×10^{16}	HA1	0.041 ±0.002	8.32×10^{-15}	2.09×10^{13}
		HA2	0.145±0.006	5.35×10^{-13}	2.74×10^{13}
		HA3	0.406 ± 0.006	1.89×10^{-13}	1.67×10^{14}
NU1363 (311)A	1×10^{16}	HB1	0.014 ± 0.006	1.03×10^{-15}	9.83×10^{14}
		HB2	0.017 ± 0.004	1.56×10^{-16}	7.85×10^{14}
		HB3	0.305± 0.006	5.84×10^{-16}	1.74×10^{13}
		HB4	0.400± 0.003	3.92×10^{-10}	7.35×10^{13}
		HB5	0.430 ± 0.003	$1.49\ 10^{-12}$	3.24×10^{14}
NU1364 (100)	3×10^{16}	HC1	0.356 ± 0.013	1.45×10^{-14}	1.37×10^{13}
		HC2	0.383 ±0.003	8.32×10^{-13}	8.01×10^{13}
		HC3	0.403±0.004	8.32×10^{-13}	8.01×10^{13}
		HC4	0.554 ± 0.007	2.29×10^{-13}	7.68×10^{13}
NU1365 (311)A	3×10^{16}	HD1	0.013 ± 0.001	1.58×10^{-16}	1.43×10^{14}
		HD2	0.450 ± 0.004	2.49×10^{-13}	3.42×10^{14}
NU1366 (100)	1×10^{17}	HE1	0.021 ± 0.002	3.84×10^{-19}	2.88×10^{13}
		HE2	0.130 ± 0.005	1.38×10^{-18}	4.69×10^{13}
NU1367 (311)A	1×10^{17}	HF1	0.028 ± 0.004	3.83×10^{-15}	8.47×10^{13}

7.2.4 EFFECT OF ELECTRIC FIELD ON EMISSION RATES

The emission rates of some defect levels are dependent on the applied electric field as mentioned in section 3.3. To check the dependence of the emission rate on junction electric field, the Laplace DLTS measurements were carried out for each trap using the experimental procedure described in chapter 5.

In order, to investigate the effect of the junction electric field on the hole traps emission rates and consequently on their activation energies, the LDLTS double pulse method [41] is employed. The difference between the two pulse heights is kept constant during each measurement at a constant temperature. A considerable change in emission rate of traps HA1, HA2, HB1, HB3, HC1, HC2, HD1 with respect to different filling pulse heights is observed. The electric field-dependent emission data are analysed using Poole–Frenkel and phonon-assisted tunnelling models following the simple criteria proposed by Ganichev et al. [42] to differentiate between both mechanisms. It is evident that the obtained emission rates satisfy the Poole–Frenkel model [Figure 7.5]. The calculated value of Poole–Frenkel constant for each trap are given in Table 7.2.

The field-dependent Arrhenius plots and activation energies versus electric field data for the deep levels mentioned above are shown in Figure 7.6, Figure 7.7, Figure 7.8, and Figure 7.9.

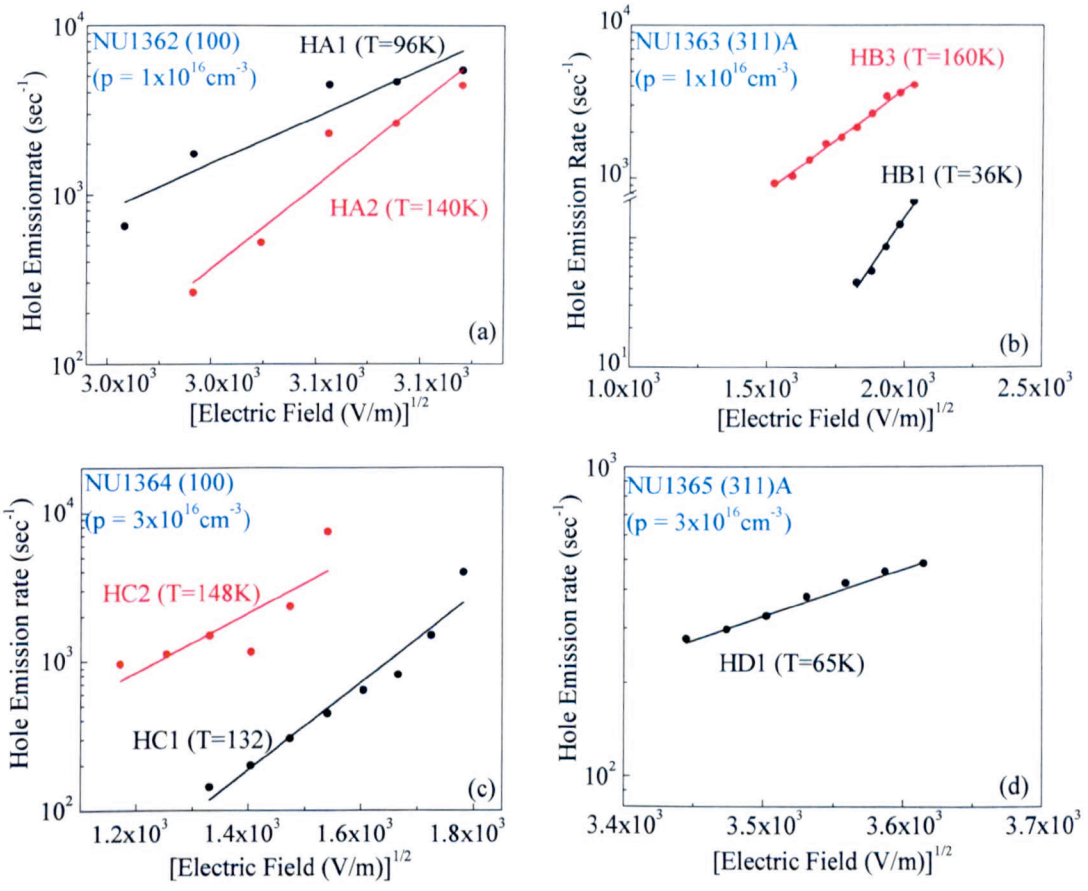

Figure 7.5: Traps showing electric field-dependent emission rates. The data are analysed using Poole–Frenkel model.

Table 7.2: Poole-Frenkel constant of the defects calculated from field dependent emission rates and their respective rate of change of activation energy with respect to electric field are illustrated

Sample ID	**Doping (cm^{-3})**	**Trap**	**Poole-Frenkel Constant (α_{PF}) × 10^{-5} eV $m^{1/2}$ $V^{-1/2}$**	**Rate of change of activation energy with electric field ($\times 10^{-8}$ eV m/V)**
NU1362 (100)	1×10^{16}	HA1	10. 5	-1.725
		HA2	27.3	-3.009
NU1363 (311)A	1×10^{16}	HB1	2.2	-0.693
		HB3	4.2	-7.429
NU1364 (100)	3×10^{16}	HC1	7.7	-8.293
		HC2	6.2	-6.763
NU1365 (311)A	3×10^{16}	HD1	2.0	-1.315

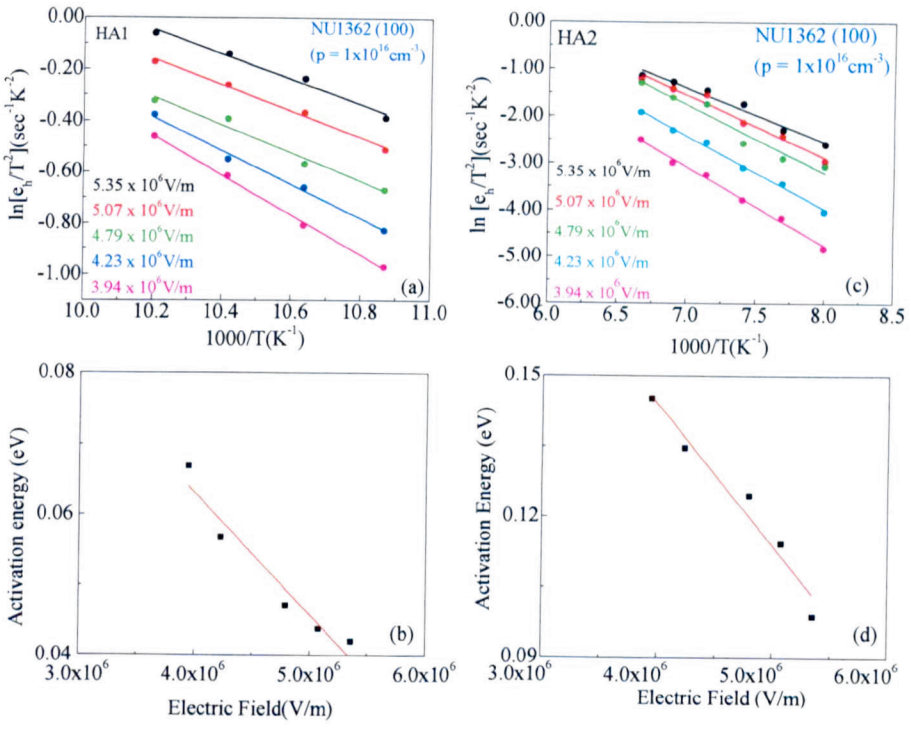

Figure 7.6: (a) and (c) Arrhenius plot of traps HA1 and HA2, respectively, (b) and (d) show the change of activation energy as a function of electric field of HA1 and HA2, respectively.

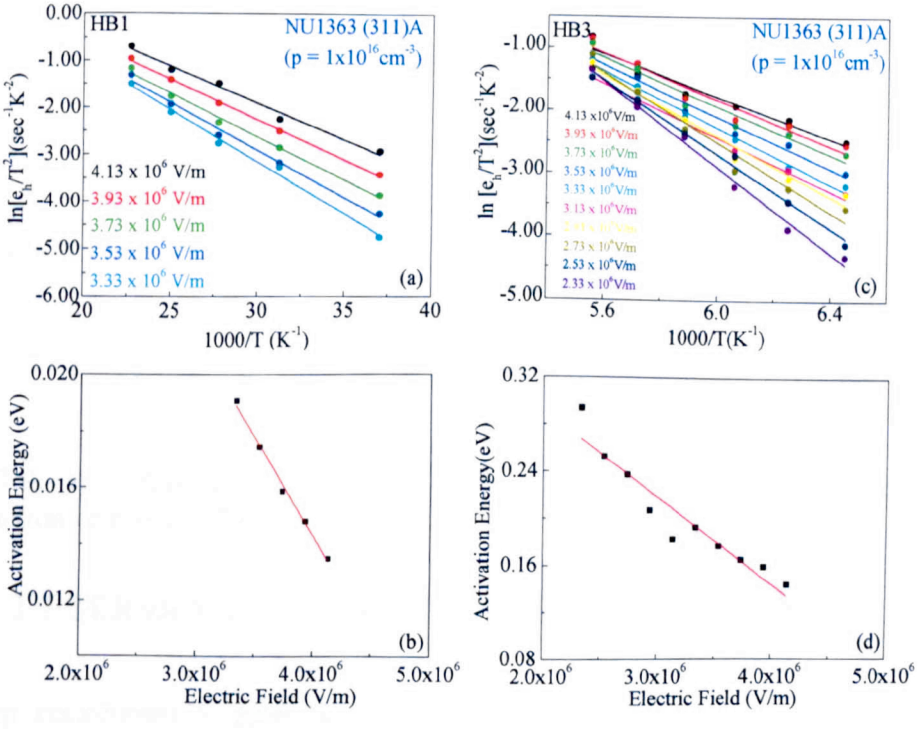

Figure 7.7: (a) and (c) Arrhenius plot of traps HB1 and HB3, respectively, (b) and (d) show the change of activation energy as a function of electric field of HB1 and HB2, respectively.

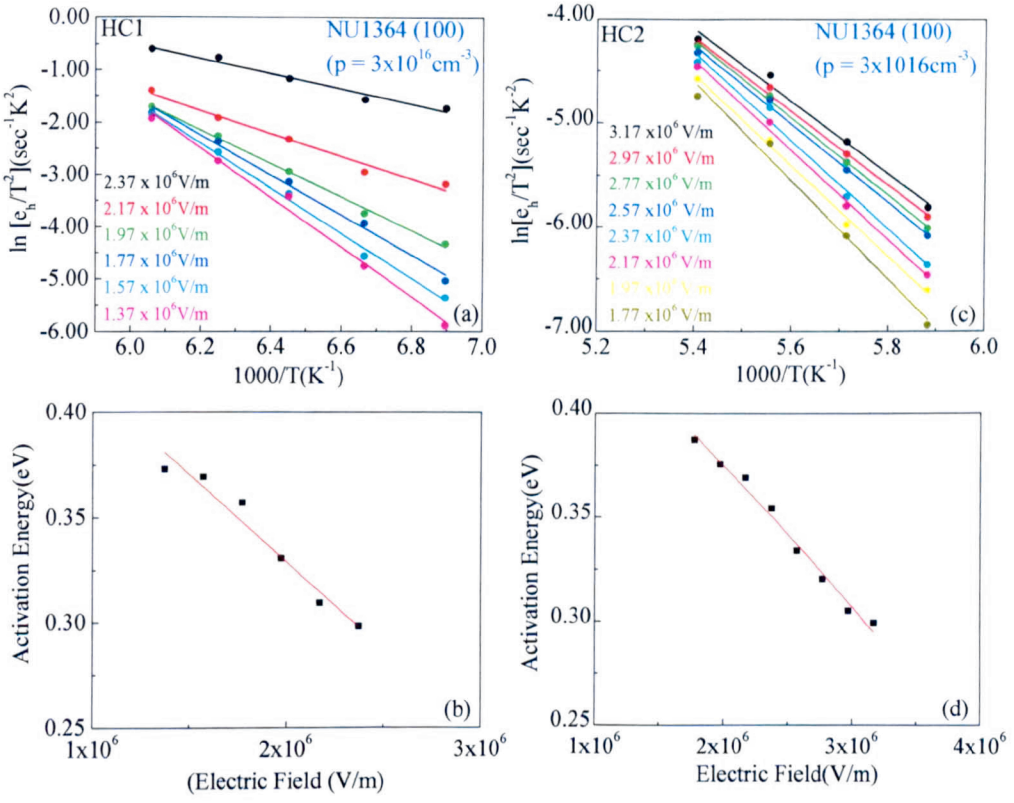

Figure 7.8: (a) and (c) Arrhenius plot of traps HC1 and HC2, respectively, (b) and (d) show the change of activation energy as a function of electric field of HC1 and HC2, respectively.

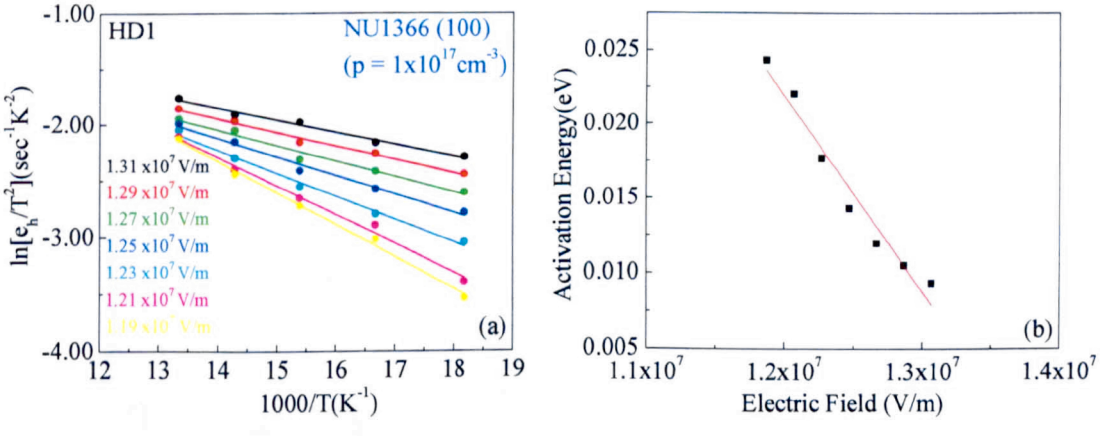

Figure 7.9: (a) Arrhenius plot of traps HD1 (b) show the change of activation energy as a function of electric field of HD1.

7.2.5 DETERMINATION OF TRAP CONCENTRATION

The trap concentration determination was described in chapter 4. The average concentration of each defect level is shown in Table 7.1.

7.2.6 BEHAVIOUR OF TRAP CONCENTRATION VERSUS DEPTH

In order to investigate the propagation of the defect levels within the epitaxial layers, their concentration are measured with respect to depth by utilising the value of the area under the peak obtained from Laplace DLTS measurements. In these types of measurements the double pulse technique is applied in the same way as in the measurement of the electric field dependent emission rate. The depth is calculated from C-V measurements at each reverse bias. The concentration-depth profiles of each trap are shown in Figure 7.10 [(a) – (f)] for NU1362 –NU1367, respectively.

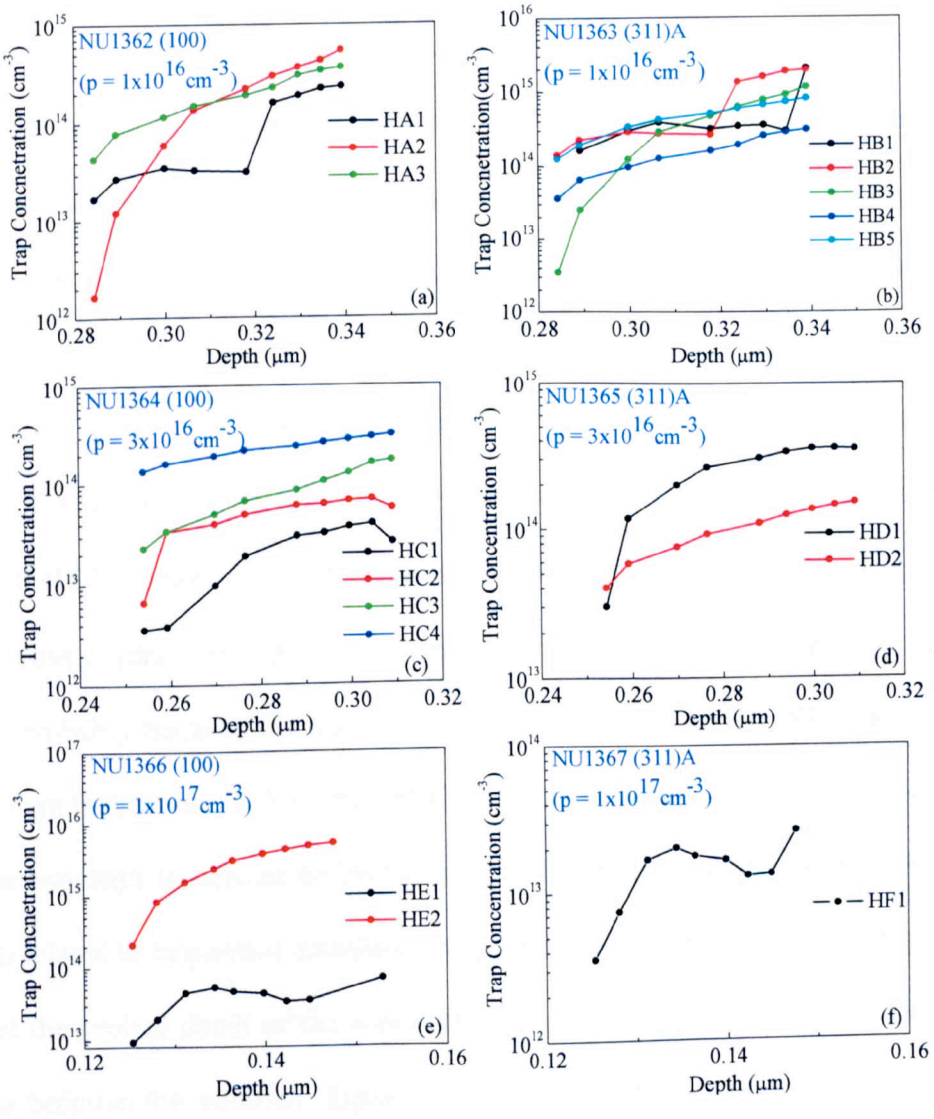

Figure 7.10: Concentration depth profile of each defect level.

7.3 DISCUSSION

For analysis purposes, the trap energies are compared with the available published data in the literature and it is found that few of the traps detected in these studies have been reported previously. However, as far as we are aware most of the traps investigated in our Be-doped AlGaAs epitaxial layers are new.

The traps HA2 (0.145 ± 0.006 eV) and HE2 (0.130 ± 0.01 eV) have almost the same activation energy as that of H1 (0.14 eV) [112], but seem to be different in nature than that of H1. For example the capture cross-section of H1 was found to be temperature-dependent, whereas in this study the capture cross-sections of HA2 and HE2 are temperature insensitive, which confirms that there is no evidence of phonon interaction during the capture of the carriers [77]. In addition, HA2 shows electric field-dependent emission rate and obeys the Poole–Frenkel model [42] [Figure 7.5] with a constant $\alpha_{PF} = 27.3 \times 10^{-5}$ eV$(m/V)^{1/2}$ whereas, the carrier emission rate of HE2 are electric field-independent. The apparent activation energy of this trap is 0.145 eV at 3.94×10^6 V/m and 0.098 eV at 5.35×10^6 V/m. The extrapolated energy of HA2 at zero electric field is 0.264 eV. The concentration of both traps HA2 and HE2 [Figure 7.10 (a) and (e), respectively] increases with depth. It is worth noting from Figure 7.10 that the concentration of HE2 is higher than that of HA2. This is probably because the Be-doping concentration in sample NU1366 (HE2) is higher than that in sample NU1362 (HA2). One may conclude that the concentration of these two traps is affected by Be-doping concentration, and therefore these defects may be related to impurities associated with Be complex defects. It is worth pointing out that the probed depth of the concentration profile of HA2 and HE2 is different. This is because the junction depletion width (w) depends on the intentional Be-

doping concentrations; sample NU1362 (Be-doping = 1×10^{16} cm^{-3}) has a larger w than NU1366 (Be-doping =1×10^{17} cm^{-3}). The DLTS technique does not probe the microscopic nature of the defects, and therefore, it is difficult at this stage to explain how these levels are created and to assign them to any known defect. However, the electric field dependence of the emission rates for defect HA2 suggest that it is a charged center [42, 112], whereas, HE2 is a neutral defect level.

The traps HA3 (0.406 ± 0.006eV), HB4 (0.400 ± 0.003 eV) and HC3 (0.403 ± 0.004 eV) have similar activation energies as that of H3 (0.4 eV) [112] which is possibly related to a defect formed when an As atom is replaced by a Ga atom, i.e. Ga antisite defect (Ga_{As}) [113]. In addition, the average concentration of HA3 ($1.67\times10^{14}cm^{-3}$), HB4 (7.35×10^{13} cm^{-3}) and HC3 (8.01×10^{13} cm^{-3}) [Table 7.1] indicates that HA3 and HC3 present in samples grown on (100) plane have higher concentrations than the similar trap HB4 detected in sample grown on (311)A plane. Assuming that HA3 and HC3 are of the same nature, then it is worth noting that this trap density decreases when the Be-doping increases from 1×10^{16} cm^{-3} to 3×10^{16} cm^{-3} for the (100) plane. The concentration versus depth profiles of HA3, HB4, and HC3 have similar trends, i.e. the density increases with depth, as shown in Figure 7.10 (a), (b) and (c), respectively.

Traps HB5 (0.430 ± 0.003eV) and HD2 (0.450 ± 0.004 eV), detected in samples grown on (311)A with different Be-doping concentration of 1×10^{16} cm^{-3} and 3×10^{16} cm^{-3}, respectively, have similar activation energies as that of H4 (0.46 eV) [112]. Both levels have nearly the same average concentration [Table 7.1]. However, the concentration-depth profile [HB5: Figure 7.10 (b); HD2: Figure 7.10 (d)] shows that the concentration of HB5 increases continuously from 1.24×10^{14} cm^{-3} at 0.28 μm to

7.93×10^{14} cm^{-3} at 0.34 μm, whereas, for HD2 it increases from 4.03×10^{13} cm^{-3} at 0.25 μm to 1.52×10^{14} cm^{-3} at 0.31μm. The emission rates of HB5 and HD2 showed no electric field dependence, and therefore one can conclude that these defects are neutral [42, 112] in Be-doped AlGaAs epitaxial layers.

Trap HC4 (0.554 ± 0.005 eV) has exactly the same activation energy as H5 (0.55 eV) [114] but with higher capture cross-section and concentration. It was identified as Cu-related trap in MBE grown p-type AlGaAs [114]. The concentration-depth profile [Figure 7.10 (c)] shows that the concentration varies from 1.25×10^{14} cm^{-3} at 0.25 μm to 3.07×10^{14} cm^{-3} at 0.31 μm. The emission rates of HC4 were electric field independent and therefore this deep level is neutral.

In addition to above deep traps some new shallow and deep traps are detected for the first time in our Be-doped sample. These traps include shallow levels namely; HA1 (0.041 ± 0.002 eV), HB1 (0.014 ± 0.006 eV), HB2 (0.017 ± 0.004 eV), HD1 (0.013 ± 0.001 eV), HE1 (0.021 ± 0.002 eV) and HF1 (0.028 ± 0.004 eV), and deep levels namely; HC1 (0.356 ± 0.013 eV) and HC2 (0.383±0.003eV).

For the deep traps HB3 (0.305±0.006eV), HC1 (0.356±0.013eV), and HC2 (0.383±0.003eV), we observed that their emission rates are sensitive to the applied electric field, and follow the Poole-Frenkel model as shown in Figure 7.5 (b) and (c), respectively. It is found that the activation energies decrease with increasing electric field; from E_{HB3} = 0.294 eV at 2.33 $\times10^6$ V/m, E_{HB3} = 0.144 eV at 4.13 $\times10^6$ V/m; E_{HC1} = 0.373 eV at 1.37 $\times10^6$ V/m; E_{HC1} = 0.298 eV at 2.37 $\times10^6$ V/m; E_{HC2} = 0.387 eV at 1.77 $\times10^6$ V/m; E_{HC2} = 0.299 eV at 3.17 $\times10^6$ V/m. The extrapolated energy at zero electric field of HB3, HC1 and HC2 is 0.441 eV, 0.494 eV and 0.510 eV, respectively. The enhancement of emission rates with field suggest that HB3, HC1

and HC2 are charged defects in Be-doped AlGaAs epitaxial layers. The concentration profile measurements illustrated in Figure 7.10 (b) and (c), respectively, show that the density of these traps increases with depth; [HB3] = 2.43 × 10^{12} cm^{-3} at 0.28 μm to 1.13 × 10^{15} cm^{-3} at 0.34 μm, [HC1] = 3.56 × 10^{12} cm^{-3} at 0.25 μm to 2.57 × 10^{13} cm^{-3} at 0.31 μm, and [HC2] = 6.51 × 10^{12} cm^{-3} at 0.25 μm to 5.52 × 10^{13} cm^{-3} at 0.31 μm.

The emission rates of levels HA1 (0.041 ± 0.002 eV), HB1 (0.014 ± 0.006 eV), and HD1 (0.013 eV ± 0.001 eV) are sensitive to the electric field and this confirms that these shallow levels are charged. These emission rate enhancements follow the Poole-Frenkel model. It has been observed from field dependent emission rate data that the energies of these traps are affected by the electric field: E_{HA1} = 0.067 eV at 3.94 × 10^{6} V/m, E_{HA1} = 0.042 eV at 5.35 × 10^{6} V/m; E_{HB1} = 0.019 eV at 3.33 × 10^{6} V/m, E_{HB1} = 0.014 eV at 4.13 × 10^{6} V/m; E_{HD1} = 0.024 eV at 1.19 × 10^{7} V/m, E_{HD1} = 0.009 eV at 1.31 × 10^{7} V/m. The extrapolated energies at zero electric field for these defects are found to be 0.132 eV, 0.042 eV and 0.179 eV, respectively and the rate of change of respective activation energies with respect to applied electric field is mentioned in Table 7.2. The concentration of the traps changes with depth; [HA1] = 1.62 × 10^{13} cm^{-3} at 0.28 μm to [HA1] = 2.33 × 10^{14} cm^{-3} at 0.34 μm; [HB1] = 1.62 × 10^{14} cm^{-3} at 0.29 μm to [HB1] = 2.00 × 10^{15} cm^{-3} at 0.34 μm; [HD1] = 3.03 × 10^{13} cm^{-3} at 0.25 μm to [HD1] = 3.56 × 10^{14} cm^{-3} at 0.31 μm.

In addition to charged shallow levels some neutral shallow levels are found in this work. These are HB2 (0.017 ± 0.004 eV), HE1 (0.021 ± 0.002 eV) and HF1 (0.028 ± 0.004 eV). Their concentration changes with depth; [HB2] = 1.4 × 10^{14} cm^{-3} at 0.28 μm to [HB2] = 1.93 × 10^{15} cm^{-3} at 0.34 μm; [HE1] = 9.22 × 10^{12} cm^{-3} at 0.13 μm to

[HE1] = 6.85×10^{13} cm^{-3} at 0.15 μm; [HF1] = 3.54×10^{12} cm^{-3} at 0.13 μm to [HF1] = 2.63×10^{13} cm^{-3} at 0.15 μm.

This study reveals that the number of traps, including some electron emitting deep levels, increases with increasing Be-doping for the samples grown on (100) plane. On the other hand, the number of hole traps decreases with increasing Be-doping concentrations for (311)A samples. These results are in agreement with the reported optical studies [11, 115] where it was shown that superior PL efficiencies are obtained in Be-doped AlGaAs samples grown on (311)A substrates. The appearance of electron traps in the samples grown on (100) plane for higher doping level is probably due to residual unintentionally background Si-doping [97]. All the samples used in this study were grown under the same experimental conditions except the variation of Be-doping concentration. The existence of electron traps in the samples grown on (311)A plane is not expected because silicon behaves as a p-type dopant on A-faces [106, 107].

It is suggested [42] that in case of Poole-Frenkel the emission rates are enhanced due to the lowering of Coulomb potential surrounding the defect centre. This also suggests that the defect centres carry no charge when they are filled, and become charged when empty. The nature of the traps before and after the emission can be summarised as $C^0 \rightarrow C^- + C^+$, where C^0 is the charge state of the defect when it is filled, C^- is defect charge state when it emits a hole, and C^+ is the carrier (hole in this case) that is emitted by the trap. Following this argument we are confident to confirm that hole traps found in this study namely; HA1, HA2, HB1, HB3, HC1, HC2 and HD1 are acceptor like traps [112, 114].

It is worth noting that all the traps have similar concentration versus depth behaviour i.e. increasing with the depth, except HE1 and HF1 whose concentrations first increase, then decrease up to a certain depth, and again increase. Traps HB1, HC2 and HC4 have a more uniform concentration depth profile.

7.4 CONCLUSION

In summary, the effect of Be-doping concentrations on deep electrically active defects has been investigated in AlGaAs layers grown on (100) and (311)A GaAs substrates. It is found that for (100) samples the number of hole traps increases for doping level from 1×10^{16} cm^{-3} to 3×10^{16} cm^{-3}. In addition, electron emitting levels are detected in (100) sample doped to 1×10^{17} cm^{-3}. The nature of these negative defects is not known, but they could be related to Si residual dopant in the MBE system. For (311)A samples the number of hole traps decrease with increasing Be-doping level. It is obvious from the electric field studies that both charged and neutral like defects exist in the samples. Some of the traps detected in the samples doped with 1×10^{16} and 3×10^{16} cm^{-3} have carrier emission rates that are dependent of the electric field, and therefore, are ionised after carrier emission and carry an electric charge. However, the traps detected in 1×10^{17} cm^{-3} do not show any field dependence on their emission rates. Finally few shallow level and deep level traps are detected for the first time in Be-doped AlGaAs grown by MBE, some of which have an electric field dependent emission rate. The rate of change of activation energy with respect to the electric field is higher for the defect levels detected in the samples grown on (100) plane than those detected in (311)A samples. Further studies are needed to explore the nature and origin of these defects.

In addition, the common defects levels detected in Be-doped AlGaAs are given below:

(a) HA3 (100), HB4 (311)A and HC3 (100) are related to Ga-antisite (Ga_{As}) defect.

(b) HC4 level detected in only (100), is assigned to the Cu related defect.

Furthermore, these studies confirm for the first time the existence of a number of both shallow and deep level defects:

(1) **Shallow levels:**

(a) Charged levels: HA1in (100) and HB1 in (311)B

(b) Neutral levels: HB2 in (311)B, HE1 (100) and HF1 (311)A

(2) **Deep levels:**

(a) The defects HA2 in (100), HE2 in (100), HB5 in (311)A, HD2 (311)A, HB3 in (311)A, HC1 in (100) and HC2 in (100) are related to Be-doping concentration.

(b)Traps HA2 in (100), HB3 in (311)A, HC1 in (100) and HC2 in (100) are charged defect levels, whereas, HE2 in (100), HB5 in (311)A and HD2 in (311)A are neutral defect levels.

CHAPTER 8

DEEP LEVEL DEFECTS IN GaAs/AlGaAs MULTI-QUANTUM WELL STRUCTURES

This chapter comprises DLTS and Laplace DLTS results of defects in two different sets of Multi-Quantum Well (MQW) structures. The first set was grown on conventional (100) and high index (311)B GaAs substrates. The second set was grown on (100) GaAs substrates at different growth temperatures, arsenic species, i.e. using As_2 and As_4 and arsenic overpressures.

8.1 GaAs/$Al_{0.33}Ga_{0.66}As$ MQWs GROWN ON (100) AND (311)B GaAs SUBSTRATES

During the last few decades, heterostructure-based devices have contributed to the advancement of diode lasers, high speed electrical devices [116] and THz detectors [117]. Electrically and optically active defect states in the band gap of semiconductor materials can play an important role in their carrier transport properties. Previous DLTS studies of defects in GaAs/AlAs/GaAs quantum wells [118] showed at least six out of eight sub-bands in the heterostructures are occupied by defect states. Using DLTS technique, Jia et al. [119] investigated Si-doped GaAs/AlGaAs quantum wells and superlattices and demonstrated that the energy of the well-known DX centre in AlGaAs epilayers decreases in the case of MQWs and increases for superlattices.

Arbaoui et al. [120] have also reported defects states in MBE-grown AlGaAs/GaAs MQW structures which can affect the carrier transport properties.

Most of the studies on defects in GaAs/AlGaAs quantum wells and superlattices reported so far are on samples grown on the conventional (100) GaAs plane. The crystallographic orientation of the substrate has a strong influence on incorporation of impurities and defects and hence on optical and electronic properties of III–V materials. It is therefore important to probe similar structures grown on non-(100) planes. In this work, DLTS [39] and LDLTS [80] techniques have been employed to investigate the electrical properties of defect states present within the band gap of (311)B Si-doped GaAs/AlGaAs MQWs. For comparison purpose similar structure grown on (100) GaAs substrate was investigated.

In summary, one dominant electron-emitting level is observed in the quantum wells structure grown on (100) plane whose activation energy varies from 0.47 to 1.3 eV as the junction electric field varies from zero field to 4.7×10^6 V/m. Two defect states with activation energies of 0.24 and 0.80 eV are detected in the structures grown on (311)B plane. The E_c-0.24 eV trap shows that its capture cross-section is strongly temperature dependent, whilst the other two traps show no such dependence. The value of the capture barrier energy of the trap at E_c-0.24 eV is 0.39 eV.

8.1.1 EXPERIMENTAL RESULTS AND ANALYSIS

8.1.2 I-V AND C-V CHARACTERISTICS

Current–voltage (I–V) characteristics were assessed prior to DLTS measurements to select the Schottky diodes with the lowest leakage currents. The I-V measurements shown in Figure 8.1 were performed following the experimental method discussed in

Chapter 5. Typical leakage currents of 2.4×10^{-9}A and 1.2×10^{-9}A at reverse bias of -5 V were obtained on (100) and (311)B devices, respectively. The very small reverse current of the diodes makes them very suitable for DLTS and Laplace DLTS measurements.

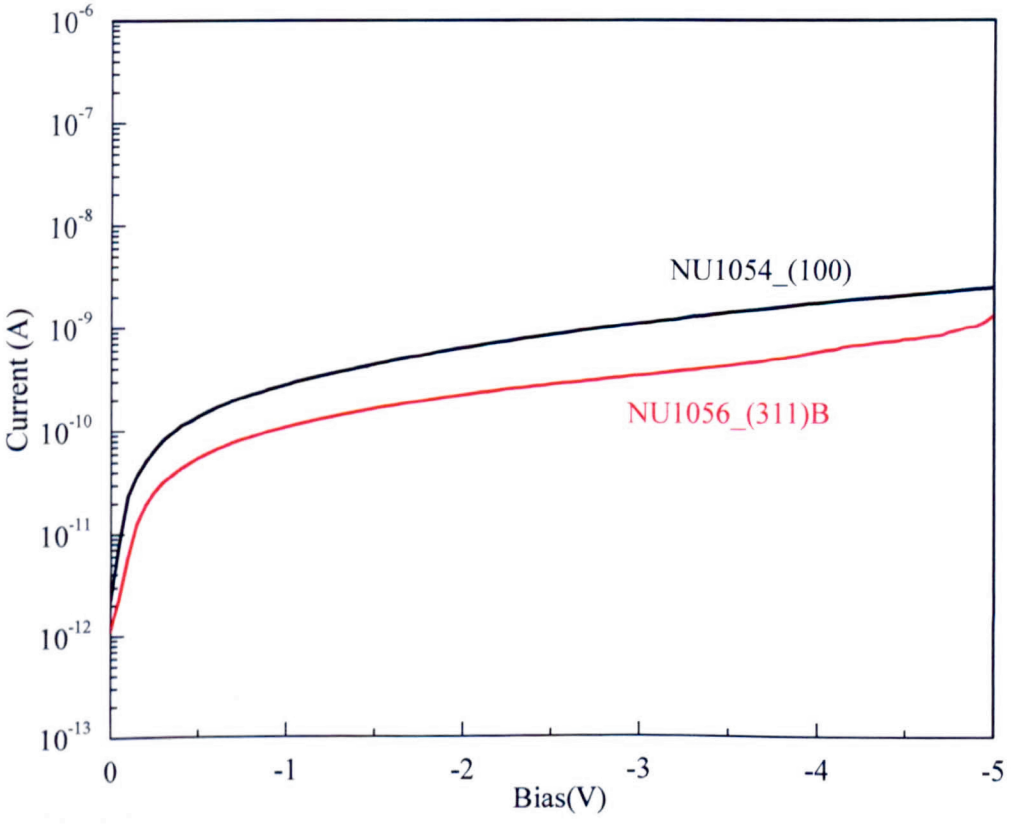

Figure 8.1: Current-Voltage (I-V) characteristics of the Schottky diodes fabricated on (100) and (311)B MQW structures.

In order to determine the background doping concentration, the capacitance–voltage (C–V) characteristics of the diodes were measured by following the experimental method discussed in Chapter 5. The doping concentration deduced from the slope of Figure 8.2 was 1.64×10^{16} cm^{-3} and 2.21×10^{16} cm^{-3} for (100) and (311)B samples, respectively. These values of background concentration are used to determine the concentrations of the traps.

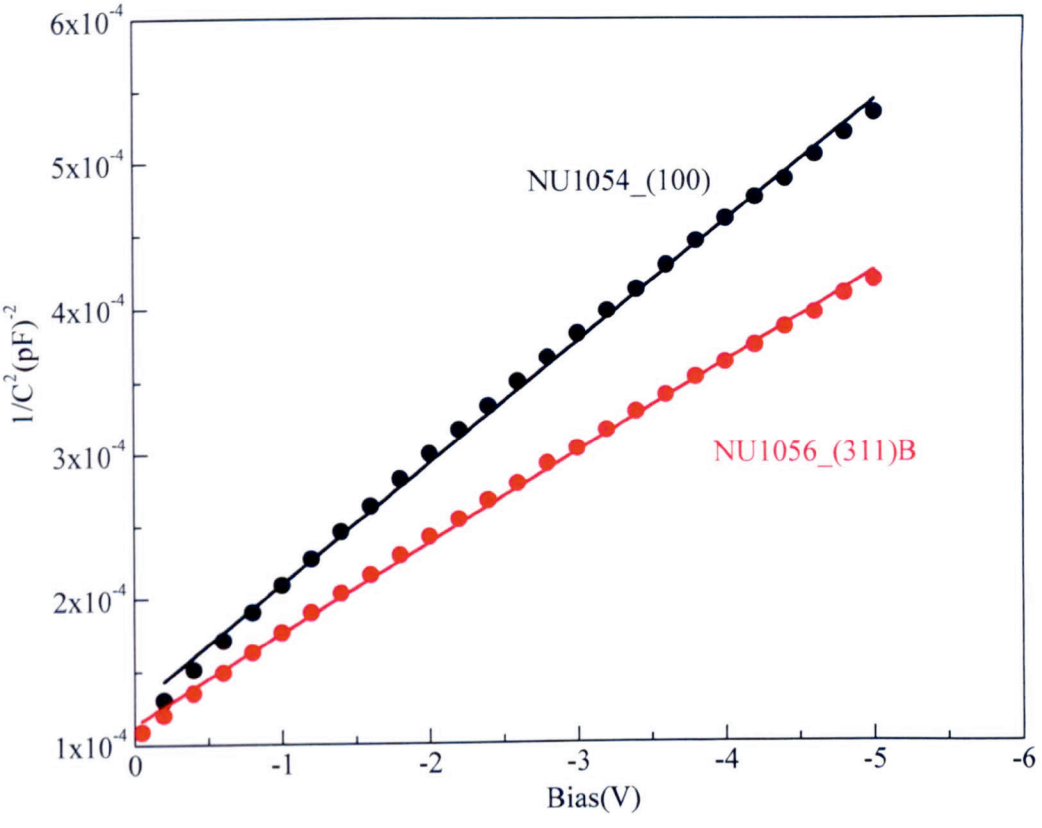

Figure 8.2: $1/C^2$ versus reverse bias characteristics of (100) and (311)B MQW structures.

8.1.3 DLTS DATA

The devices were mounted in a 10K closed-cycle helium cryostat. The DLTS spectra of the samples grown on (100) and (311)B devices are shown in Figure 8.3 (a) and (b), respectively. These scans were taken using a sampling rate window of 2.5 sec^{-1}, a quiescent reverse bias of -5 V and a filling pulse of 1 ms. A prominent peak associated with the electron trap labelled E1 is detected in (100). The broader feature that appears in the tail of E1 at a temperature ~350 K is not resolved by either techniques, i.e. DLTS and Laplace DLTS. The (311)B samples show two peaks associated with defect states labelled EB1 and EB2. Trap EB1, which appears as a shoulder of the main peak EB2 at temperature ~390 K, is resolved by using LDLTS as shown in Figure 8.4.

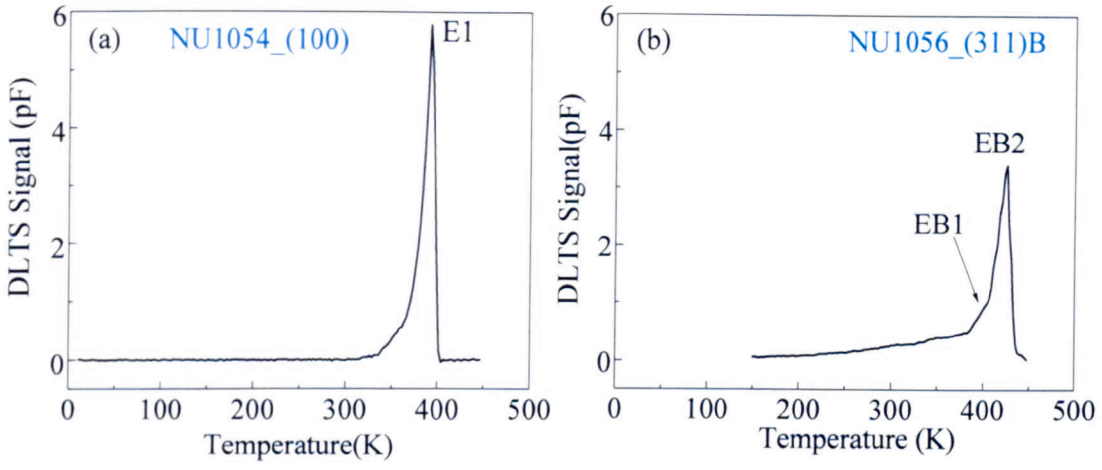

Figure 8.3: Conventional DLTS signals for two MBE grown MQW's using (a) (100) and (b) (311)B substrates.

8.1.4 DETERMINATION OF ACTIVATION ENERGIES OF TRAPS

Further to the conventional DLTS investigations, the Laplace DLTS measurements were performed to determine the carrier emission rates of the deep levels. The Arrhenius plots of the emission rates (e_n) are shown in Figure 8.5. The slope and intercept of the $\ln(e_n/T^2)$ versus 1000/T plot were used to deduce the activation energy and apparent capture cross-section of the detected deep levels. The calculated defect parameters are illustrated in Table 8.1.

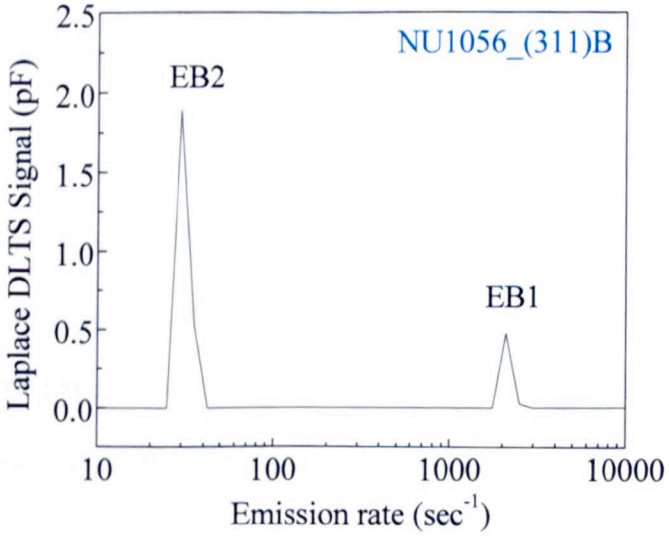

Figure 8.4: Two closely spaced peaks are well resolved by using high resolution Laplace DLTS.

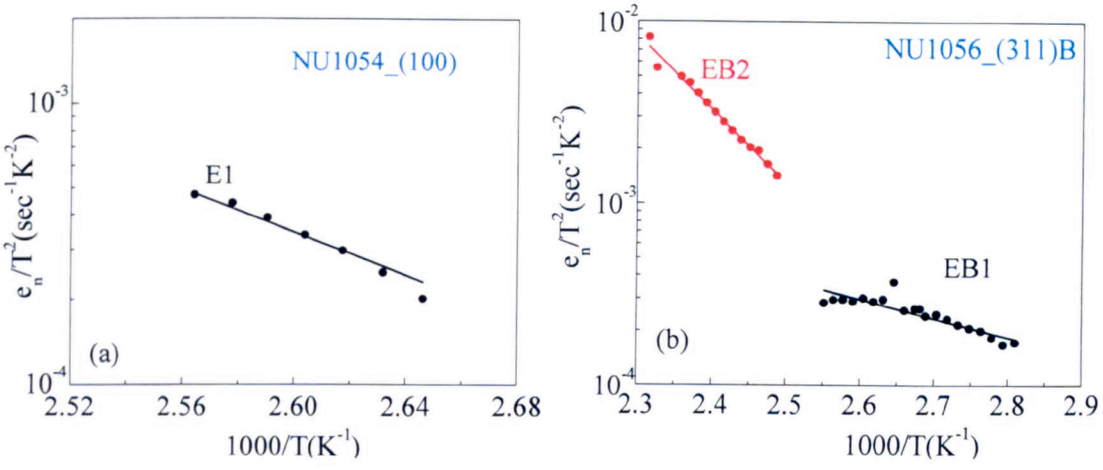

Figure 8.5: Arrhenius plots obtained from Laplace DLTS data of each detected trap in (a) (100) MQWs (E1), (b) (311)B MQWs (EB1 and EB2)

Table 8.1: Trap parameters calculated from DLTS and Laplace DLTS data

Sample	**Trap**	**Activation Energy (eV)**	**Capture Cross-section (cm^2)**	**Concentration (cm^{-3})**
NU1054 (100)	E_1	0.47 to 1.3	1.86×10^{-14}	4.4×10^{15}
NU1056 (311)B	E_{B1}	0.24	1.51×10^{-18}	4.1×10^{14}
	E_{B2}	0.80	1.32×10^{-15}	3.0×10^{15}

8.1.5 DETERMINATION OF TRAP CAPTURE CROSS-SECTION

As mentioned in Chapter 4, there are certain cases when the apparent capture cross-section of some defect centers may not represent the real value, i.e. the capture cross-section may be temperature dependent. In order to test this dependency and to determine the real values of σ_n and E_T, the direct measurements of σ_n of all the traps have been performed using the filling pulse method as described in Chapter 4.

The measured σ_n data of the traps and the effect of temperature on σ_n are shown for trap E1 in Figure 8.6 , and for trap EB1 in Figure 8.7. It is clear from Figure 8.6 (b)

and Figure 8.7 (d) that the capture cross-sections of traps E1 and EB2 are not temperature dependent. However, σ_n of EB1 [Figure 8.7 (b)] is strongly affected by temperature, and increases with increasing temperature. The mechanism involved in this phenomenon will be examined in the discussion section using the phonon interaction model given by Henry and Lang [121] for defects in GaAs and GaP.

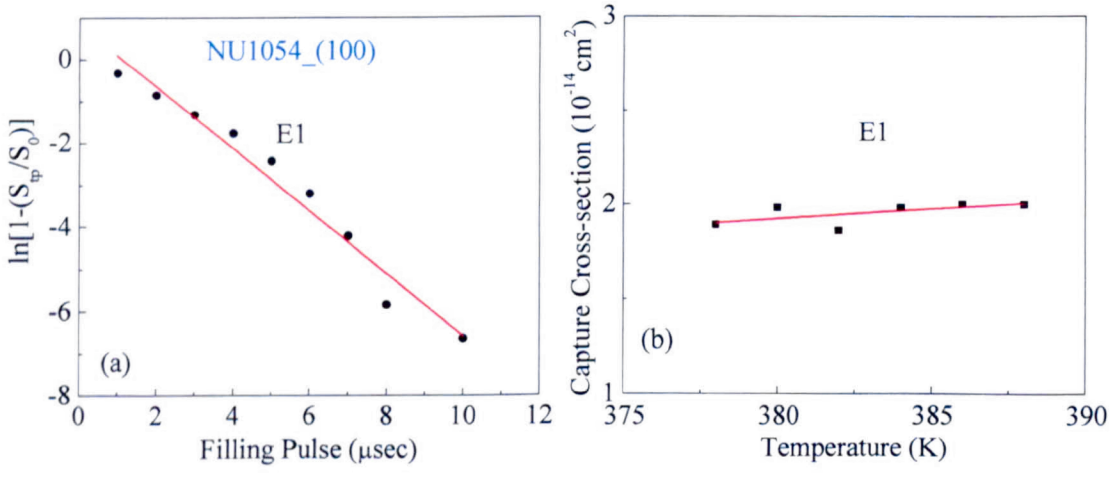

Figure 8.6: (a) Direct capture cross-section measurement data of trap E1, (b) effect of temperature on its capture cross-section.

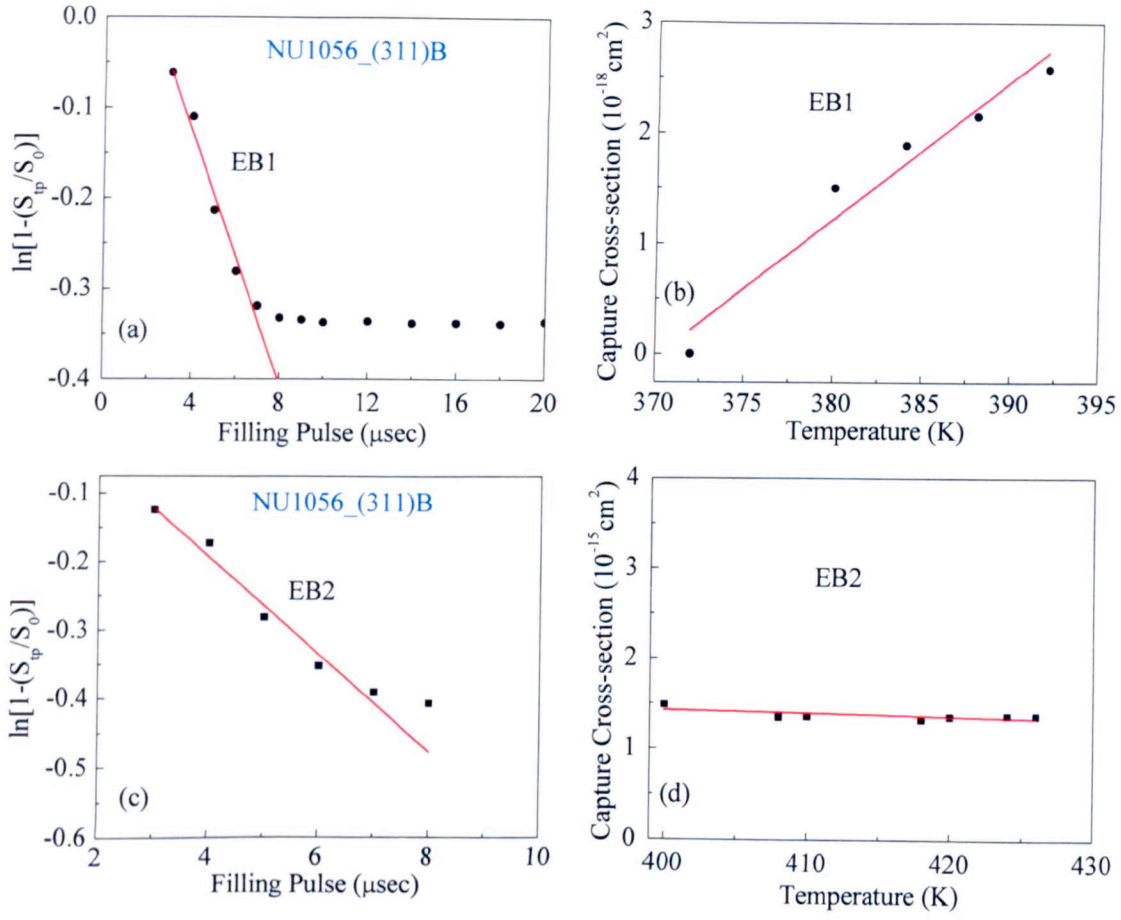

Figure 8.7: Direct capture cross-section measurement data of traps (a) EB1 and (c) EB2; effect of temperature on the capture cross-section (b) EB1 and (d) EB2.

8.1.6 EFFECT OF ELECTRIC FIELD ON EMISSION RATES

The effect of the junction electric field on the trap carrier emission rates was investigated using Laplace DLTS measurements by applying the double pulse method as discussed in Chapter 4. It was observed that only the E1 trap has properties which are electric field dependent. Figure 8.8 (a) and Figure 8.8 (b) illustrate the effect of the junction electric field on the trap emission rates and activation energy. The respective change in activation energy with applied electric field is plotted in Figure 8.8 (c).

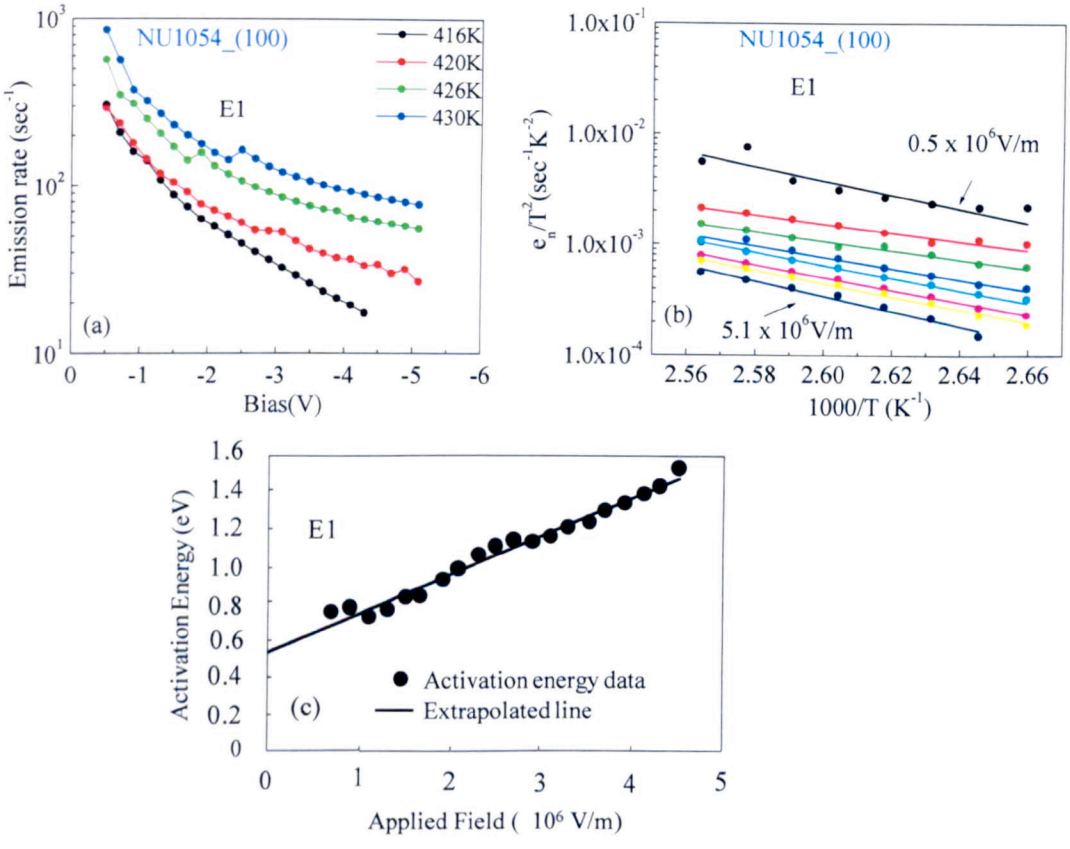

Figure 8.8: (a) Change of trap E1emission rate versus reverse bias, (b) Electric field dependent Arrhenius plot and (c) the change in the trap activation energy versus electric field.

8.1.7 DETERMINATION OF TRAP CONCENTRATION

The concentration of each trap shown in Table 8.1, is calculated using the amplitude of conventional DLTS signal as given by equation 4.32. The concentration of trap E1 is higher than the concentration of both EB1 and EB2 traps, which are found in (311)B MQW samples.

8.1.8 DISCUSSION

Our results demonstrate that trap E1 in (100) samples is strongly influenced by the external applied electric field. The broad feature that appears in the tail of this peak could be due to the existence of a closely spaced defect that cannot be resolved

because of its very small concentration. It was observed that the E1 emission rates in the 416K – 430 K temperature range [Figure 8.8 (a)] decrease as the junction reverse bias increases. This kind of behaviour is not compatible within the framework of the well-known Poole–Frenkel mechanism in which the emission rate is enhanced with the increase of the junction electric field [122]. However, this sort of trend of carrier emission as a junction of electric field has also been observed for DX-related centres in GaAs/AlGaAs MQWs structures by Jia et al. [123]. In addition, this effect was found to be dependent on the Al composition. Their results show that the decrease in the thermal emission rates with increasing field is biggest for the layers having medium Al compositions (Al: 30–40%) and smallest for the large Al content layers (Al: 50–60%). Our emission rates versus electrical field results in the MQWs samples that have 33% Al composition confirm their observations. Furthermore, Jia et al. [123] suggested that these changes in the emission and capture rates at different field strengths are due to the traps which are closely located and interacting with each other. It is important to add that if the electric field is not uniform in the depletion region of the Schottky junction, emission rates contribute non-uniformly from the depletion layer edge to metal-semiconductor interface [124]. The decrease in the carrier emission rate of E1 might be due to its interaction with some other traps such as the one that appears in the tail of its DLTS signal. The dependence of the emission rate on the electric field indicates that the trap can acquire a different net charge after the emission of the carriers from the trap. The trap E1 is electrically charged upon electron emission, and it becomes neutral by capturing an electron. This suggests that E1 should be a donor-like level. From the activation energy results [Figure 8.8 (c)], the exact location of the trap in the bandgap of the material is

difficult to identify. Extrapolation to zero field in Figure 8.8 (c) gives an activation energy of 0.47 eV which could correspond to the DX centre.

Since Laplace DLTS was able to resolve the broad peak in (311)B sample, thermal emission rates of both traps (EB1 and EB2) were analysed separately at different reverse biases and no such behaviour to what has been seen in the (100) sample has been observed. Thus, the emission rate signatures of EB1 and EB2 are electric field independent, and their charge state is neutral. The activation energies determined from their emission rates are 0.24 and 0.80 eV, respectively. The emission rate signatures of EB2 are comparable with those of E4 studied by Hayakaw et al. [6] in MBE-grown Si-doped AlGaAs layers. They have considered the influence of V/III ratio and assigned this trap to a complex that can include both group III vacancy (arsenic interstitial or antisite defect As_{III}) and arsenic vacancy (group III interstitial or III_{As}).

The capture cross-section (σ_n) results determined at different temperatures show that carrier capture rates are thermally activated for EB1[Figure 8.7 (b)], whereas the defect states E1 and EB2 show no such dependence upon temperature as depicted in Figure 8.6 (b) and Figure 8.7 (d), respectively. Although σ_n of E1 does not depend on the temperature, but due to the strong influence of the junction electric field, the apparent capture cross-section determined from the intercept of the Arrhenius plot of the emission rates shows large fluctuations in its value from 1.75×10^{-15} to 3.45×10^{-10} cm^2 as the field varies from zero to 4.7×10^6 V/m. The direct σ_n measurements of this trap at 380K and applied bias of -5 V give a value of 1.89×10^{-14} cm^2, which is much smaller than its apparent value 3.45×10^{-10} cm^2. The value of σ_n of trap EB2 [Figure 8.7] is found to be 1.48×10^{-15} cm^2. Figure 8.7 clearly shows the increase of σ_n from

1.04×10^{-18} to 2.58×10^{-18} cm^2 as the temperature increases from 372 to 392 K. The capture barrier energy calculated using relation (4.34) is 0.39 eV, which suggests a strong interaction of carriers with the lattice [6, 121].

8.1.9 CONCLUSION

We reported here the DLTS and LDLTS studies of MQWs samples grown by MBE on (100) and (311)B GaAs substrates. The activation energy of the dominant trap E1 observed in the sample grown on (100) is found to be dependent on the junction electrical field. The measured value for this trap varies from 0.47 to 1.3 eV as the junction electric field varies from zero to 4.7×10^6 V/m. Since the emission rates of E1 are dependent on electric field, it can be concluded that E1 is a donor-like level. On the other hand, EB1 and EB2 traps in (311)B showed no evidence of a field dependence, and therefore their charge states can be confirmed to be neutral. In addition, we observed that the capture cross-section of EB1 is thermally activated, while those of E1 and EB2 are not.

8.2 MQWs GROWN ON (100) GaAs SUBSTRATES USING DIFFERENT ARSENIC SPECIES, ARSENIC OVERPRESSURES AND GROWTH TEMPERATURES

MBE growth of III-V compound semiconductors, for example GaAs, AlAs and $Al_xGa_{1-x}As$ compounds, use two types of group V sources such as dimeric (As_2) or terameric (As_4) arsenic [12, 125]. As_4 and As_2 can be produced by subliming solid arsenic and by dissociating As_4 molecules using a special two-zone furnace, respectively. C.T Foxon [12] reported that for the growth of GaAs, the use of As_2 and As_4 results in different growth mechanisms of GaAs. It was found that the sticking coefficient of As_2 is proportional to the gallium flux, and approaches unity when the surface is gallium-rich. However, the maximum sticking coefficient of As_4 is only 0.5.

Kim et al. [125] investigated the effect of As_2 and As_4 during the MBE growth of $Al_{0.5}Ga_{0.5}As$ using reflection high-energy electron diffraction (RHEED). They found that the growth front morphology of $Al_{0.5}Ga_{0.5}As$ improves using As_4, whereas it degrades for As_2. In another study, Kim et al. [126] observed that the roughness of $Al_{0.5}Ga_{0.5}As$ layers increase faster for As_2 as compared to As_4. The difference in roughness employing two As species depends on the surface mobility of group III atoms.

Photoluminescence (PL) and RHEED techniques were utilised by Kim et al. [127] to study MBE grown $GaAs/Al_xGa_{1-x}As$ heterostructures. They observed that the PL spectra depended on the substrate temperature. The full width at half maximum of the main PL peak decreases with increasing the substrate temperature from 590°C to 635°C. This finding provides evidence that the optical and structural quality of the

heterostructures improve with increasing the growth temperature. The authors also concluded that at As-stabilized growth conditions the surface migration range of group III atoms depend on the substrate temperature; it increases with increasing growth temperature, and this results in a smooth growth front.

PL, RHEED and DLTS investigations by Moneey et al. [128] on MBE grown n-type AlGaAs layers using As_2 and As_4 did not reveal any prominent effect of As species on the defect levels. The findings of Hayakawa et al. [129] show that: (i) surface morphology is As dependent; a specular smooth surface is obtained using As_4 for high growth temperatures, (ii) PL intensity is independent of As species for low substrate temperatures; however, at high substrate temperature (> 650 °C) the PL efficiency of As_2 samples is lower than that of As_4. The authors suggested that the reason of degradation of the PL intensity could be due to the presence of defects.

In this thesis DLTS, Laplace DLTS and I-V-T techniques are employed for the detailed investigations of the presence of electrically active defects in GaAs/AlGaAs MQW samples grown at temperatures of 600, 650 and 675 °C using As_2 and As_4 species. The arsenic overpressures used for the growth of these samples depended on the growth temperature. The growth details are given in section (5.1.6).

In summary, it is observed that the current flow through the devices is proportional to the concentration of DX center. In addition, the overall concentration of defects is less in the samples grown using As_2 as compared those grown using As_4 species. Furthermore, it is also found that the concentration of arsenic-vacancy related trap decreases with increasing growth temperature.

8.2.1 EXPERIMENTAL RESULTS AND ANALYSIS

8.2.2 I-V AND C-V CHARACTERISTICS

I-V measurements were performed using the procedure discussed in Chapter 5. The selected Schottky diodes investigated by DLTS and Laplace DLTS are those showing the lowest reverse current. Typical I-V characteristics are illustrated in Figure 8.9 with reverse currents < 1 μA at -5V.

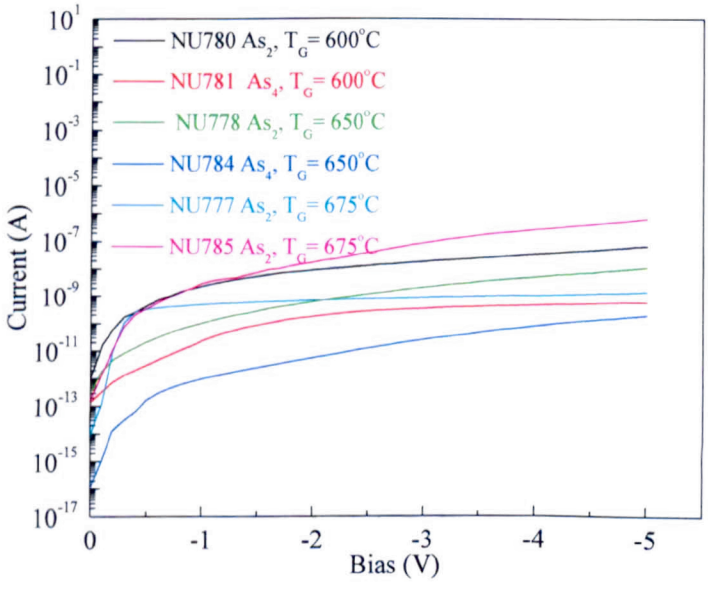

Figure 8.9: Current-Voltage (I-V) characteristics of Schottky diodes processed on MQW samples grown on (100) GaAs plane using As_2 and As_4 at different growth temperatures.

The C–V characteristics of the diodes were measured by following the experimental method outlined in Chapter 5, and background doping concentration was calculated from the slope of $1/C^2$ versus reverse bias. Typical relationship between $1/C^2$ and reverse bias is depicted in Figure 8.10 for the sample grown at 600°C using As_2 (NU780). The deduced doping concentration was [NU780] = 2.25×10^{16} cm^{-3}, [NU781] = 4.52×10^{16} cm^{-3}, [NU778] = 2.12×10^{16} cm^{-3}, [NU784] = $1.15 \times 10^{16}cm^{-}$

^{3}, [NU777] = 1.77 × 10^{16} cm^{-3}, and [NU785] = 3.66 × 10^{16} cm^{-3}. These values are used for the determination of the concentration of the detected traps.

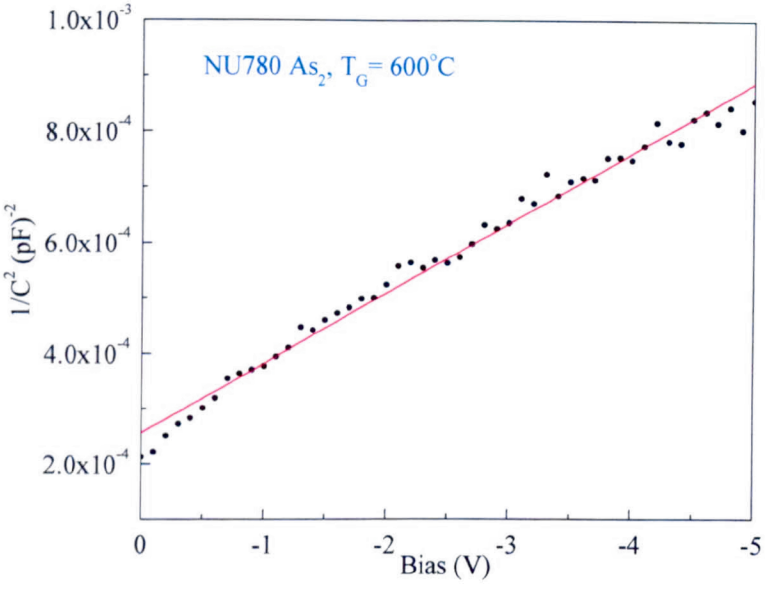

Figure 8.10: $1/C^2$ versus reverse bias of MQW sample grown on (100) GaAs plane at 600°C using As_2.

8.2.3 DLTS DATA

The samples were mounted in a closed-cycle helium-cryostat and cooled down to a temperature of 10 K in a similar way as for the samples used in Chapters 6 and 7. The temperature was then ramped to ~ 400K at the rate of 2K/min and the DLTS signal was recorded as shown in Figure 8.11 (a) NU780, (b) NU781, (c) NU778, (d) NU784, (e) NU777 and (f) NU785. The measurement parameters used are; a rate window of 50 Hz, quiescent reverse bias V_R = –5 V, filling pulse V_p = – 0.5 V and filling pulse duration t_p = 1 ms which was sufficient to fill completely the traps with carriers.

The DLTS measurements reveal that three defects are detected in each sample grown with As_2 at different growth temperatures (600°C, 650°C and 675°C),

whereas the number of traps for the samples grown with As_4 at 600°C and 650°C is one, and three for 675°C. For convenience, the defects are labelled as As_2T_1E, As_4T_1E, As_2T_2E, As_4T_2E, As_2T_3E and As_4T_3E in NU780, NU781, NU778, NU784, NU777 and NU785, respectively; and T_1 = 600°C, T_2 = 650°C and T_3 = 675°C. The digits, 1, 2, 3 etc with E correspond to a particular trap in each sample.

It is worth pointing out that there are no traps detected in NU784 within the temperature range ~10K to ~400K; only a single DLTS peak is observed above 400K.

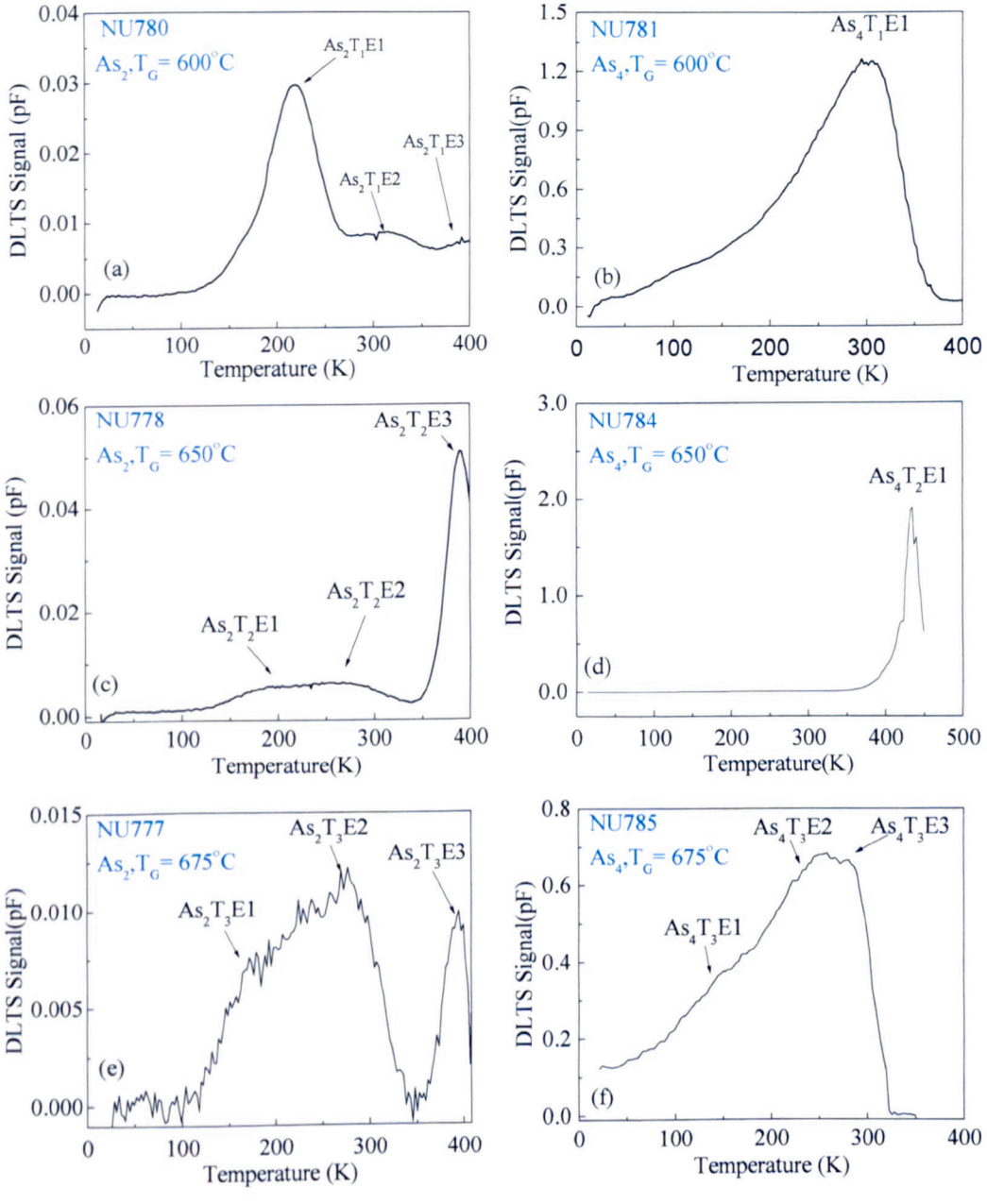

Figure 8.11: Conventional DLTS scans for the MQW samples grown on (100) GaAs substrate with As_2 at growth temperatures of 600 °C, 650 °C and 675 °C shown in (a), (c) and (e), respectively (b), (d) and (f) show the spectra for the samples grown with As_4 at growth temperatures of 600 °C, 650 °C and 675 °C, respectively.

8.2.4 DETERMINATION OF ACTIVATION ENERGIES OF TRAP

In order to find out the activation energy of each defect level, the emission rates were measured using high resolution Laplace DLTS technique following the procedure described in Chapter 4. The temperature corrected emission rates of the traps are

plotted as $\ln(e_n/T^2)$ versus 1000/T [Figure 8.12]. As explained in section 4.2.3 the slope and intercept of these plots are used to determine the activation energies and the apparent capture cross-sections of the traps as displayed in Table 8.2.

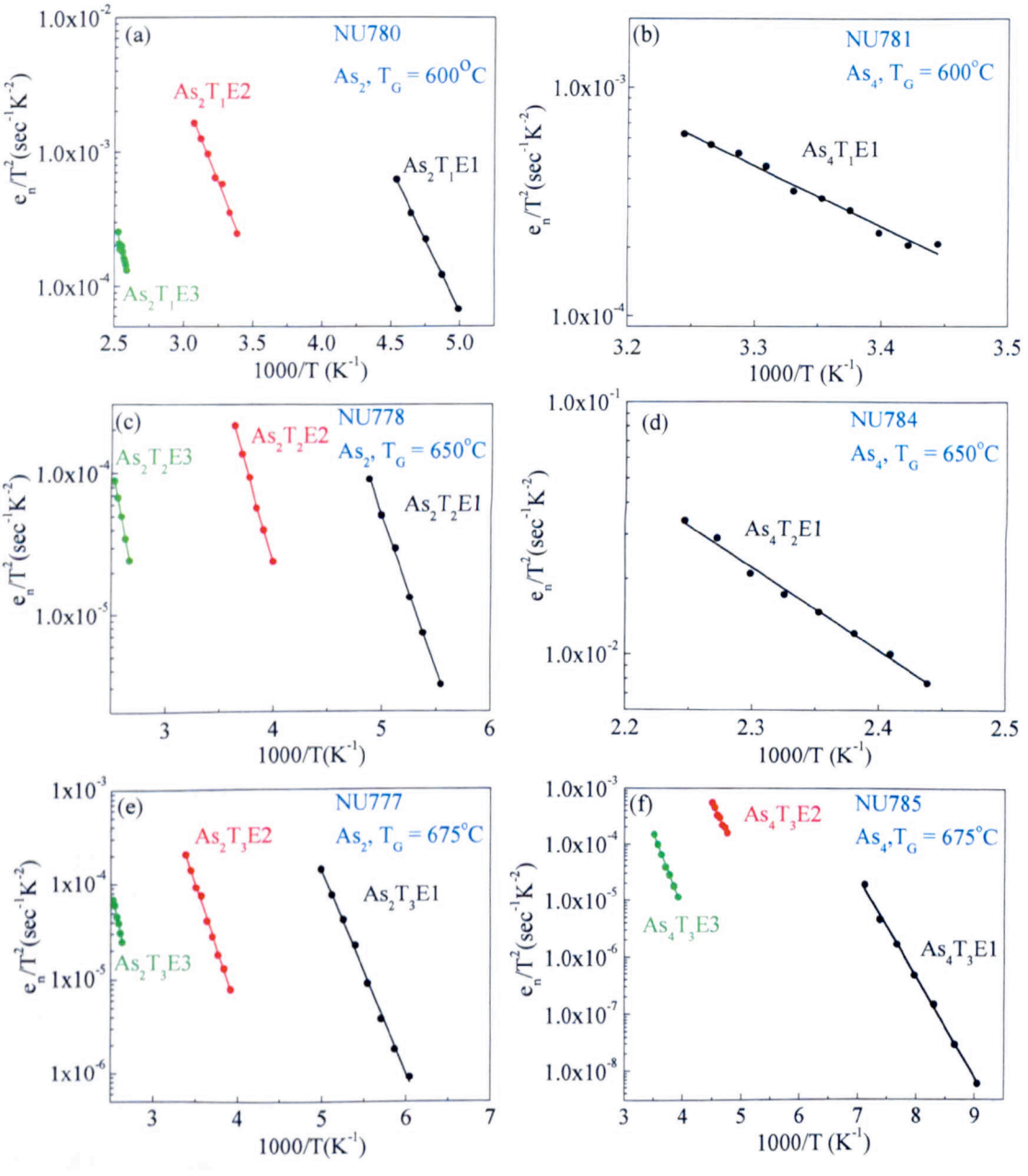

Figure 8.12: Arrhenius plots of the temperature corrected emission rates of each defect level in the MQW samples; (a) NU780, (b) NU781, (c) NU778, (d) NU784, (e) NU777 and (f) NU785 are shown.

Table 8.2: Trap activation energy and apparent capture cross-section calculated from Laplace DLTS data and concentration from conventional DLTS peak amplitude, respectively.

Sample Name	Sample Identity	Trap	Activation energy (eV)	Capture Cross-section (cm^2)	Concentration (cm^{-3})
NU780	As_2 $T_G = 600°C$	As_2T_1E1	0.421±0.003	1.79×10^{-14}	3.91×10^{13}
		As_2T_1E2	0.519±0.007	1.26×10^{-15}	1.12×10^{13}
		As_2T_1E3	0.824±0.005	5.11×10^{-14}	1.02×10^{13}
NU781	As_4 $T_G = 600°C$	As_4T_1E1	0.529±0.005	1.94×10^{-15}	4.22×10^{14}
NU778	As_2 $T_G = 650°C$	As_2T_2E1	0.431±0.007	2.34×10^{-14}	4.69×10^{12}
		As_2T_2E2	0.518±0.003	4.21×10^{-15}	5.33×10^{12}
		As_2T_2E3	0.826±0.003	2.79×10^{-14}	3.69×10^{12}
NU784	As_4 $T_G = 650°C$	As_4T_2E1	0.656±0.004	5.99×10^{-15}	4.48×10^{14}
NU777	As_2 $T_G = 675°C$	As_2T_3E1	0.422±0.010	3.91×10^{-14}	2.22×10^{12}
		As_2T_3E2	0.529±0.006	1.49×10^{-15}	3.45×10^{12}
		As_2T_3E3	0.836±0.003	2.07×10^{-14}	2.81×10^{12}
NU785	As_4 $T_G = 675°C$	As_4T_3E1	0.352±0.003	4.44×10^{-13}	9.57×10^{13}
		As_4T_3E2	0.421±0.010	1.27×10^{-14}	1.73×10^{14}
		As_4T_3E3	0.532±0.005	2.39×10^{-15}	1.69×10^{14}

8.2.5 BEHAVIOUR TRAP CONCENTRATION VERSUS DEPTH

In order to determine the defects depth concentration profile, the concentration are obtained by integrating the Laplace DLTS peaks following the procedure described for Be-doped AlGaAs layers in Chapter 7, and the depth was calculated from C-V measurements at room temperature. In order to compare the effects of As_2 and As_4, and growth temperatures, only the concentration-depth profiles of traps of similar activation energies, and possibly of similar origins, are plotted in Figure 8.13; (a) $E_T \sim 0.42$ eV, (b) $E_T \sim 0.52$ eV, (c) $E_T \sim 0.82$ eV and (d) some new traps $E_T \sim 0.352$ eV and $E_T \sim 0.656$ eV.

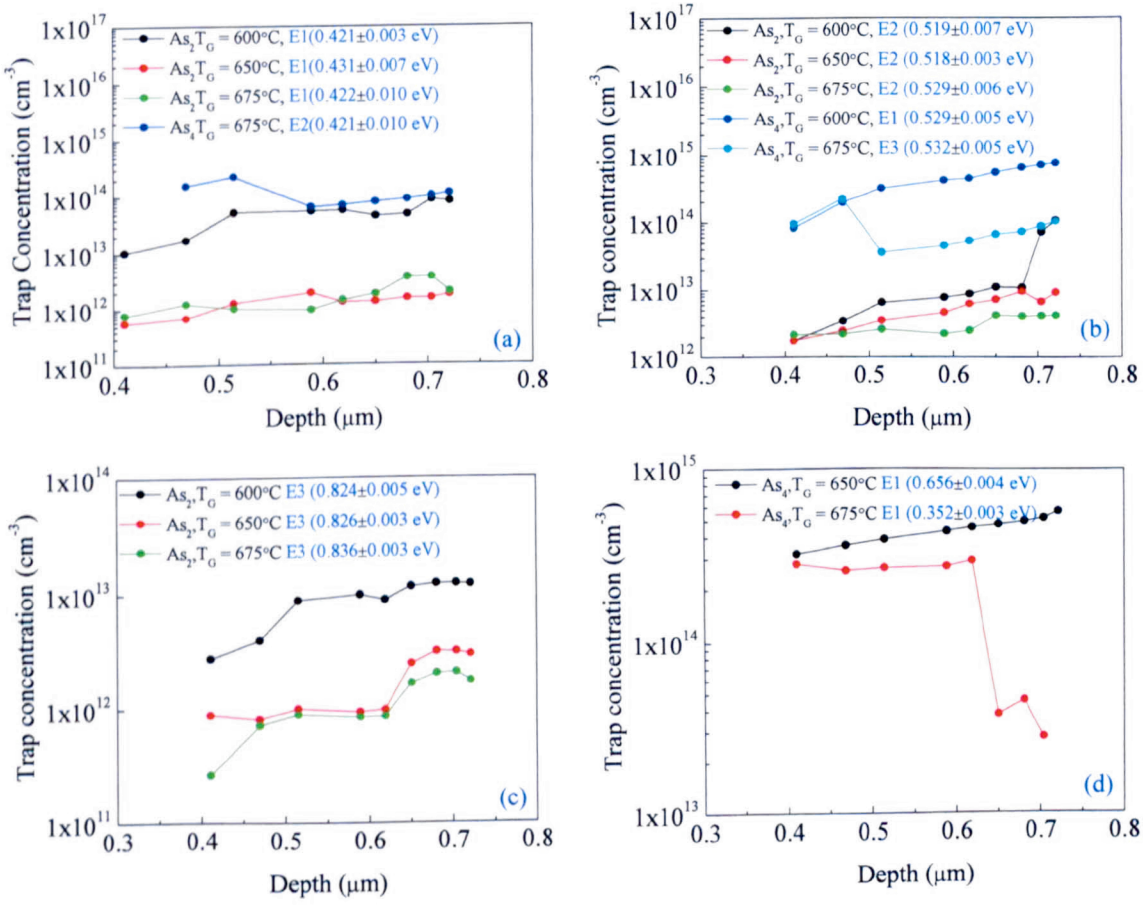

Figure 8.13: Concentration-depth profiles of the traps found in the MQW structures grown with As_2 and As_4 for different growth temperatures.

8.2.6 I-V-T CHARACTERISTICS

According to Shockley-Read-Hall (SRH) theory some deep level defects, called generation-recombination centers, can actively contribute to the reverse current as it was observed in Chemical Beam Epitaxy (CBE) grown GaAsN samples [130]. The carriers generated by these centers are swept out of the space charge region because of the presence of electric field within the junction, and the motion of these carriers produces an electric current through the devices.

In order to find out the activation energy of the dominant center, Current-Voltage characteristics were measured at different temperatures ranging from 20K to 400K. The I-V-T data at constant reverse bias is analysed by using equation

$$I_d(T) = I_\infty \exp\left(\frac{-\Delta E}{kT}\right) \qquad 8.1$$

where I_d is the reverse current through the diode at a certain reverse bias, T is temperature, I_∞ is saturation current, ΔE is thermal activation energy and k is Boltzmann constant.

The reverse current at a constant reverse bias is plotted in Figure 8.14. The activation energy of the defect level is obtained from the slope of $\ln(I_R)$ versus 1000/T using equation 8.1.

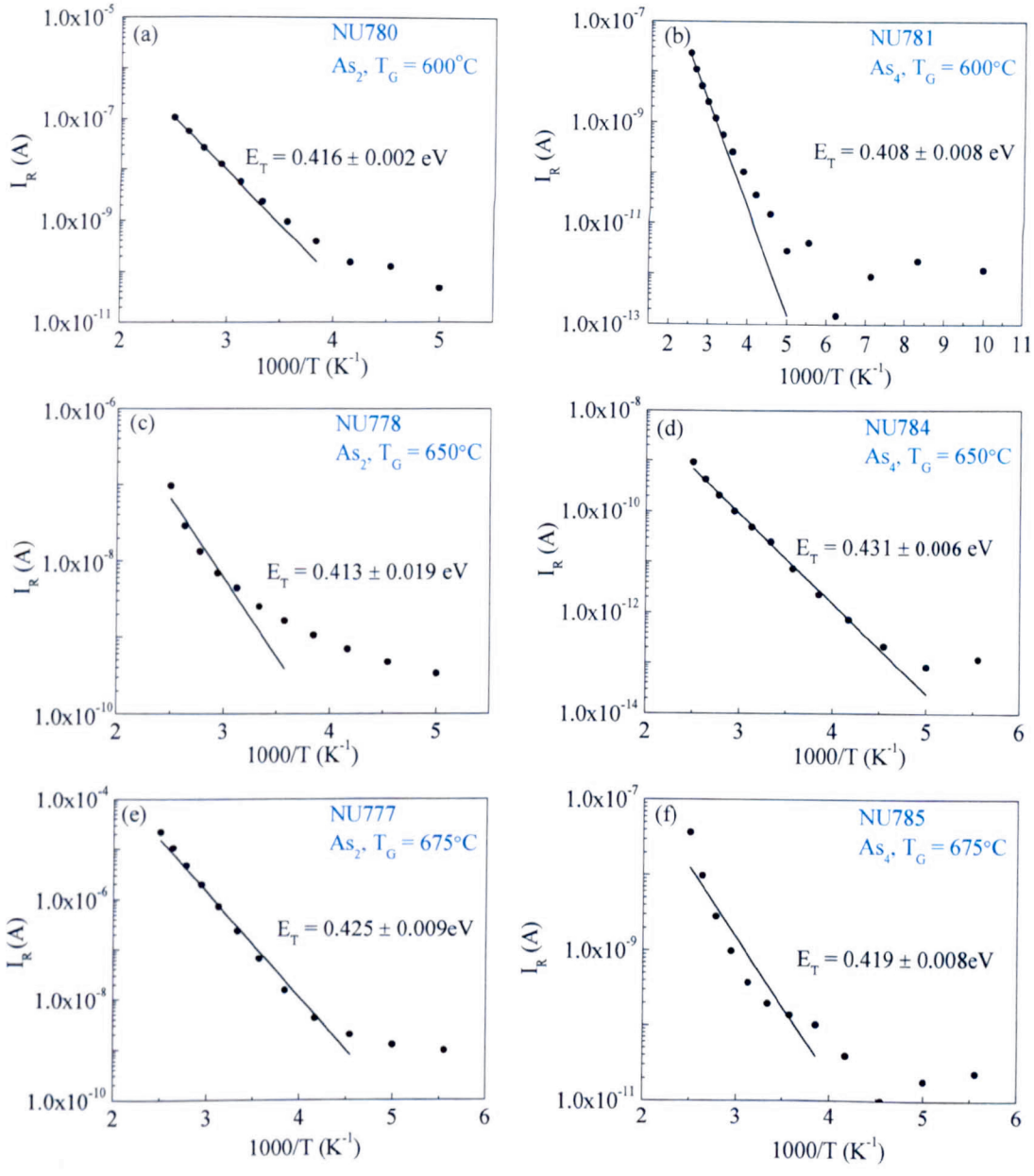

Figure 8.14: Arrhenius plots of Current-Voltage-Temperature (I-V-T) characteristics of all the samples.

8.2.7 DISCUSSION

In order to shed some light on the possible origin of the traps, the activation energy (E_T) of each defect level is compared with published literature. It is found that E_T of the traps As_2T_1E1 (0.421 ± 0.003 eV), As_2T_2E1 (0.431 ± 0.007 eV), As_2T_3E1 (0.422 ± 0.010 eV) and As_4T_3E2 (0.421 ± 0.010 eV); and As_2T_1E2 (0.519 ± 0.007 eV), As_4T_1E1 (0.529 ± 0.005 eV), As_2T_2E2 (0.518 ± 0.003 eV), As_2T_3E2 (0.529 ± 0.006

eV), and As_4T_3E3 (0.532 ± 0.005 eV) are comparable to levels P3 and P4 [131], respectively, detected in MBE grown GaAs/AlGaAs heterostructures. The structures of Qurashi et al. [131] were grown using As_4 only. The authors attributed both P3 and P4 to arsenic-vacancy (V_{As}) related point defects in the AlGaAs layers. In case of As_2 samples, we observed that the concentration of the deep level at ~0.42 eV level is more sensitive to growth temperature, i.e. it rapidly decreases from 3.91×10^{13} cm^{-3} at 600 °C to 2.22×10^{12} cm^{-3} at 675 °C [Figure 8.15], whereas for level ~0.52 eV it decreases from 1.12×10^{13} cm^{-3} at 600°C to 3.45×10^{12} cm^{-3} at 675°C in As_2 samples, and from 4.22×10^{14} cm^{-3} at 600°C to 1.69×10^{14} cm^{-3} at 675°C for As_4 samples. It is worth noting that the observed concentration of ~0.52 eV level is higher in As_4 samples than in As_2 samples. Moreover, the concentration of ~0.52 eV level in As_4 samples are in agreement to the concentration of P4 [131].

The observation of the lower concentration of trap ~0.52 eV (tentatively assigned to V_{As} related point defect) in As_2 samples as compared to As_4 samples, is probably related to the higher sticking coefficient of As_2 than of As_4 [12]. However, the rate of decrease with growth temperature is more pronounced in As_2 than in As_4 samples [see Figure 8.15 (a)]. It is worth pointing out that in order to compensate for the arsenic loss with substrate temperature, the arsenic overpressure was increased with the growth temperature for all As_2 and As_4 samples (see samples details in Chapter 5). Although the samples were grown at different arsenic overpressures and temperatures, it is assumed that the net number of arsenic atoms contributing to the growth of the epitaxial layers is the same. Based on this assumption, it is expected that the rate of decrease of the trap concentration should be similar. Our findings do not support this argument. This effect can be explained by considering the sticking coefficients of As_2 and As_4; As_2 has a higher sticking coefficient than As_4, and this

can account for the lower trap (~0.52 eV) concentrations for the higher arsenic overpressures and substrate temperatures. In order to investigate the nature of the 0.52 eV trap and its relation to the V_{As} related point defects, it is proposed for future work to grow several samples at constant growth temperatures with different arsenic overpressures.

The emission rates of traps As_2T_1E3 (0.824 ± 0.005 eV), As_2T_2E3 (0.826 ± 0.003 eV) and As_2T_3E3 (0.836 ± 0.003 eV) are comparable to those of level C (0.82 eV) in MOCVD grown GaAs/AlGaAs superlattice [132, 133] and in MOCVD epitaxial AlGaAs layers [133]. The authors attributed this level to EL2 defect (Ga vacancy), but there are contradicting suggestions about the origin of EL2 defect. For example it suggested that EL2 is a complex between As_{Ga} + X [134], where X might be a double-vacancy complex with As interstitial. Kaminska and his co-workers, however, suggested that EL2 could be an isolated arsenic antisite defect [135], or an arsenic antisite defect surrounded by four arsenic atoms [136]. It is important to note that there are no reports for the existence of EL2 defect in MBE epitaxial GaAs layers grown in the temperature range similar to the one used for the growth of the samples investigated this part of the thesis. In addition, it is well known in the literature that the emission rates of EL2 level are electric field dependent. However, our studies showed no evidence for such electric field dependence. It is, therefore, concluded that this level is not exactly the same as the famous EL2 electron trap, but due to the similar activation energy it can be said that this is an EL2-like defect found in MBE grown GaAs/AlGaAs MQW structures. From Figure 8.15 (b) one can easily observe that the concentration of this defect level follow nearly similar trend with growth temperature as that of level having activation energy of ~0.52 eV. The

concentration-depth profile [Figure 8.13 (c)] shows that the concentration of this level is not uniform with depth.

In addition, to the above discussed traps, two new traps As_4T_2E1 (0.656 ± 0.004 eV) and As_4T_3E1 (0.352 ± 0.003 eV) are found in As_4 samples grown at temperatures 650 °C and 675 °C, respectively. Both traps did not appear in any of the samples grown under As_2 and As_4 conditions at 600 °C. Although the origin of these levels is still unknown, their emission rates are insensitive to the junction electric filed, and therefore can be assigned to neutral defect levels. Figure 8.13 (d) shows that the concentration of As_4T_2E1 increases uniformly from 3.22×10^{14} cm^{-3} at 0.41μm to 5.70×10^{14} cm^{-3} at 0.72μm, whereas the concentration of As_4T_3E1 is almost constant ~ 2.79×10^{14} cm^{-3} from 0.41 μm to 0.62 μm and then suddenly drops to 2.77×10^{13} cm^{-3} at 0.7 μm.

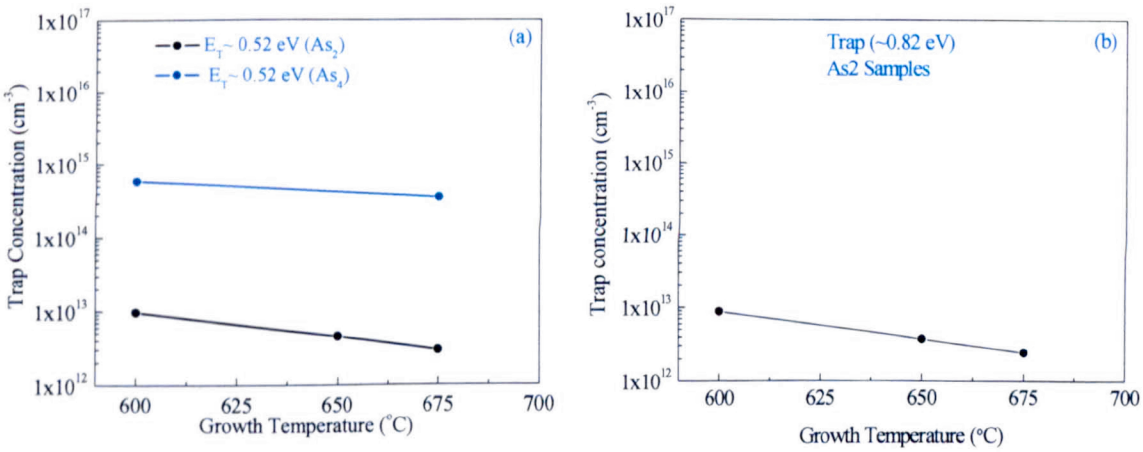

Figure 8.15: Effect of growth temperature on the concentration of common traps (0.52 eV) in GaAs/AlGaAs MQW structures MBE grown using As_2 and As_4 species

The activation energy of the recombination center deduced from I-V-T measurements [Figure 8.14] confirms that the deep level with activation energy ~0.42 eV is the dominant trap in all samples. Although DLTS measurements also reveal other deep levels with higher activation energies, i.e. ~0.52 eV, ~0.656 eV and

~0.82 eV, the deep level at ~0.42 eV is the main trap that contribute to the reverse current. It is worth noting that higher concentration of recombination centers results in higher reverse currents [Figure 8.9]. From Table 8.2 it can also be seen that the ~0.42 eV level has the highest apparent capture cross-section.

8.2.8 CONCLUSION

In summary, a set of six MBE grown GaAs/$Al_{0.33}Ga_{0.67}As$ MQW samples were investigated using I-V-T, DLTS and Laplace DLTS techniques. It is observed that the reverse current flow through these devices is directly related to the concentration of the main recombination center, whose activation energy of ~0.42 eV calculated from I-V-T measurements is in close agreement with the activation energy deduced from Laplace DLTS measurements. The undetected recombination center DLTS peak in NU781 (As_4, T_G = 600°C) and NU784 (As_4, T_G = 600°C) is probably due to its very low trap concentration. This is also further confirmed by the very low leakage current observed in these two devices.

In addition, the main findings of this part of the thesis are summarised below, where T_1 (600°C), T_2 (650°C) and T_3 (675°C), and As_2 and As_4 refer to the growth temperature and the arsenic species, respectively, used to grow each set of samples.

(a) $As_2T_1E_1$, $As_2T_2E_1$, $As_2T_3E_1$ and $As_4T_3E_2$ have an activation energy similar to that of the defect level P3 identified as an arsenic-vacancy (V_{As}) defect.

(b) The activation energies of $As_2T_1E_2$, $As_4T_1E_1$, $As_2T_2E_2$, $As_2T_3E_2$ and $As_4T_3E_3$ levels are similar to the defect level P4 whose origin is related to arsenic-vacancy (V_{As}).

(c) The concentration of V_{As} defects decreases with increasing growth temperature. in samples grown with As_2 and As_4.

(d) V_{As} (P3) behaves as a generation-recombination centre.

(e) Levels $As_2T_2E_3$, $As_2T_3E_3$, $As_4T_2E_1$ and $As_4T_3E_1$ are newly detected in Si-doped AlGaAs. The origin of these defects is still not clear at this stage.

CHAPTER 9

DEEP LEVEL DEFECTS IN 2DEG AND HEMT DEVICES

The purpose of this chapter is to characterise and compare deep level defects in commercially grown MBE High Electron Mobility Transistors (HEMTs) and GaAs/AlGaAs Two Dimensional Electron Gas (2DEG) devices grown in our in-house MBE system. The main reason of investigating the HEMTs was to find out why two batches, grown within six months interval under the same experimental conditions, exhibited different frequency responses. The 2DEG samples details are given in Chapter 5, whereas, due to confidential agreement with the commercial company, the HEMT layer structure is not disclosed here. The deep levels were characterised by means of electrical techniques such as DLTS, Laplace DLTS and Current-Voltage-Temperature (I-V-T) measurements.

9.1 INTRODUCTION

GaAs/AlGaAs based-heterostructures such as 2DEG and HEMT devices have got paramount applications in satellite communications [137], and high power switching devices [138].

The heterojunction devices are formed by two different types of semiconductors having different energy gaps, in which the high energy gap material (e.g. AlGaAs) is Si-doped and the low energy gap (e.g. GaAs) is undoped. When these two materials

are brought into physical contact, the carriers (electrons) from doped AlGaAs diffuse to undoped GaAs and accumulate at the interface on the GaAs side and posses 2D motion. These types of devices, where the electrons in GaAs are separated from their parent donors in AlGaAs, are called Two Dimensional Electron Gases (2DEG). This technique of doping is termed modulation-doping. It is well-known that impurities in semiconductor materials dramatically affect the charge carrier mobility. In order to reduce ionised impurity scattering and hence increase the electrons mobility [18, 139], 2DEG-based devices are employed where the electrons move in pure GaAs away from the ionised doping impurities which are in AlGaAs.

Historically, L. Esaki and R. Tsu in 1969 introduced the concept of charge accumulation at heterojunction interface and its importance for the device applications. Practically, the growth of high quality heterostructures, i.e. quantum wells and superlattices became possible after the development of MBE and MOCVD epitaxial growth technologies in 1970s. The first demonstration of mobility enhancement in modulation-doped GaAs/AlGaAs superlattice was presented in 1978 and similar effect was observed in AlGaAs/GaAs single heterojunction in 1979. The above studies were carried out on two terminal devices without a third terminal control gate used in field effect transistors. It was not until 1980 when Mimura et al. demonstrated the first three terminal transistor device based on single heterostructure. The device was named High Electron Mobility Transistor (HEMT) [18].

Carrier mobility degradation, which reduces the efficiency of devices, is believed to cause problems for example during the operation of high speed switching devices. The reduction in mobility occurs mainly due to (i) phonon scattering, dominant at

high temperatures (ii) Coulomb interaction that takes place between ionised donor atoms and charge carriers, and (iii) impurity scattering, dominant at low temperatures.

In order to provide feedback knowledge regarding the existence and characteristics of impurity centers, i.e. electrically active defect levels that play major role in carrier mobility degradation, Conventional DLTS, Laplace DLTS and I-V-T measurements were employed to investigate defect levels in MBE grown 2DEG and commercially grown HEMT devices.

DLTS and Laplace DLTS results confirm the existence of a common defect level (~0.36 eV) in 2DEG and HEMT devices. Its concentration is maximum in the 2DEG sample (NU1280) which has the maximum Si-doping of $1.33 \times 10^{18}cm^{-3}$ in the AlGaAs layer, whereas comparing HEMT1536 and HEMT1541 the concentration of ~0.36 eV level is less in HEMT1536.

9.2 EXPERIMENTAL RESULTS AND ANALYSIS

9.2.1 I-V AND C-V CHARACTERISTICS

Laplace DLTS measurements, the current-voltage (I-V) characteristics of each device were measured at room temperature (300K). The devices having low reverse current were selected for further investigations. Typical I-V characteristics are shown Figure 9.1. It is observed that the maximum reverse current of ~10 μA at -1V is obtained for NU1280, the highly doped ($n = 1.33 \times 10^{18}$ cm^{-3}) 2DEG sample. Whereas, very low reverse current (< μA) is obtained for the other devices demonstrating their suitability for defect characterisation. All the devices have very

low reverse current and are most suitable for DLTS and Laplace DLTS measurements.

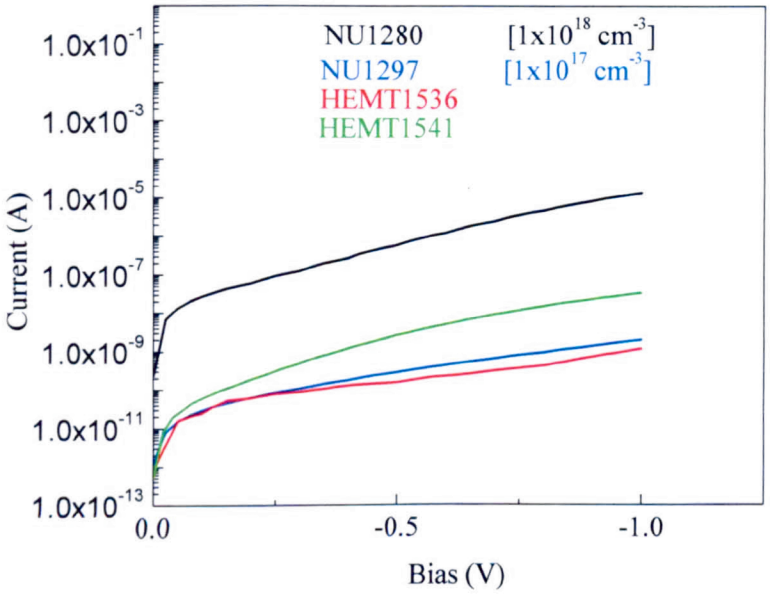

Figure 9.1: I-V characteristics of 2DEG and HEMT devices.

In order to determine the background doping concentration (N_d) of each sample, Capacitance-Voltage (C-V) measurements were carried out at room temperature (300K) for each device and the C-V data was analysed using equation 4.8. Figure 9.2 represents the C-V data of one of the samples (NU1280) in the form of $1/C^2$ versus V_R. The deduced value of N_d will be used to calculate the trap concentration.

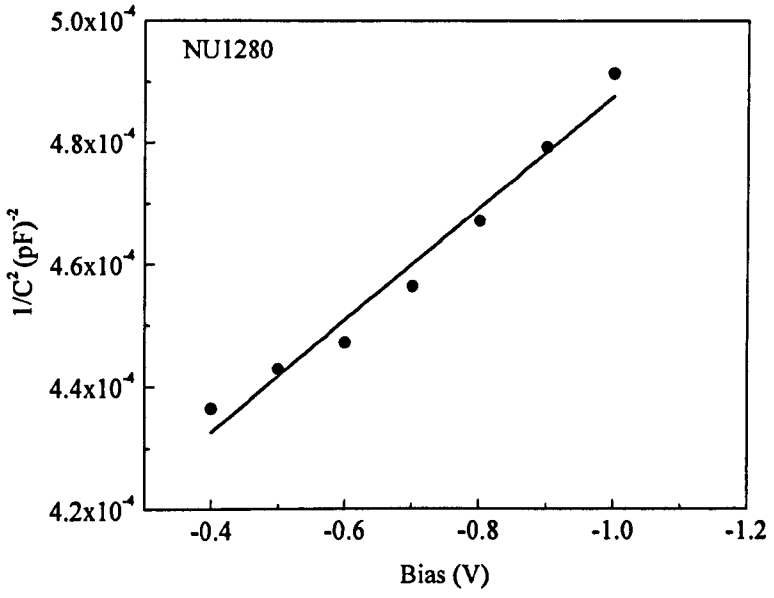

Figure 9.2: $1/C^2$ versus reverse bias V characteristics of AlGaAs/GaAs 2DEG device.

9.2.2 DLTS DATA

The DLTS measurements were carried out using similar procedure as explained in section 5.2.3. The DLTS signals for samples NU1280, NU1297, HEMT1536 and HEMT1541 are shown in Figure 9.3 (a) – (d), respectively. The measurement parameters used are: a rate window of 50 Hz, quiescent reverse bias $V_R = -1$ V, filling pulse $V_p = 0$V and a filling pulse duration t_p of 1 ms was sufficient to fill the traps with carriers.

Figure 9.3 (a) and (b) show that NU1280 and NU1297 2DEG samples grown on (100) GaAs plane with doping concentrations of 1.33×10^{18} cm^{-3} and 1×10^{17} cm^{-3}, reveal one and three electron traps, respectively. Whereas, only one trap is detected in each commercially grown HEMT1536 and HEMT1541 samples [Figure 9.3 (c) and (d)]. For convenience, electron traps in 2DEG samples are labelled as NA1 for NU1280 and NB1, NB2 and NB3 for NU1297. Similarly, CA1 and CB1 are detected in commercially grown HEMT1536 and HEMT1541, respectively.

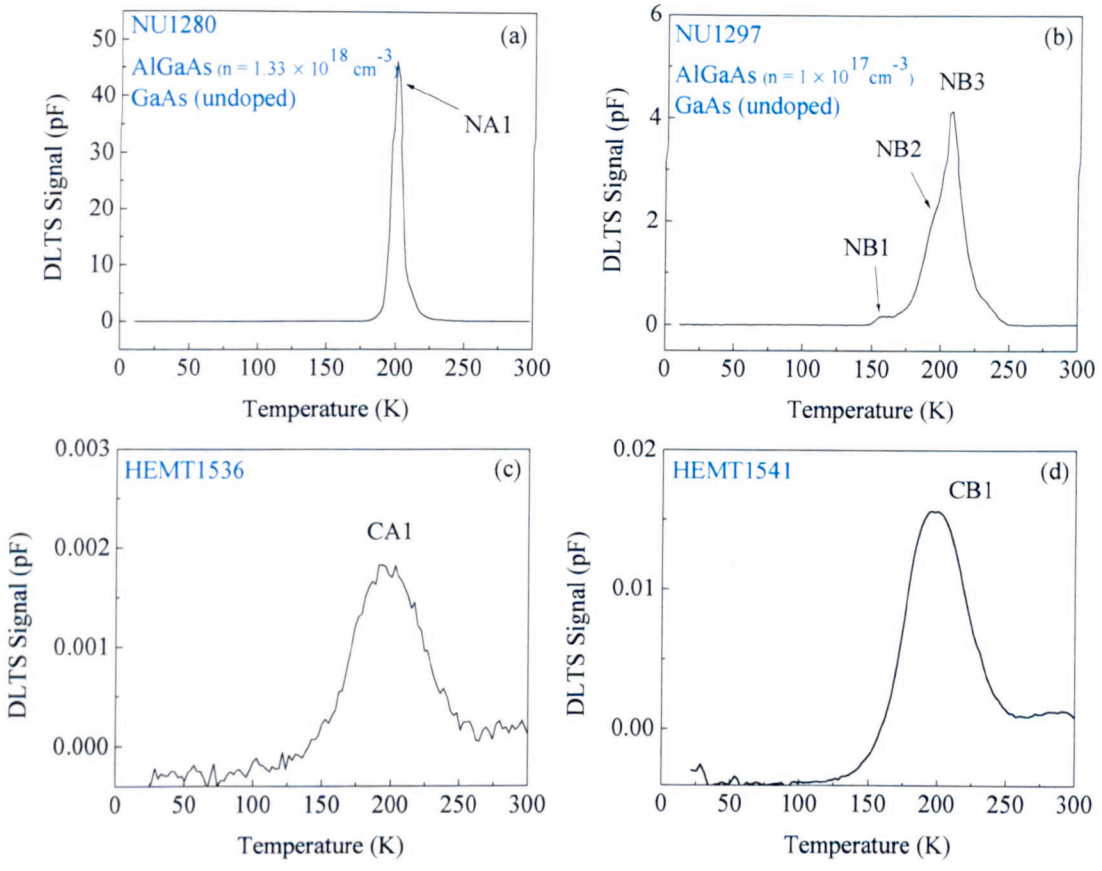

Figure 9.3: Conventional DLTS scans for 2DEG and commercially grown HEMT devices (a) NU1280, (b) NU1297, (c) HEMT1536 and (d) HEMT1541.

9.2.3 DETERMINATION OF ACTIVATION ENERGIES OF TRAPS

In order to find out the activation energy of the defects in 2DEG and HEMT samples, the emission rates of each trap were measured using High Resolution Laplace DLTS technique.

The temperature corrected emission rates of the traps are plotted in ln (e_n/T^2) versus 1000/T in Arrhenius plots [Figure 9.4]. As explained in section 4.2.3 the slope and intercept of these plots are used to determine the activation energies and apparent capture cross-section of these defects. These are displayed in Table 9.1.

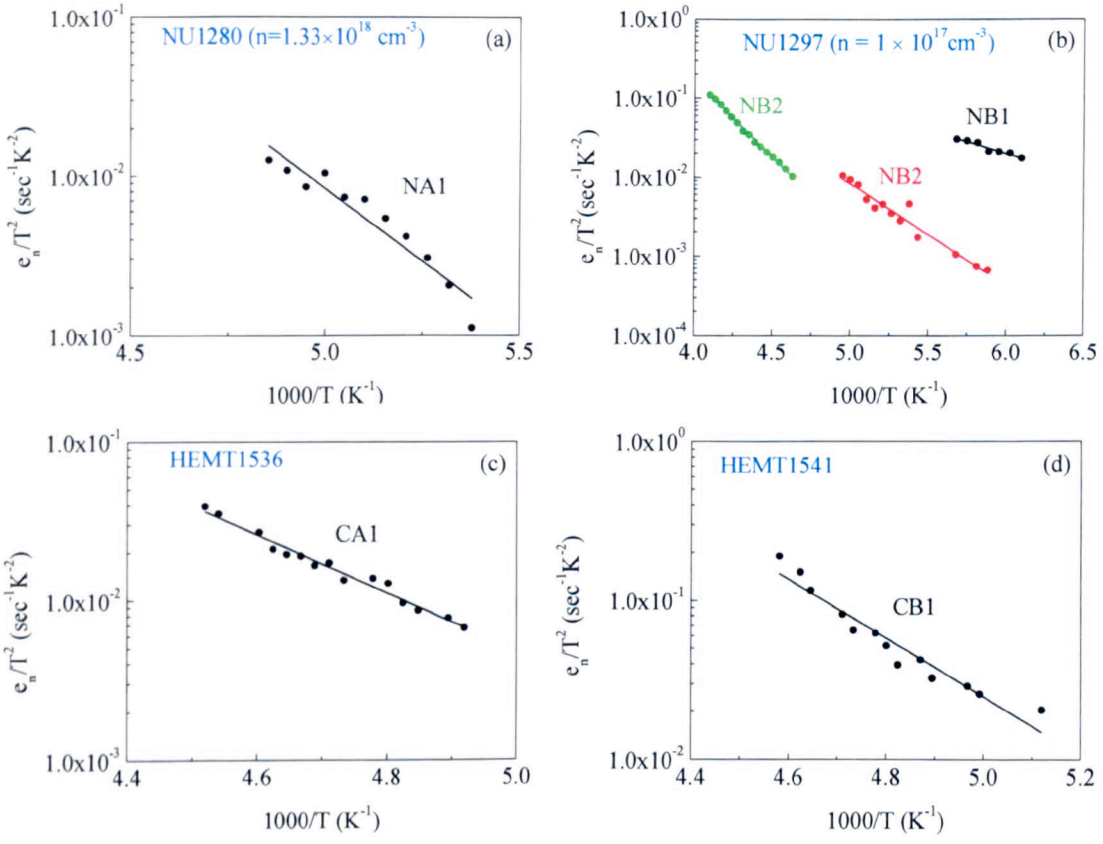

Figure 9.4: Arrhenius plots of the temperature corrected emission rates of the deep levels for (a) NU1280, (b) NU1297, (c) HEMT1536 and (d) HEMT1541.

Table 9.1: Trap parameters calculated from DLTS and Laplace DLTS measurements.

Sample ID	Trap	Activation energy (eV)	Capture Cross-section (cm^2)	Concentration (cm^{-3})
NU1280	NA1	0.371 ± 0.045	1.31×10^{-15}	2.04×10^{18}
NU1297	NB1	0.117 ± 0.005	7.10×10^{-21}	7.51×10^{14}
	NB2	0.254 ± 0.022	2.18×10^{-18}	1.06×10^{16}
	NB3	0.382 ± 0.002	8.31×10^{-16}	1.84×10^{16}
HEMT1536	CA1	0.362 ± 0.007	6.59×10^{-16}	1.03×10^{15}
HEMT1541	CB1	0.366 ± 0.016	4.39×10^{-15}	6.22×10^{15}

9.2.4 DETERMINATION OF TRAP CAPTURE CROSS-SECTION

The apparent capture cross-section of defects can be determined from the intercept of the plot $\ln(e_n/T^2)$ versus 1000/T, as shown in Table 9.1, assuming that it is temperature independent. For certain deep centers this is not the case, and therefore, the direct measurement of trap capture cross-section has been performed using the filling pulse method as explained in Chapter 4.

Figure 9.5 (a) and (b) illustrates the capture cross-section data of level NA1 in sample NU1280. It is clearly shown that the capture cross-section of this level is temperature insensitive. Similar behaviour is observed for all the other traps detected 2DEG (Figures 9.5 and 9.6) and HEMT (Figure 9.7) samples.

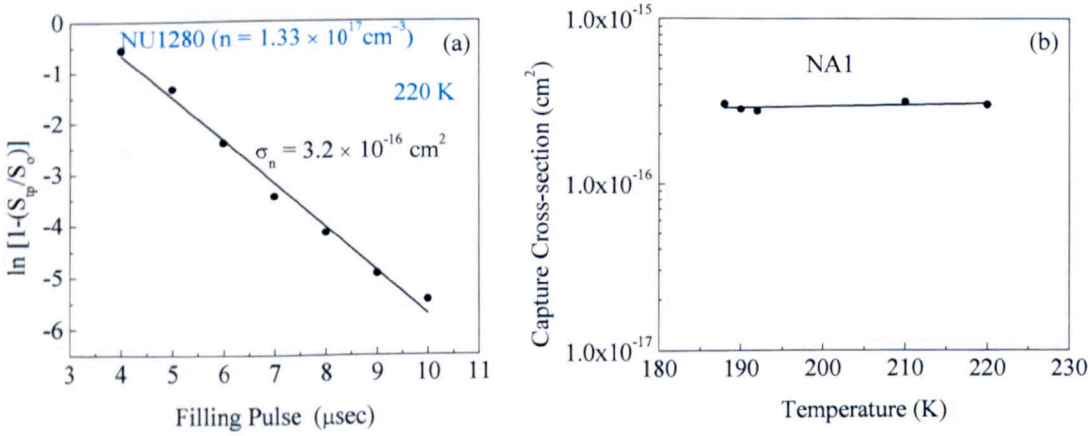

Figure 9.5: (a) Direct capture cross-section measurement data of trap NA1, (b) effect of temperature on the capture cross-section.

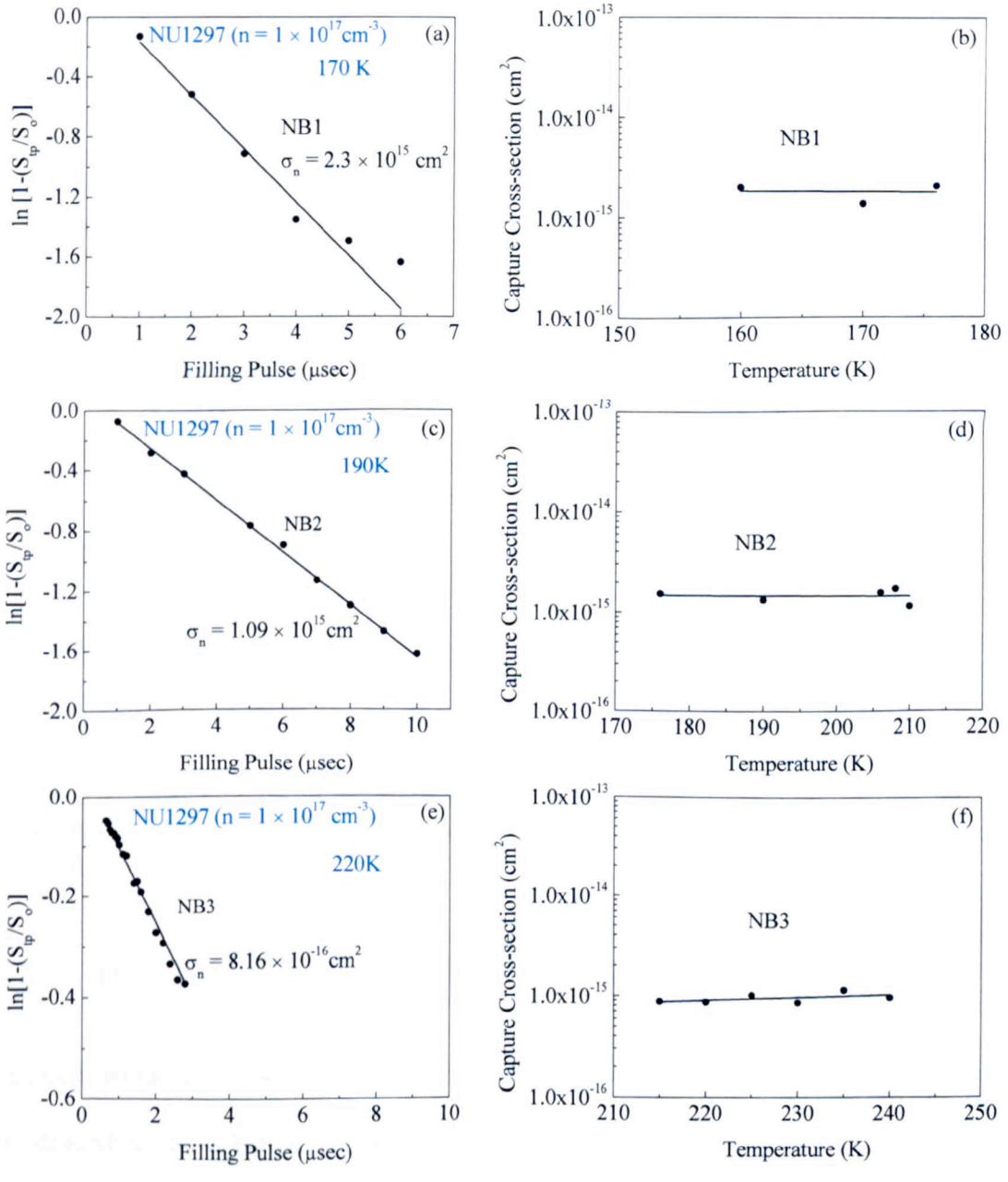

Figure 9.6: Direct capture cross-section measurement data of traps (a) NB1, (c) NB2 and (e) NB3; and the effect of temperature on respective capture cross-section (b) NB1, (d) NB2 and (f) NB3.

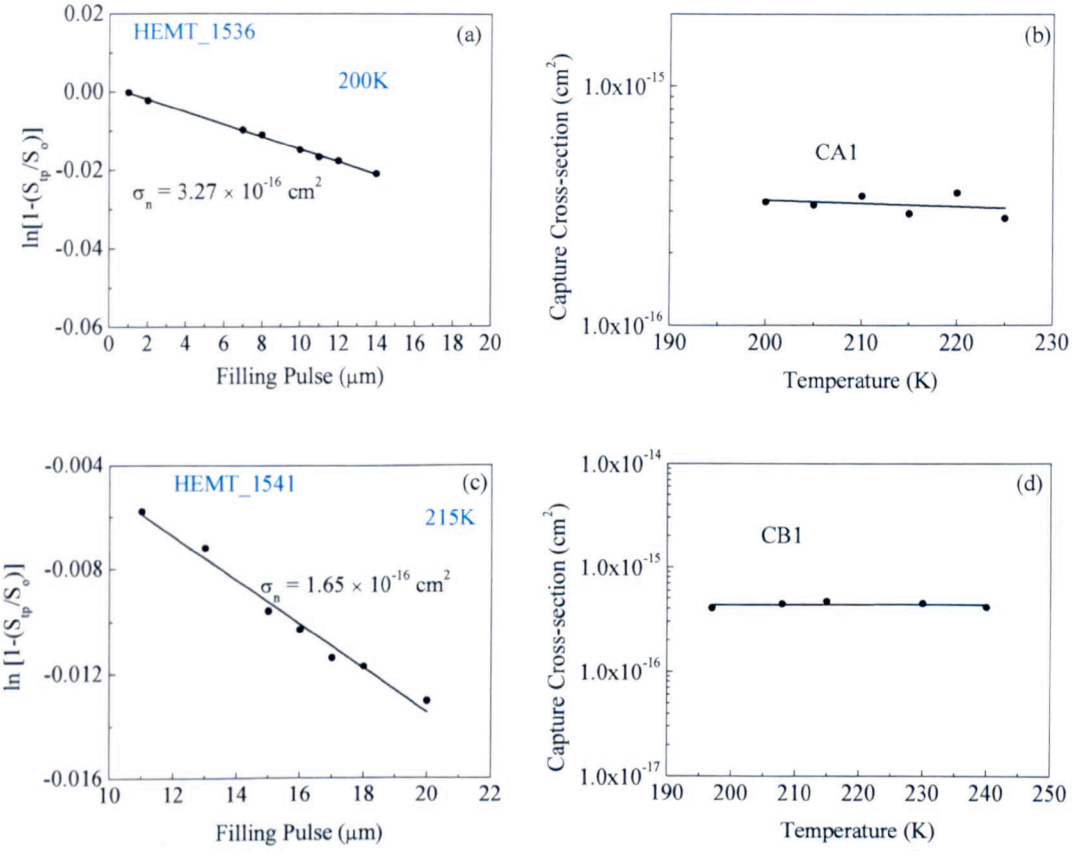

Figure 9.7: Direct capture cross-section measurement data of traps (a) CA1 and (c) CB1; and the effect of temperature on respective capture cross-section (b) CA1 and (d) CB1, respectively.

9.2.5 DETERMINATION OF TRAP CONCENTRATION

The concentration of each defect level is deduced from the amplitude of DLTS signal as described in Chapter 4 and is illustrated in Table 9.1. In addition, the concentration of the common defect (~0.37 eV) level in all the samples is shown in Table 9.2. It is observed that this deep level in sample NU1280, which is doped with the highest Si-doping density (n = 1.33×10^{18} cm^{-3}), has the highest trap concentration of 2.04×10^{18} cm^{-3} as compared to that of NU1297 (n = 1×10^{17} cm^{-3})and HEMT1536 devices [Table 9.1].

Table 9.2: Concentration of a common defect level for each sample.

Sample ID	Common Trap Concentration (cm^{-3})
NU1280 (2DEG)	2.04×10^{18}
NU1297 (2DEG)	1.84×10^{16}
HEMT1536	1.03×10^{15}
HEMT1541	6.22×10^{15}

9.2.6 I-V-T CHARACTERISTICS

In order to find out the energy of the dominant trap that contribute to the reverse current flow through the devices, I-V-T measurements were performed at different temperatures and the data is analysed in a similar way as mentioned in section 8.2.3.

Figure 9.8 illustrates the I-V-T data for: (a) NU1280, (b) NU1297, (c) HEMT1536 and (d) HEMT1541, respectively. All the samples show that the activation energy of the dominant trap is within range of the activation energy of the famous DX center activation energy ranges from 0.36 to 0.50 eV [140, 141].

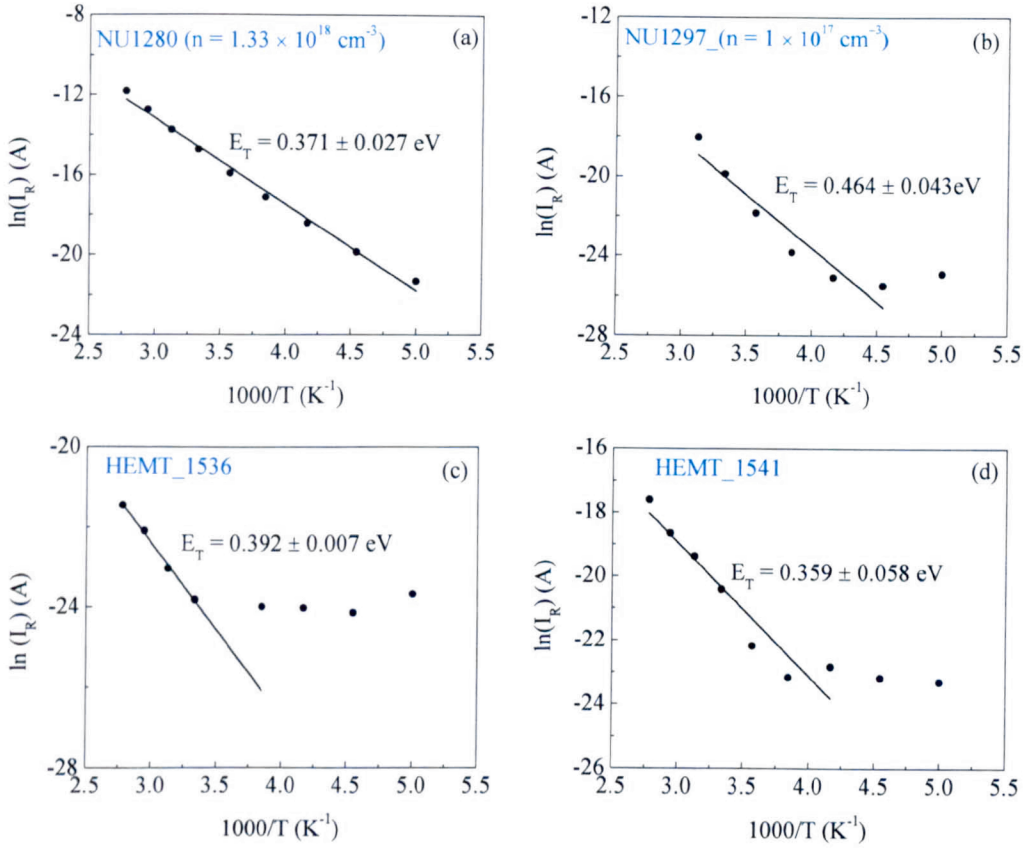

Figure 9.8: I-V-T data of NU1280, NU1297, HEMT1536, and HEMT1541is illustrated in (a)-(e), respectively.

9.3 DISCUSSION

From the experimental results it is evident that a common defect level having activation energy 0.371 ± 0.045 eV (NU1280), 0.382 ± 0.002 eV (NU1297), 0.362 ± 0.007 eV (HEMT1536) and 0.366 ± 0.016 eV (HEMT1541) exists in all the samples under investigation. The other parameters such as apparent capture cross-section and concentration are also illustrated in Table 9.1. It is worth noting that the activation energy of these traps is comparable to that of B5 (0.37 eV) detected in AlGaAs/InGaAs/GaAs MODFET. B5 was assigned to the DX center which is associated with Si doping in AlGaAs layer [142]. The origin of the DX center, which controls the electrical properties of AlGaAs materials, is still controversial. It is

proposed [65, 66] to be associated to a complex center formed by substitutional donor atom (D) and an unknown lattice defect (X), possibly the As vacancy in $Al_xGa_{1-x}As$. It was also suggested [6, 66] that the DX-center could be related to group III vacancy, namely arsenic interstitial or antisite defect (As_{III}) in $Al_xGa_{1-x}As$. Moreover, substitutional donor atoms were put forward as possible candidates for the origin of the DX center [67, 143]. Our experimental results for the in-house grown 2DEG samples support the latter findings, since the concentration of the dominant trap in our devices is dependent on the Si-doping densities in the AlGaAs layer. Its concentration increased by a factor ~100 when the Si-doping in the 2DEG samples changed from 1×10^{17} cm^{-3} (NU1297) to 1.33×10^{18} cm^{-3} (NU1280) (Table 9.1 and Table 9.2). This suggests our dominant trap, which is tentatively assigned to the DX center, is related to the donor doping level in the AlGaAs layer as proposed by [143].

As shown in Table 9.1 and Table 9.2, the concentration of the trap center, tentatively assigned to the DX defect, is about six times greater for HEMT1541 as compared to HEMT1536. Although the reason for this large difference is unknown, it may be possible that some additional background dopants, which can affect the concentration of the defect level, are incorporated during the growth of this specific batch. It is therefore concluded in this study, as predicted, that the frequency response is affected by the trap concentration, the higher the concentration the worse frequency response.

The direct measurements of the capture cross-section of our "DX" center as a function of temperature have shown that the capture cross-section is temperature independent. This implies that there is no evidence of multiphonon capture process for this level [77, 144, 145].

Previous studies [146] believed that an oxygen related (0.48 eV) trap behaved as a recombination center in MBE grown AlGaAs/GaAs heterojunctions. However, the activation energy of our dominant trap, acting as a generation-recombination center, calculated from I-V-T data [Figure 9.8] confirm that the DX center has major contribution in the reverse current flow through these devices. Our results are in agreement with Kunets et al. [140] where they established that the DX center acts as a generation-recombination center in modulation doped $Al_{0.2}Ga_{0.8}As/In_{0.1}Ga_{0.9}As/GaAs$ structures.

The activation energy of NB2 (0.254 ± 0.022 eV) is comparable to that of the defect level having energy of 0.255 eV detected in Si-doped $GaAs/Al_xGa_{1-x}As$ quantum well structures [147]. The authors attributed this defect level in the GaAs layer whose origin is still unknown. It is evident from the capture cross-section data at 190K and the effect of temperature on the capture cross-section (Figure 9.6 (c) and (d), respectively), that there is no evidence found of multiphonon interaction during the capture process [121].

We were unable to measure these devices at higher reverse bias, i.e. >1V due to high reverse current (~10 μA at -1V) is obtained for NU1280, the highly doped ($n = 1.33 \times 10^{18}\ cm^{-3}$) 2DEG sample and it was expected that high reverse current will flow for higher reverse bias and may cause a serious damage to the device. Therefore, the effect of electric field on the carrier emission rates is unknown in this case, and it is very difficult to draw some conclusion on the charged or uncharged nature of this defect level.

In addition to two known traps; NB2 and NB3, another unknown deep level NB1 (0.117 ± 0.022 eV) is detected in 2DEG sample NU1297. It is believed that NB1is

reported here for first time in GaAs/$Al_{0.33}Ga_{0.67}As$ 2DEG structures. From the direct measurements of its capture section, there is no proof of multiphonon interaction during carrier capture. The nature of the charge state of this level was not possible to investigate due to the high leakage current at voltages greater than 1 V.

9.4 CONCLUSION

In summary, DLTS and Laplace DLTS techniques have been employed to characterise the electrically active deep level defects in MBE grown GaAs/$Al_{0.33}Ga_{0.67}As$ 2DEG and commercially grown HEMT devices. It is observed that the DX center is the dominant trap in these samples, with the highest concentration in the highly Si-doped 2DEG (NU1280) sample. This is in agreement to early published literature that suggests the origin of DX center to be related to donor atoms.

The activation energy calculated from I-V-T measurements is in agreement with that obtained from Laplace DLTS measurements and confirms that the DX center is responsible for the reverse current flow mechanism through these devices.

In addition to the common DX center trap, two other deep levels (NB1 and NB2) are detected in NU1297 2DEG sample having a lower Si-doped AlGaAs layer. The activation energy of NB2 is comparable to a GaAs related trap (origin is not known yet) reported in GaAs/AlGaAs MQW structures. NB1 is observed for the first time in MBE grown GaAs/AlGaAs heterostructures.

The capture cross-section of all the traps was found to be temperature insensitive, which confirms that the capture process does not involve multiphonon interaction.

The Laplace DLTS results confirm that the different trap concentration in HEMT1536 and HEMT1541 is responsible for the different frequency response of these HEMT devices.

CHAPTER 10

CONCLUSION AND FUTURE WORK

This chapter summarises the research work carried out on the electrically active deep level defects in GaAs- and AlGaAs-based structures an heterostructures. In addition, suggestions for future work will be highlighted. The MBE samples used in this thesis were investigated by Current-Voltage–Temperature (I-V-T), Capacitance-Voltage (C-V), Deep Level Transient Spectroscopy (DLTS) and Laplace DLTS techniques.

10.1 CONCLUSION

10.1.1 Silicon-Doped n-Type GaAs Grown on High Index Substrates

A set of five MBE n-GaAs samples grown on conventional (100) and high index (211)B, (311)B, (411)B and (511)B oriented GaAs substrates were investigated by DLTS and Laplace DLTS. It is revealed that the reverse leakage current at a given voltage in the (n11)B (n = 2-5) samples decreases with increasing n, i.e. it is highest for (211)B and lowest for (511)B. The (100) samples showed reverse currents lower than (211)B samples. This finding can be explained by the fact that the overall density of defects in (211)B is higher than the defect concentrations in all other GaAs orientations. Some traps, which are common in all samples, have been identified with known defects.

Although, there is no evidence in the literature about the existence of EL2 in as-grown MBE GaAs, the observed mid-gap C3 (0.714±0.002 eV) trap in (311)B is probably related to the EL2-like defect in MBE GaAs. The emission rates of EL2 are known to be sensitive to the junction electric field. However, in this work no such dependence is found for C3. This is a further proof that C3 is not exactly the same as EL2 defect. Further experimental studies are needed to explore the origin of this mid-gap level in as-grown MBE GaAs layers. The levels B1 and B4 are observed in (211)B oriented samples. The activation energy of B1 is related to the reported level M4. There are two controversial suggestions regarding the origin of M4: (i) a complex between chemical impurity and native defects, and (ii) impurity related point defect. Level B4 is similar to EL3 defect which was related to access arsenic.

The neutral defect D3 in (411)B, identified with level EL16 in VPE grown GaAs, is reported here for the first time. Defect levels A1 and A2 in (100), D1 in (411)B, and E1 in (511)B are reported here for the first time. Their origin is not known. However, D1 and E1 are electrically charged levels related to substitutional impurities, whereas, A1, A2, B1, and B4 are substitutional impurities related levels with a neutral nature.

In addition it is also observed that the common and undesirable carbon background impurity in MBE layers is more susceptible to be incorporated in (100) than in high index GaAs substrates. This suggest that devices grown on the conventional (100) could have inferior electrical and optical properties than those grown on (n11)B orientations, where n = 2-5.

10.1.2 Beryllium-Doped $Al_{0.29}Ga_{0.71}As$ Epitaxial Layers Grown on (100) an (311)A

The effect of Be-doping concentrations on deep electrically active defects has been investigated in AlGaAs layers grown on (100) and (311)A GaAs substrates. It is found that for (100) samples the number of hole traps increases when the Be-doping level increases from 1×10^{16} cm^{-3} to 3×10^{16} cm^{-3}. In addition to two hole traps, electron emitting levels are detected in samples doped to 1×10^{17} cm^{-3}. The nature of these negative defects is not known, but they could be related to Si residual dopant in the MBE system. To the contrary of (100) samples, the number of hole traps in (311)A samples decreases with increasing Be-doping level. From the electric field studies both charged and neutral like defects have been confirmed to exist for the samples doped to $1\text{-}3\times10^{16}cm^{-3}$. The traps HA1, HBA2, HB1, HB3, HC1, HC2 and HD1 in samples doped with 1×10^{16} and 3×10^{16} cm^{-3} are ionised after carrier emission and carry an electric charge. However, the traps detected in samples doped to 1×10^{17} $cm^{-3}$are neutral. Finally, few shallow and deep levels traps are detected for the first time in Be-doped AlGaAs grown by MBE, some of which have an electric field dependent emission rates. The rate of change of the activation energy with the electric field is higher for the defect levels detected in the samples grown on (100) plane than those in (311)A samples.

10.1.3 $GaAs/Al_{0.33}Ga_{0.67}As$ MQW Grown on (100) and (311)B GaAs Substrates

$GaAs/Al_{0.33}Ga_{0.67}As$ MQWs grown on (100) and (311)B GaAs substrates were investigated using DLTS and Laplace DLTS techniques. Our experimental results reveal that one and two defect levels are detected in (100) and (311)B samples, respectively. The concentration of trap in (100) orientation is higher. The activation

energy of the dominant trap E1 observed in the sample grown on (100) is found to be dependent on the junction electrical field. The measured value for this trap changes from 0.47 to 1.3 eV as the junction electric field is increased from zero to 4.7×10^6 V/m. Since the emission rates of E1 are dependent on the electric field, it can be concluded that E1 is a charged defect level. On the other hand, EB1 and EB2 traps in (311)B showed no evidence of a field dependence, and therefore their charge states can be confirmed to be neutral. In addition, we observed that the capture cross-section of EB1 is thermally activated, while those of E1 and EB2 are not.

10.1.4 GaAs/$Al_{0.33}Ga_{0.67}As$ MQWs Grown on (100) using As_2 and As_4 Species

A set of six (100) GaAs/$Al_{0.33}Ga_{0.67}As$ MQW samples grown under As_2 and As_4 species, and growth temperatures (600 – 675 °C) were investigated using I-V-T, DLTS and Laplace DLTS techniques. The main finding of this study is that the concentrations of the traps detected in As_2 samples is less than those of As_4 samples, which indicates that better quality MBE grown samples can be obtained by using As_2 instead of As_4 species. It is also found that the reverse leakage current is directly related to the concentration of the main recombination center which has an activation energy of ~0.42 eV as determined from I-V-T and Laplace DLTS measurements. The undetected DLTS peak of the recombination center in NU781 (As_4 and T_G = 600°C) and NU784 (As_4 and T_G = 650°C) is probably due to its very low trap concentration. This is also further confirmed by the very low leakage current observed in these two devices.

The reduction in the concentration of the V_{As}-related point defect with increasing growth temperatures seems to be related with increasing arsenic overpressures. This

argument still needs further confirmation by studying the effect of arsenic overpressures at constant growth temperatures.

10.1.5 GaAs/AlGaAs 2DEG and HEMT Devices

Electrically active defects in in-house MBE grown GaAs/Al0.33Ga0.67As 2DEG heterostructures and commercial HEMT devices have been investigated using DLTS and Laplace DLTS. It is observed that the DX center is the dominant trap in all these samples. In the 2DEG structures the DX center has the highest concentration in the samples with the highest Si-doping in the AlGaAs layer. In addition, the I-V-T experimental results confirm that the DX center is responsible for the reverse leakage current. Furthermore, it is observed that the capture process does not involve multiphonon interaction.

It was also confirmed that the inferior frequency response of HEMT1541 is due to the fact that it has a higher trap concentration as compared to HEMT1536.

10.2 FUTURE WORK

The experimental results carried out in this thesis work lead to the following future directions;

(a) In order to explore the device applications of these novel materials in satellite communications and as detectors, it would be worth to investigate the effect of different sources of irradiations on the defects.

(b) The defect level E1 detected in n-type GaAs/AlGaAs MQW grown on (100) GaAs substrate shows a decrease in its emission rates with increasing reverse bias. This behaviour of emission rates does not follow the existing field dependent models such as Poole-Frenkel, phonon-assisted tunnelling and pure

tunnelling. It would be highly useful to develop a theoretical model to explain this unusual behaviour.

(c) In case of As_2 and As_4 grown GaAs/AlGaAs MQWs it will be of paramount importance to carry out a systematic study to investigate the effect of arsenic overpressure on the concentration of arsenic vacancy (V_{As}) related defects at constant growth temperatures.

(d) The nature of new defects found in 2DEG and HEMT devices need further investigations to find out their nature and microscopic composition.

(e) Confirm the existence of unwanted impurities like carbon or oxygen using Secondary Ion Mass Spectroscopy (SIMS).

REFERENCES

[1] D. B. Holt and B. G. Yacobi, *"Extended Defects in Semiconductors"* (2007) Cambridge University Press: Cambridge, New York, Melbourne, Madrid, Cape Town, Singapore, São Paulo.

[2] L. Pavesi, M. Henini and D. Johnston, *"Influence of As Overpressure During the Molecular Beam Epitaxy Growth of Si-doped (211)A and (311)A GaAs"* Applied Physics Letters, 1995. 66(21): p. 2846.

[3] R. A. Lewis, T. S. Cheng, M. Henini, and J. M. Chamberlain, *"Energy States of Be in GaAs"* Physical Review B, 1996. 53(19): p. 12829.

[4] W. I. Wang, E. E. Mendez, T. S. Kuan, and L. Esaki, *"Crystal Orientation Dependence of Silicon Doping in Molecular Beam Epitaxial AlGaAs/GaAs Heterostructures"* Applied Physics Letters, 1985. 47: p. 826.

[5] Y. G. Chai, R. Chow and C. E. C. Wood, *"The Effect of Growth Conditions on Si Incorporation in Molecular Beam Epitaxial GaAs"* Applied Physics Letters, 1981. 39 (10): p. 800

[6] T. Hayakawa, M. Kondo, T. Suyama, K. Takahashi, S. Yamamoto, S. Yano, T. Hijikata, *"Effect of Group V/III Flux Ratio on Deep Electron Traps in AlxGa1-xAs (x = 0.7) Grown by Molecular Beam Epitaxy"* Applied Physics Letters, 1986. 49(13): p. 788.

[7] J. Xu, E. Towe, Q. Yuan and R. Hull, *"Beryllium Doping and Silicon Amphotericity in (110) GaAs-based Heterostructures: Structural and Optical Properties"* Journal of Crystal Growth, 1999. 196: p. 26.

[8] W. Q. Li, P. K. Bhattacharya, S. H. Kwok and R. Merlin, *"Molecular Beam Epitaxial Growth and Characterization of Silicon-doped AlGaAs and GaAs on (311)A GaAs Substrates and their Device Applications"*. Journal of Applied Physics, 1992. 72(7): p. 3129.

[9] P. P. Gonz´alez-Borrero, M. V. Alves and E. Marega Jr, *"Morphological, Electrical and Optical Properties of Si-doped GaAs Grown by MBE on GaAs non-(100)-Oriented Substrates"* Revista Ci^encias Exatas e Naturais, 2001. 3(2): p. 143.

[10] J. Xu, E. Towe, Q. Yuan and R. Hull, *"Beryllium doping and silicon amphotericity in (1 1 0) GaAs-based heterostructures: structural and optical properties"* Journal of Crystal Growth, 1999, 196(1): p. 26.

[11] N. Galbiati, E. Grilli, M. Guzzi, M. Henini and L. Pavesi, *"Is the Be Incorporation the Same in (311)A and (100) AlGaAs?"* Microelectronics Journal, 1997. 28(8-10): p. 993.

[12] C. T. Foxon, *"MBE Growth of GaAs and III-V Alloys"*. Journal of Vacuum Science and Technology B, 1983. 1(2): p. 293.

[13] S. Yamada, J. Okayasu, S. Gozu, C.U. Hong and H. Hori, *"Dependencies of low-temperature electronic properties of MBE-grown GaAs/AlGaAs single heterojunctions upon arsenic species"* Journal of Crystal Growth, 1999, 201(1): p. 800.

[14] P. Y. Yu, and D. H. C. M. Cardona, *"Fundamentals of Semiconductors"*. 2005: Springer Berlin Heidelberg New York.

[15] N. W. Ashcroft and N.D. Mermin, *"Solid State Physics"*. Book. 1976.

[16] A. M. Glazer, *"The Structure of Crystals"* Book.

[17] Y. M. Galperin, *"Introduction to Modern Solid State Physics"* Book

[18] S. M. Sze and K.K. Ng, *"Physics of Semiconductor Devices"*. 3rd ed. 2007: Wiley-Interscience, A John Wiley & Sons, Inc, Publication.

[19] D. Wood, *"Optoelectronic Semiconductor Devices"*. Book 1994.

[20] L. Pauling, *"The Nature of The Chemical Bond. IV. The Energy of Single Bonds and The Relative Electronegativity of Atoms"* Journal of American Chemical Science, 1932. (54): p. 3570.

[21] R. L. Anderson, *"Germanium-Gallium Arsenide Heterojunction"* IBM Journal of Research and Development, 1960. 4(3): p. 283.

[22] H. Kroemer, *"Nobel Lecture: Quasielectric Fields and Band Offsets: Teaching Electrons New Tricks"* Reviews of Modern Physics, 2001. (73): p. 783.

[23] A. R. Denton and N.W. Aschcroft, *"Vegard's law"*. Physical Review A, 1991. 43(6): p. 3161.

[24] J. P. Colinge and C. A. Colinge, *"Physics of Semiconductor Devices"*. Book

[25] D. K. Schroder, *"Semiconductor Material and Device Characterization"*. 2nd ed. 1998: Wiley-Interscience.

[26] D. K. Schroder, *"Semiconductor Material and Device Characterization"*. 3rd ed. 2006: Wiley-Interscience.

[27]. J. D. Bernal, M. A., F. *"The Goldschmidt Memorial Lecture"*. Journal of the Chemical Society (Resumed), 1929 Republished 1949: p. 2108. [V. M. B. Goldschmidt, J. D, *The Goldschmidt Memorial Lecture.* Journal of the Chemical Society (Resumed), 1929 Republished 1949: p. 7.]

[28] J. S. Blakemore, *"Semiconducting and other Major Properties of Gallium Arsenide"*. Journal of Applied Physics, 1982. 53(10): p. R123.

[29] S. Adachi, *"GaAs, AlAs, and $Al_xGa_{1-x}As$: Material Parameters for use in Research and Device Applications"*. Journal of Applied Physics 1985. 58(3): p. 29.

[30] I. Vurgaftman, J. R. Meyer and L. R. Ram-Mohan, *"Band Parameters for III–V Compound Semiconductors and their Alloys"* Journal of Applied Physics, 2001. 89(11): p. 61.

[31] J. A. Van Vechten and T. K. Bergstresser, *"Electronic Structures of Semiconductor Alloys"*. Physical Review B, 1970. 1(8): p. 8.

[32] I. Kudman and R. J. Paff, *"Thermal Expansion of $In_xGa_{1-x}P$ Alloys"* Journal of Applied Physics 1972. 43(9): p. 3760.

[33] C. Kittel, *"Introduction to Solid State Physics"*. 8th ed: John Wiley & Sons.

[34] C. Van de Walle and J. Neugebauer, *"First-Principles Calculations for Defects and Impurities: Applications to III-nitrides"*. Journal of Applied Physics, 2004. 95(8): p. 3851-3879.

[35] J. Dabrowski and M. Scheffler, *"Theoretical Evidence for an Optically Inducible Structural Transition of the Isolated As Antisite in GaAs - Identification and Explanation of EL2"*. Physical Review Letters, 1988. 60: p. 2183-2186.

[36] D. Chadi, and K. Chang, *"Metastability of the Isolated Arsenic-Antisite Defect in GaAs"*. Physical Review Letters, 1988. 60(21): p. 2187-2190.

[37] S. T. Pantelides, *"The Electronic Structure of Impurities and other Point Defects in Semiconductors"*. Reviews of Modern Physics, 1978. 50 (4): p. 797–858.

[38] W. Shockley and W.T. Read Jr, *"Statistics of the Recombinations of Holes and Electrons"*. Physical Review, 1952. 87(5): p. 835–842.

[39] D. V. Lang, *"Deep-level Transient Spectroscopy: A New Method to Characterize Traps in Semiconductors"*. Journal of Applied Physics, 1974. 45(7): p. 3023.

[40] G. Vincent, A. Chantre and D. Bois, *"Electric Field Effect on the Thermal Emission of Traps in Semiconductor Junctions"*. Journal of Applied Physics, 1979. 50(8): p. 5484.

[41] V. Markevich, A. R. Peaker, V. V. Litvinov, L. I. Murin and N.V. Abrosimov, *"Electric Field Enhancement of Electron Emission from Deep Level Traps in Ge Crystals"*. Physica B, 2006. 376-377: p. 200-203.

[42] S. D. Ganichev, E. Ziemann, W. Prettl, I. N. Yassievich, A. A. Istratov, E. R. Weber, *"Distinction Between the Poole-Frenkel and Tunneling Models of*

Electric-Field-Stimulated Carrier Emission from Deep Levels in Semiconductors". Physical Review B, 2000. 61(15): p. 10361-10365.

[43] S. D. Ganichev, I. N. Yassievich, V. I. Perel, H. Ketterl and W. Prettl, *"Tunneling Ionization of Deep Centers in High-Frequency Electric Fields"*. Physical Review B, 2002. 65(8): p. 085203.

[44] S. D. Ganichev, I. N. Yassievich and W. Prettl, *"Tunnelling Ionization of Deep Centres in High-Frequency Electric Fields"*. Journal of Physics: Condensed Matter, 2002. 14: p. R1263.

[45] A. O. Evwaraye, *"Phonon-Assisted Tunneling from Z1/Z2 in 4H-SiC"*. Journal of Electronic Materials, 2010. 39(6): p. 751.

[46] K. K. Kobayashi, N. Fujimoto, I. Okada, M. T. Suzuki, *"Effect of Growth Conditions on Stoichiometry in MBE-Grown GaAs"*. Journal of Vacuum Science & Technology B, 1985. 3(2): p. 753.

[47] N. H. Ky, D. Martin, and F. K. Reinhart, *"Extrinsic and Intrinsic Defects at Molecular-Beam-Epitaxy Regrown GaAs Interfaces"*. Physica B, 1999. 273-274: p. 729-732.

[48] G. M. Martin, A. Mitonneau, D. Pons, A. Mircea and D. W. Woodward, *"Detailed Electrical Characterisation of the Deep Cr Acceptor in GaAs"*. Journal of Physics C, 1980. 13(20): p. 3855.

[49] H. J. von Bardeleben, J. C. Bourgoin, and D. Stievenard, *Comment on ''Atomic Model for the EL2 Defect in GaAs''*. Physical Review B, 1989. 39(3): p. 1966.

[50] L. Samuelson, P. Omling'H. Titze and H. G. Grimmeiss, *"Electrical and Optical Properties of Deep Levels in MOVPE Grown GaAs"*. Journal of Crystal Growth, 1981. 55(1): p. 164.

[51] P. K. Bhattacharya, J. W. Ku, S. J. T. Owen, V. Aebi, C. B. Cooper, R. L. Moon, *"The Trend of Deep States in Organometallic Vapor-Phase Epitaxial*

GaAs with Varying As/Ga Ratios". Applied Physics Letters, 1980. 36(4): p. 304.

[52] M. D. Miller, G. H. Olsen and M. Ettenberg, *"The Effect of Gas-Phase Stoichiometry on Deep Levels in Vapor-Grown GaAs"*. Applied Physics Letters, 1977. 31(8): p. 538.

[53] P. A. Schultz and O. A. von Lilienfeld, *"Simple Intrinsic Defects in Gallium Arsenide"*. Modelling and Simulation in Materials Science and Engineering, 2009. 17(8): p. 084007.

[54] S. T. Lai, D. Alexiev, and B. D. Nener, *"Comparison between deep level defects in GaAs induced by gamma, 1 MeV electron, and neutron irradiation"*. Journal of Applied Physics, 1995. 78(6): p. 3686.

[55] Katsuhiro. Yokota, Hideto. Kuchii, Kazuhiro. Nakamura, Masanori. Sakaguchi, Hiromichi. Takano, Yasunori. Ando, *"EL2, EL3, and EL6 Defects in GaAs Highly Implanted with Sulphur"*. Journal of Applied Physics, 2000. 88(9): p. 5017.

[56] J. R. Morante, A. Perez-Rodriguez, J. Samitier, A. Romano-Rodriguez, *"On the Artificial Creation of the EL2 Center by Means of Boron Implantation in Gallium Arsenide"*. Journal of Applied Physics, 1991. 70(8): p. 4202.

[57] R. Yakimova, T. Paskova and C. Hardalov, *"Behavior of an EL5-Like Defect in Metalorganic Vapor-Phase Epitaxial GaAs:Sb"*. Journal of Applied Physics, 1993. 74(10): p. 6170.

[58] Elmar E.Wagner, Dan E. Mars, Gil Hom, G. B. Stringfellow, *"Deep Electron Traps in Organometallic Vapor Phase Grown $Al_xGa_{1-x}As$"*. Journal of Applied Physics, 1980. 51(10): p. 5434.

[59] A. S. Tabata, M. A. A. Pudensi and A. M. Machado, *"Metastable Defects in GaAs Grown by Metalorganic Chemical Vapor Deposition: Dependence on the V/III Ratio"*. Journal of Applied Physics, 1989. 65(10): p. 4076.

[60] D. V. Lang, R. A. Logan and L. C. Kimerling, *"Identification of the Defect State Associated with a Gallium Vacancy in GaAs and $Al_xGa_{1-x}As$"*. Physical Review B, 1977. 15(10): p. 4874.

[61] D. Pons, A. Mircea and J. Bourgoin, *"An Annealing Study of Electron Irradiation-Induced Defects in GaAs"*. Journal of Applied Physics, 1980. 51(8): p. 4150.

[62] H. Z. Zhu, Y. Adachi and T. Ikoma, *"Deep Levels in MOCVD GaAs Grown under Different Ga/As Mol Fractions"*. Journal of Crystal Growth, 1981. 55(1): p. 154.

[63] Z. Q. Fang, T. E. Schlesinger and A. G. Milnes, *"Evidence for EL6 (Ec−0.35 eV) Acting as a Dominant Recombination Center in n-type Horizontal Bridgman GaAs"*. Journal of Applied Physics. 1987. 61(11): p. 5047.

[64] K. Yamanaka, S. Naritsuka, K. Kanamoto, M. Mihara, M. Ishii, *"Electron Traps in AlGaAs Grown by Molecular-Beam Epitaxy"*. Journal of Applied Physics, 1987. 61(11): p. 5062.

[65] P. M. Mooney, *"Deep Donor Levels (DX centers) in III-V Semiconductors"*. Journal of Applied Physics, 1990. 67(3): p. R1.

[66] D. V. Lang and R. A. Logan, *"Large-Lattice-Relaxation Model for Persistent Photoconductivity in Compound Semiconductors"*. Physical Review Letters, 1977. 39(10): p. 635.

[67] Masashi Mizuta, Masami Tachikawa, Hiroshi Kukimoto and Shigeru Minomura1, *"Direct Evidence for the DX Center Being a Substitutional Donor in AlGaAs Alloy System"*. Japanese Journal of Applied Physics, 1985. 24: P. L143

[68] E. Calleja, A. Gomez and E. Muñoz, *"Direct Evidence of the DX Center Link to the L-Conduction-Band Minimum in GaAlAs"*. Applied Physics Letters, 1988. 52(5): p. 383.

[69] S. Azema, V. Mooser, J. Camassel, R. Piotrzkowski, J. L Roberts, P. Gimbart, J. P Contour, J. Massie, A. Marty, *Defects in Semiconductors*. 1989 (Book)

[70] W. I. Wang, E. E. Mendez, T. S. Kuan, and L. Esaki, *"Crystal Orientation Dependence of Silicon Doping in Molecular Beam Epitaxial AlGaAs/GaAs Heterostructures"*. Applied Physics Letters, 1985. 47(8): p. 826.

[71] N. Galbiati, E. Grilli, M. Guzzi, L. Brusaferri, L. Pavesi and M Henini, *"Photoluminescence Investigation of Si as p-type Dopant in AlGaAs Grown by Molecular Beam Epitaxy on High-Index Planes"*. Semiconductor Science and Technology, 1996. 11(12): p. 1830.

[72] T. Ohachi, *"MBE growth of AlGaAs/GaAs heterostructure and silicon doping on GaAs(n11)A (n = 1-4) substrates"*. Journal of Crystal Growth 1999. 201/202(3): p. 226.

[73] L. Pavesi and M. Henini, *"Photoluminescence Investigation of Si-doped GaAs Grown by Molecular Beam Epitaxy on non-(100) Oriented Surfaces"*. Microelectronics Journal, 1997. 28(6): p. 717.

[74] R. Sarmiento, A. Somintac, L. Guiao, F. Agra and A. Salvador, *"Electron Traps in GaAs Grown by Molecular Beam Epitaxy on On-axis (100) and Off-axis Substrates"*. Science Diliman, 2003. 15(1): p. 6.

[75] User's Manual *"Keithley Source Meter/236"*

[76] A. Telia, B. Lepley, and C. Michel, *"Experimental-Analysis of Temperature-Dependence of Deep-Level Capture Cross-Section Properties at the Au Oxidized InP Interface"*. Journal of Applied Physics, 1991. 69(10): p. 7.

[77] C. H. Henry, and D. V. Lang, *"Nonradiative Capture and Recombination by Multiphonon Emission in GaAs and GaP"*. Physical Review B, 1977. 15(2): p. 989.

[78] A. Akbar, M. Shafi and A. Majid, *"Electron Capture Cross-Section of Au–Fe Complex in Silicon"*. Physica Scripta, 2006. 74(4): p.450.

[79] K. Ikossi-Anastasiou, and K.P. Roenker, *"Refinements in the Method of Moments for Analysis of Multiexponential Capacitance Transients in Deep-*

Level Transient Spectroscopy". Journal of Applied Physics, 1987. 61(1): p. 182.

[80] L. Dobaczewski, A. R. Peaker and K. B. Nielsen, *"Laplace-Transform Deep-Level Spectroscopy: The Technique and its Applications to the Study of Point Defects in Semiconductors"*. Journal of Applied Physics, 2004. 96(9):p. 4689.

[81] L. Dobaczewski, P. Kaczor, I. D. Hawkins and A. R. Peaker, *"Laplace Transform Deep-Level Transient Spectroscopic Studies of Defects in Semiconductors"*. Journal of Applied Physics 1994. 76(1): p. 194.

[82] P. Deixler, J. Terry, I. D. Hawkins, J. H. Evans-Freeman, A. R. Peaker, L. Rubaldo, D. K. Maude, J.-C. Portal, L. Dobaczewski, K. Bonde Nielsen, A. Nylandsted Larsen, A. Mesli, *"Laplace-Transform Deep-Level Transient Spectroscopy Studies of the G4 gold–hydrogen Complex in Silicon* Applied Physics Letters, 1998. 73(21): p. 3126.

[83] M. N. Jirmanus, *Introduction to Laboratory Cryogenics,[Manual]*. I. Janis Research Company, Editor: Wilmington.

[84] E. Maloof, *"User's Manual Model 331 Temperature Controller"*. 2005, LakeShore.

[85] Boonton, *"Model 7200 Capacitance Meter Instruction Manual"*, Boonton. 1996.

[86] *"User's Guide Agilent 33220A 20MHz Function/Arbitrary Waveform Generator". 2007*, Agilent Technologies, Inc.

[87] L. Dobaczewski, *"Laplace Transform Transient Processor and Deep Level Spectroscopy Manual"*. Last Modification 2010.

[88] M. Henini, *"Proceedings of 5th International Workshop on Epitaxial Semiconductor on Patterned Surfaces and Novel Index Surfaces (ESPS-NIS)"*. 2004, Physica E. (introductory page)

[89] B. Lee, S. S. Bose, M. H. Kim, A. D. Reed, G. E. Stillman ,W. I. Wang, L. Vina, P. C. Colter. *"Orientation Dependent Amphoteric Behavior of Group*

IV Impurities in the Molecular Beam Epitaxial and Vapor Phase Epitaxial Growth of GaAs". Journal of Crystal Growth, 1989. 96(1): p. 27.

[90] A. Kitagawa, A. Usami and T. Wada, *"Effect of Rapid Thermal Processing on Electron Traps in Molecular-Beam-Epitaxial GaAs"*. Journal of Applied Physics, 1989. 65(2): p. 606.

[91] A. Ito, A. Kitagawa, Y. Tokuda, A. Usami, H. Kano, H. Noge and T. Wada, *"A Comparison of Deep Levels in Rapidly Thermal-Processed GaAs Films Grown by Molecular Beam Epitaxy on Si and GaAs Substrates"*. Semiconductor Science and Technology, 1989. 4(5): p. 416.

[92] Naresh Chand, A. M. Sergent, J. P. van der Ziel, and D. V. Lang, *"Reduction and Origin of Electron and Hole Traps in GaAs Grown by Molecular-Beam Epitaxy"*. Journal of Vacuum Science and Technology B, 1989. 7(2): p. 339.

[93] DeJule, R.Y., M.A. Haase, and G.E. Stillman, *"Measurements of Deep Levels in High-Purity Molecular Beam Epitaxial GaAs"*. Journal of Applied Physics, 1985. 57(12): p. 5287.

[94] Yoshitaka Okada, James S. Harris and Werner Götz, *"Deep Level Defects in GaAs on Si Substrates Grown by Atomic Hydrogen-assisted Molecular Beam Epitaxy"*. Journal of Applied Physics, 1996. 80(8): p. 4770.

[95] D. V. Lang, A. Y. Cho, A. C. Gossard, M. Ilegems and W. Wiegmann, *"Study of Electron Traps in n-GaAs Grown by Molecular Beam Epitaxy"*. Journal of Applied Physics, 1976. 47(6): p. 2558.

[96] W. C. Dautremont-Smith, J. C. Nabity, V. Swaminathan, Michael Stavola, J. Chevallier, C. W. Tu and S. J. Pearton, *"Passivation of Deep Level Defects in Molecular Beam Epitaxial GaAs by Hydrogen Plasma Exposure"*. Applied Physics Letters, 1986. 49(17): p. 1098.

[97] M. B. Stanaway, R. T. Grimes, D. P. Halliday, J. M. Chamberlain, M. Henini, O. H. Hughes, M. Davies, G. Hill: *"Residual Impurities in Autodoped n-GaAs Grown by MBE"*. Institute of Physics Conference Series 95: Chapter 4.

Presented at International Conference on Shallow Impurities in Semiconductors Linkoping, Sweden; 1988.

[98] G. M. Martin, A. Mitonneau and A. Mircea, *"Electron Traps in Bulk and Epitaxial GaAs Crystals"*. Electronics Letters, 1977. 13(7): p. 191.

[99] D. Liu, T. Zhang, R. A. LaRue, J. S. Harris and T. W. Sigmon, *"Deep Level Transient Spectroscopy Study of GaAs Surface States Treated with Inorganic Sulfides"*. Applied Physics Letters, 1988. 53(12): p. 1059.

[100] D. S. Day, J. D. Oberstar, T. J. Drummond, H. Morkoc, A. Y. Cho, B. G. Streetman, *"Electron Traps Created by High-Temperature Annealing in MBE n-GaAs"*. Journal of Electronic Materials 1981. 10(3): p. 445.

[101] Miyoko Oku Watanabe, Atsushi Tanaka, Takatosi Nakanisi and Yasuhito Zohta, *"Effects of the Growth Conditions on Deep Level Concentrations in MOCVD GaAs"*. Japanes Journal of Applied Physics, 1981. 20(6): p. L429.

[102] N. P. Khuchua, L. V. Khvedelidze, M. G. Tigishvili, N. B. Gorev, E. N. Privalov and I. F. Kodzhespirova, *"Deep-Level Effects in GaAs"* Russian Microelectronics, Vol. 32, No. 5, 2003, pp. 257–274. Translated from Mikroelektronika, Vol. 32, No. 5, 2003, pp. 323–343.

[103] J. C. Bourgoin, H. J. von Bardeleben and D. Stievenard, *"Native Defects in Gallium Arsenide"*. Journal of Applied Physics, 1988. 64(9): p. R65.

[105] C. Nyamhere, J. R. Botha and A. Venter, *"Electrical Characterization of Deep Levels in n-type GaAs after Hydrogen Plasma Treatment"*. Phyaica B, 2011. 406: p. 2274.

[106] R. Ferragut, A. Calloni, A. Dupasquier and G. Isella, *"Defect Characterization in SiGe/SOI Epitaxial Semiconductors by Positron Annihilation"*. Nanoscale Research Letters, 2010. 5: p. 1942.

[107] N. Galbiati, E. Grilli, M. Guzzi, P. Albertini, L. Brusaferri, L. Pavesi, M. Henini and A. Gasparotto *"Investigation of Si as an n-type Dopant in AlGaAs*

Grown by Molecular Beam Epitaxy on High Index Planes". Semiconductor Science and Technology, 1997. 12(5): p. 555.

[108] L. Pavesi, M. Henini, D. Johnston and I. Harrison, *"A Comparison of Si-doped (100), (111)A, (111)B and (311)B $Al_xGa_{1-x}As$ Samples Grown by Molecular Beam Epitaxy"*. Semiconductor Science and Technology, 1995. 10(1): p. 49.

[109] S. S. Bose, B. Lee, M. H. Kim, G. E. Stillman, W. I. Wang, Bose, *"Influence of the Substrate Orientation on Si Incorporation in Molecular-Beam Epitaxial GaAs"*. Journal of Applied Physics, 1988. 63(3): p. 743.

[110] Kazuhiro Mochizuki, Shigeo Goto and Chuushiro Kusano, *"(311) A Substrates Supperession of Be Transport During GaAs Molecular Beam Epitaxy"*. Applied Physics Letters, 1991. 58(25): p. 2939.

[111] D. H. Zhang, K. Radhakrishnan, S. F. Yoon and Z. Y. Han, *"Photoluminescence in Degenerate p-type GaAs Layers Grown by Molecular Beam Epitaxy"* Materials Science and Engineering B, 1995. 35(1-3): p. 449.

[112] Shigeo Fujita, S. M. Bedair, M. A. Littlejohn and J. R. Hauser, *"Doping Characteristics and Electrical Properties of Be-doped p-type $Al_xGa_{1-x}As$ by Liquid Phase Epitaxy"*. Journal of Applied Physics, 1980. 51(10): p. 5438.

[113] J. Szatkowski, E. Płaczek-Popko, and K. Sieran'ski, *"Deep Hole Traps in Be-doped $Al_{0.5}Ga_{0.5}As$ Layers Grown by Molecular Beam Epitaxy"*. Journal of Applied Physics, 1999. 86(3): p. 1433.

[114] S. Kalem and G. E. Stillman, *"Deep Acceptor Levels in Molecular Beam Epitaxial High Purity p-type GaAs"*. Japanese Journal of Applied Physics, 1994. 33(11): p. 6086.

[115] J. Szatkowski, K. Sieranski, A. Hajdusianek, E. Placzek-Popko: *"Deep Hole Traps in Be-Doped $Al_{0.2}Ga_{0.8}As$ Layers Grown by Molecular Beam Epitaxy"*. Physica B 2003, 340-342: p. 345-348.

[116] N. Galbiati, L. Pavesi, E. Grilli, M. Guzzi and M. Henini, *"Be Doping of (311)A and (100) $Al_{0.24}Ga_{0.76}As$ Grown by Molecular Beam Epitaxy"*. Applied Physics Letters, 1996. 69(27): p. 4215.

[117] R. Ajjel, and H. Maaref, *"Electrical Properties of GaAs-$Al_{0.46}Ga_{0.54}As$ Superlattice within a Wider Quantum Well"*. Microelectronics Journal, 2006. 37(11): p. 1404.

[118] M. S. Kagan, I. V. Altukhov, E. G. Chirkova, V. P. Sinis, R. T. Troeger, S. K. Ray and J. Kolodzey, *"THz Lasing of SiGe/Si Quantum-Well Structures due to Shallow Acceptors"*. Physica Status Solidi B, 2003. 235(1): p. 135.

[119] Qin-Sheng Zhu, Zong-Quan Gu, Zhan-Tian Zhong, Zeng-Qi Zhou and Li-Wu Lu, *"Determination of the X-Conduction-Subband Energies in Type-II GaAs/AlAs/GaAs Quantum-Well by Deep-evel Transient Spectroscopy"*. Applied Physics Letters, 1995. 67(24): p. 3593.

[120] Y. B. Jia, H. G. Grimmeiss and L. Dobaczewski, *"Deep Acceptorlike States in Si Doped Molecular-Beam-Epitaxial-Grown $Al_xGa_{1-x}As$"*. Journal of Applied Physics, 1996. 80(2): p. 859.

[121] A. Arbaoui, B. Tuck, C. J. Paull and M. Henini, *"Deep Levels in GaAs/AlGaAs Multi-Quantum-Well Structures"*. Journal of Materials Science-Materials in Electronics, 1990. 1(2): p. 75-78.

[122] C. H. Henry and D. V. Lang, *"Nonradiative Capture and Recombination by Multiphonon Emission in GaAs and GaP"*. Physical Review B, 1977. 15(2): p. 989.

[123] J. Frenkel, *"On Pre-Breakdown Phenomena in Insulators and Electronic Semi-Conductors"*. Physical Review, 1938. 54(8): p. 647.

[124] Y. B. Jia and H. G. Grimmeiss, *"Field Dependence of Emission and Capture Rates of DX-related Centers in $Al_xGa_{1-x}As$"*. Physical Review B, 1993. 47(4): p. 1858

[125] C. Y. Chang, W. C. Hsu, S. J. Wang and S. S. Hau, *"Capture-Emission Process in Double Poole–Frenkel Well Traps: Theory and Experiments"*. Journal of Applied Physics, 1986. 60(3): p. 1042.

[126] J. Y. Kim, D. Bassi and L. Jostad, *"Reflection High-Energy Electron Diffraction Dynamics Study of GaAs, AlAs, and $Al_{0.5}Ga_{0.5}As$ Layer Growth under As_4 and/or As_2 Molecular Beam Species"*. Applied Physics Letters, 1990. 57(20): p. 2107.

[127] J. Y. Kim, D. Bassi, J. Ellis and L. Jostad Kim, *"Photoluminescence and Reflection High-Energy Electron Diffraction Study of GaAs/$Al_xGs_{1-x}As$(100) Single Quantum Wells Grown via Molecular Beam Epitaxy Employing two forms (As_2 and As_4) of Arsenic"*. Applied Physics Letters, 1990. 57(22): p. 2333.

[128] J. Y. Kim, P. Chen, F. Voillot and A. Madhukar, *"Photoluminescence and Reflection High-Energy Electron Diffraction Dynamics Study of the Interfaces in Molecular Beam Epitaxially Grown GaAs/$Al_{0.33}Ga_{0.67}As$(100) Single Quantum Wells"*. Applied Physics Letters, 1987. 50(12): p. 739.

[129] P. M. Mooney, R. Fischer, and H. Morkoc, *"Transient Capacitance Study of Electron Traps in AlGaAs Grown with As2"*. Journal of Applied Physics, 1985. 57(6): p. 1928.

[130] T. Hayakawa, M. Nagai, M. Morishima, H. Horie and K. Matsumoto, *"Molecular Beam Epitaxial Growth of $Al_xGa_{1-x}As$ (x = 0.2-0.7) on (111)B-GaAs using As_4 and As_2"*. Applied Physics Letters, 1991. 59(18): p. 2287.

[131] Boussairi Bouzazi, Hidetoshi Suzuki, Nobuaki Kojima, Yoshio Ohshita and Masafumi Yamaguchi, *"Nitrogen-Related Center in GaAsN Grown by Chemical Beam Epitaxy"*. Japanese Journal of Applied Physics, 2010. 49: p. 051001.

[132] Umar S. Qurashi, Nazir A. Naz, M. Naeem Khan, Nasim Zafar, M. Zafar Iqbal, P. Krispin and R. Hey, *"Deep Levels in GaAs/$Al_{0.78}Ga_{0.22}As$ Heterostructures"*. Physica B, 2007. 401-402: p. 266-269.

[133] P. A. Martin, K. Hess, M. Emanuel and J. J. Coleman, *"Deep-Level Transient Spectroscopy Studies of Defects in GaAs-AlGaAs superlattices"*. Journal of Applied Physics, 1986. 60(8): p. 2882.

[134] Hoon Young Cho, Eun Kyu Kim and Suk-Ki Min Cho, *" A Relation Between EL2 (Ec - 0.81 eV) and EL6 (Ec - 0.35 eV) in Annealed HB-GaAs by Hydrogen Plasma Exposure"*. Journal of Applied Physics, 1989. 66(7): p. 3038.

[135] M. Kaminska, M. Skowronski and W. Kuszko, *"Identification of the 0.82-eV Electron Trap, EL2 in GaAs, as an Isolated Antisite Arsenic Defect"*. Physical Review Letters, 1985. 55(20): p. 2204.

[136] M. Kaminska, *"EL2 Defect in GaAs"*. Physica Scripta, 1987. T19B: p. 551.

[137] Jin-Hee Lee, Hyung-Sup Yoon, Chul-Soon Park, Hyung-Moo Park, *"Ultra Low Noise Characteristics of AlGaAs/InGaAs/GaAs Pseudomorphic HEMT's with Wide Head T-Shaped Gate"*. IEEE Electron Device Letters, 1995. 16(6): p. 271.

[138] J. H. Hur, C. W. Myles and M. A. Gundersen, *"Avalanche Breakdown in p-n AlGaAs/GaAs Heterojunctions"*. Journal of Applied Physics, 1990. 67(11): p. 6917.

[139] B. G. Yacobi, *"Semiconductor Materials: An Introduction to Basic Principles"*. 2003-2004: Kluwer Academic/Plenum Publishers, New York

[140] V. P. Kunets, R. Pomraenke, J. Dobbert, H. Kissel, U. Muller, H. Kostial, E. Wiebicke, G. G. Tarasov, Y. I. Mazur, W. T. Masselink, *"Generation-Recombination Noise in Pseudomorphic Modulation-Doped $Al_{0.2}Ga_{0.8}As/In_{0.1}Ga_{0.9}As/GaAs$ Micro-Hall Devices"*. IEEE Sensors Journal 2005. 5(5): p. 883.

[141] J. C. Nabity, Michael Stavola, J. Lopata, W. C. Dautremont-Smith, C. W. Tu and S. J. Pearton, *"Passivation of Si Donors and DX Centers in AlGaAs by Hydrogen Plasma Exposure"*. Applied Physics Letters, 1987. 50(14): p. 921.

[142] I. Dermoul, F. Chekir, M. Ben Salem, A. Kalboussi and H. Maaref, *"Deep Level Investigation in AlGaAs/InGaAs/GaAs Cryoelectronic MODFET"*. Solid-State Electronics, 2001. 45(7): p. 1059.

[143] L. Dobaczewski, P. Kaczor, M. Missous, A. R. Peaker and Z. R. Zytkiewicz, *"Structure of the DX State from by Donors in (Al,Ga)As and Ga(As,P)"*. Journal of Applied Physics, 1995. 78(4): p. 2468.

[144] C. Hemmingsson, N. T. Son, O. Kordina, E. Janzén and J. L. Lindström, *"Capture Cross Sections of Electron Irradiation Induced Defects in 6H-SiC"*. Journal of Applied Physics, 1998. 84(2): p. 704.

[145] D. V. Lang and C. H. Henry, *"Nonradiative Recombination at Deep Levels in GaAs and GaP by Lattice-Relaxation Multiphonon Emission"*. Physical Review Letter, 1975. 35(22): p. 1525.

[146] Shigekazu Izumi, Masayuki Sakai, Teruyuki Shimura, Norio Hayafuji, Kazuhiko Sato, and Mutsuyuki Otsubo, *"Evaluation of Molecular Beam Epitaxially Grown AlGaAs/GaAs Heterjunctions for Bipolar Transistor with InGaAs Emitter Contact Layer"*. Applied Physics Letters, 1996. 69(17): p. 2516.

[147] Y. B. Jia, Z. Y. Han, H. G. Grimmeiss, L. Dobaczewski, *"Deep Levels in Uniformly Si dooped GaAs/$Al_xGa_{1-x}As$ Quantum Well and Superlattices"*. Journal of Applied Physics, 1996. 80(5): p. 2860.